Deciphering the Tectonics of the Caucasus from Post-Collisional Volcanism

Thesis

Deciphering the Tectonics of the Caucasus from Post-Collisional Volcanism

Samuel Bewick
MSci (University of London) 2010

A thesis presented for the degree of
Doctor of Philosophy

Department of Environment, Earth and Ecosystems
The Open University, United Kingdom
September 2016

What I offer you is little more than a number of questions; but questions are the buds on the tree of knowledge.

Eduard Suess
American Journal of Science, 31, 1911, p. 108

Abstract

The southern margin of the Eurasian plate is a well-studied region of continental collision. The Caucasus mountains lie at the centre of the Alpine-Himalayan orogenic belt, and differ from their better studied neighbours by the presence of intense, largely mantle-derived post-collisional magmatism. Volcanism began 5–15 Ma after the initial collision occurred, and after the crust had already thickened to 45–60 km. This thesis presents bulk-rock and mineral element and isotope geochemistry to assess the role of asthenosphere, lithosphere and crust in generating contemporaneous volcanism across the region. Broad similarities are seen between volcanism in the Greater and Lesser Caucasus, dominated by calc-alkaline basalt-dacite (48–72 wt% SiO_2) compositions. High Mg# cores (>85) of olivines suggest significant fractionation has occurred. Trace element patterns show a distinctive supra-subduction setting, suggesting the fluid-enriched source remained in place, and hydrated >10 Ma following collision. Isotope ratios require an asthenospheric component in the early Lesser Caucasus melts, whilst sediment-enrichment of the source is observed across the region. Little interaction with the thickened crust is observed. For the Lesser Caucasus, a model of Palaeo-Tethyan slab break-off is proposed, resulting in asthenospheric upwelling and melting of an enriched lithosphere. Small-scale convection continues to produce drips, leading to episodic pulses of magmatism. Subduction of back-arc crust with slab-breakoff is proposed beneath the Greater Caucasus, allowing melting of enriched lithosphere, with distinguishable fluid, and slab-melt components. Although contemporaneous, and volcanism in the Lesser and Greater Caucasus being geochemically similar in many respects, a shared source is ruled out because of tectonic constraints. Strike-slip faulting, the result of a tectonic regime shift at 5 Ma, determined the location of volcanoes. Although the style of post-collisional magmatism may not be characteristic of all continental collision zones, where present it has a high preservation potential. It may therefore play a significant role in the formation, and composition of continental crust that is largely unrecognised in models of continental crust evolution.

Acknowledgments

Firstly I would like to thank my supervisors, Nigel Harris, Sam Hammond, Ian Parkinson and Shota Adamia, for their support, advice, and giving me this opportunity in the first place. Particular thanks has to go to Nigel for letting me get on and do it my own way. I would also like to thank Clare Warren (I hate to say it, but sometimes your advice and notes really were what I needed to hear). Thanks also goes to Fran, Bruce, Nick, and the rest of the geochemistry group for all the discussions. A huge thanks has to go to Nino, Nato, Guram and Levan. This project wouldn't have been possible without their field knowledge, and the huge eort they put in to the logistical side of the field work. Thanks again for all the help, and making us feel so welcome in Georgia, and showing us some of the best scenery, food, wine and cha cha that your country has to offer.

გმადლობთ დახმარებისთვის

This project would not have been possible without the generous funding from the Natural Environment Research Council (NERC project reference NE/K501074/1)

I also have to thank all the people that have helped me in the labs, including John Watson, Michelle Higgins, Kaye Green, Andy Tindle, Manuela Fehr, Bruce Charlier and Marie-Laure Bagard. But special thanks has to go to Sam Hammond who would always be there, willing to help, no matter how stupid what I had done wrong was. Before even reaching the Open University, I had the opportunity to work with many inspirational teachers at school (thanks Mr Donnally and Mr Slack) and staff at Royal Holloway who kept me loving geology.

Thanks has to go to everyone who has helped me survive four years in Milton Keynes. Starting with all those that have put up with me in the office, and shared a cha cha or a beer on those bad days, or offered a game of squash on those days when hitting a little ball solved so many problems (So big thanks to Tom, Adele, Kerry, Anouk, Pete, Fraser and Hayley). Thanks to all my other friends at the Open University, and around Milton Keynes who have kept me relatively sane throughout this time. Thanks also has to go to my family for their constant support (and constantly asking when I'd be done and getting a proper job). The final thanks is saved for Mike. I'm not sure what I would have done without you, all the adventures, the amazing dinners to come home to (sometimes), the cakes to keep me happy, and even persuading me to get a dog (I suppose I also have to thank Hugo for being such a cute and loving distraction in the last few months). I don't know how you've put up with me, but you've helped me more than you can believe by just being there.

Table of Contents

List of Figures

List of Tables

Page

Chapter 1

Introduction and Thesis Overview

The theory of plate tectonics has provided an excellent framework to understand the location and styles of volcanism around the world. It has also helped explain how mountains are built. Convergent margins are of particular interest as they represent the transition between initial subduction, through a period of major arc volcanism, and terminating in a mountain building event, before relaxation, collapse and extension can occur, beginning the cycle again. It has also been recognised that this cycle plays a vital role in the formation of continental crust through magmatic addition and accretion of terranes. Finally they play a key role in the global budgets of many trace elements and volatiles. One area of this system that has traditionally received less attention than the others is post-collisional volcanism which occurs after the collision has occurred, but prior to the extensional phase beginning. This may be because it is less commonly observed, the volcanism is less voluminous than the initial arc phase, or that is just not (yet) present in the most well-studied, archetypal collision-zone, the Himalayas.

The southern Eurasian margin is dominated by continental collision, with the Alps and the Himalayas. Situated between those two, but receiving far less attention, are the Caucasus mountains. Politically, this region has been quite volatile. However, since the break-up of the Soviet Union, the region has become far more accessible, and that is reflected by the increase in publications in the western literature focusing on the region from the past 15–20 years. Not only do the Caucasus provide a contrasting orogen with the Himalayas to contribute to our understanding of the early part of continent collision, but they also preserve the largest region of post-collisional volcanism in the world, covering much of Georgia, Armenia, East Anatolia (Turkey), and parts of Azerbaijan, Iran and Russia.

This type of volcanism can be difficult to understand due to the complex nature of its

tectonic setting. The pre-collision subduction phase introduces many constituents, such as the incoming plate, subduction slab, arc-trench complex and mantle wedge. With the subducting slab comes pelagic and terrigenous sediments, the oceanic basaltic crust, often strongly serpentinised, and the lithospheric mantle, all of which have different geochemical signatures. Volcanism has to pass through the recently thickened crust, with its highly variable lithologies, and multiple faults and pathways. Asthenospheric material can be introduced into the system by either slab breakoff, or delamination beneath the orogen.

Throughout this thesis, the term 'post-collisional' will be used to describe the volcanism within the Caucasus. The Caucasus is still an active collision zone, so it could be referred to as syn-collisional. The 'post-' refers to the fact that the volcanism began after a significant change in the collision, from N-S compression, to a stress-field where a significant amount of the shortening involves the easterly expulsion of the Anatolian Plate, a change which occurred around 5 Ma, and is discussed in more detail in section 2.2.2. Post-collisional in this thesis does not refer to the extensional regime often exhibited significantly after collision, relate to orogenic collapse.

This thesis will use a combined approach involving field observations, detailed petrography, and geochemical analyses of both mineral phases, and major-, trace- and isotopic (Sr-Nd-Pb-Hf) bulk-rock analyses. This will be used to help distinguish, and evaluate the roles of the various inputs into the system, all the way from the source, through to interactions at the surface. When combined with published seismic, and field studies, a petrogenetic model of the volcanics, is proposed to constrain the geodynamic evolution of the region. The elucidation of this poorly understood style of volcanism contributes to understanding of mountain building events, and the formation of continental crust.

This will be done in order to answer whether voluminous post-collisional volcanism, such as that present in the Caucasus, is expected to occur as a intrinsic part of continental-collision, or if the traditional model of collision (i.e. Himalayan), which lacks volcanism, should still be regarded as the go-to model, with the Caucasus having special conditions producing such a large volume of magma.

1.1 Thesis Overview

Chapter 2 provides an overview of the geology of the Arabia-Eurasia collision zone. The geological history from the Palaeozoic, through the Mesozoic, and into the early Cenozoic is discussed, covering active subduction of the Tethys Ocean, and the onset of continental collision. Then the development of the collision zone, and active geodynamics is discussed,

before moving onto current thoughts and models for post-collisional volcanism, focusing predominantly on East Anatolia and Armenia.

Chapter 3 outlines the current exposures of post-collisional volcanism in the Georgian Greater and Lesser Caucasus. Field localities, volcanic morphology, and outcrop styles are described for samples used in this study. Dating of the lavas is reviewed, covering the temporal relationships between outcrops. Appendix A gives details of sample localities and ages.

Chapter 4 presents major-, trace- and isotopic data for lavas of the Lesser Caucasus. Detailed petrography and mineral chemistry are also presented. These data are used to assess the role of fractional crystallisation, crustal contamination and source enrichment during the magma evolution. The roles of lithosphere and asthenosphere during melt generation are considered, whilst pressure and temperature estimates help to constrain the nature of the source region.

Chapter 5 presents major-, trace- and isotopic data for lavas of the Greater Caucasus. Detailed petrography and mineral chemistry are also presented. The geochemical data are used in tandem with textural information from amphibole and plagioclase to consider the role of fractional crystallisation, crustal contamination and magma mixing. Enrichment of a lithospheric source by sediment- and fluid-dominated slab derived material is considered. An attempt to constrain the pressure and temperature conditions of the source and the conditions during crystallisation is made, to better understand the geodynamics that shaped the orogen. Sample preparation techniques, methods and operating conditions of instruments used to measure the data are explained in Appendix B. Precision, accuracy, and uncertainties associated with the data are covered in detail, whilst reproducibility of standard data is also presented. Major-, trace- and isotopic data for the Lesser and Greater Caucasus and crustal samples are presented in Appendix C.

Chapter 6 presents a geodynamic model for the northern section of the Eurasian-Arabian collision zone. Models for the Lesser and Greater Caucasus are discussed, in relation to the regional setting, the nature of other volcanic rocks in the region, and to seismic data. A brief discussion follows, considering the wider implications this type of post-collisional magmatism for mountain building and the formation of continental crust.

Chapter 7 states the main conclusions of the project, and discusses potential future work to develop the study further. The main conclusions of the study are then stated, followed by a brief description of potential future work that could enhance our understanding of the orogenic evolution of the Caucasus.

Chapter 2

Regional Geology and Tectonic Evolution

The southern margin of the Eurasian Plate is a region of well studied continent-continent collision. The collisions of Africa and India, forming the Alps and Himalaya respectively, dominate the literature. A third major collision occurs between these two, involving the broadly northward movement of the Arabian Plate.

The Arabian-Eurasian collision zone encompasses East Anatolia, NW Iran, and the Greater and Lesser Caucasus. The Caucasus lie between the Black and Caspian Seas, covering large areas of Georgia, Armenia, Azerbaijan and part of southern Russia. The Greater Caucasus are an ENE-WSW striking, linear mountain range, containing the highest peak in Europe (Mt. Elbrus, 5642 m). The Lesser Caucasus are a sub-parallel, arcuate mountain belt, with slightly lower topography (highest peak is Aragats, 4090 m). They lie on average around 100 km south of the Greater Caucasus, separated by the Rioni and Kura intermontane basins. The north-convex arcuate configuration is consistent with all other terranes in the zone, except the Greater Caucasus, due to the shape of the Arabian indenter.

2.1 Pre-Collision Geology

The geology of the Eurasian-Arabian collision zone is a mosaic of Eurasian, Tethyan and Gondwanan terranes (Fig. 2.1). These have been brought together and accreted onto the Scythian Platform (the southern margin of the Eurasian Continent in this region) throughout the Phanerozoic (Saintot et al., 2006). As a result the region can be split into a number of parallel, broadly E-W striking terranes. From north to south these are:

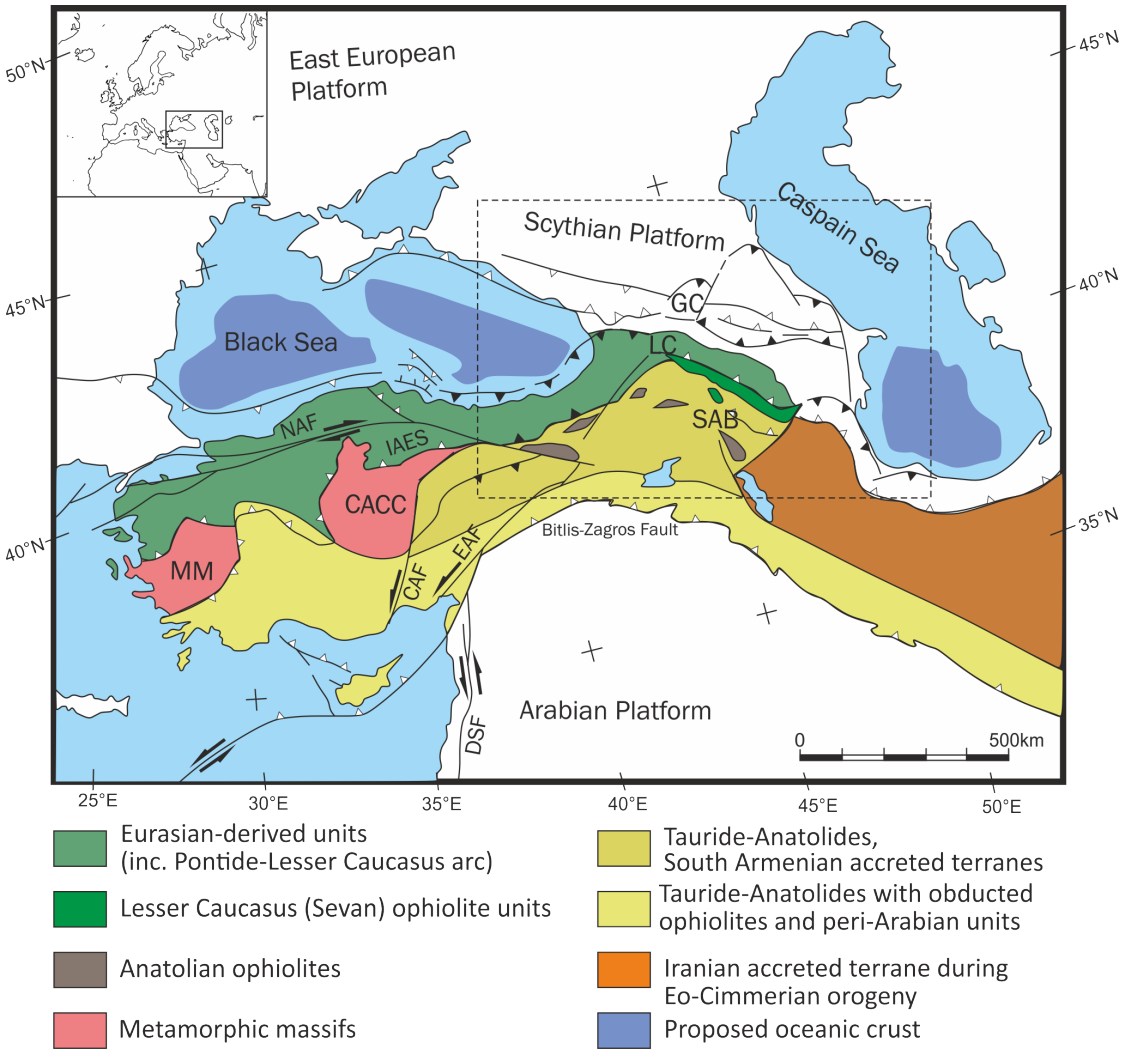

FIGURE 2.1: A structural sketch map showing the major terranes and faults of the Eurasian-Arabian collision zone. Inset map showing the location of the Caucasus. MM-Menders Massif, CACC-Central Anatolian Crystalline Complex, SAB-South Armenian Block, LC-Lesser Caucasus, GC-Greater Caucasus, NAF-North Anatolian Fault, CAF-Central Anatolian Fault, EAF-East Anatolian Fault, IAES-Izmir-Ankara-Erzinkan Suture, DSF-Dead Sea Fault. Modified after Sosson et al. (2010).

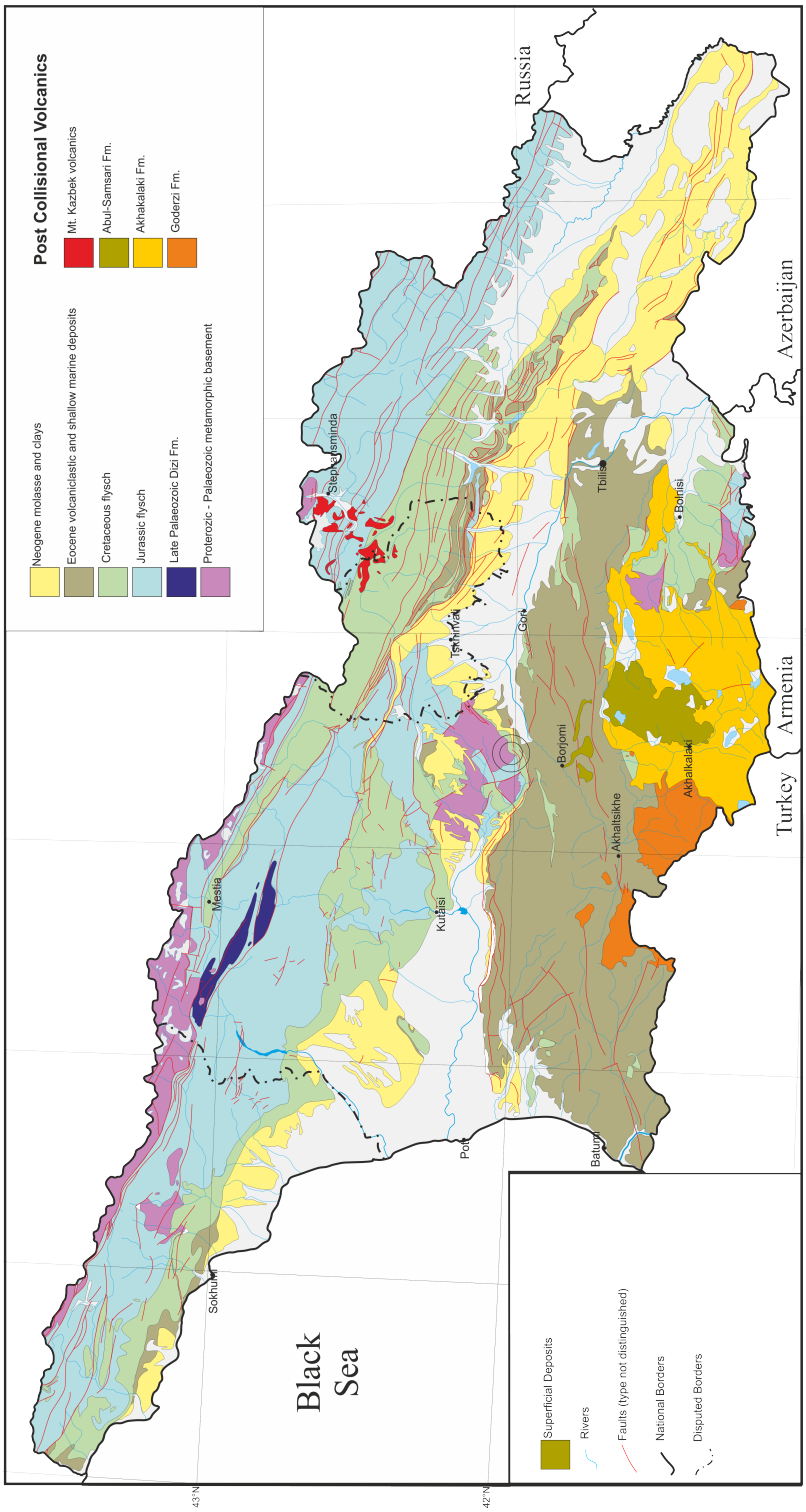

FIGURE 2.2: A simplified geological map, showing all the major formations discussed in this report. Based on the map of Gudjanidze (2003)

The Scythian Platform, the Greater Caucasus fold and thrust belt, the Trans-Caucasus depression, the Pontides-Lesser Caucasus Arc, the Turkish-Iranian Plateau, and the Arabian Platform. Figure 2.2 is a simplified geological map of Georgia, showing all the main features discussed in this chapter.

2.1.1 Eurasian Margin

The oldest rocks in the Caucasus are exposed in the Trans-Caucasus depression as part of the Dziula Massif, an inlier of basement (Fig. 2.3, Adamia et al., 2011) These amphibolites, meta-gabbros, migmatites and gneisses represent the early Palaeozoic, although the interpretation of the geology from them is strongly debated (Zakariadze et al., 2007; Mayringer et al., 2011). These rocks have a strong overprint from Variscan age metamorphism Mayringer et al. (2011). Similar basement is exposed in the Greater Caucasus mountain, as the Main Range Zone in Georgia (Fig. 2.3) and the Fore-range Zone in Russia (see Somin, 2011, , for a review). During the Variscan orogeny there was major emplacement of granites across all the basement massifs and the Greater Caucasus (Zakariadze et al., 2007; Somin, 2011; Mayringer et al., 2011), and a regional low-pressure, high-temperature metamorphic event at 330–340 Ma (Mayringer et al., 2011). Similarities in petrographic and geochronological data between the Greater Caucasus basement and Transcaucasus inliers suggest a similar geological evolution throughout the Palaeozoic, and that they were brought together prior to the Variscan orogeny (Somin, 2011). The northern margin of the Greater Caucasus terrane was then accreted onto the Scythian Platform during the Variscan orogeny along a suture that presently lies in the foreland basin to the north of the Greater Caucasus mountain belt (Mayringer et al., 2011).

2.1.2 Gondwanan Terranes

During the Early Mesozoic continental terranes broke off from the northern Gondwanan margin (Fig. 2.4), including the Iranian Block (Golonka, 2004; Saintot et al., 2006) and the South Armenian-Tauride Block (Sosson et al., 2010; Adamia et al., 2011), although some models place these blocks as a single long terrane (Stampfli and Borel, 2002). At the southern Eurasian margin a volcanic arc developed (Fig. 2.4), and subduction caused these Gondwanan terranes to drift northwards.

The basins around the arc now form the Lesser Caucasus, and continue west into Turkey as the Pontides. The Variscan basement beneath these arc-like deposits (Khrami and Loki massifs) are similar to that of the Greater and Trans-Caucasus, supporting the idea that this arc was at the southern Eurasian margin (Sosson et al., 2010; Mayringer

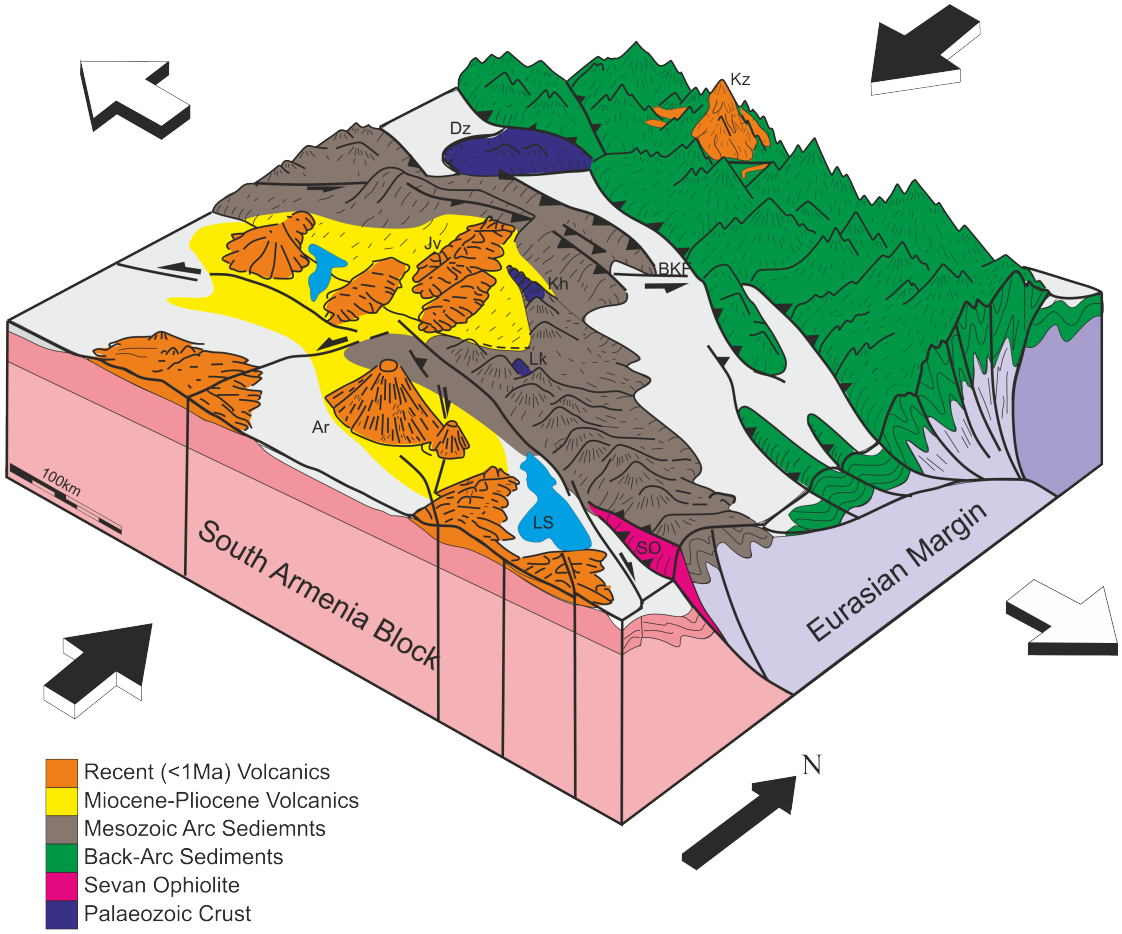

FIGURE 2.3: Block diagram of the Caucasus. Volcanic centres (Kz - Mt. Kazbek, Jv - Javakheti Highlands, Ar - Aragats), basement massifs (Dz - Dzirula, Kh - Khrami, Lk - Loki) and Lake Sevan (LS) are shown in relation to the assymetrically folded Greater Caucasus and the lower lesser Caucasus. Modified after Rebaï et al. (1993)

et al., 2011). The Middle Jurassic (Bajocian) to Early Cenozoic is dominated by thick, predominantly calc-alkaline volcanogenic and volcanoclastic deposits (Sosson et al., 2010). Behind the arc (to the north), a back-arc basin developed (Fig. 2.4: Adamia et al., 2011). Initially (Bajocian) deposits comprised MORB-like pillow lavas, volcanoclastic calc-alkaline andesites, pyroclastic and tuff turbidites (Adamia et al., 2011). From the Late Jurassic until the Eocene there was almost uninterrupted deposition of terrigenous and carbonate turbidites (Adamia et al., 2011), with a total thickness greater than 10 km (Sosson et al., 2010). The width of the back-arc basin is poorly constrained.

Ophiolites exposed along the Sevan-Akera Suture Zone (Fig. 2.3) can be used to constrain the timing of the collision of the first Gondwanan terrane (South Armenia-

Tauride Block) with the southern Eurasian margin. High pressure metamorphism of blueschists is dated at 94–90 Ma, and exhumation at 74–71 Ma (Rolland et al., 2012), suggesting by the end of the Mesozoic the terranes forming the Caucasus had all been accreted onto the Eurasian margin (Fig. 2.4).

2.2 Collisional Phase

The collision phase began following closure of the Tethys ocean, and Arabia collided with the Eurasian margin. Estimates for the timing of this range from 50–60 Ma (Mazhari et al., 2009) to 5 Ma (Philip et al., 1989). The wide range of these ages is likely to be due to the complex geology within the Tethys and a number of smaller collision events. We assume final closure occurred along the Zagros-Bitlis suture (Fig. 2.4). Robertson (2000) dated this event to ~16–23 Ma, based on deformation on the north side of the Arabian plate, related to overthrusting of nappes of Eurasian origin, which agrees with apatite fission dating which suggests exhumation at 18 Ma, requiring oceanic lithosphere to be consumed by 20 Ma (Okay et al., 2010), which agrees with retrodeformation models (McQuarrie and van Hinsbergen, 2013). Allen and Armstrong (2008) suggest a date for final closure of ~35 Ma, which agrees with estimates of initial uplift in the Greater Caucasus (Vincent et al., 2007). A possible explanation of these two different dates is a two stage collision, with an initial 'soft collision at ~36 Ma (Fig. 2.4) involving stretched Arabian continental lithosphere that was still being subducted (Ballato et al., 2011), and the East Anatolian Accretionary Complex buffering the collision (Şengör, 2003), before a second 'hard collision at ~20 Ma of unstretched Arabian lithosphere causing significant upper plate deformation (Ballato et al., 2011). However McQuarrie and van Hinsbergen (2013) puts the earlier event down to activity at the volcanic arc slowing down to a background state, causing the back-arc to change from extensional, to mildly compressional.

Since the initial collision, Arabia has moved 300–500 km north relative to Eurasia (Allen et al., 2004; McQuarrie and van Hinsbergen, 2013). Uplift and foreland basin development occurred in the Middle Eocene, suggesting deformation began at this time, pre-dating initial collision (Allen et al., 2004).

The total amount of shortening across the Greater Caucasus has been estimated at 200–300 km (Ershov et al., 2003). Current N-S shortening rate across the Lesser and Greater Caucasus is 10 ± 2 mm.yr^{-1}, with 60% occurring in the Greater Caucasus. At the present day shortening rate (~6 mm.yr^{-1}) it would require 30–50 million years to account for the 200–300 km shortening, which is significantly longer than the duration

of the collision event. The same issue arises when investigating deformation across the Turkish-Iranian Plateau (Allen et al., 2004). In other zones of active deformation in the region, such as the North and East Anatolian faults, the Zagros Simple Folded Zone and Alborz mountain range, the opposite is observed, and at current rates of deformation, shortening would exceed estimates within as little 3 Ma (Allen et al., 2004). Taken together this points to a situation where convergence in the Arabian-Eurasian collision zone has not remained constant since the onset of collision 16–23 Ma.

2.2.1 Structure of the Greater Caucasus

The young age of the collision gives us a unique opportunity to observe some of the early stages of orogenesis. The main structure of the Greater Caucasus (Fig. 2.3) is a doubly vergent fold and thrust belt (Mosar et al., 2010; Forte et al., 2014). Total uplift is in excess of 3700 m since the initial collision (Mosar et al., 2010), and large foreland basins have developed on both sides of the orogen (Ershov et al., 2003; Mosar et al., 2010). The structure is highly asymmetrical perpendicular to strike, with a gentle monocline to the north, and strongly deformed Mesozoic back-arc sediments forming the southern slopes. The crust in the region is significantly thickened to 50–60 km (Philip et al., 1989; Adamia et al., 2011). Throughout the collision, the thrust front has migrated southwards into the Kura Basin, and Kura fold and thrust belt (Mosar et al., 2010). The structure, and position of the Main Caucasus Fault is still unclear. The structure of the Greater Caucasus varies significantly along strike (Fig. 2.5). Both convergence rates (Reilinger et al., 2006), and the depth of seismicity increases eastwards (Mumladze et al., 2015), whilst volcanism is only present in the west (Mumladze et al., 2015).

Recent seismic studies have generally supported the idea of subduction beneath the Greater Caucasus. Studies of earthquake data (Mellors et al., 2012; Mumladze et al., 2015) report sub-crustal (>50 km) earthquakes, up to a depth of 158±4 km (Mellors et al., 2012), beneath the eastern Greater Caucasus (Fig. 2.5), which has been interpreted as the subduction of the Greater Caucasus back-arc basin (Mumladze et al., 2015). This is supported by a positive S-wave anomaly in the same area (Skobeltsyn et al., 2014) extending to a depth of 250 km. Other deep (>150 km), high-velocity anomalies which could provide support for the presence of a slab, have instead been interpreted as evidence for lithospheric delamination (Koulakov et al., 2012) which has been supported by a negative anomaly also in the same region (Zor, 2008), representing hot asthenosphere that has risen to replace the delaminated lithosphere.

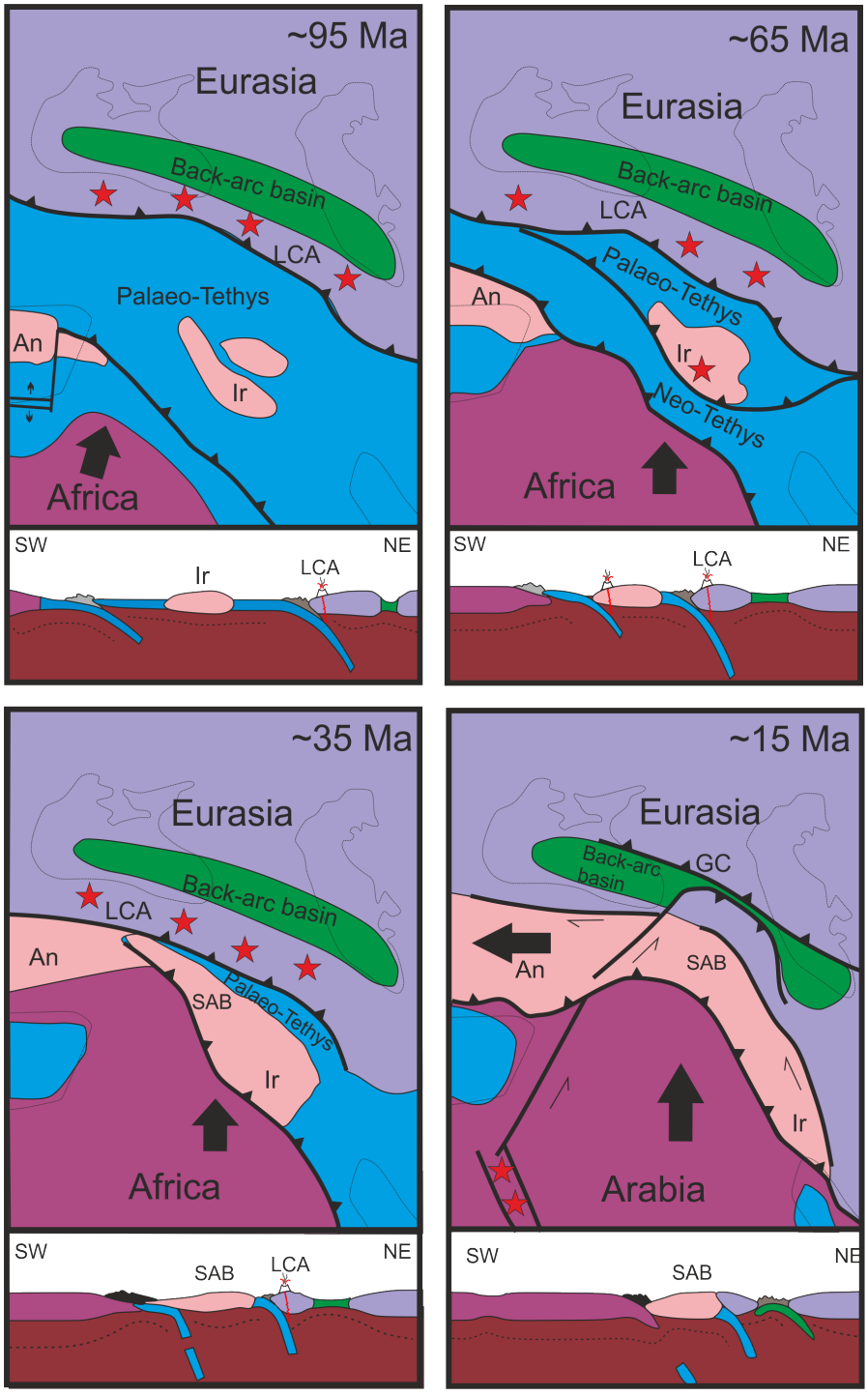

FIGURE 2.4: Tectonic evolution of the Eurasian-Arabian section of the Tethys Ocean from the Cretaceous to the Miocene. Schematic cross-sections run from SW-NE from Africa-Arabia to Eurasia. An -Anatolian Micro Plate, Ir - Iranian-South Armenian Block (SAB), LCA - lesser Caucasus Arc, GC - Greater Caucasus. Modified after Philip et al. (1989) and Avagyan et al. (2005)

Along strike to the east of this proposed subduction zone, there is evidence to support South Caspian oceanic crust (which belonged to the same basin as the Kura crust, Fig. 2.1) subducting northwards beneath the Aspheron Sill (Allen et al., 2002; Brunet et al., 2003; Mumladze et al., 2015). However it is unclear, with significant variation in crustal structure along strike, whether or not subduction beneath the Greater Caucasus would continue eastwards into the Caspian Sea (Allen et al., 2003; Skobeltsyn et al., 2014).

In the western Greater Caucasus, there are no sub-crustal earthquakes (Fig. 2.5; Mumladze et al., 2015) and low upper mantle seismic velocities (Maggi and Priestley, 2005; Koulakov et al., 2012). This suggests there is no present day subduction in this area. Low subsidence rates in the NW foreland basin can be explained by dynamically driven uplift of the basin (Ershov et al., 1999) that could have been caused by a delamination event beneath the western Greater Caucasus, such as slab break-off, or the removal of a dense crustal root.

Convergence rates increasing eastwards along strike of the Greater Caucasus

It has been shown that slab detachment can be initiated in collisional orogens by subduction of continental lithosphere (e.g. Davies and von Blanckenburg, 1995). The Dzirula Massif is one such continental block and may be continuous into the Black Sea as the Shatsky Ridge. Both of these lie south of the region where the slab is assumed to have detached.

The west and east segments of the Greater Caucasus may also be separated by the Borjomi-Kazbegi Fault. The exact nature of this sinistral, strike-slip fault is still debated. Its presence has been well defined in the Lesser Caucasus, and has been extrapolated northward into the Greater Caucasus, across into the upper plate of the subduction zone, and offsetting both the topographic crest of the range, and the Moho (Philip et al., 1989). Whether this fault is still active is also debated, with little field evidence for displacement on marker beds (O'Connor et al., 2006; Adamia et al., 2008; Martin et al., 2012), and little seismic evidence for significant motion along the fault (Reilinger et al., 2006). Mumladze et al. (2015) restrict the fault to the lower plate, acting as a transform fault caused by the different rate of shortening between the east and west Greater Caucasus.

2.2.2 Tectonic Rearrangement at 5 Ma

Unlike the age of the onset of initial collision, the timing of a tectonic rearrangement event at ~5 Ma is more widely agreed upon. Major changes that occurred included the initiation of strike-slip movement on the North and East Anatolian faults (Westaway, 1994) and the transition from the eastward escape of Iran to the expulsion of the Anatolian block

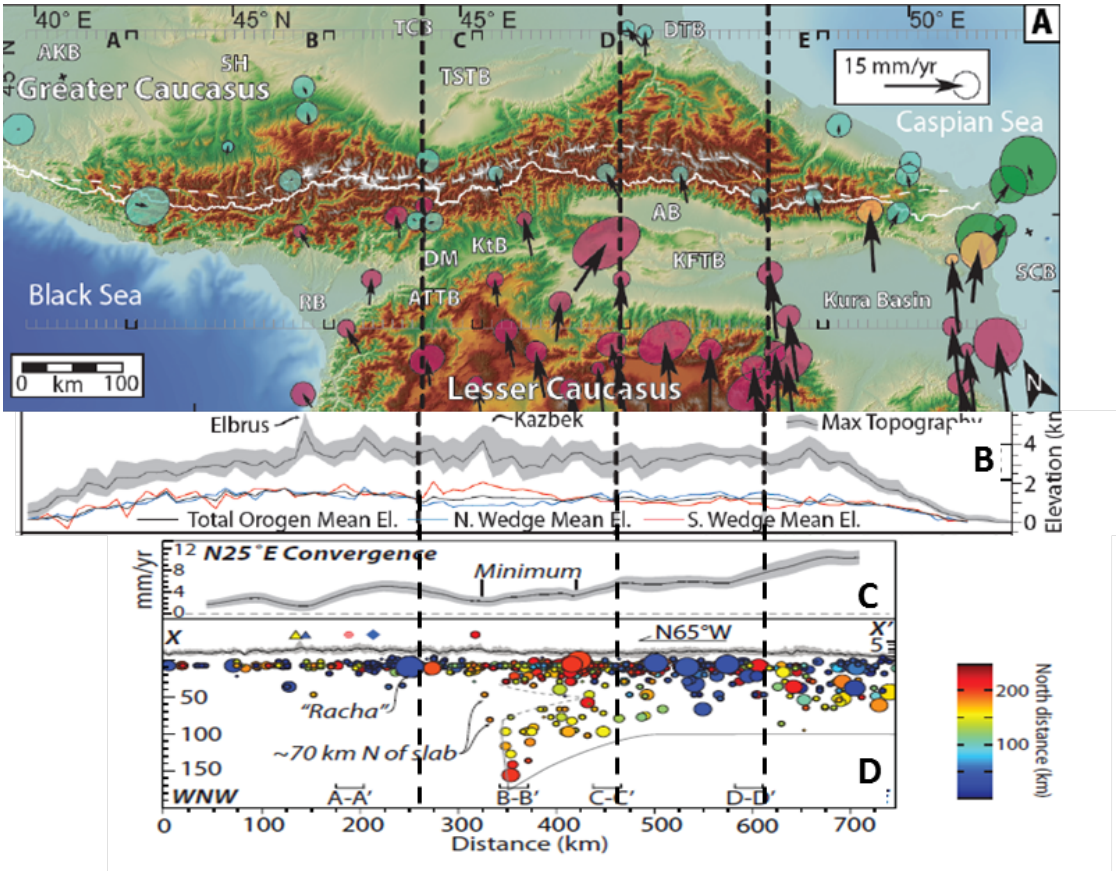

FIGURE 2.5: Variations along-strike in the Greater Caucasus. A. Topography and geography of the Greater Caucasus. Arrows are GPS velocities relative to a stable Eurasian plate (Reilinger et al., 2006). Colours indicate whether the motion is from the Greater Caucasus (Teal), Lesser Caucasus (Pink), Kura Basin (Yellow) or Aspheron Peninsular (Green). B. Maximum elevation across the region. Mt. Elbrus and Kazbek, two volcanic centres are marked (Forte et al., 2014). C. Convergence rates (Mumladze et al., 2015). D. Earthquake data beneath the Greater Caucasus. Colours represent distance of epicentre to the north (showing the dip of the slab). Location of the Racha earthquake also marked (Mumladze et al., 2015).

westwards (Allen et al., 2011). Related to this, normal faults developed in the Turkish-Iranian Plateau (Copley and Jackson, 2006). Deposition in the Rioni and Kura Basins evolved from shallow marine to sub-aerial facies (Adamia et al., 2008). Convergence slowed down (Austermann and Iaffaldano, 2013) and changed in orientation from NW-SE to NNE-SSW (Avagyan et al., 2005). Finally, regional major uplift occurred along the full strike of the Greater Caucasus, with exhumation rate increasing by a factor of four (Avdeev and Niemi, 2011).

The cause of the tectonic reorganisation remains unclear. Allen et al. (2004) propose

that there was a phase of initial thickening in the Greater Caucasus and Turkish-Iranian Plateau, creating a buoyant crust. As it is easier to accommodate shortening in thinner and lower crust, deformation switched to the flanks of the buoyant areas as fold and thrust belts such as the Zagros Simple Folded Zone and Kura fold and thrust belt (Allen et al., 2004; Forte et al., 2009, 2013). A similar model to this has also been proposed for the Tibetan Plateau (England and Houseman, 1988). Rather than thickening, Copley and Jackson (2006) suggest low density, hot mantle created uplift in the Turkish-Iranian Plateau, creating the buoyant region that resisted deformation.

The reorganisation could have been the result of a large delamination event, such as slab break-off (van Hunen and Allen, 2011), or delamination of a lithospheric root (Ershov et al., 2003), both of which were suggested to have occurred less than 10 Ma ago.

The closure of the Greater Caucasus back-arc basin, and the resulting collision of the Lesser Caucasus Arc with the Eurasian margin (Avdeev and Niemi, 2011; Forte et al., 2014) have also been suggested. These may also be related to the slab break-off event beneath the western Greater Caucasus, and attempted subduction of buoyant crust.

Today in the Greater Caucasus, the majority of the collision is absorbed on the southern flank of the range, with 30–45 % occurring in the Kura fold and thrust belt (Forte et al., 2009). Evidence for current deformation in these areas include Quaternary molasse deposits at the margins between the intermontane basins and strong folding along the southern slopes of Greater Caucasus are strongly deformed (Adamia et al., 2008). Active seismicity in the fold and thrust belts also present a hazard with over a hundred deaths from the 1991 Racha earthquake in Georgia (Magnitude 7.2), whilst the 1988 Spitak earthquake (magnitude 6.9) caused the deaths of over 25000 people, left half a million homeless, and caused an estimated 8 billion USD of damage to property (Adamia et al., 2008).

2.3 Post-Collisional Volcanism

Prior to collision there was an Eocene peak in volcanism across the region (Dilek et al., 2010) followed by a magmatic gap during the syn-collisional phase, before magmatism recommenced in Anatolia at 11 Ma (Keskin et al., 1998), 8 Ma in the Lesser Caucasus (Lebedev et al., 2011d) and 5 Ma in the Greater Caucasus (Lebedev et al., 2011d). The presence of extensive post-collisional volcanism is what sets the Eurasia-Arabian collision zone apart from other major collision zones. In other collisional settings, such as Himalaya-Tibet, post-collisional volcanism is restricted to small-volume potassic lavas (Williams et al., 2004; Guo et al., 2006)). Recent post-collisional volcanism does occur in

the Carpathian region ranging from calc-alkaline to alkali, but volcanism is on a much smaller scale than in the Caucasus (Seghedi et al., 2011). Another possible comparison can be made to recent andesitic volcanism in Papua New Guinea, which occurs in a complex tectonic setting, but not above active subduction, which ceased up to 15–10 Ma (Smith and Milsom, 1984; Zhang et al., 2015).

In more ancient orogens post-collisional magmatism is more difficult to identify, but where it is apparent it appears to be related to an extensional regime associated with post-orogenic collapse, such as Neoproterozoic volcanics in Brazil (de Sant Ana Barros et al., 2009) and Egypt (Khalaf, 2012), Palaeoproterozoic Australian dykes and lavas (Li et al., 2013), and Tertiary examples from Spain (Zeck et al., 1998).

2.3.1 Geographical Distribution and Timing of Volcanism

Volcanics cover the full extent of the collision zone, from Zagros to the Greater Caucasus, and Turkey to Iran (Fig. 2.6). Neill et al. (2013) compared the great extent of this volcanism to the large volume, Late Cenozoic volcanic fields of the western USA (Johnson and Rutherford, 1989).

The extensive, young volcanism covering large parts of the East Anatolian plateau lie to the south of the Caucasus, and are not considered in this study. These volcanics have been well documented, and details of their chemistry and petrogenesis are covered in comprehensive studies by Pearce et al. (1990) and Keskin et al. (1998).

2.3.2 Timing of Volcanism

In the last 20 years there have been numerous K-Ar geochronological studies of both the volcanic and intrusive bodies across the Caucasus published in a number of papers (See Fig. 2.7; Lebedev et al., 2011d; Lebedev and Vashakidze, 2014, and references therein). These suggest small scale pulses of magmatism separated by quiescent periods of less than 100 ka (e.g. Chernyshev et al., 2006; Lebedev and Vashakidze, 2014), but whether the methodology can resolve magmatism into such closely spaced periods is questionable.

Chernyshev et al. (2006) details the method used by the Russia group who have dated the majority of the rocks from this area. The errors quoted are often large enough that they would overlap across the small scale pulses of magmatism. Using the Abul-Samsari data as an example, dates of 410±30 ka and 320±70 ka are classified as erupting in two separate pulses (Chernyshev et al., 2006). This should be less of a problem for the older (>2 Ma) rocks of the Lesser Caucasus, but they contain significantly lower concentrations of K_2O than the examples used in Chernyshev et al. (2006), which would result in less

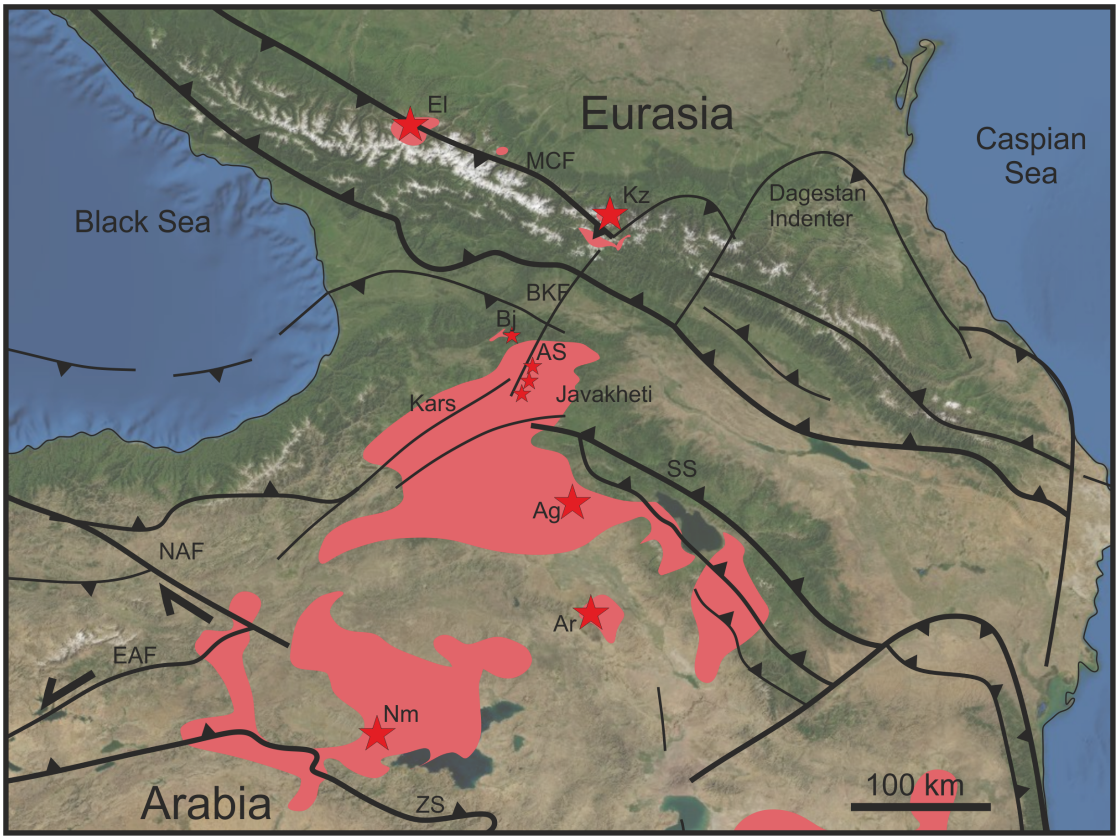

FIGURE 2.6: Map showing distribution of volcanics in the Arabia-Eurasia collision zone, and the relationship with major crustal structures. Red areas show extent of volcanism. Red stars show location of major volcanoes, and the Abul-Samsari and Borjomi formations. El - Mt. Elbrus, Kz - Mt. Kazbek, Bj - Borjomi Fm., AS - Abul-Samsari ridge, Ag - Aragats, Ar Ararat, Nm - Nemrut, MCF - Main Caucasus Thrust, BKF - Borjomi-Kazbek Fault, SS Sevan Suture, NAF - North Anatolian Fault, EAF - East Anatolian Fault, ZS - Zagros Suture. Distribution of volcanism based on Adamia et al. (2011).

radiogenic argon, and therefore larger errors. The even younger samples of Mt. Kazbek also produce large errors because of the little time for the decay of potassium to radiogenic argon (Lebedev et al., 2011d). A single sample was measured using Ar-Ar dating at the Open University before this project began by N. Harris and S. Sherlock. The sample did not give a reliable age as too little radiogenic argon was present. Therefore the literature dates are being used as they represent the most reliable dates readily accessible.

The broader scale pulses of magmatism, often separated by long (>1 Ma) periods of quiescence (Lebedev et al., 2011d), seem to correlate with clear unconformities observed in the field. At this scale we treat their dates, and their interpretations of pulses of magmatism, as reliable. Recent work has also confirmed many of the dates correlating to

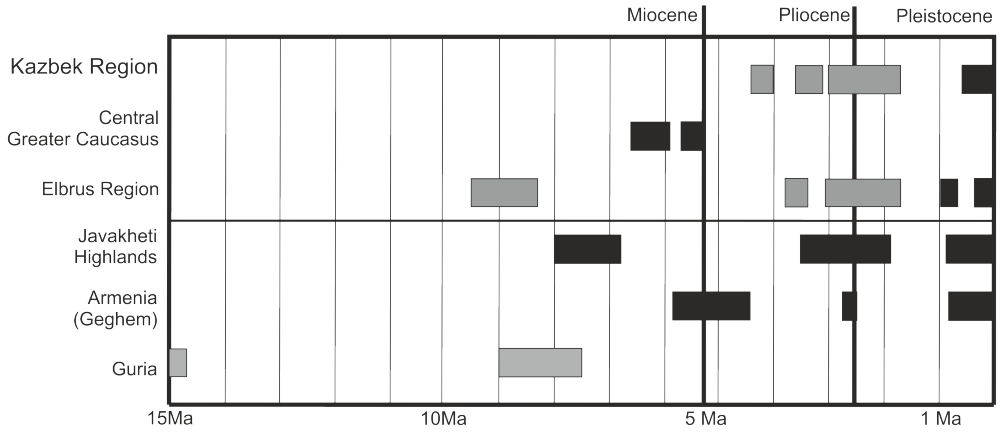

FIGURE 2.7: Timing of magmatism across the Lesser (Javakheti, Armenia, Guria) and Greater (Kazbek, Central Georgia, Elbrus) Caucasus. Intrusive magmatism shown in grey, volcanism in black. Collation based of Lebedev et al. (2011d) and Lebedev and Vashakidze (2014)

observable geomorphological changes (Koronovskii, 2016)

Over the last 9 Ma the region has been continually active located in different centres and displaying a range of eruptive styles (Lebedev et al., 2011d). There is however no clear evidence of spatial and temporal correlation (Lebedev et al., 2011d; Kaislaniemi et al., 2014).

2.3.2.1 Greater Caucasus

Mt. Elbrus Region Mt. Elbrus is the highest peak in Europe (5642 m), and forms the most northerly exposure of post-collisional volcanism in the Eurasian-Arabian collision zone (Fig. 2.6).

The oldest known magmatism in the Greater Caucasus is represented here by sub-volcanic granitoids dated at 8.3±0.2 Ma (Lebedev and Bubnov, 2006), followed by a second pulse of acidic intrusive magmatism at 2.5–1.6 Ma (Lebedev and Bubnov, 2006).

The oldest volcanism in the Elbrus region is related to the Chegem volcanic centre, east of Mt. Elbrus. An early pulse of basaltic-andesitic lavas (3.85–3.65 Ma; Lebedev and Bubnov, 2006), was followed by the formation of the Verkhnechemskaya caldera at 2.82±0.02 Ma (Gazis et al., 1995). This event was associated with a continuous 2 km thick section of dacitic-rhyolitic tuff (Gazis et al., 1995).

After a period of quiescence, the Mt. Elbrus region became active again ~800 ka, with predominantly dacitic flows, with minor andesites (Chernyshev et al., 2014). The youngest magmatic phase (<250 ka; Lebedev et al., 2010b) is related exclusively to the Mt. Elbrus stratovolcano, and is predominantly dacitic (Chugaev et al., 2013). The

most recent eruption of Mt Elbrus is recorded at 50 AD (Global Volcano Project), and some authors suggest that Elbrus may still become active again, possibly associated with catastrophic caldera collapse (Chernyshev et al., 2014).

Kazbegi Region The Kazbegi volcanic region is centred around Mt. Kazbek, and the towns of Stepansminda and Gudauri. Similarly to Mt. Elbrus, the earliest magmatism in this region was small granitoid bodies (4–2 Ma; Lebedev et al., 2011d, 2009).

Volcanism started around 400 ka (Lebedev and Vashakidze, 2014) on Mt. Kazbek. Flow direction was predominantly to the south, and the north east (Lebedev et al., 2011d). A caldera collapse event occurred around 200–250 ka, marking the end of this period of Mt. Kazbeks evolution (Lebedev and Vashakidze, 2014). Mt Kazbek began to grow again, with a series of surrounding satellite volcanoes, and generally eastward flows (Lebedev et al., 2011d). This has persisted for the past 120 ka (Lebedev and Vashakidze, 2014), with predominantly andesitic lavas (Lebedev et al., 2011d) and some small, young explosive vents (Lebedev and Vashakidze, 2014). The youngest flow in the region has been dated at 6000 yr by radiocarbon dating of organic material in a lake the flow is thought to have dammed (Djanelidze et al (1982) cited in Adamia et al., 2011).

The Qabarjina Fm. (Kabardzin in Russian literature), to the south east of Mt. Kazbek, is a mostly dacitic volcanic centre, that shows explosive activity, and is related to the Sakakhe cinder cone near the town of Gudauri, which itself is related to a large volcanic flow, dated at 300–180 ka (Lebedev et al., 2011d).

The Keli Highlands is a volcanic area to the west of the Krestovoi Pass. It is composed of 35 monogenetic volcanos, with andesitic-rhyolitic compositions (Lebedev et al., 2011b, 2008b). Volcanism is younger than 250 ka, and may have been active within the last 30 ka (Lebedev et al., 2007b).

The Dzhava volcanic centre is a small volcanic centre in South Ossetia, composed of andesitic fissure eruptions, dated to 180–60 ka (Lebedev et al., 2011d).

Central Georgia Volcanic Region This late Miocene (Lebedev et al., 2006; Tutberidze, 2012) region produced basaltic lava flows, with some pyroclastic material (Tutberidze, 2012). Magma volumes are relatively small (Lebedev et al., 2011a), but the region is included here for completeness.

2.3.2.2 Lesser Caucasus

Guria The small-scale Guria volcanic region lies in Western Georgia. Syenites from this region have been dated at ~15 Ma (Lebedev et al., 2011a), making them the oldest

known post-collisional magmatic rocks in the Caucasus. A second pulse of magmatatism at 9–7.5 Ma produced basalts and related subvolcanic gabbroic intrusions (Lebedev et al., 2011a). Although this early magmatism was not extensive or intense in the Caucasus, it may correlate with activity of the same age observed around Lake Van in East Anatolia (Lebedev et al., 2010c).

Javakheti Highlands Covering areas of southern Georgia, Armenia and Turkey, the Javakheti highlands is an important, long-lived centre of voluminous post-collisional volcanism.

The oldest volcanics in the region pre-date the regional 5 Ma tectonic rearrangement, and are dated at ~7.5 Ma (Lebedev et al., 2011a). Volcanics of this age are referred to as the Goderdzi Formation and outcrop at the western part of the Javakheti Highlands. Explosive volcanism has produced predominantly dacitic pyroclastic deposits, with andesite-dacite flows becoming more common higher in the formation (Tutberidze, 2012).

The most productive period of volcanism occurred towards the end of the Pliocence (3.8-1.6 Ma; Lebedev et al., 2008a, 2011d). Lavas of this age lie unconformably over the gently folded Goderzi Fm., and are known as the Akhalkalaki Formation. The style of volcanism changed from explosive to effusive, possibly fissure related flows (Lebedev et al., 2008a; Tutberidze, 2012). Thick accumulated flows formed large plateaus (such as the Tsalka Plateau), as well as large valley filling flows, such as the Khrami flow, which is over 60 km in length (Lebedev et al., 2007a). Thickness of the flows locally reaches up to 300 m (Lebedev et al., 2007a). Compositionally they are predominantly basaltic andestic, with minor acidic units (Lebedev et al., 2008c; Tutberidze, 2012). The acidic volcanism may correspond to the end of pulses of the dominant mafic volcanism (Lebedev et al., 2008a). It has been suggested that volcanism migrated from the west to the east of the plateau from the middle to the late Pliocene (Lebedev et al., 2008c).

Rising above the Javakheti Highlands is the 40 km long Abul-Samsari Ridge. It is composed of a number of volcanic peaks, the highest of which are Samsari (3285 m) and Didi-Abuli (3301 m). Activity on the ridge began 800 ka and continued as recently as <50 ka (Lebedev et al., 2003), making it the youngest volcanism in the Javakheti Highlands. Volcanism initially was concentrated on the large peaks, but the most recent volcanism is related to smaller satellite cones (Lebedev et al., 2003). It is mostly dacitic in composition, with minor andesite (Lebedev et al., 2003).

The Bakuriani-Borjomi region lies to the north of the Javakheti Highlands, and is separated from it by the Trialeti mountain range. It does however show many similarities with the Javakheti Highlands, and may be considered either part of it, or analogous to it

(Lebedev et al., 2009). An initial andesitic plateau building phase at 3.1–2.8 Ma (Lebedev et al., 2009) corresponding to the early Akhalkalaki Formation was followed by a second pulse of valley filling flows occurring at 400–200 ka (Lebedev et al., 2009), synchronously with the formation of the Abul-Samsari ridge. However the dacites of the Abul-Samsari ridge are more evolved than the andesitic flows of Borjomi (Lebedev et al., 2009).

Armenian Lesser Caucasus Although this project concentrates on the post-collisional volcanism in Georgia, it is important to note that the Lesser Caucasus volcanism continues south into Armenia and Turkey (Fig. 2.6). The following provides a brief introduction to the timing and style of volcanism in the major centres located in the Lesser Caucasus outside of Georgia.

Aragats is a large stratovolcano (4095 m) in Armenia. It evolved with three pulses of significant volcanism (Lebedev et al., 2011d). Late Miocene intermediate-acidic lavas only outcrop on the northeastern slopes, but coincide with the 5 Ma tectonic rearrangement (5.8–4.7 Ma; Lebedev et al., 2011d). This was followed by Pliocene (2.5–1.5 Ma) plateau building basalts, with minor acid flows (Chernyshev et al., 2006), and then the main cone building phase of basaltic, andesite-dacitic lavas, with satellite cones, which began ~900 ka ago (Chernyshev et al., 2006). This igneous history is very similar to that observed from the Georgian Javakheti Highlands. Intense magmatism beginning at 1 Ma–800 ka seems to be a coeval event across the Lesser and Greater Caucasus.

The Porak volcanic group is located to the SE of Lake Sevan. There is evidence here for eruptions as recently as the 5th Millennium BC, including six petroglyphs depicting the eruption itself (Fig. 2.8; Karakhanian et al., 2002).

The Geghem Highlands are located to the SW of Lake Sevan, with over one hundred volcanoes forming a 65 km long ridge (Karakhanian et al., 2003). Volcanism here follows the same pattern and Javakheti and Aragats, with early dacitic-rhyolitic eruptions (5.7–4.5 Ma), followed by late Pliocene plateau forming basalts (2.5–2.0 Ma), and then recent volcanism commencing at 800 ka (Lebedev et al., 2011d). It is thought that volcanism migrated eastward throughout the Geghem area. The youngest flows have been dated to 4000–2000 years BP (Karakhanian et al., 2003). The most recent eruption in the Arabian-Eurasian collision zone is thought to be the 1840 AD eruption on the northern flank of Mt. Ararat just to the south of the Lesser Caucasus (Karakhanian et al., 2003).

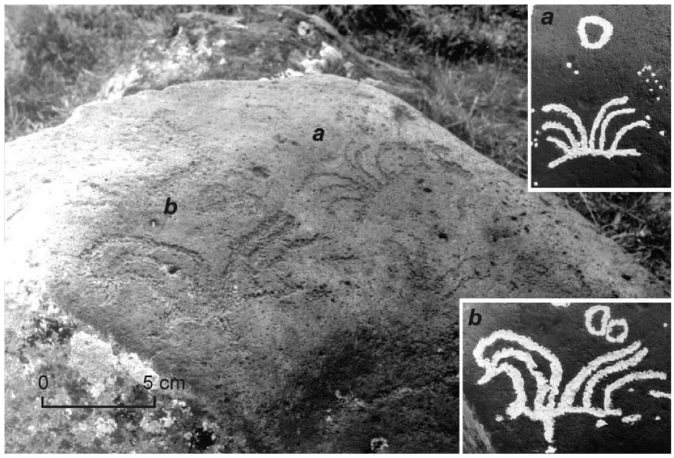

FIGURE 2.8: Two petroglyphs from the Porak volcano, Armenia, which are thought to depict a volcanic eruption from the 5th Millennium BC, corresponding with evidence of extensive forest fires and a large earthquake. Photograph from Karakhanian et al. (2002).

2.3.3 Structural Controls on Volcanism

Volcanism in the Lesser Caucasus occurs in elongated clusters (Avagyan et al., 2005) oriented predominantly N-S to NW-SE in Armenia, but when considering Georgia and Turkey, a third NNE-SSW direction is also observed (Avagyan et al., 2005). The variation in orientation correlate strongly with stress fields (Avagyan et al., 2005), and support the rotation of smaller continental blocks controlling local stress (Avagyan et al., 2005). The stress fields are also related to faulting, resulting in pull-apart basins, which are thought to control the locations of the volcanics (Avagyan et al., 2005; Karakhanian et al., 2002, 2003). In the Javakheti Highlands, a domino effect has been proposed, in which volcanism is controlled by sub-meridonal zones of extension, where the cessation of extension in one zone triggers the formation of a next zone (Lebedev et al., 2008a).

Unlike in the Lesser Caucasus where fault controlled volcanic ridges are quite common (e.g. Geghem Highlands, Porak Group, Abul-Samsari ridge; Avagyan et al., 2005; Karakhanian et al., 2002, 2003), relations with crustal features are harder to see in the Greater Caucasus. The Borjomi-Kazbek fault has been suggested to relate to volcanism (Philip et al., 1989), albeit in the Bakuriani-Borjomi region. However volcanic edifices seem to be alligned E-W along the Bakuriani fault in this region (Lebedev et al., 2009).

2.4 Causes of Volcanism

The heterogeneous nature of the mantle beneath the Eurasian-Arabian collision zone, both in terms of composition and structure, has led to a wide range of mechanisms to explain the major melting and volcanism in the region.

All the proposed models assume a mantle that has already experienced metasomatism by subduction related fluids, which has been observed from geochemical studies of the volcanism across the region (e.g. Pearce et al., 1990; Kheirkhah et al., 2009; Neill et al., 2013).

2.4.1 Mantle Plume

The large volume of volcanism in an intra-continental setting has led some authors to speculate that it was caused by a mantle plume (Ershov and Nikishin, 2004; Sharkov et al., 2014). In this model melts are sourced from this plume, and subsequently interact with the crust to generate the wide variety of compositions seen in the region (Sharkov et al., 2014). Deformation within the collision zone has made the plume asymmetric (Sharkov et al., 2014), which can partially explain the asymmetric uplift of the Turkish-Iranian Plateau (Şengör, 2003). Ershov and Nikishin (2004) suggest that the plume beneath the region is actually a northern extension of the African-Afar superplume, in which asthenospheric flow has occurred along a channel of thinned lithosphere from Kenya, through Syria, then beneath Anatolia and most recently Armenia.

2.4.2 Collisional Processes

Sarker and Abers (1999) observed that regions of active mountain building, such as the Greater Caucasus, retain steep geothermal gradients (i.e. heating rates exceed cooling rates, from processes such as advective cooling, and that this was still true over a period of at least 10–20 Myr). Small scale partial melts can be generated in the mantle lithosphere by shear heating (Kincaid and Silver, 1996). Viscosity and shear stresses are decreased with heating and the production of melt, which limits this as an affective process to 12–15 Myr (Kincaid and Silver, 1996). Allen et al. (2013) speculate that this is a possibility in the thickened lithosphere of Iran, although note that links between surface geology and Quaternary shearing at depth are unclear, unlike in the Caucasus where the Borjomi-Kazbek fault is thought to be a recently active strike-slip fault (Mumladze et al., 2015). High temperatures beneath the Greater Caucasus may extend too deep for shear heating on faults to occur, hence promoting ductile deformation (Sarker and

Abers, 1999).

Post-collisional magmatism has been explained in Tibet by rapid convergence of thick continental lithosphere of India and Asia, uplifting the intervening weaker lithosphereic mantle between, creating an upwelling of hot asthenosphere (Fig. 2.9A; Guo et al., 2006). Melts produced from this scenario would be expected to show a contribution from both slabs, as well as astenosphere. A similar effect could possibly occur between the thick Eurasian lithosphere and the South Armenian block. Upwelling could be encouraged by steepening of a slab in one of these convergence zones (Guo et al., 2014).

Crustal thickening has occured in the Caucasus, and as the lithosphere thickens, the lower regions are heated and ultimately melt at its base. This process has been suggested for regions of the Turkish-Iranian Plateau (Dewey et al., 1986), Lesser Caucasus (Koronovsky and Demina, 1996) and Iran (Allen et al., 2013). As the metasomatised, hydrous, base of the lithosphere is forced deeper due to thickening, amphibole will dehydrate to garnet, releasing water (Pearce et al., 1990). Allen et al. (2013) suggest that as a weakly hydrated amphibole peridotite is forced deeper due to lithospheric thickening, it crosses a backbend in the amphibole peridotite solidus (Green and Falloon, 2005), producing melts at a depth of around 90 km (Fig. 2.9B). Another consequence of lithospheric thickening is a lowering of geotherm, so although localised melting may be initiated, most of the metasomatised layer (which is most likely to melt) remains below the solidus (Pearce et al., 1990). However, in collision zones thermal heterogeneity suggests that processes such as under-thrusting, may create anomalously hot areas and so cause melting (Allen et al., 2013).

2.4.3 Extensional Processes

Extension is a common occurrence in late-orogenic settings. It is a process that has been suggested for volcanism in the Eastern Mediterranean

Post-collisional volcanism in extensional settings have been described by many authors in varying settings, including the Appenines, Anatolia and the Sierra Nevada (e.g. Fitton et al., 1991; Dilek and Moores, 1999; Dilek and Altunkaynak, 2007; Bianchini et al., 2008), and often link it to tectonic collapse of an orogen (e.g. Bianchini et al., 2008). However, the Caucasus are still a compressional region, with some lateral escape, have not yet entered into a tectonic collapse phase, and there is no structural evidence at the surface to suggest any significant extension is occurring.

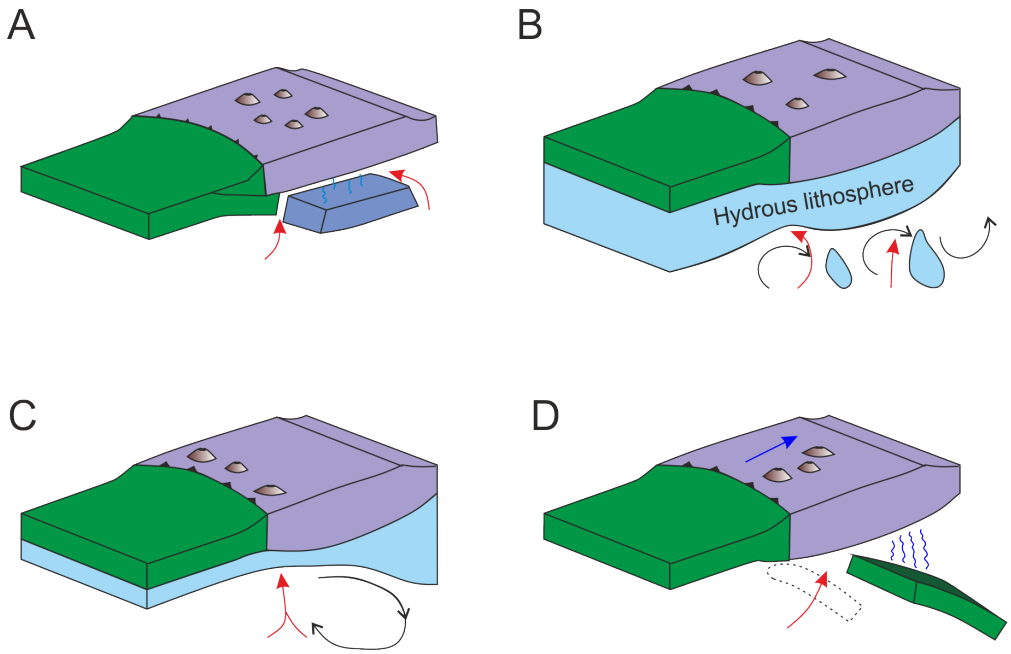

FIGURE 2.9: Block diagrams showing two potential causes of melting in collision zones. A) Convergence of thick continental lithosphere, squeezing asthenosphere beneath weaker lithosphere between them. Diagram modified after Guo et al. (2014). B) Lithospheric thickening pushing amphibole-bearing lithosphere deeper, to higher pressures than a back-bend in the amphibole solidus, resulting in dehydration and melting, which can then migrate upwards. Diagram modified after Allen et al. (2013), amphibole peridotite solidus curve from Green and Falloon (2005).

2.4.4 Lithospheric Delamination

Delamination of the cold lower part of the thickened mantle lithosphere in mountain belts could result in magmatism at the surface (Platt and England, 1994). As the delamination occurs, asthenosphere can convectively replace the dense lower lithosphere, and so elevate the thermal structure of, the remaining metasomatised lithosphere, causing the geotherm to cross the hydrated peridotite solidus (Pearce et al., 1990; Williams et al., 2004). The sinking lithospheric block may also dehydrate as it sinks, releasing water, and promoting melting (Fig. 2.10A; Elkins-Tanton, 2005). This process has been used to explain melting beneath East Anatolia (Pearce et al., 1990; Keskin et al., 1998), where there is thought to be a thin or absent lithosphere, whilst being characterised by voluminous magmatism (Keskin et al., 1998).

This model may not be appropriate in other areas in the region where thicker lithosphere is likely to be present, and melting is on a much smaller scale, and hence is unlikely to be caused by a catastrophic delamination event. However smaller localised

events can produce melting in a similar way (Kaislaniemi et al., 2014).

Kaislaniemi et al. (2014) propose a model for magmatism that relies on the over-riding plate having a hydrous lithosphere, a remnant from the earlier subduction, which creates a viscosity contrast with the ambient mantle, instability at the boundary between the two, and therefore promotes small scale convection (Fig. 2.10B). The irregular spatial and temporal distribution of volcanic centres across the region is readily explained by this model (Kaislaniemi et al., 2014). As the mantle beneath the collision zone is likely to remain hydrous well after the onset of collision, this process can also explain the long-lived nature of volcanism in the region, well after the collision of Arabia with Eurasia (Kaislaniemi et al., 2014).

Another form of small scale convection, known as edge-driven convection, has been proposed for volcanic regions such as the Atlas mountains (Missenard and Cadoux, 2012) and NE Brazil (Knesel et al., 2011). Edge-driven convection occurs as significant changes in the lithospheric thickness (Fig. 2.10C), such as the boundary between thick cratonic lithosphere, and thin, young continental lithosphere (Missenard and Cadoux, 2012). The contrast in temperature between the cold cratonic lithosphere, and warm asthenosphere underlying the thinner lithosphere induces the convection (King and Anderson, 1998). This process can produce volcanism far from the initial collision suture, and close to the craton the other side of the collsion zone. It can also explain volcanism parallel the the craton edge (Missenard and Cadoux, 2012), and the lack of age progression in the volcanics across the region (Knesel et al., 2011).

2.4.5 Slab Breakoff

Slab breakoff is the most commonly cited cause of magmatism in the region (e.g. Keskin, 2003; Şengör, 2003; Neill et al., 2013). Slab breakoff acts in a similar fashion to lithospheric delamination, in so much as when the slab breaks off it opens a window that the asthenosphere can rise into (Fig. 2.10D), where processes such as thermal erosion of the lithosphere (Williams et al., 2004) and decompression melting (Davies and von Blanckenburg, 1995) can occur. Above the slab, the mantle wedge has been metasomatised by subduction related fluids, so when the slab breaks off, upwelling asthenosphere interacts with this enriched mantle (Keskin, 2003), and that produces the subduction signature seen in many lavas in the region (e.g. Keskin et al., 1998; Kheirkhah et al., 2009; Neill et al., 2013).

For East Anatolia, slab steepening prior to breakoff has been proposed (Keskin, 2003). This allows a large area to be affected by subduction related metasomatism before the

breakoff that causes a pulse of melting in the mantle wedge well after the time of initial collision.

Armenia is a region with a thicker lithosphere than East Anatolia. Neill et al. (2013) propose a modified version of the slab-breakoff hypothesis to explain this. Before the slab breaks off, it can stall in the mantle for up to 20 Ma after the final collision (van Hunen and Allen, 2011). The mantle wedge would cool, and form an enriched lithospheric mantle beneath the over-riding plate, a process that takes 15–25 Ma following the end of collision (Holt et al., 2010). Eventually the slab would break off, and the influx of asthenosphere would melt the enriched lithosphere (Neill et al., 2013). Further dehydration of the slab could occur as it breaks off, further enriching the source region.

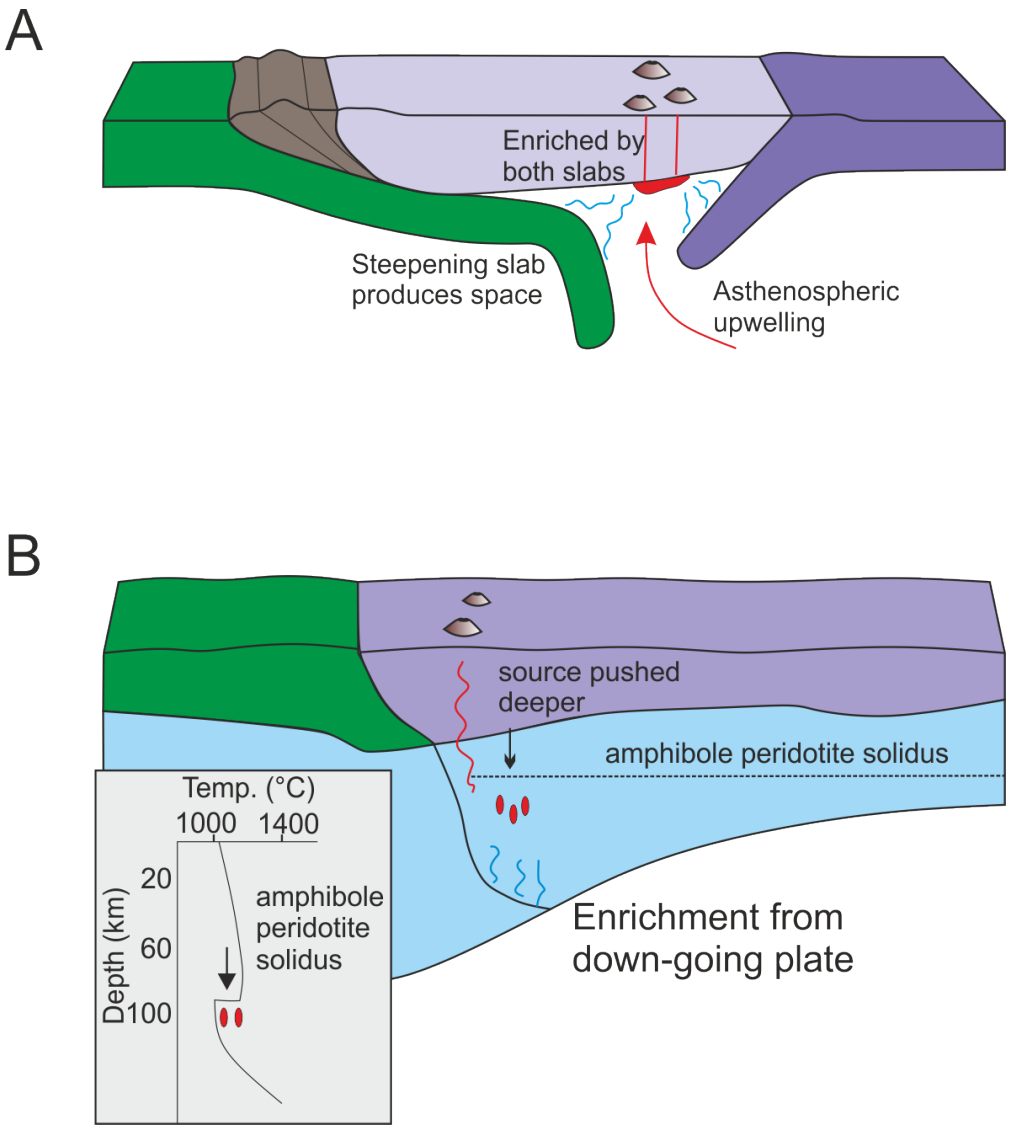

FIGURE 2.10: Block diagrams showing potential causes of melting in collision zones due to delaminations, and asthenospheric upwellings (red arrows). A) Delamination of dense lower crust, and lithosphere. Lithosphere dehydrates as it delaminates, and produces space for upwelling asthenosphere. Modified after Keskin (2003) B) Hydrous lithosphere can result in density contrasts, and small-scale convection cells (Kaislaniemi et al., 2014), resulting in small lithospheric drips, and asthenosphere rising to fill the space. Random distribution of volcanics is expected. C) Contrast between thick and thin lithosphere produces edge-driven convection (Missenard and Cadoux, 2012). Upwellings should produce volcanism parallel the the strike of the thickening. D) Slab-breako model. Down-going slab, dehydrates, enriching the mantle wedge, before break-off allows an upwelling of asthenosphere. Volcanism is expected to show younging in direction of dip of slab (blue arrow).

Chapter 3

Field Relations and Petrography

During the course of two field seasons in May 2013 and June 2014, samples were collected across Georgia from sites representing the post-collisional volcanics of the Greater Caucasus and Lesser Caucasus, the Palaeozoic basement of the Main Range Zone, and Palaeo- and Mesozoic basement of the Dzirula, Khrami and Loki massifs in the Transcaucasian depression. Samples were collected for petrographical and geochemical analyses. Most volcanic samples were fine grained, so fist sized hand samples sufficed to be a representative sample of an outcrop, however larger samples were collected for highly porphyritic samples. Most samples were collected along roadside outcrops allowing coverage of a large area and a comprehensive suite of as many flows (and various compositions) in the region as possible. Basement samples were collected for their composition and role as a possible contaminant. As complete a range of compositions as possible was required, rather than their detailed stratigraphic position and petrology, so some samples, from inaccessible outcrops, were collected from proximal float deposits, rather than in situ. This allows for a comprehensive classification of the volcanism.

Sample localities are tabulised in Appendix A, with most samples also labeled on Figures 3.1 and 3.9 in this chapter.

3.1 Lesser Caucasus Volcanics

The volcanics of the Lesser Caucasus are mostly located on the Javakheti Plateau (Fig. 3.1). This high volcanic plateau extends south into Armenia and Turkey. The northern edge is bordered by the Trialeti Range of the Lesser Caucasus Mountains. The western edge is marked by the Mtkvari River, whilst the eastern edge is marked by the Palaeozoic Khrami and Loki massifs. The plateau is split into two by a sub-meridional ridge

composed of the Abul-Samsari volcanics. Young volcanics also outcrop off the plateau in the west, at the Goderzi Pass, and to the north, close to the town of Borjomi. A time-scale of the volcanics is shown in Figure 3.2.

3.1.1 Goderzi Formation

The Goderzi Formation is predominantly exposed in the west of the Javakheti Highlands. Outcrop of this formation is more limited than other more recent volcanics, which overlay it. In the west it is relatively undeformed. It can be seen to be unconformably overlying strongly deformed Palaeogene deposits, on the western ank of the Javakheti Plateau at Uraveli. Exposure of the lowermost Goderzi Formation (~7.5 Ma; Lebedev et al., 2004) are limited, and the best outcrop is close to the town of Tskordza. It is dominated by highly vesicular dolerites. Vesicles show evidence of significant secondary alteration by fluids, and are often filled with zeolites. Stratigraphically above this sub-aerial flow are diatomite deposits, inter-bedded with coarser sandy layers with cross-bedding, rip-up clasts and load casts, representative of a semi-closed, euxinic basin.

Deposits coarsen upwards, from the diatomite, to fine, then coarse sandstone, and conglomerates at the top. This may correspond to the rapid uplift of the surrounding Lesser Caucasus during this time, with increased erosion into the low lying basins. Volcanism is likely to have been intermittent during this early stage of development. Thick layers of volcaniclastic conglomerates to the west of Tskordza, interpreted to represent lahar style pyroclastic deposits, pre-date the effusive activity. Clasts are mostly older volcanics, ranging from Jurassic arc lavas in the west, to early Cenozoic back-arc style basalts in the east. Some of these pyroclastic deposits have preserved petrified wood, and other organic material (Fig. 3.3), which has been dated at 9 Ma (Lebedev et al., 2011a).

The upper most Goderzi Fm. is poorly exposed. An outcrop of dacite at the Goderzi Pass, ~55 km west of the Javakheti Plateau, is thought to represent this age. However, it is strongly weathered, poorly dated and is isolated so lacks stratigraphic constraints, so cannot be confirmed as the Goderzi Fm. However, it is generally regarded as the upper part of the formation (S. Adamia, pers. comms.), and has been classified as such in this investigation.

The only outcrop of the Goderzi Formation east of the Abul-Samsari Ridge, occurs as a strongly folded flow, likely to be part of the lower section, based on its proximity to the contact with the underlying Eocene volcanics. It can be assumed that deformation increased eastwards after the eruption of the Goderzi Formation, as it is overlain here by

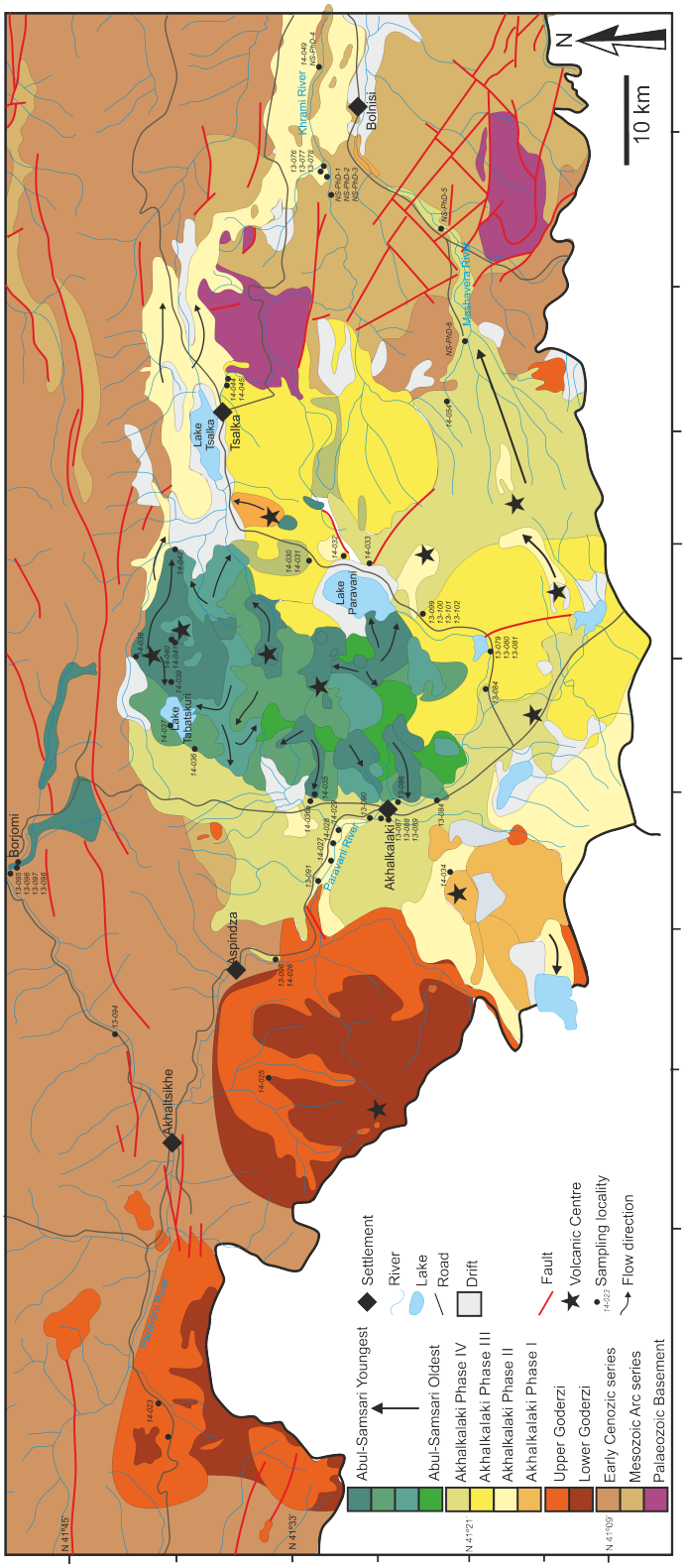

FIGURE 3.1: A sketch map of the post collisional volcanic rocks of the Georgian Lesser Caucasus. Adapted from (Lebedev et al., 2011c), N.Sadradze(pers.comms.),and field observations.

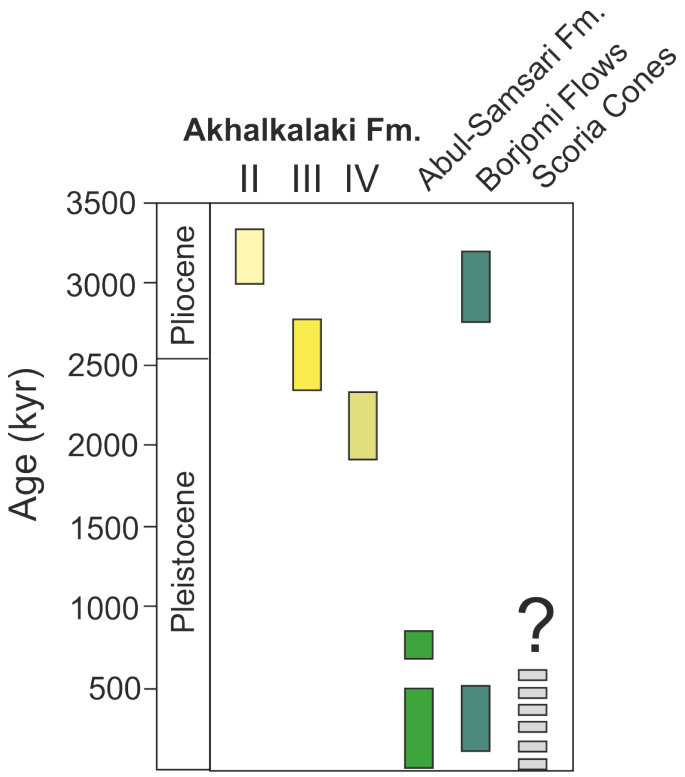

FIGURE 3.2: Time-scale of volcanics in the Lesser Caucasus. Goderzi Fm. not shown as it is so much older (~7.5 Ma). Colours correspond to Figure 3.1. K-Ar ages from Lebedev et al. (2003, 2007b, 2008a, 2009) and Nomade et al. (2016).

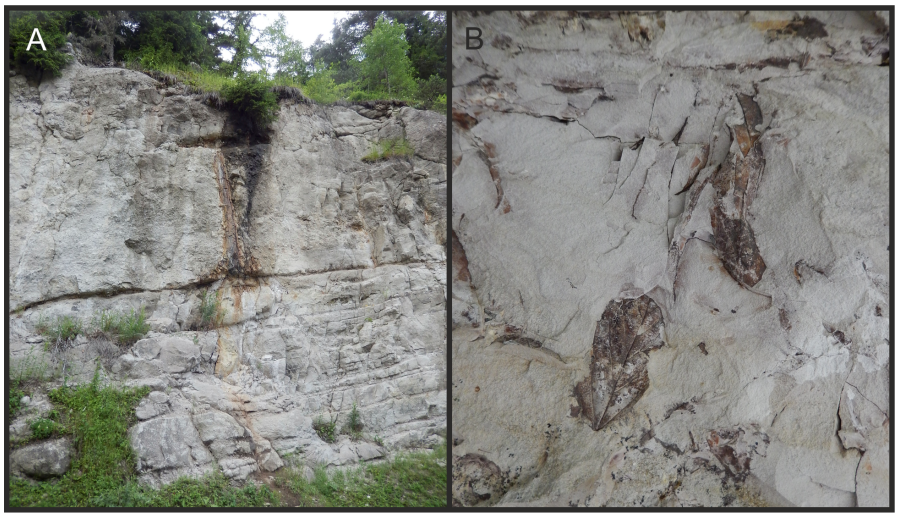

FIGURE 3.3: Pyroclastic deposits, possibly from lowest Goderzi Fm. A) Petrified tree, B) Well preserved leaf.

flat lying Akhalkalaki Fm.

3.1.2 Akhalkalaki Formation

The most widespread volcanics of the Javakheti Highlands belong to the Akhalkalaki Formation (Fig. 3.1). This was a major plateau building phase comprising numerous volcanic cones, fissure eruptions and major lava flows, up to tens of kilometres long. Activity lasted from 3.75 Ma to 1.55 Ma, with five discrete pulses being identified (Lebedev et al., 2008b). All dates from (Lebedev et al., 2008a,b) are K-Ar dates using the method of (Chernyshev et al., 2006) for young rocks, and are consistent with palaeomagnetic and palaeontological data.

Phase 1 is thought to be limited to the south-west of the highlands, where it is observed to be unconformably overlying the Goderzi Fm. (Lebedev et al., 2008a). No rocks were sampled from this phase. (Lebedev et al., 2008a) dated this pulse to 3.75–3.55 Ma, and believe it erupted sub-aqueously.

Phase 2 lasted from 3.44–3.22 Ma (Lebedev et al., 2008b). Outcrop is mostly limited to the southwest of the highlands. It also outcrops in the northeast as the large Khrami flow.

Phase 3 eruptions cover large areas of the east of the region, where they are thought to have originated from the Akha and Biketi cones. The area south of the Samsari ridge is also thought to be mostly of this phase, however outcrop here is limited. This southern activity produced the large valley filling flow of the Debed River in Armenia (Lebedev et al., 2008b). This phase of volcanism was also important and highly productive even further south in the Aragats region (Chernyshev et al., 2002). Phase 3 lasted from 2.65–2.45 Ma. This phase may also have been active in areas to the west of the region, but has now been covered by younger volcanics. It is clear that this was a highly productive, plateau forming phase.

The fourth phase shows significant activity across the whole plateau, except the south-west corner. This pulse has been dated at 2.15–1.95 Ma (Lebedev et al., 2008b). A sub-meridonal chain of cones to the east of Lake Paravani erupted lavas that flowed eastward over the earlier plateau surface, and formed the valley filling lava river of the Mashavera River. In the west, lavas flowed westwards from centres currently covered by the volcanics of the Abul-Samsari ridge (Lebedev et al., 2008c). The fifth and final phase was isolated to the northeastern section of the highlands, and was not investigated in this project.

Deep incision by rivers has produced exposure of >300 m thick stacks of the lava

flows that formed the Javakheti Plateau, and cut through multiple phases of volcanism. One such example is the Paravani River section beneath the town of Toki. It is exposed along roadside outcrops, on the northern side of the river valley. It is composed of over 20 flows

Fluvial and lacustrine sediments are present between some flows (Fig. 3.4A). The base of the flow in contact with the lake deposits are typically very vesicular (Fig. 3.4B), suggesting that the lava flowed over the lake when it was still wet, and the contact is conformable. Flows are also sometimes inter-bedded with lacustrine deposits, supporting the conformable relationships. However, in other outcrops the contact seems unconformable, with lacustrine, coarsening to fluvial sediments, incising the flows below. It is likely the whole section is an unconformable stack of lava flows, with the lacustrine deposits predominantly occurring between phases 2 and 3. The region must have been low-lying and still being deformed whilst these eruptions occurred, allowing some flows to preserve the conformable relationship. Vesicle tubes are common features (Fig. 3.4C), and very well preserved, with sharp edges. how they formed is unclear, and a full understanding is not necessary for this investigation. Two common suggestions for their formation are by gas filter pressing (Sisson and Bacon, 1999) or fractional crystallisation, followed by extraction of volatile enriched melts (Hartley and Thordarson, 2009). Both of these could have a major effect on the geochemistry of these rocks, particularly fluid mobile elements. It also suggests these lavas were rich in volatiles.

A lava stack near the town of Tsalka in the northeast of the plateau was also sampled. It has been exposed by incision of the Khrami River beneath the settlement of Dashbashi (Figure 3.5). Outcrop on the southern side of the valley is >100 m thick, and shows at least 7 flows. The contact with the underlying red granites, belonging to the Palaeozoic Khrami Massif is exposed here, with no evidence for volcanics of the Goderzi Formation volcanics, suggesting that this formation pinches out to the east. This section, like the Paravani section, also cuts through phases 2 and 3, with the base of the section ~3.25 Ma, and the higher flows dated at ~2.45 Ma (Lebedev et al., 2008b). The relationship between the older and younger volcanics is unclear, as exposure is poor. The opposite side of the valley (shown in Fig. 3.5) shows an almost continuous stack of lava flows, but it is not clear if they belong to the same eruption as the ones sampled.

The most easterly Alkhalkalaki Fm. is represented by three long tongues of lava, rather than the plateau sections of the Paravani and Dashbashi sections. The longest of these flows has not been included in this study as it flows south-east into the Debed River valley in Armenia.

The northernmost lava tongue is the Khrami Flow. The source of the flow is thought

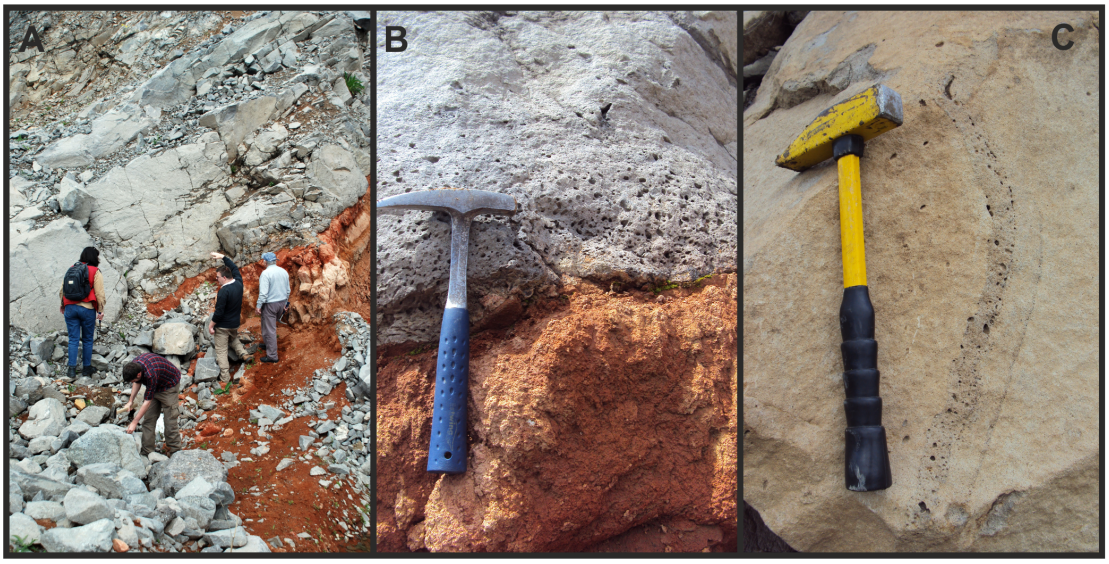

FIGURE 3.4: A) Interbedded lava ow (grey) and lacustrine sediment (red). B) Closeup of lava-sediment contact from A. Lava is highly vesicular at the contact. C) Vesicle tube (with thinner one next to main one).

FIGURE 3.5: Stack of at least 10 lava flows, with considerable continuity in the Khrami river valley, beneath the town of Dashbashi. Flows overlie Hercynian granites.

to be covered by the younger Quaternary lavas of the Abul-Samsari Fm. (Lebedev et al., 2008b), to the north-west of Tsalka. It flows for 60 km eastwards down the Khrami River palaeovalley towards Bolnisi. In parts it reaches 10 km wide. The maximum thickness, close to the source, is over 100 m (Lebedev et al., 2007a), before thinning towards Bolnisi. It formed during phase 2 (3.16–3.26 Ma; Lebedev et al., 2008a), a similar age, but different eruptive style to the base of the Paravani and Dashbashi sections. Samples were only collected from the more distal part of the flow, close to Bolnisi.

A second significant flow filled the Mashavera River valley. This is to the south of the Khrami flow, between the Loki and Khrami Palaeozoic basement massifs. Unlike the Khrami flow, the Mashavera flow is narrow (<2 km), around 35 km long, and maintains a constant thickness (50–100 m) throughout the majority of its length (Lebedev et al., 2007a). Lebedev et al. (2008b) assign this flow to phase 4 (2.0–2.2 Ma). However, significant work by other authors has been undertaken on this flow in particular because of its importance as the location of the earliest known Homo erectus fossils in Europe. The most commonly quoted age is 1.85±0.01 Ma, measured by $^{40}Ar/^{39}Ar$ (Gabunia et al., 2000). This is clearly younger than the Lebedev et al. (2008b) ages, and would extend the duration of phase 4 by over 200 ka. Dating of material from ash layers in which hominid fossils were found yield even younger ages (1.81±0.03 Ma; Garcia et al., 2010), which is important to show both that the activity was not purely effusive, and not only were humans living in the region whilst it was still volcanically active, but may have perished because of the volcanoes too (de Lumley et al., 2008).

Outcrop is poorer in the centre of the plateau, where there has been less incision by rivers. However there are areas around Lake Paravani where the contact between flows is seen to be clearly unconformable, reinforcing the ideas of significant deformation during this plateau building phase. Despite a lack of dating, it is thought samples collected here belong to phase 3 (Lebedev et al., 2008a).

In the north of the plateau, particularly NE of the Abul-Samsari Ridge, there is evidence of volcanic benching, which may underlie the ridge. There is a large number of thin (<5 m) flows, covering a large area. It is likely this is how the Javakheti Plateau formed. This may also be related to stage 2, and have been the region from which the large Khrami flow initiated.

3.1.3 Scoria Deposits

Particularly around the eastern and southern edges of the Abul-Samsari Ridge, and the shores of Lake Paravani, there are a number of quarries exposing large scoria deposits.

FIGURE 3.6: Roadside outcrop showing poorly consolidated scoria outcrop. Large bombs seen cutting across well bedded layers.

The age of these scoria cones is unclear. Lebedev et al. (2011c) has them related to phase 2 of the Akhalkalaki Fm. However, deposits seen in roadside cuttings and quarries can be 50 m high, and very poorly consolidated (Fig. 4.9). It seems likely that these are young deposits as they have undergone little erosion. We are treating them as a separate entity, rather than assigning them to any phase of the Akhalkalaki Fm. or the Abul-Samsari volcanics, as the age and stratigraphic position is so poorly constrained.

The deposits are composed of a fine, scoraceous matrix, containing large bombs (>1 m or more) of aphyric black lava, and smaller clasts of scoria, mafic lava, highly porphyritic material and obsidian. In the smaller mafic clasts two types of xenolith were found. Typically ~1 cm across they were either siliceous (crustal) material, or deeper ultra-mafic material. In some quarries feeder dykes were seen, and others seemed to be topped by lava flows (probably of Abul-Samsari affinity). Samples were taken of the freshest material, which was typically very hard to break. This was despite many of the quarries being severely reddened due to oxidation in places.

3.1.4 Abul-Samsari Formation

Over 20 volcanoes form the 40 km long, N-S trending Abul-Samsari ridge. It is situated between the town of Akhalkalaki and Lake Tabatskuri to the west and Lake Paravani in the east. Volcanoes erupted through, and stand topographically proud of the surrounding Akhalkalaki Fm.

Lebedev et al. (2003) suggest that three phases of volcanism formed the ridge. Mt. Didi-Abuli (3300 m) is the oldest volcano in the ridge, the predominantly dacitic flows

are 400–250 ka, Mt. Samsari (3284 m) is younger, around 200 ka. The smaller cones of Tavkvetili and Godorebi are younger than 30 ka (and possibly Holocene) and represent the youngest volcanism in the Lesser Caucasus (Lebedev et al., 2003). For the purpose of this investigation, the volcanism of this formation is treated as a single event. This is because the ages are very young, the apparent hiatuses between phases of volcanism are small, and errors are large (Lebedev et al., 2003), making it problematic to distinguish events.

Samples were collected from the northern flows of the ridge, which includes some of the youngest eruptions in the Lesser Caucasus (290–170 ka; Lebedev et al., 2003). This included float and in situ sampling. Typically samples are very fresh, with a glassy matrix.

3.1.5 Borjomi Flows

Around the town of Borjomi, north of the Javakheti Highlands and the Trialeti Ridge, is a small centre of Quaternary volcanism. Flows are up to 13 km long, and have been erupted from one of four volcanoes. The Tsitelidabadzveli vent was active 2.85–3.20 Ma, at the same time as the Lower Akhalkalaki Fm. (Lebedev et al., 2009). The Tsikhisdzhvari and Sargavi volcanoes were active 0.360.45 Ma, and the Mukhera volcano is the youngest at 0.19–0.25 Ma (Lebedev et al., 2009), both of these are contemporaneous with the Abul-Samsari Ridge volcanics. Samples were taken from the 11 km long flow from the young Mukhera volcano. The flow originates from the 15 km^2 plateau west of the volcanic vent, and then extends northwards filling the Borjomula river valley, terminating close to the confluence with the Kura River, and the town of Borjomi, were the samples were collected.

3.2 Greater Caucasus Volcanics

Post-collisional volcanism in the Greater Caucasus is contemporaneous with the Abul-Samsari Fm. (<800,000 years), the youngest stages of volcanism in the Lesser Caucasus. In Georgia, these volcanics outcrop close to the Russian border, near the towns of Gudauri and Stepantsminda, either side of the Tergi River valley, and into the disputed territory of South Ossetia (Fig. 3.7). In this region there are various styles of volcanism occurring within a small spatial and temporal range, focused on four areas: Mt. Kazbek, Gudauri, Qabarjina and the Keli Highlands. Age relationships between the volcanics is shown in Figure 3.8.

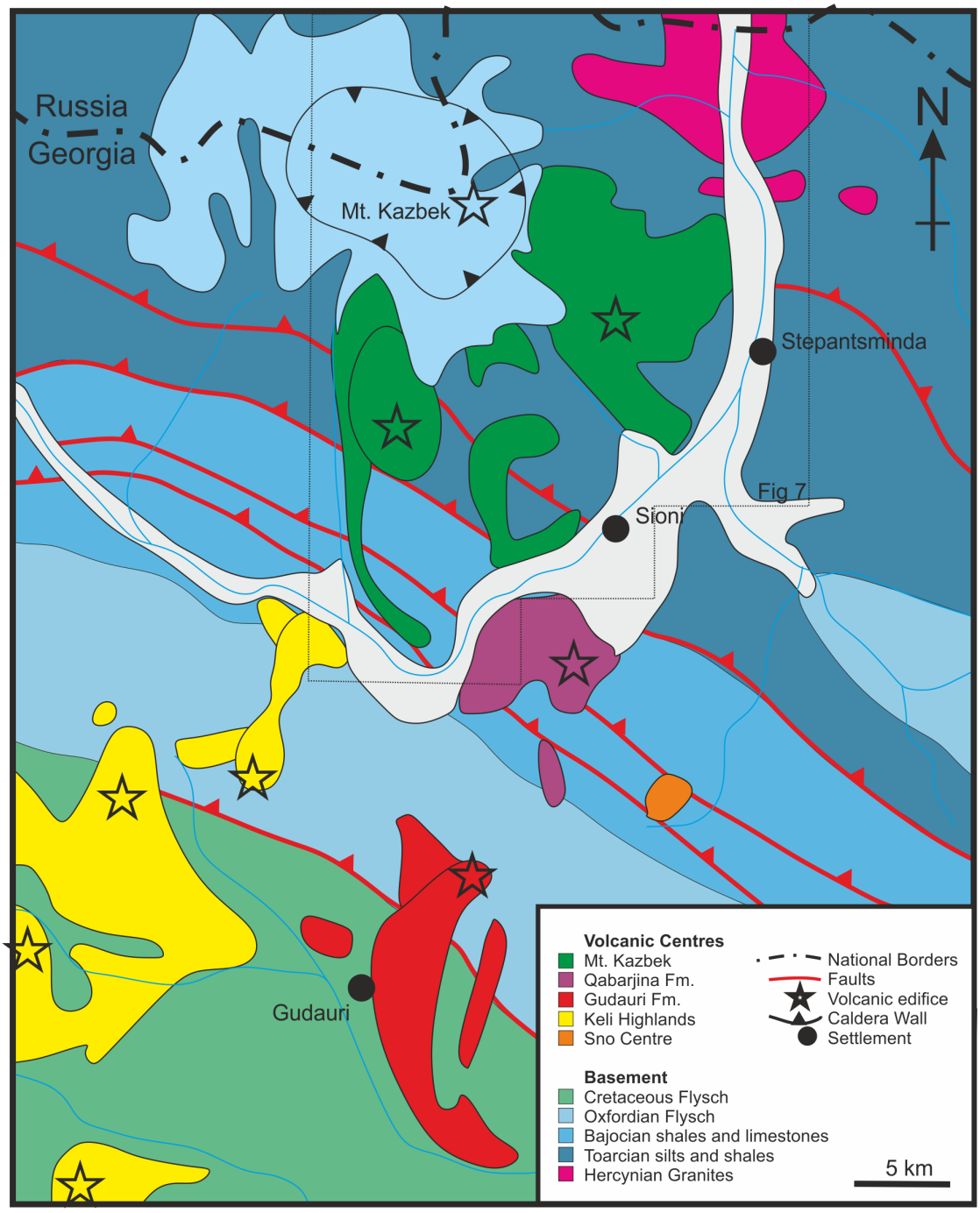

FIGURE 3.7: A sketch map of the post-collisional volcanic rocks in the Mt. Kazbek section of the Greater Caucasus, and underlying basement rocks. Dotted line shows location of Fig. 3.9. Adapted from (Gudjanidze, 2003) and N. Sadradze (pers. comms.).

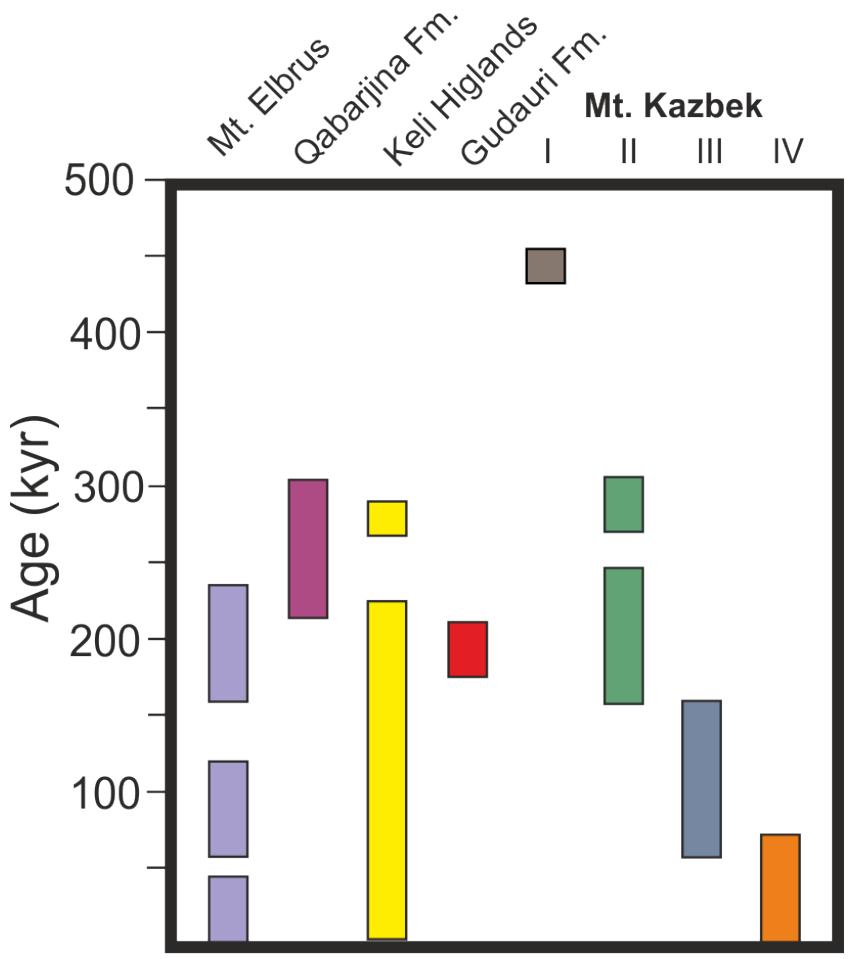

FIGURE 3.8: Time-scale of volcanics in the Greater Caucasus. Age of Mt. Elbrus volcanics shown as a comparison. Colours correspond to Figure 3.7. K-Ar ages from Chernyshev et al. (2002), and Lebedev et al. (2007b, 2012).

3.2.1 Mt. Kazbek

Mt. Kazbek is the largest stratovolcano in the Georgian Greater Caucasus, and the largest volcanic centre in this region. Lebedev et al. (2014) have separated volcanic activity into four age groups: Stage I is older than 400 ka, stage II lasted from 250–200 ka, prior to a caldera collapse event, stage III from 120–90 ka, and stage IV, ¡50 ka, both post-dating the caldera collapse (Fig. 3.9). This classification fits with morphological observations made in the field, discussed in the following sections.

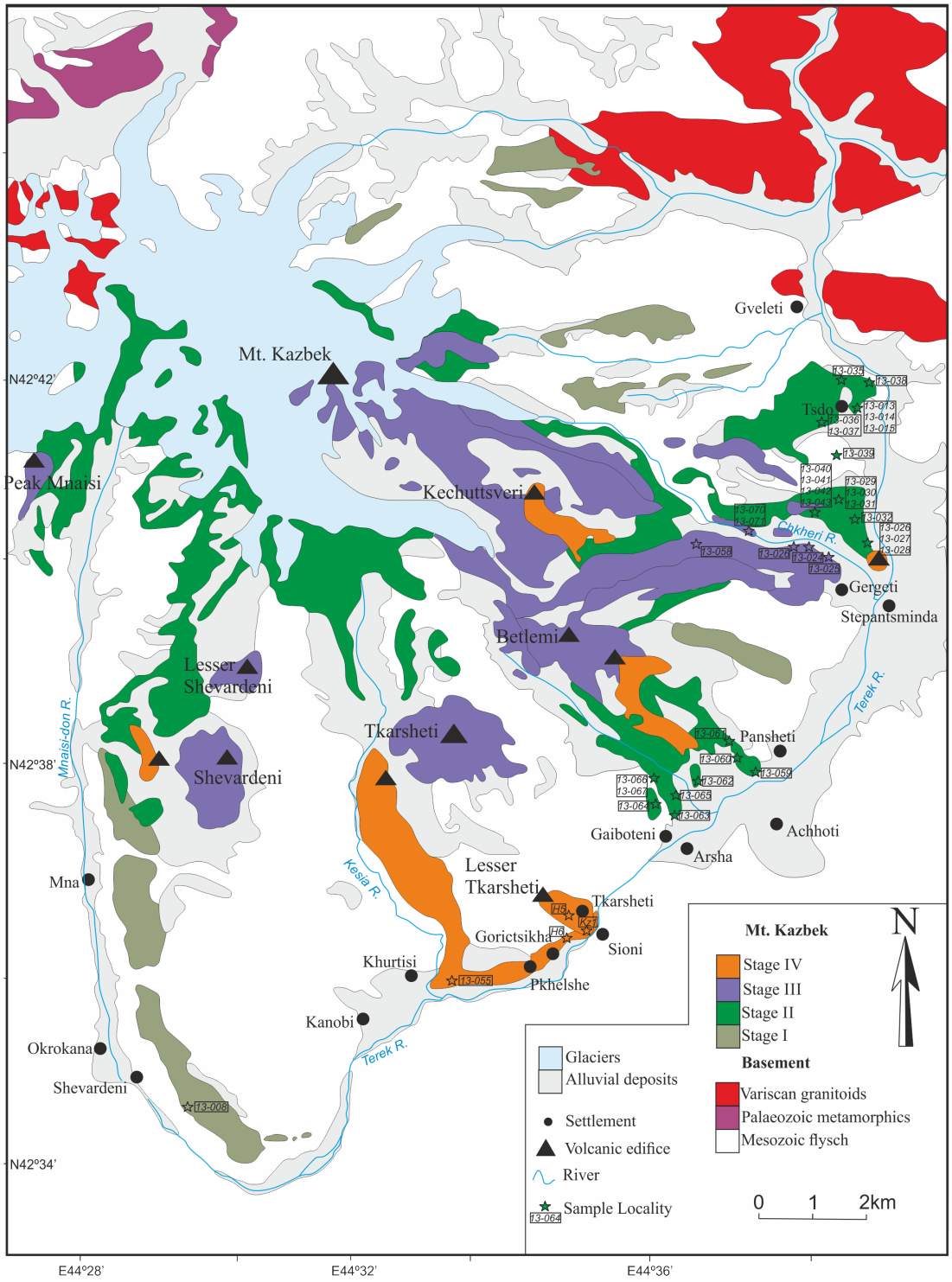

FIGURE 3.9: Sketch map of the lava flows from Mt. Kazbek. Location shown in Fig. 3.7. Map adapted from Lebedev et al. (2014).

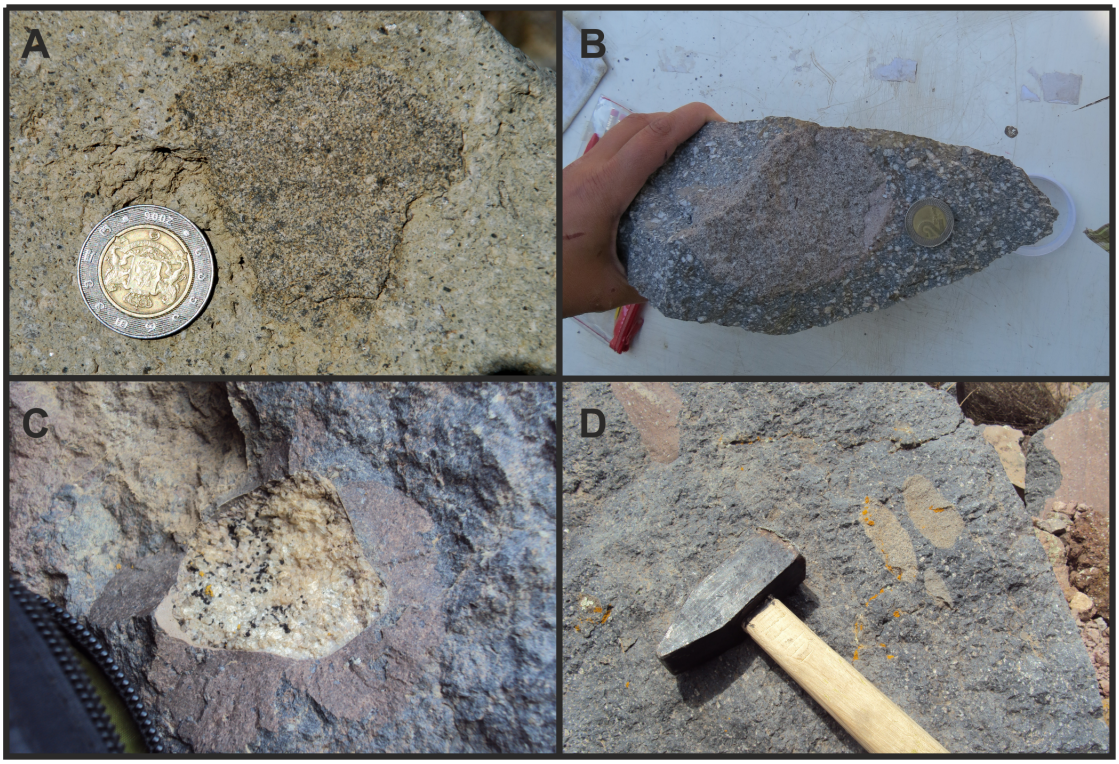

FIGURE 3.10: Dierent inclusion types found in the lavas erupted from Mt. Kazbek. A) Dolerite inclusion, mac material within a more evolved rock. B) Coarser grained version of the surrounding magma. C) Granitic inclusion, similar to local basement. D) Sedimentary inclusions.

3.2.1.1 Stage I

The oldest flow sampled from stage I, was also the most southerly sampled from Mt.Kazbek. It is an 8 km long flow forming the northern ridge of the Tergi River in the Truso Gorge, near the South Ossetian border. It is possibly the product of a fissure eruption related to the main up-thrust of the Greater Caucasus (Lebedev et al., 2014). It shows well developed columnar jointing. It is strongly porphyritic, with plagioclase up to 1 cm long. Fine grained mafic xenoliths suggest magma mixing had occurred (Fig. 3.10A). There are also common xenoliths of a coarser grained version of the bulk material (Fig. 3.10B).

3.2.1.2 Stage II

Stage II volcanics are from the main stage of stratovolcano formation of Mt. Kazbek. Most of the flows seem to originate directly from the main vent itself (Lebedev et al., 2014). Some of the best exposure is observed in the Chkheri River valley, west of Stepantsminda

FIGURE 3.11: Dierent inclusion types found in the lavas erupted from Mt. Kazbek. A) Dolerite inclusion, mac material within a more evolved rock. B) Coarser grained version of the surrounding magma. C) Granitic inclusion, similar to local basement. D) Sedimentary inclusions.

(Fig. 3.11). The northern side of the valley allowed a traverse across at least 15 flows, each flow being between 2 and 10 m thick. Flows could be readily distinguished by the presence of brecciated flow tops, and erosional surfaces. Within each unit, compositional flow banding, and alignment of plagioclase phenocrysts were commonly observed. Xenoliths of coarser material with similar bulk mineralogy to the host flow were relatively common (Fig. 3.10B). Less common, although present, were microgranite xenoliths (Fig. 3.10C), with a composition similar to that of crustal lithologies less than 10 km to the north.

The lateral continuity of the flows is uncertain. Sedimentary layers between flows were not continuous, often pinching out before reappearing. This may reflect complex topography of the area whilst Mt. Kazbek was still active, prior to glaciation, and incision by the Chkheri River. In sections that have been cut across by smaller tributaries, it is difficult to trace individual flows across the valley.

Evidence for explosive activity is provided by occasional tuff units between flows. Clasts within the tuff include the surrounding lava flows, pumice, and cumulate rocks. Large blocks of this cumulate material can be found on the valley floor. An in situ outcrop of this material was not seen, although a local farmer suggested the lithology outcrops up one of the tributaries.

In addition to the lava stacks forming the valley sides, there is evidence for activity post-dating glaciation (and formation of the Chkheri River valley). At the eastern end of the northern ridge there are explosive volcaniclastic deposits, representing a late flank

eruption (Lebedev et al., 2014), and this is topped by further mafic flows suggesting this is not a terminating explosive event. This probably related to stage IV (Lebedev et al., 2014).

To the north of the Chkheri valley, up the Dariali Gorge, the village of Tsdo is sited on another flow. This flow, and at least two others between Tsdo and the Chkheri valley, flowing into the valley show impressive columnar jointing and sit on top of fluvial deposits. These are also easterly flows of stage II.

The south-eastern flows of Mt. Kazbek outcrop along the Tergi River, near the towns of Pansheti, Toti and Gaiboteni also belong to this highly productive stage II (Lebedev et al., 2014). Flows here are typically 5–20 m thick, and show well developed columnar jointing. They occur as tongues between strongly folded Mesozoic flysch, and probably originate either from Mt. Kazbek, or from the Betlemi flank volcano that became active during the latter stages of the evolution of Mt. Kazbek. The flows are more evolved than the stack forming flows of the Chkheri valley, with phenocryst assemblages typically of plagioclase and amphibole, sometimes with biotite, and lacking in pyroxenes.

The flows overlie volcanic breccias, containing only volcanic clasts, so likely they have erupted quite late in the history of the volcano, after significant lava had already built up on the surface. Clasts range from glassy, mafic material, to more dacitic compositions, similar to the overlying flows. Clast size ranges from a few mm's to >1 m. The clasts are bound by a cement of angular volcanics.

Further up section volcanic agglomerates are seen between flows. Fluvial deposits with well developed cross bedding, and finely laminated layers are also observed, with cross-cutting flows that suggest the relationships between adjacent flows is unconformable.

These are the most southerly flows sampled of Stage II. There are flows further south, higher up the slopes, flowing southward from the main vent, but these were inaccessible during our field season. Lebedev and Vashakidze (2014) have dated these at 245±50 ka.

3.2.1.3 Stage III

The south side of the Chkheri valley also exposes a stack of lava flows like the north side, however these were less accessible. These flows have been dated as belonging to stage III (110±40 ka; Lebedev et al., 2014), post-dating the caldera collapse event, and flowing ENE from the Betlemi flank volcano. However there is no field evidence suggesting these are any younger than the flows on the opposite side of the valley. The most accessible samples from this stack were at the top, and therefore most exposed to the elements, and had normally been heavily weathered. It is possible that a stage III flow sits on the

top of the stage II stack of flows on the north side of the Chkheri valley (Lebedev and Vashakidze, 2014). However, in the field it is unclear if this is the case or not.

The clearest indication of stage III activity is the form of valley filling flows. The largest of these is at least 3 km long and occurs beneath the village of Gergeti on the south side of the Chkheri valley. Flows from the section furthest up the valley shows a trachytic texture, flattened vesicles, and flow banding. Towards the toe of the flow, the flow features weaken, and columnar cooling joints dominate as the flow cooled. Two other flows, further up on the northern side of the valley show similar features (Fig. 3.11). It is unclear which vent these erupted from, but they may be related to Mt. Kazbek itself.

3.2.1.4 Stage IV

Activity related to Stage IV is relatively limited. A fresh looking, blocky flow could be seen on top of the north Chkheri lava stack high up the valley, having flowed down from the higher reaches of Mt. Kazbek. It's distinct morphology and fresh appearance contrasts with the stack forming flows. and is assumed to be younger, erupted from the Kechuttsveri cone, close to the peak of Mt. Kazbek (25±25 ka; Lebedev and Vashakidze, 2014). Although inaccessible, a sample was collected from the float that was significantly fresher than all other volcanic samples, and may have come from this flow.

The most accessible stage IV flow erupted from the Tkarsheti flank cones, south of Mt. Kazbek. The longest flow is 7 km long, flowing down to the present day Terek river valley, and flowing parallel to it for 3 km, and showing well developed columnar joints.

At one point it is assumed to have dammed a river, and created a lake at the town of Gorictsikha (Fig. 3.12). Carbon dating of organic material in the lake gave an age of 6000 years, making it the youngest dated flow in the area. Deposits of this flow look very fresh and glassy, with no evidence of recrystallisation. They may be a small second flank cone (Lesser Tkarsheti) that also produced stage IV volcanics in this area.

3.2.2 Qabarjina Formation

The Qabarjina Formation represents a relatively short lived volcanic complex, and the earliest in the Kazbek area. Close to the village of Ukhati is a spectacular outcrop of a columnar jointed, 30 m thick flow (Fig. 3.13A). The columns splay out, possibly representing the filling of a palaeo-valley. This is the only evidence of significant effusive activity in the complex, and allowed in situ sampling to take place.

The western side of the complex exposes a matrix-supported, laterally extensive

FIGURE 3.12: View of a lake dammed by a lava flow. Material from the lake has been used to date the flow. The dam has since been breached and the lake has drained.

(>3 km), volcaniclastic unit, with regular cooling joints, and a clast supported rubbly flow top (Fig. 3.13C). The matrix is predominantly fine ash (Fig. 3.13D). Clasts range from less than a centimetre, up to 1.5 m long blocks. Clast lithology also varies greatly. Mafic clasts show similar compositions to the Ukhati flow, possibly representing the early history of the complex. The other main clast type is blocks of the surrounding Mesozoic country rock. These clasts are evidence of the explosive nature of this volcanic centre.

The high topography and steep slopes made sampling the centre of the complex more difficult than the edges. No fresh, in situ samples could be collected. Samples of float were collected in a cirque-like feature on the eastern side of the complex (Fig. 3.13B). The steep-sided nature, and at base to this river valley make it probable that float was derived locally to the high peaks, and only short transport had occurred. These float litholgies reflect similar compositions to the Ukhati flow, and to the volcaniclastic breccias, and also contained more evolved andesites and dacites.

3.2.3 Keli Highlands

The Keli Highlands (Fig3.7) have been active for the past 270 ka (Lebedev et al., 2008c). They cover a large area of around 150 km^2. It is a region dominated by monogenetic cones, but with some larger centres too (e.g. the Didi Nepiskalo and Yuzhnyi Narvan-khokh volcanoes). Unfortunately the area is almost entirely in the inaccessible territory of South

Ossetia. One flow from the highlands that we could sample, flowed north into the Truso Gorge, so must be younger than the ridge forming southern flow of Mt. Kazbek (Fig. 3.14). This sample has been affected by hydrothermal alteration. This is likely to be associated with a fault, along which other areas of hydrothermal activity are seen.

3.2.4 Gudauri Formation

Some authors have classified the flows around the town of Gudauri as being related to those of the Keli Highlands (Adamia et al., 2010; Lebedev et al., 2007b). For the purpose of this investigation we treat the flows on the east side of the Mtiuleti Aragvi valley, around the town of Gudauri and the Jvari pass as part of the 'Gudauri Formation', and separate to the Keli Highlands which we did not sample due to political reasons as mentioned above.

The largest flow is the valley filling Gudauri flow, beneath its namesake town (Fig. 3.15). It outcrops along the valley side and is at least 200 m thick. The flow is 14 km long, descending south from Mt. Sakokhe, turning eastward into the river valley. It is not clear how many flows make up this outcrop, but is likely to be at least two. The flow has been dated at 200±60 ka (Lebedev et al., 2007b). The flow shows very well developed columnar joints, splayed out towards the base, perpendicular to the original cooling surface. This is very different to concurrent volcanism in the Keli Highlands on the other side of the valley, which is dominated by dacite domes. The base of the flow is strongly porphyritic, with plagioclase and pyroxenes the main phases. Higher in the flow, it becomes more massive, flow banding is observed, and the proportion of phenocrysts diminishes.

Out of the valley, flows can be observed on the surface. These flows are closer to the proposed volcanic centre, Mt Sakokhe. One of these flows is a very fresh, holocrystalline, aphyric flow, outcropping next to Mesozoic sedimentary deposits. Other flows are highly porphyritic, often with gabbroic glomerocrysts. At the Jvari Pass an inaccessible cliff section shows a stack of at least three flows, suggesting that this centre produced both large-scale (Gudauri flow: Fig. 3.15), and smaller-scale flows. There is no evidence of any explosive volcanic activity in the area.

3.3 Basement Samples

Unlike volcanic samples, where samples from individual flows were collected for basement samples we were only interested in them as potential contaminant material. Hence

the stratigraphical and structural relationships between different lithologies were less important. Therefore basement samples were often collected from the float of regions with steep topography, and at the base of glaciers, because, 1) the samples were significantly more accessible, and, 2) the steep terrain means the samples are likely to be proximal to their float location.

3.3.1 Main Range Zone

The basement exposed in the main range outcrops on some of the tallest peaks in the Greater Caucasus, in the region of Svaneti. Similar basement underlies most of the Greater Caucasus, including beneath Mt. Kazbek and the volcanics in that area. With the limited time we had available and the relatively inaccessible terrain, float samples were collected from fresh looking rockfalls, in two valleys, to the east and west of Mt. Ushba (4710 m). The western valley ran north of the town of Mazeri, while samples in the eastern valley, north of Mestia, were collected at the base of the Chalaadi glacier. In the western valley, the tectonic contact of the metamorphic Main Range complex could be seen, thrust over Jurassic flysh.

Basement samples contained four lithological types, granites, schists, gneisses and amphibolites. Three types of granite were collected. The first was a weathered granite, comprising of only quartz and two feldspars. These may represent a eutectic melt formed during crustal melting as seen in migmatite leucosomes. The second contained significant amounts of amphibole and mica. The third, the so-called 'Ushba Granite', which formed most of the mountain, contained large, broken-up garnets, in a badly weathered groundmass.

The schists typically contained significant amounts of biotite, often fragmented garnets (sometimes forming veins), and commonly graphite flecks cutting across the fabric, as defined by the micas. The gneisses contained biotite, amphibole, potassium feldspar, chlorite, and in one case sillimanite, suggesting these rocks had been subjected to high temperatures, in the amphibolite or granulite facies. The fourth major lithology found was an amphibolite, often containing significant amounts of sphene.

In situ basement was exposed 10 km north of Stephantsminda near Mt. Kazbek on the Russian border. Here Hercynian granites, granodiorites, and gneisses outcrop. The Palaeozoic basement was cut by numerous Jurassic dykes, which was a regional feature of all in situ basement.

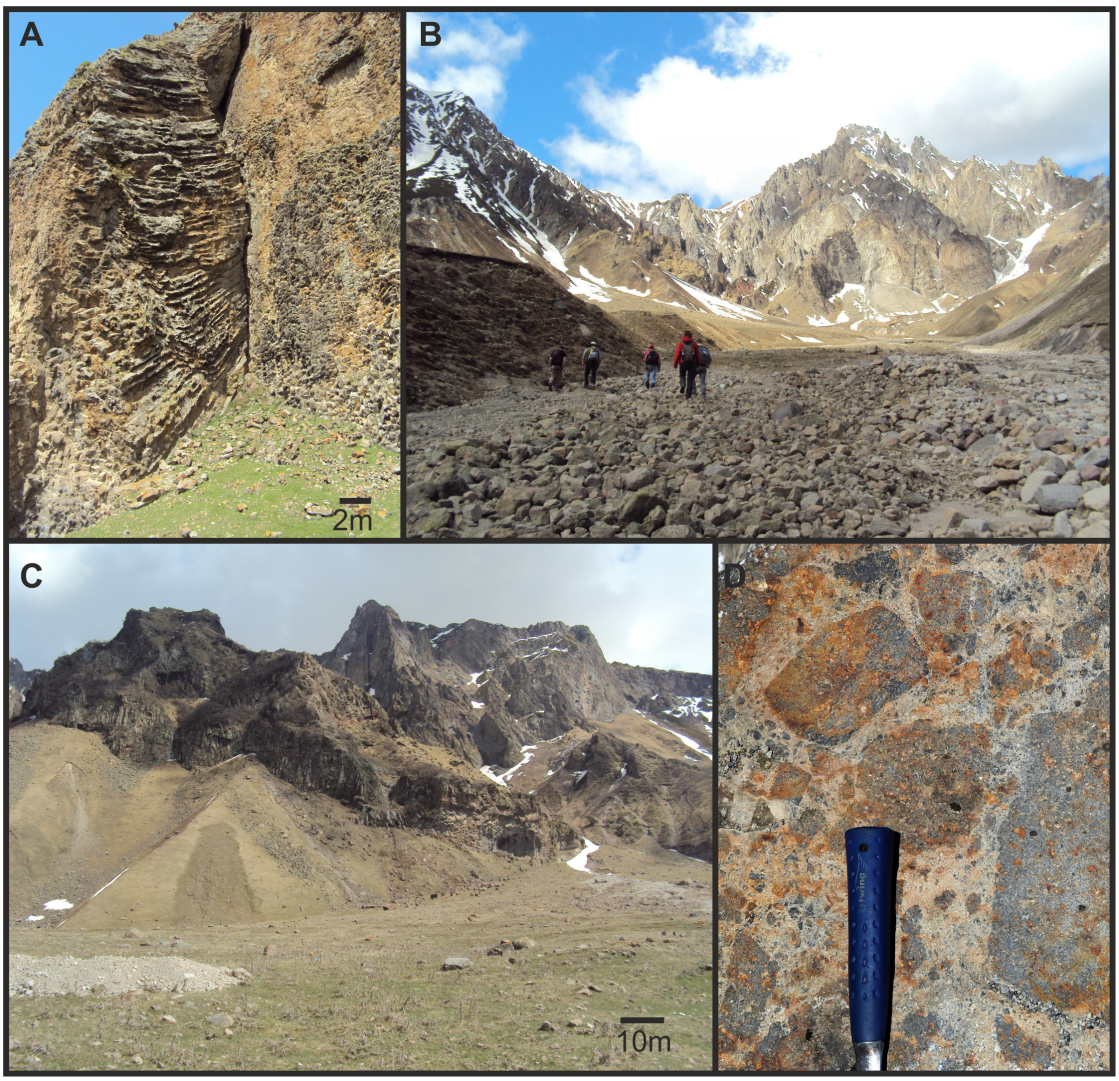

FIGURE 3.13: Dierent lithologies and volcanic styles shown in the Qabarjina Fm. A) Lava flow with spectacular columnar jointing (bases of columns seen) at Ukhati. B) Steep topography from which the float of the Qabarjina Fm. was collected. C) Volcaniclastic flow, showing lateral continuation and regular cooling fractures. D) Close up of the volcanic breccia from C.

FIGURE 3.14: Lava flow, flowing into the Truso Gorge from the Keli Highlands (flowing in direction of arrows). Red colour shows hydrothermal alteration. Steeply tilted Mesozoic flysch seen in background. Photo taken from beneath a phase I lava flow of Mt. Kazbek.

FIGURE 3.15: Impressive columnar jointing of the largest flow of the Gudauri Fm.

3.3.2 Transcaucasian Massifs

Samples of in situ basement were collected from the three Transcaucasian massifs in Georgia. These represent basement beneath the Lesser Caucasus, and possibly the southern slopes of the Greater Caucausus. The 320 Ma 'Red Granite' is found in all three of the massifs, and was emplaced during the Hercynian orogeny. In the Dzirula massif the contact of the Red Granite with the surrounding Cretaceous limestone can be seen to be intrusive, rather than tectonic. In the Khrami Massif, flows of the Akhalkalaki Fm. can be seen in contact with the erosional surface on top of this granite. Petrographically, it contains quartz, plagioclase and significant amounts of potassium feldspar, with common granophyric texture. The 'Red Granite' may be the same as the first granite type described in the Main Range Zone (Section 3.3.1).

Two other igneous lithologies were found. A tonalite/quartz diorite, which possibly represents an early Palaeozoic arc affinity, was found in the Dzirula and Loki Massifs. The Red Granite can be seen cutting the diorite in the Loki Massif. Also in the Loki Massif was a granodiorite, containing significant amounts of potassium feldspar and amphibole. The outcrop also contained a lot of sedimentary, basaltic, and granitic xenoliths. A similar looking rock was found in the Dzirula Massif, although it is unclear if they share the same affinity.

The Loki massif also contains schists, overlying the Red Granites. Although these meta-sediments are altered along cleavage planes, they do contain relatively fresh lenses of amphibolites (thought to represent metamorphosed basalts). It is not clear if the granites intruded (and metamorphosed) the schists, or if they have been juxtaposed tectonically.

The Khrami Massif includes a biotite-graphite gneiss, similar to the schists of the Main Range Zone. The freshest outcrop of migmatite was found in the Dzirula Massif. It was rich in potassium feldspar, including >1 cm porphyroblasts. In the absence of muscovite, this constrains the metamorphic temperature to >650°C.

To summarise the basement lithologies:

- **Diorite** - Early Palaeozoic, arc affinity, found in all Transcaucasian Massifs, and possibly the amphibole bearing granite in the Main Range Zone.

- **Red Granite** - Found in all Transcaucasian Massifs, rich in potassium feldspar, lacks amphibole, mica and garnet. Also observed in the Main Range Zone, although rarely as red, and more weathered. Possibly the same as the granitic rocks found in situ on the Russian border close to Mt. Kazbek. Hercynian in age.

- **Ushba Granite** - Limited to Mt. Ushba in the Main Range Zone. Unclear if similar granites form surrounding peaks.
- **Amphibolite** - Despite being found in all basement outcrops, it is the least common of the lithologies.
- **Biotite Schist** - Occurring in the Main Range Zone, and the three massifs, this lithology commonly suggests high temperatures were reached during metamorphism, and muscovite had broken down. Sometimes containing sillimanite, and typically containing graphite. Sometimes developed gneissose banding, rather than a schistosity.
- **Migmatite** - Migmatite is a common lithology across the Transcaucasian massifs. Samples were taken of the gneisses, amphibolites and eutectic melts that form the migmatites.

Chapter 4

Petrogenesis of the Lesser Caucasus Volcanics

4.1 Introduction

The most extensive recent magmatism in Georgia occurs in the Lesser Caucasus. The timing of volcanism ranges from syn-collisional (Goderzi Fm.), through the most voluminous pulse between 3 and 2 Ma (Akhalkalaki Fm.), and the most recent post-collisional Abul-Samsari and Borjomi volcanism, which is contemporaneous with volcanism in the Greater Caucasus (<1 Ma). A wide range of volcanic styles occurred over this time, ranging from plateau building flood-stlye lavas, valley filling flows, explosive cones, and monogenetic cones (Reviewed in more detail in Chapter 2). All this volcanism erupted through a ~40 km thick crust, underlain by a thin mantle lithosphere (Skobeltsyn et al., 2014).

This chapter investigates the most significant differences between the volcanism of different ages using a combination of petrography, mineral chemistry, major and trace elements and radiogenic Sr-Nd-Pb(-Hf) isotope data. The roles of fractional crystallisation and crustal contamination will be discussed, as an attempt is made to interpret the source composition and melt generation processes, and evaluate the changing roles of asthenosphere, lithosphere and crust in producing the temporal variation in the chemistry of these lavas. The significance of these interpretations are put into a tectonic framework for the region (combined with interpretations from the Greater Caucasus in Chapter 5.)

4.2 Petrography

Thin sections were made and analysed of representative samples from the various formations of the Lesser Caucasus. Modal abundances of phases were estimated by eye from thin sections and hand specimens. Textural information was gained from optical microscopy and back-scattered electron images. Mineral compositions were measured using an electron microprobe analyses (EMPA) at the Open University (Details of analytical method and uncertainties can be found in Appendix B.)

Throughout this project, trying to obtain the full range of mineral compositions was the main aim. Samples of the Lower Akhalkalaki Fm. tended to have rather heterogeneous mineral compositions, so have fewer analyses than the Abul-Samsari samples. The scoria samples tended to be quite altered, as did the Goderzi Fm., so they also have fewer analyses. In an ideal world, the number of analyses would be proportional to the frequency of a given mineral and composition, however due to time constraints and the focus of the investigation, this was not the case.

4.2.1 Goderzi Fm.

The most mafic sample of the Goderzi Fm. (14-025) was strongly altered in the field. However the mafic nature could be inferred from the highly vesicular nature and red colouration, suggesting high ferrous iron content. Mineralogically these rocks are porphyritic, with phenocrysts of plagioclase, cpx and amphibole.

Phenocrysts of plagioclase are usually concentrically zoned (Fig. 4.1). Reverse zoning, with sodic cores ($An_{25–32}$) and more calcic rims ($An_{47–52}$), is common, although at least three compositional zones can be seen in some grains (Fig. 4.1). The boundaries between zones often show large steps in composition. Individual zones show normal zoning. One grain analysed had a calcic core, then a sudden drop to a sodic zone, then back to calcic, whereas most other grains had a sodic core with calcic rim. It may be that most grains had an earlier calcic core, but were fully resorbed as the sodic zone grew. The calcic rims are normally zoned, preserving the crystallisation history of the magma that it erupted in. The calcic zones also have higher Fe contents, suggesting they grew after the influx of a more mafic magma, rather than just changing conditions within a single magma chamber (Ruprecht and Wörner, 2007).

Cpx phenocrysts have Mg# of 82 (Fig. 4.2), which is not in equilibrium with the bulk rock where a much lower Mg# would be expected. However it may be in equilibrium with one of the more mafic pulses of melt that also produced the calcic zones of the plagioclase. It is unclear texturally whether it grew as part of the Goderzi magma after

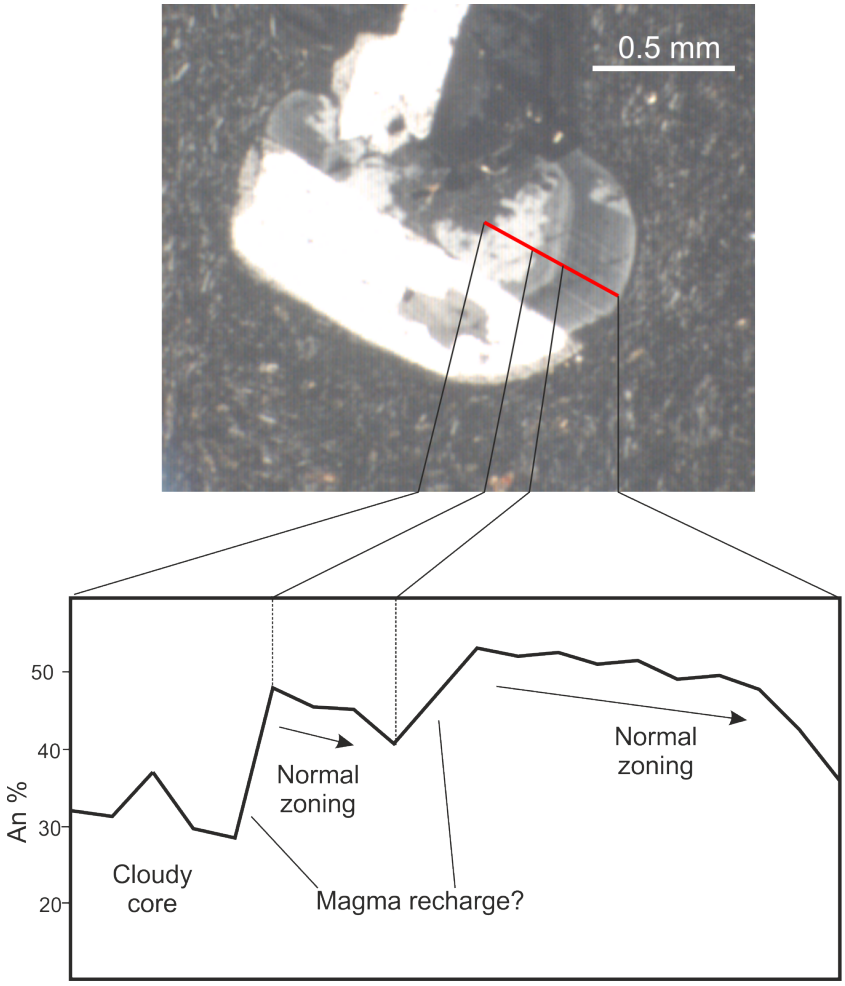

FIGURE 4.1: Microphotograph (xpl) of a zoned plagioclase grain, showing concentric zoning, Carlsbad twinning, and a cloudy core. Below is a chemical profile across the plagioclase grain with variation in anorthite content measured by EMPA.

enrichment from a mafic melt, or if it is xenocrystic and was part of the mineral cargo of one of these melts. Also present are typically fresh, tschermakitic or magnesio-hastinsitic hornblendes.

4.2.2 Lower Akhalkalaki Fm.

Samples from the Lower Akhalkalaki Fm. are typically quite coarse and holocrystalline (Fig. 4.3a, b and c). Mineralogically they contain plagioclase, cpx, opx, olivine and an oxide phase (in order of decreasing abundance). Plagioclase composes up to 60 % of these samples, and is rarely compositionally zoned (Fig. 4.3b). Where zoning is

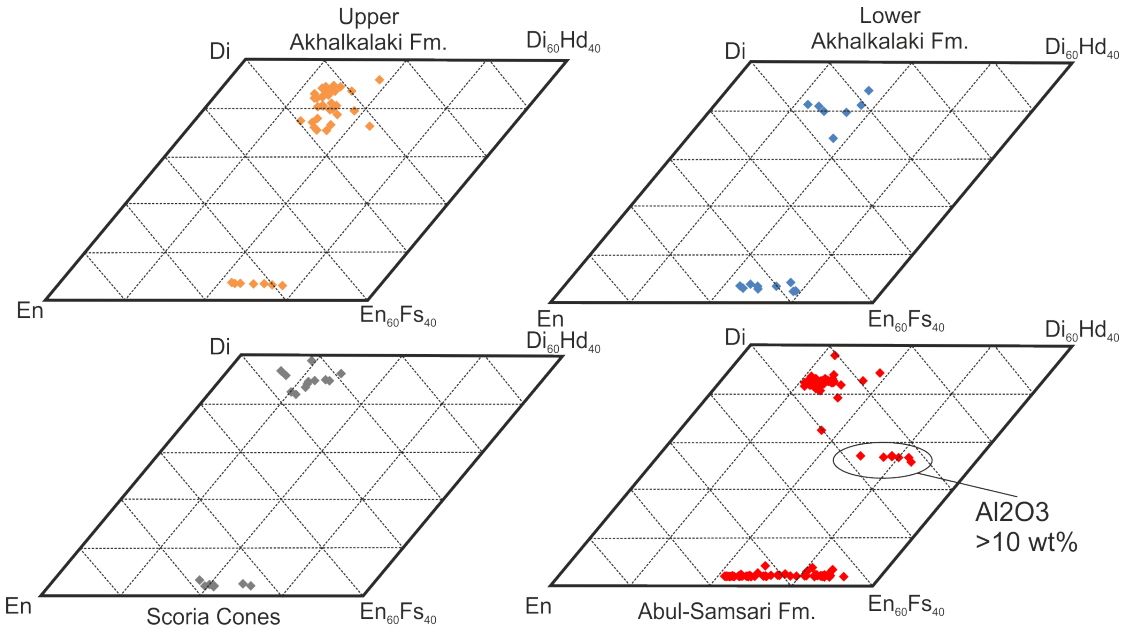

FIGURE 4.2: Stacked pyroxene quadrilaterals, showing compositions for each age/formation. The colours used in this figure are used for these formations throughout the chapter. The number of samples is not an accurate representation of the number of pyroxenes in a given formation, as during analysis the focus was getting the full range of compositions.

present, rounding of interior zones is only seen in a few examples, suggesting the zoning formed in equilibrium with the melt changing composition. Most grains are andesines and labradorites ($An_{44–64}$), although a single (possibly xenocrystic) anorthite ($An_{96.6}$) and two (very likely xenocrystic) oligoclase ($An_{15–29}$) grains were also present (Fig. 4.4). Samples from the Khrami flow show the full range of compositions, while the Paravani sample shows a more restricted range ($An_{54–58}$). Samples taken from the Khrami flows show a very well developed ophitic texture (Fig. 4.3a). Clinopyroxene (Mg# = 65–79) is more abundant than orthopyroxene (Mg# = 70–78) (Fig. 4.2), although both only occur as oikocrysts rather than phenocrysts. They are in equilibrium with the bulk-rock, and show also showing evidence of fractionation (Fig. 4.5). In some sections the pyroxene have undergone major recrystallisation (Fig. 4.3c). The ophitic texture has developed around earlier sub-hedral olivine phenocrysts which exhibit significant alteration to iddingsite along grain boundaries and cracks (Fig. 4.3c). Compositionally they range from $Fo_{63.5}$ to $Fo_{82.5}$ (Fig. 4.6), although individual grains are not zoned. Despite NS-PhD-1 and 14-034 both being collected from the Khrami flow, all olivines analysed in 14-034 are in equilibrium with the bulk rock (See Rhodes diagram in Fig. 4.6), whereas olivines in NS-PhD-1 show significant differentiation to lower Fo%. In some cases slight rounding of

olivine has occurred, whilst others are embayed, reflecting the disequilibrium of some of the olivines. Deformation textures, such as undulose extinction are not present, reflecting the post-collisional nature of the lavas, and their position on the southern flank of the Lesser Caucasus fold and thrust belt. The olivines contain oxide inclusions, likely to be early forming chrome-spinels. A later generation of oxides can make up to 10 % (by volume) of the rocks. They are found as euhedral grains. Under reflected light only a single oxide phase is identifiable, which analyses show to be Fe-Ti oxides. Samples from the Paravani section are similar to the Khrami flows, showing a holocrystalline to sub-ophitic texture but rarely contain olivine.

Unlike other samples from the Lesser Caucasus, rocks from the Paravani section contain significant amounts of carbonate minerals (Fig.4.3d and e). Carbonates have not been described in any other post-collisional formations in the Arabian-Eurasian collision zone. Two generations are present. One is typically calcitic, and is a low temperature alteration product. The other generation is represented by strongly zoned mesostasis material from the magnesite-siderite solid-solution (Figs. 4.3d and e, and Fig. 4.7a). The cores often preserve a euhedral morphology, as the outer zones fill the interstices. Based on a three end-member (Mg^{2+}, Fe^{2+} and Ca^{2+}) system, compositionally most examples of this follow the same pattern. The core is typically high-Mg (~70 % Mg^{2+}, 25–29 % Fe^{2+}, <4 % Ca^{2+}), showing slightly increasing Fe^{2+} with corresponding decrease in Mg^{2+} (Fig. 4.7b). This variation is expected during cooling and differentiation (Davidson, 1994). A second zone, similar to the core, but with a patchy texture, is commonly found, with lower Mg^{2+} (55–65 %) and higher Fe^{2+} (29–36 %), suggesting a further reduction in temperature. Between these two zones is a transitional area that has a peak in Ca^{2+} (up to 15%), with corresponding spike in Fe^{2+}, and drop in Mg^{2+}. This spike can be repeated once or twice, sometimes without the Ca^{2+} peak. Overall this transition is superimposed on the increasing Fe^{2+} trend. The final outer zone, often present, continues the gradually increasing Fe^{2+} (~37%), but is characterised by a sudden drop in Mg^{2+} (<35 %), and increase in Ca^{2+} (<27 %). This could be the result of a drop in pressure and/or temperature.

The CO_2 is likely derived from a subducting slab, that also provided the water interpreted from trace element data. The reaction Olivine + CO_2 = Enstatite + Carbonate (Poli and Schmidt, 2002) may also be responsible for producing the low-Ca carbonates observed in these rocks. There is little evidence in these samples showing olivine reacting in close proximity to the carbonates, although olivine and enstatite are both present in these rocks. Textural features confirming this reaction were not observed.

Magnesite is stable at P >1.8 GPa (Poli and Schmidt, 2002), whilst calcite is stable

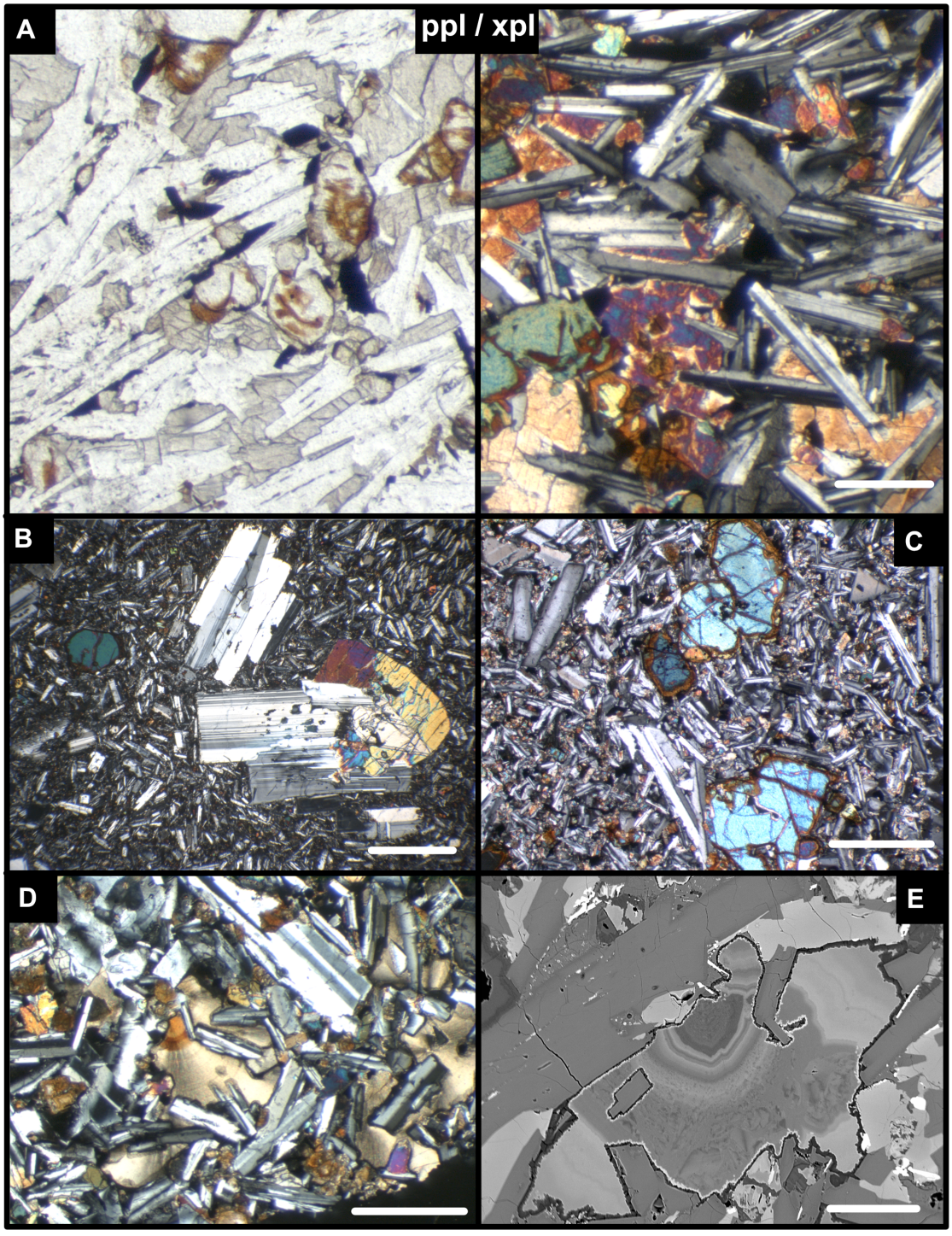

FIGURE 4.3: A) Coarse sub-ophitic texture, shown in ppl and xpl. Brown iddingsite shown on olivine phenocrysts. B) Holocrystaline texture in xpl. Two phases of plagioclase growth, groundmass microlites and large, euhedral, unzoned phenocrysts. Olivine and cpx phenocrysts also visable. C) Olivine phenocrysts, with iddingsitised rims in a plagioclase dominated groundmass with recrystallised cpx in xpl. D) Xpl image of plagioclase laths in zoned brown Mg-Fe carbonate oikocryst. E) Zoned carbonate in BSE, with concentrically zoned core, and patchier zoning towards the rim. White scale bar is 200μm.

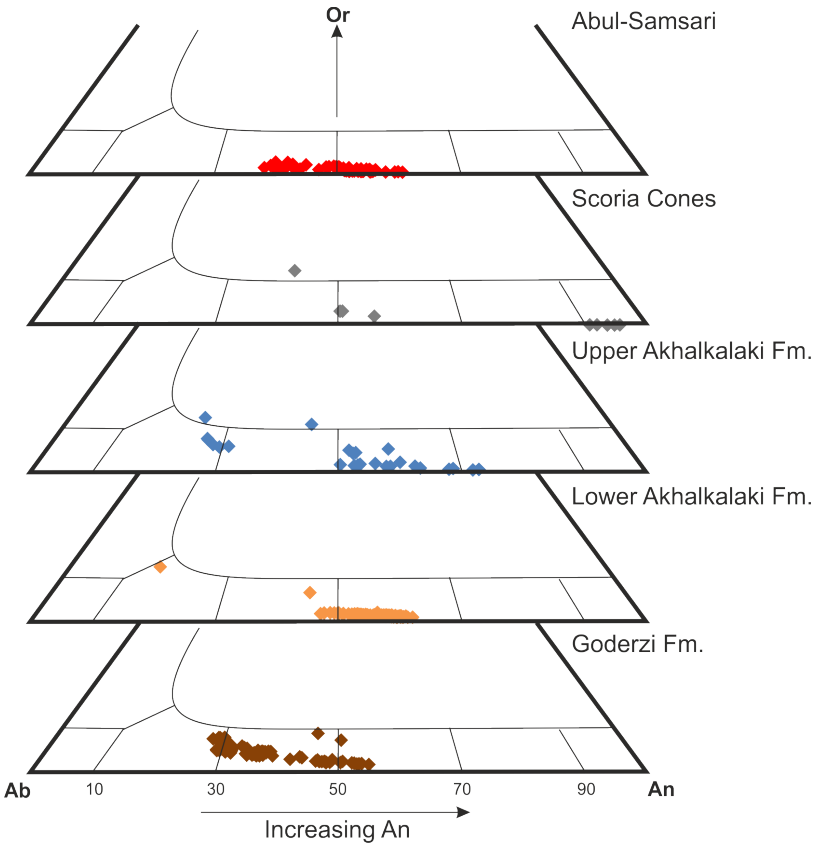

FIGURE 4.4: Ternary diagrams of plagioclase composition separated into age/formation. The number of samples is not an accurate representation of the number of plagioclase in a given formation, as during analysis the focus was getting the full range of compositions.

lower than 1.4 GPa (Poli and Schmidt, 2002). This would suggest that these rocks were fully crystallised at 55–42 km, which is just beneath the proposed depth of the Moho beneath the Lesser Caucasus (~40 km; Skobeltsyn et al., 2014)

4.2.3 Upper Akhalkalaki Fm.

The volcanics of the Upper Akhalkalaki Fm. are texturally distinct from those of the older part of the formation. The rocks of Stage III typically exhibit a very fine grained groundmass dominated by plagioclase microlites, pyroxene and Fe-Ti oxide. They usually exhibit a well developed pilotaxitic to trachytic texture, with plagioclase having a typical grain size of 0.1–0.05 mm (Fig. 4.8a and b). They also have a much smaller proportion of phenocrysts (or coarse grained minerals) than the Lower Akhalkalaki Fm., typically just 10–15 %. Phase IV looks very similar, however up to 30 % of the rock is composed of

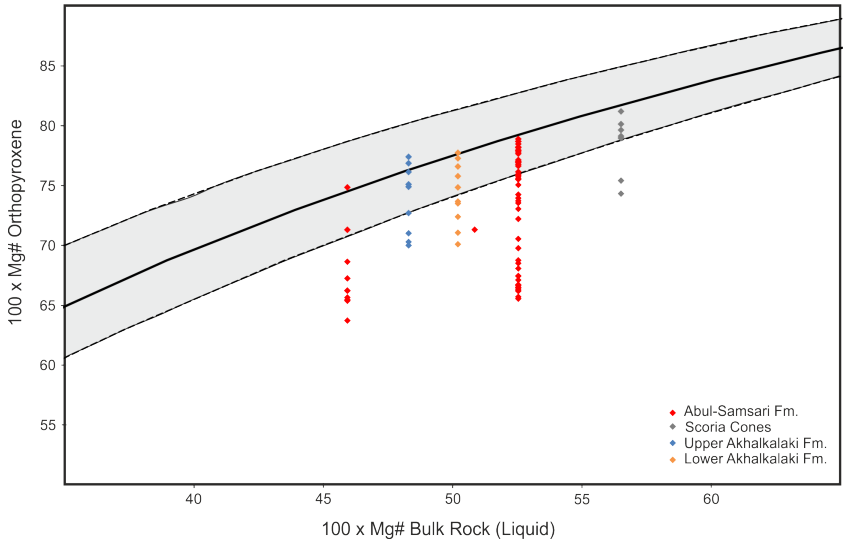

FIGURE 4.5: Rhodes diagram (Rhodes et al., 1979) comparing measured orthopyroxene composition with those predicted based on Mg# of bulk rock. Solid curve, with dashed error bounds, represents Fe-Mg exchange coefficient of 0.29±0.06 (Putirka, 2008). Analyses which plot in these bounds are considered in equilibrium with the bulk-rock.

vesicles (Fig. 4.8d). Phenocryst assemblages are dominated by plagioclase (70 %), with the remainder being olivine, opx and cpx. A wide range of olivine compositions were observed in sample 14-036a (Fig. 4.6, blue symbols), the most primitive sample from this formation, and the only sample containing significant olivine. Two populations were observed. The more primitive olivines ($Fo_{84–72}$) are the most common, and may represent grains from a primitive magma. This range extends to compositions more forsteritic than would be expected to be in equilibrium with the bulk rock ($Fo_{80–82}$; Fig. 4.6). This can be due to olivine removal, or open-system behaviour where the magnesian olivine crystallised from a more mafic melt, that has since mixed with a more evolved melt reducing the Mg# of the bulk rock, and where these grains would represent antecrysts. The lower values are from differentiation of the melt. The second group is more evolved ($Fo_{59–65}$) and cannot have crystallised from a melt of the bulk-rock composition and are likely to be part of the cargo of a second melt that has mixed with a more mafic one. Olivine shows significant amounts of low-temperature iddingsitisation (Fig. 4.8b).

Orthopyroxene (Mg# = 70–77; Fig. 4.5) and clinopyroxene (Mg# = 69–81) phenocrysts are typically relatively fresh. Although not as obvious as with the olivine, there may be a compositional gap between Mg# 73–75 (Fig. 4.2), with only the pyroxenes more primitive than this in equilibrium with the bulk-rock. Pyroxene phenocrysts are subhedral (Fig. 4.8f), however cpx found as part of mafic glomerocrysts (Fig. 4.8a), which are

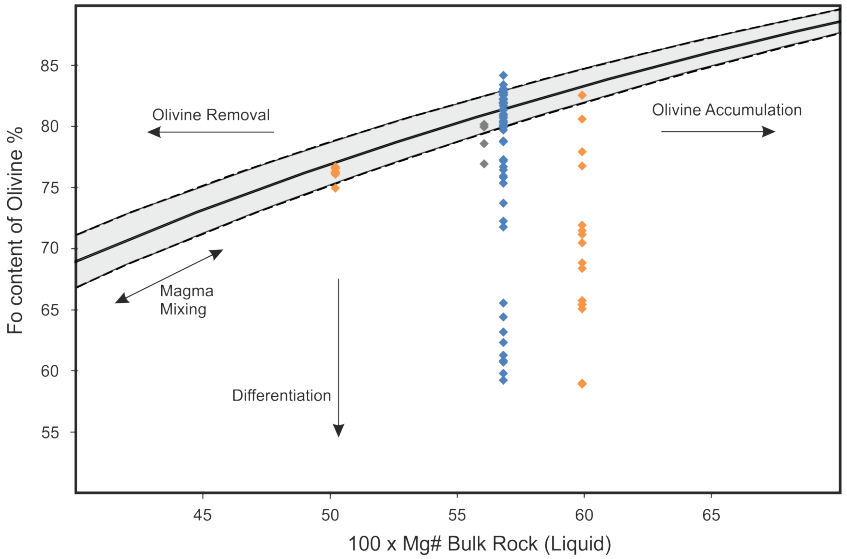

FIGURE 4.6: Rhodes diagram (Rhodes et al., 1979) comparing measured olivine composition with those predicted based on Mg# of bulk rock. Solid curve, with dashed error bounds, represents Fe-Mg exchange coefficient of 0.3±0.03 (Roeder and Emslie, 1970). Analyses which plot in these bounds are considered in equilibrium with the bulk-rock. Symbols used are same as Fig. 4.5.

relatively common in rocks of this age, and typically more rounded. Zoning is uncommon, but where present rounding of interior zones is present (Fig. 4.8f) Some examples of recrystallised cpx are also seen. Plagioclase phenocrysts are usually euhedral, without much compositional zoning (although oscilitory zoning is seen: Fig. 4.8c), reaction or alteration textures. However sieve texture is developed in many plagioclase grains (Fig. 4.8d) suggesting resorption has occurred due to either mixing with a magma it is not in equilibrium with, or through volatile loss during ascent. Two compositional groups exist, an oligoclase-andesine ($An_{50–72}$) and a bytownite ($An_{13–29}$) group (Fig. 4.4), which share a similar habit in the rock. One sample (13-083) contains potassium feldspar (Or_{38}) and quartz xenocrysts mantled by fine grained pyroxene (Figs. 4.8g and h), suggesting interaction with a more felsic medium (be it crust, or an evolved melt).

4.2.4 Scoria Cones

Unsurprisingly from the name and geological setting, rocks collected from the scoria cones were highly vesicular. The groundmass varies from glassy in the most vesicular samples, to finely trachytic in the samples with the fewest vesicles. Coarse grained mafic xenoliths were also observed from one of the cones (Fig. 4.9). The xenoliths were composed of

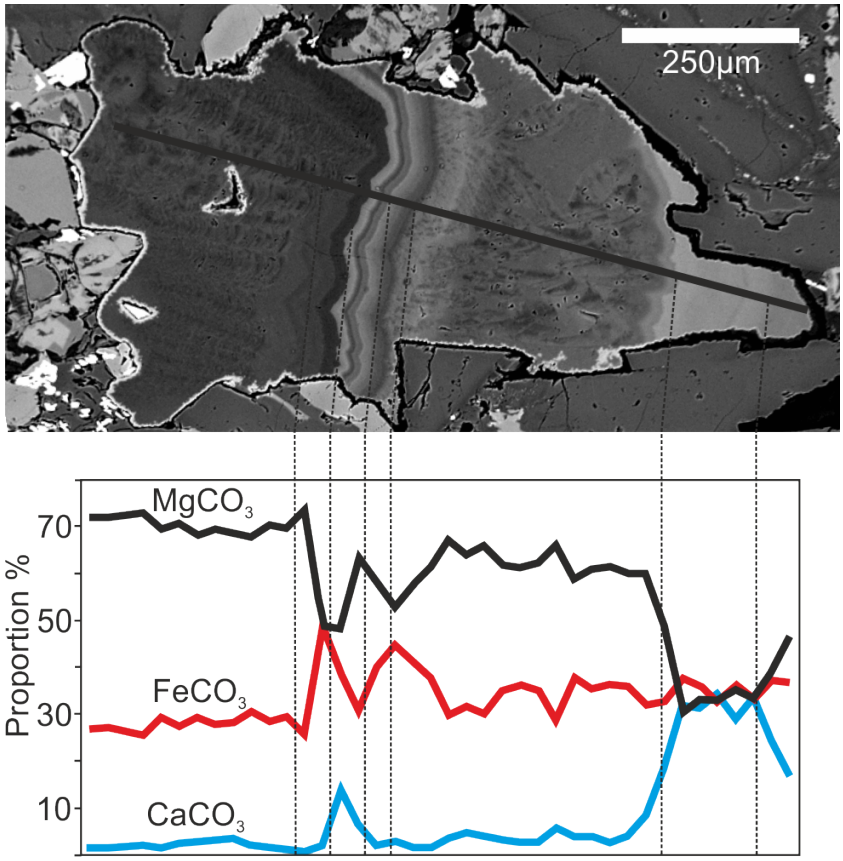

FIGURE 4.7: a) Back-scattered electron image of carbonate mesostasis, surrounded by light grey pyroxene (including enstatite) and ark grey plagioclase b) Chemical profile across a carbonate grain, showing variation of Mg^{2+}, Fe^{2+} and Ca^{2+}.

olivine ($Fo_{77–81}$; Fig 4.6), opx (Mg# = 74–81; Fig 4.5, grey symbols), cpx (Mg# = 73–88; Fig. 4.2), and one example of a high-Al pyroxene, with 9.5 wt % Al_2O_3 (These pyroxenes are discussed further in Chapter 5). The xenoliths also contained two population of plagioclase, labradorite ($An_{50–55}$) and anorthite ($An_{91–96}$) (Fig. 4.4). Sodic amphiboles (potassium- alumino- ferro- richterites) were also present. Despite having a xenolithic habit, the majority of the mafic grains are in equilibrium with the bulk-rock, bringing up the possibility that these may be cumulates in a closed-system melt.

4.2.5 Abul-Samsari Fm.

The Abul-Samsari volcanics (red symbols) tend to have a glassy to very fine groundmass. Hyalopilitic texture is common (Fig. 4.10a), and one sample shows ~15 % vesicles. All samples are porphyritic, with between 10–40 % of the rock being composed of phenocrysts

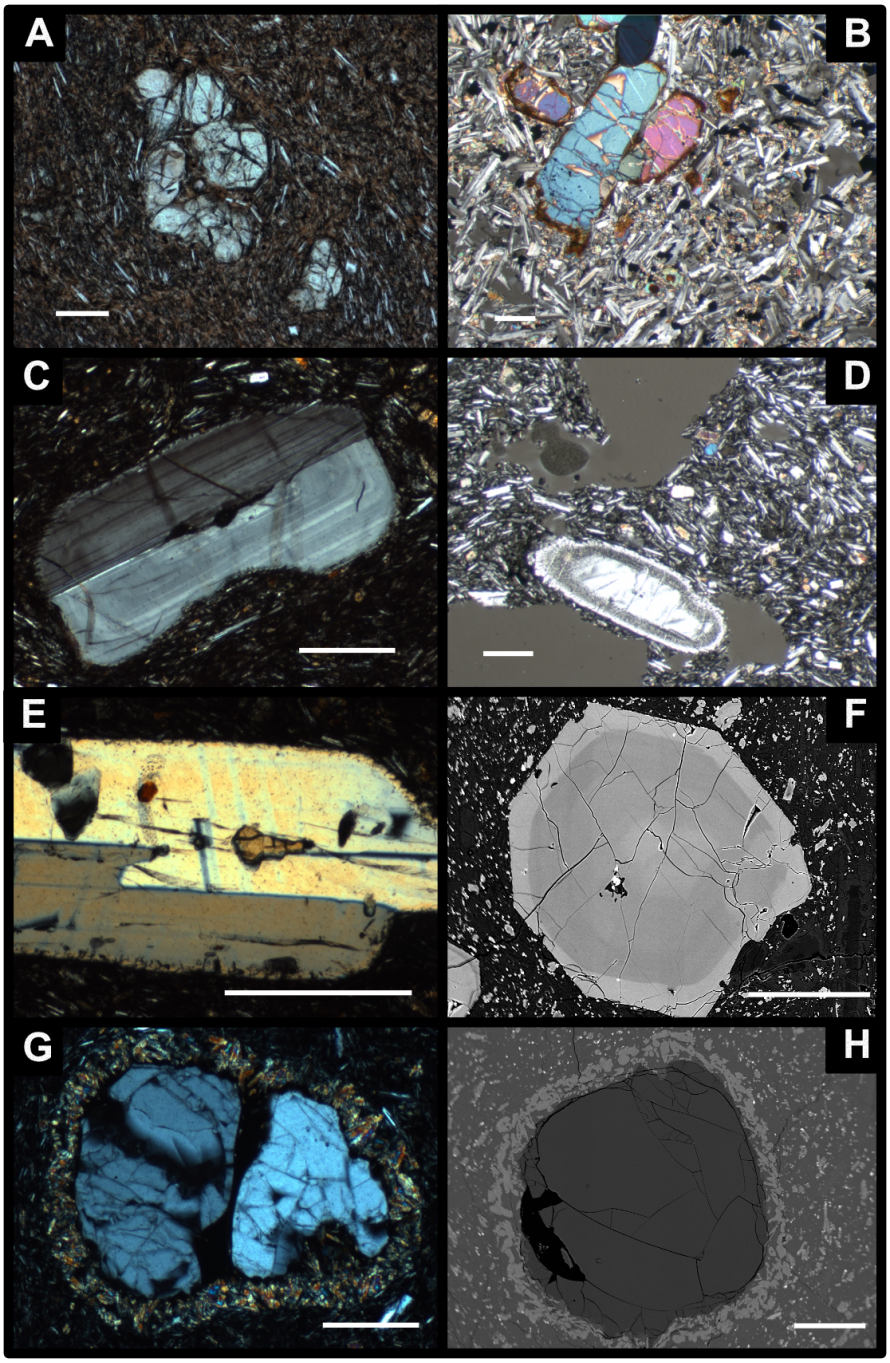

FIGURE 4.8: A) Cpx glomerocryst set in a plagioclase dominated trachytic groundmass in ppl. B) Olivine phenocryst with iddingsite rims, set in a coarse cpx, plagioclase, oxide, pilotaxitic groundmass in xpl. C) Oscillatory zoning in plagoclase. Rounding, and resorption seen on outside of grain. Image in xpl. D) ppl image of plagioclase grain with clear core and rim, but sieved zone between. Grain shows significant rounding. Large vesicles also present. E) Plagioclase in xpl with opx and spinel inclusion, and thin reaction rim. F) BSE image of a zone euhedral pyroxene. Inner zone shows significant rounding. G) xpl image of quartz xenocryst, with a cpx dominated reaction rim. H) BSE image of (dark) quartz grain, surrounded by fine grained (pale) cpx rim. White scale bar is 200 μm.

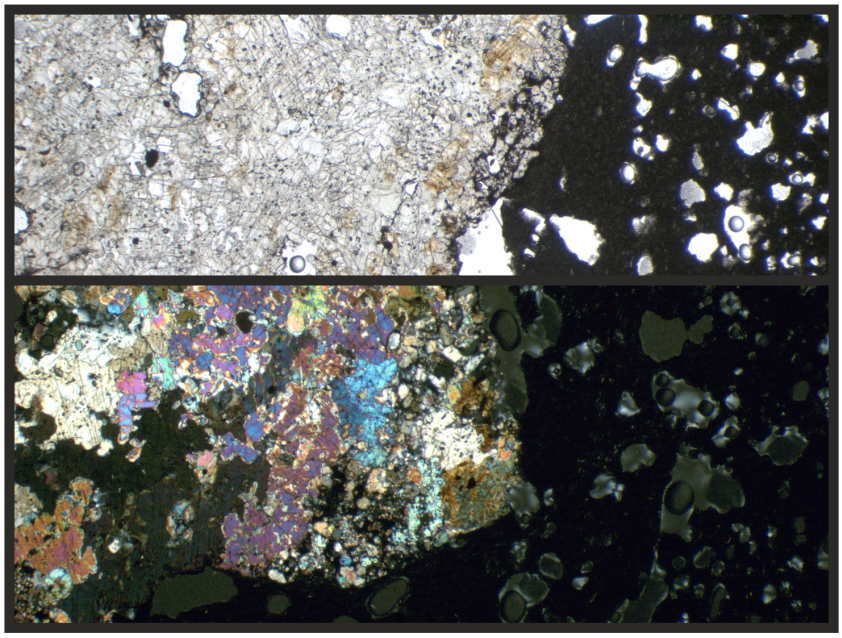

FIGURE 4.9: Mafic xenolith erupted in host glassy scoria lava. Top part of image in plane polarised light, bottom half with cross polars. Xenolith mostly composed of cpx (bright medium interfernce colours, and opx, pale first order interference colours. Total image width is 1 cm across.

(Fig. 4.10a). There is no olivine in these samples. The phenocryst assemblage is plagioclase, amphibole, opx and cpx. In the Lesser Caucasus, this is the only age group that contains hydrous phases. Phenocrysts in this youngest group of rocks also show the largest range of disequilibrium features. Plagioclase shows extensive sieve textures (Fig. 4.10a), in either just the core, just the rim, or the whole grain and often defining compositional zones. Concentric zoning is very common (Figs. 4.10b-e), with resorption features and rounded zones commonly seen, surrounded by more euhedral zones. Some plagioclase grains show inclusions of opx, oxides, and others have small fluid inclusions, that can define interfaces of zones (Fig. 4.10e). Plagioclase cores are labradoritic ($An_{50–60}$; Fig. 4.4), and grains of this, or parts of grains, of this composition often show reverse zoning to the more calcic values (Fig. 4.11). In the regions of reverse zoning, variations in An content are not reflected in variations with Fe content, suggesting mixing with other magmas is not driving compositional variability (Ruprecht and Wörner, 2007).

Temperature increase is the most likely cause (Humphreys et al., 2006). This change can be caused by advection in the magma chamber, magma chamber replenishment by a melt of similar anhydrous composition, but different volatile content (so called cryptic magma mixing; Humphreys et al., 2006), or the release of latent heat of crystallisation

where decompression is playing a key role in the crystallisation of a water-saturated melt during ascent (Blundy et al., 2006). Outer zones of larger grains are unzoned andesine (An3842), and often found with a thin, sharp, calcic rim, which does show an elevated Fe/Al (Fig. 4.11). This outermost rim, being so sharp is unlikely to represent mixing with a more mafic melt, and is probably a result of rapid degassing of H_2O driving the final stages of crystallisation (Humphreys et al., 2006).

Although the rocks are compositionally quite evolved (andesite-dacite), the cpx can be quite primitive (Mg# = 74–82; Fig. 4.2). Cpx are unzoned, or very slightly normally zoned. In some cases the composition has higher Mg# than would be in equilibrium with the bulk rock, suggesting a xenocrystic, or antecrystic nature in a mixed melt. Opx show reverse zoning, with cores of Mg# of 65–70, increasing to 78–79 towards to rim (Fig. 4.11b). Unlike in the older rocks, it is the rims that are in equilibrium with the bulk-rock, which is likely due to open-system behaviour. The total range of compositions in a whole thin section can be observed within a single zoned opx grain. Pyroxenes are rounded, and often deeply embayed (Fig. 4.10f and g). Amphiboles are usually euhedral, although usually have well developed reaction rims, or have been totally replaced by oxides (Fig. 4.10a). Alteration occurs along rims, cleavage planes, and cracks, typical of the breakdown caused by oxidation and decompression. All these features suggest these rocks have undergone a complex multi-stage history.

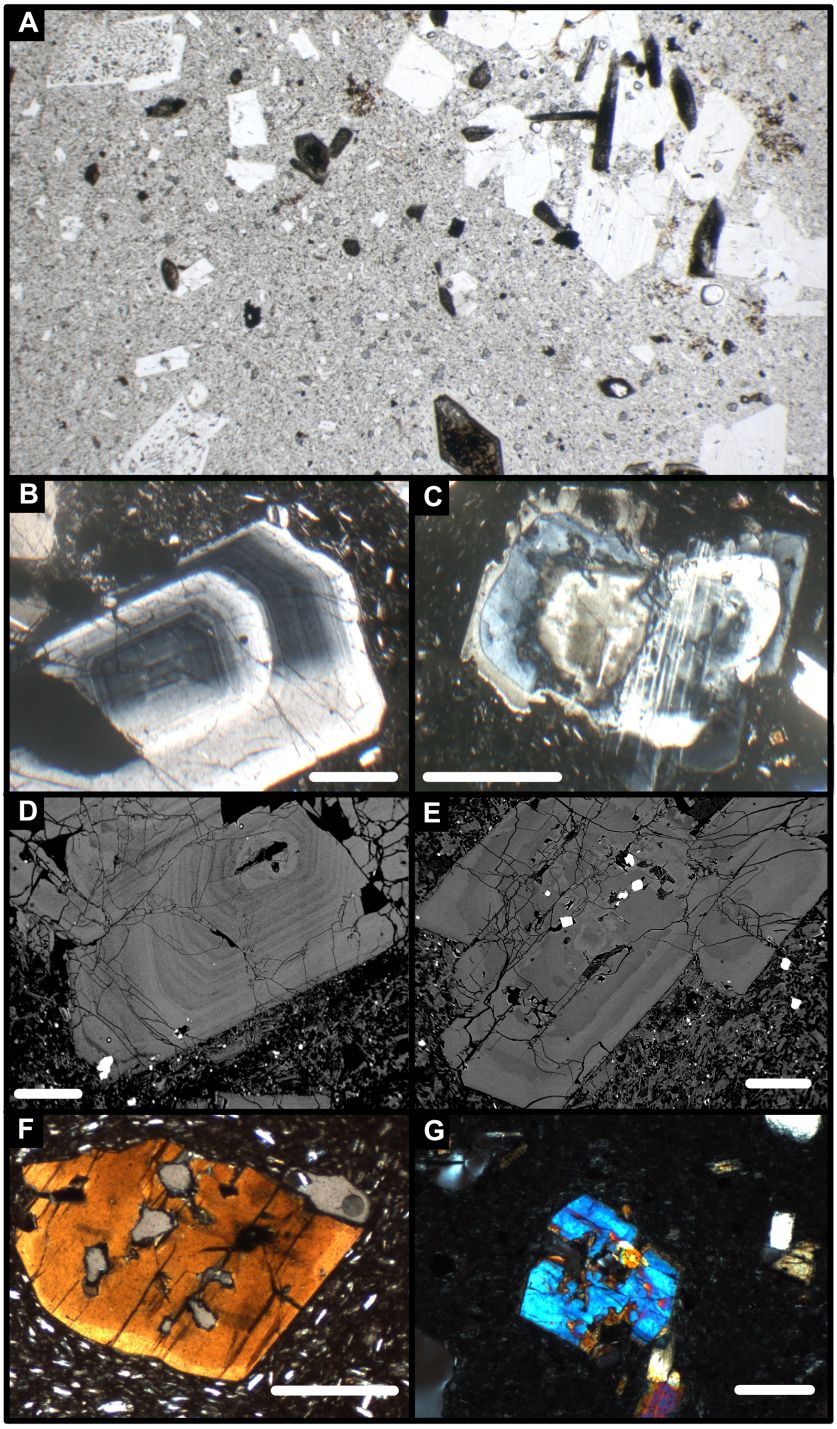

FIGURE 4.10: A) Plagioclase and amphibole phenocrysts in a hyalopilitic groundmass. Two types of plagioclase are seen, fresh grains in the top right, and sieve textured grains in the top left. All amphiboles show either euhedral or lath shape, and replacement by oxides. Frame width 15 mm B) Zoned plagioclase in xpl. Inner zones show well developed concentric zoning. The middle pale zone shows rounding. C) Plagioclase with significant resorption. Patchy zoning seen in the core, rounding seen in the outer zone. D) BSE image of plagioclase shown in B. Oscillatory zoning seen very clearly. E) Plagioclase in BSE. Oxides entrapped in the core. Zone boundaries are very irregular, showing significant resorption. F) Zoned cpx in xpl. Zone boundaries are wavey and rounded. G) Embayed cpx in xpl. White scale bars are 200 μm.

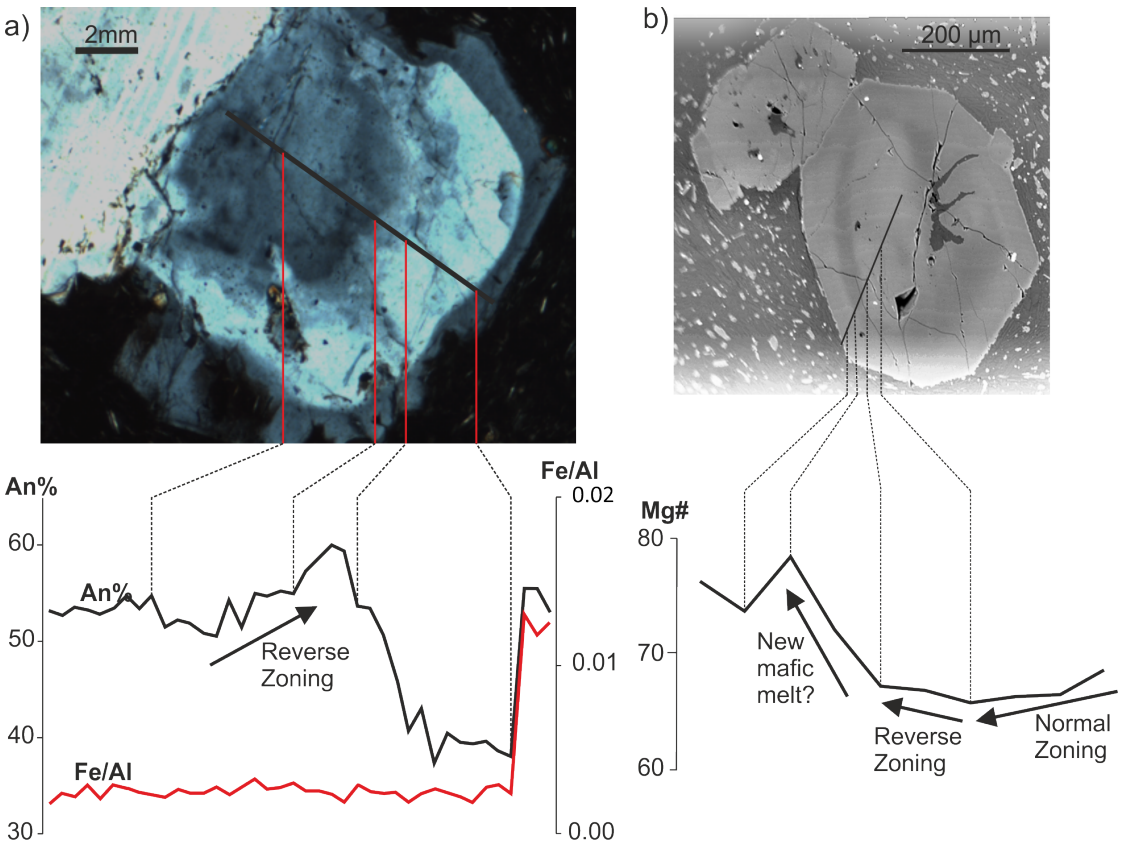

FIGURE 4.11: a) BSE image of plagioclase grain with core-rim traverse showing typical zoning pattern of plagioclase in this sample. Variations in An% are mostly uncoupled to variations in Fe/Al b) BSE image of orthopyroxene grain, with core-rim traverse showing reverse zoning

4.2.6 Mineral-Liquid Geothermobarometry

An attempt has been made to use mineral-liquid geothermobarometry for these magmas to understand the evolution through time of the region, or the different source regions of these magmas. Glassy magmas, melt- and fluid-inclusions were not present to analyse, so bulk-rock composition has been used as the liquid composition that the mineral is in equilibrium with. It is most likely that core compositions will be in equilibrium with the bulk rock (assuming a closed system), so these were the values used. As Mg/Fe decreases during fractional crystallisation, the actual melt composition (liquid) that many of these grains grew from will be less magnesian than the bulk-rock composition used in the calculations, therefore the temperatures from these thermometers will be maximum estimates. The Goderzi Fm. shows clear open-system behaviour (Fig. 4.1), therefore the bulk-rock is a hybrid of various melts, and cannot be used in this type of thermometry.

The Abul-Samsari rocks also show open-system behaviour, however a lot of the minerals are in equilibrium with the bulk-rock. Whether this is just a coincident or one end-member of the mixing melts is very dominant is not clear. Mineral-liquid thermometry may not give the most accurate answers, but should give a ball-park figure which could be of interest. The Lower Akhalkalaki Fm. shows very little open system behaviour. The Upper Akhalkalaki Fm. shows some mixing with felsic material. This mixing seems minimal (just a few xenocrysts, no significant zoning with large compositional jumps, limited disequilibrium textures) and if it is crustal assimilation rather than mixing, then the affect on bulk-rock major-elements should be negligible. Finally, volatile content of the melts (and minerals, although the minerals used are nominally anhydrous) are unknown. Therefore temperatures have been calculated on an anhydrous basis. For the Lower Akhalkalaki Fm. this is a reasonable assumption, however for the younger rocks, trace elements suggest water was present in the melt. The presence of fluids would decrease the temperature at which these minerals crystallise, again meaning these temperatures will be maximums.

Mineral analyses were tested to check if they were in equilibrium with the melt (bulk-rock) composition used. For the olivine, opx and cpx thermometers a comparison of observed and predicted Fe-Mg exchange values ($KD^{mineralliquid}_{(Fe-Mg)}$) was used. Calculated values were compared to suggested values (based on experimental data) from Putirka (2008). These are $K_D(\text{Fe-Mg})^{olivineliquid} = 0.30\pm 0.03$, $K_D(\text{Fe-Mg})^{opxliquid} = 0.29\pm 0.06$, and $K_D(\text{Fe-Mg})^{cpxliquid} = 0.27\pm 0.03$. The values for olivine and opx are independent of temperature variations, however are can be affected by SiO_2 content and pressure. The value for cpx varies slightly as a funtion of temperature. When this issue was considered and corrected for, e.g. correcting for the variation in $K_D(\text{Fe-Mg})^{cpxliquid}$ based on temperature, it had very little effect on the final results, well within the accuracy of the thermobarometers.

4.2.6.1 Geothermometry

The Lower Akhalkalaki Fm. produced relatively consistent temperatures, with opx-, cpx- and plagioclase-melt thermometers yielding temperatures of 1120–1190°C for two samples from the same flow (Fig. 4.12). The olivine-melt temperatures for NS-PhD-1 from this flow are around 1200°C. As olivine would be the earliest crystallising phase, it is expected to form at the hottest temperatures. The plagioclase thermometer of the carbonate rich sample of this age yielded higher temperatures than other rocks of this age and the cpx thermometer in the same rock. This may be due to the high volatile content.

When this is added into the calculations, the temperature would drop to values consistent with other rocks of this formation. For the other samples this should not be an issue as they are relatively anhydrous. These rocks are assumed to have crystallised at relatively shallow depths. Increasing the pressure up to 1 GPa only increases the temperature by ~30–50°C, which is similar to the error on the temperature measurements.

The Upper Akhalkalaki Fm. produced temperatures of ~1160°C for the more mafic lavas, and 1050–1100°C for the more evolved magmas (Fig. 4.12). These again showed consistency between different thermometers. These values are slightly harder to interpret because these melts are likely to be more hydrous and deeper than the Lower Akhalkalaki Fm. Increasing pressure to 2 GPa can increase the temperature by up to 100°C, whilst adding up to 5 wt% H_2O will decrease the temperature by ~50°C. Even so, these values give a ball park figure, and are certainly not asthenospheric type temperatures. The Abul-Samsari samples share similar issues with the Upper Akhalkalaki Fm. rocks. Opx-, cpx-, and plagioclase-melt thermometers are again in agreement, yielding 1050–1100°C.

As mineral-liquid thermometry was relatively limited in this suite of rocks, temperatures were also estimated using a simple liquid thermometer based on the equation of Helz and Thornber (1987), with a linear correction by Putirka (2008). This is based purely on MgO content, so mixed melts (assuming they have very different MgO contents) and contamination can affect this temperature as well. Assuming mixing is with a more felsic melt, these represent minimum temperatures for the original melt.

In general there is a trend of decreasing temperature over time (Fig. 4.13) for the post-collisional lavas. This suggests a cooling lithospheric system, without any obvious major pulses of hot asthenospheric melt entering the system. Prior to the Akhalkalaki Fm., the Goderzi Fm. formed in a cooler environment, which agrees with the high SiO_2 content and mineralogy.

4.2.6.2 Geobarometry

Pressure has been estimated using Al-exchanges in opx, cpx and amphibole (Putirka, 2008; Ridolfi and Renzulli, 2012). The Lower Akhalkalaki Fm. only contains a few pyroxenes in equilibrium with the melt, however pressures obtained from them can give a rough estimate of depth. Cpx-melt and cpx-only barometers (Putirka, 2008) both yield consistent pressures of 5–6 kbar. The carbonate bearing rocks of this age give a much shallower depth of 1.5–2.5 kbar, although this difference is based on a very small sample size (n=4 for carbonate-free and n=2 for carbonate bearing). However these depths yielded are highly distinct, and are likely to bear some significance. Opx-melt

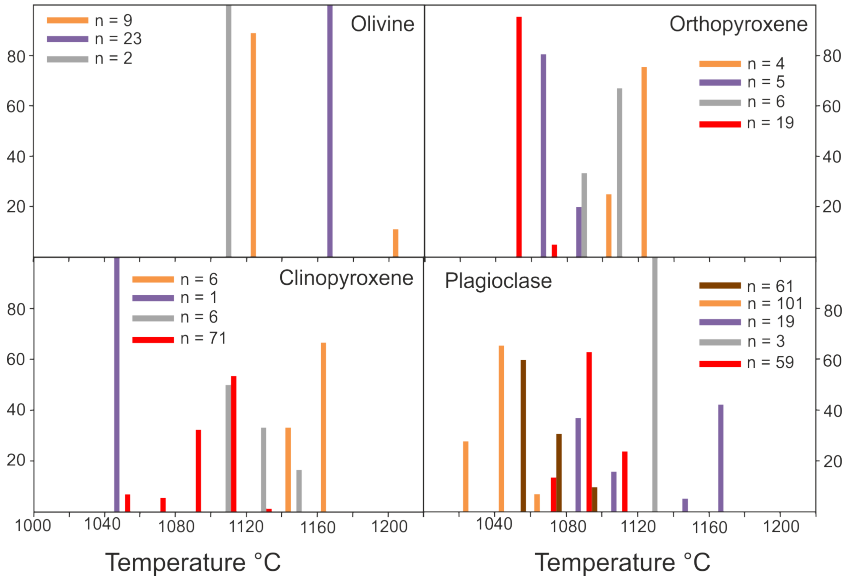

FIGURE 4.12: Histograms of results from mineral-melt geothermometry. Graphs show results for olivine-, cpx-, opx- and plag-liquid thermometers. Temperatures separated into 20°C intervals. Frequency, on the y-axes, shown as percentage of all analyses for each formation. Number of analyses is given for each formation, using each thermometer. For some formations, n is very small (1–3). The temperatures yielded from these small sample sizes have been included for completeness, although the confidence in them is lower than for the larger sample sizes. Small sample size generally is due to lack of that grain in equilibrium with the bulk-rock, or lack of that grain in the rock. In the case of the scoria rocks, all sample sizes are small due to few phenocrysts in the rock, but the results are broadly consistent between thermometers. The single cpx from the Upper Akhalkalaki Fm. yields a lower temperature than the other thermometers, so confidence in this sample is lower.

calculations are only possible for the carbonate-free rocks (there are no opx in equilibrium with the melt in the carbonate bearing samples), giving slightly shallower depths of 3.7–5 kbar. Pyroxene is a common phase in the Abul-Samsari suite of rocks, allowing the most reliable barometry to come from this group. The cpx-melt and cpx-only barometers give remarkable similar results of 5.2–10.0 kbar (mean pressures are 7.46 and 7.44 kbar respectively). Despite the large range, it is likely these rocks crystallised deeper than the older formations. Like the Lower Akhalkalaki Fm., opx-melt calculation give lower pressures, 2.4–6.0 kbar (4.0 kbar mean). Fresh amphibole was a common phase in the Goderzi Fm. An Al-in-amphibole barometer (Ridolfi and Renzulli, 2012) was applied to these grains, giving pressures of 2.4–5.8 kbar (Mean = 3.6 kbar). Pressures based on cpx-composition only yielded 3.9–4.3 kbar, which is consistent with the amphibole. All these depths are relatively shallow (<30 km). There is also quite a bit of variation with age, perhaps pointing towards a complex plumbing system beneath the region.

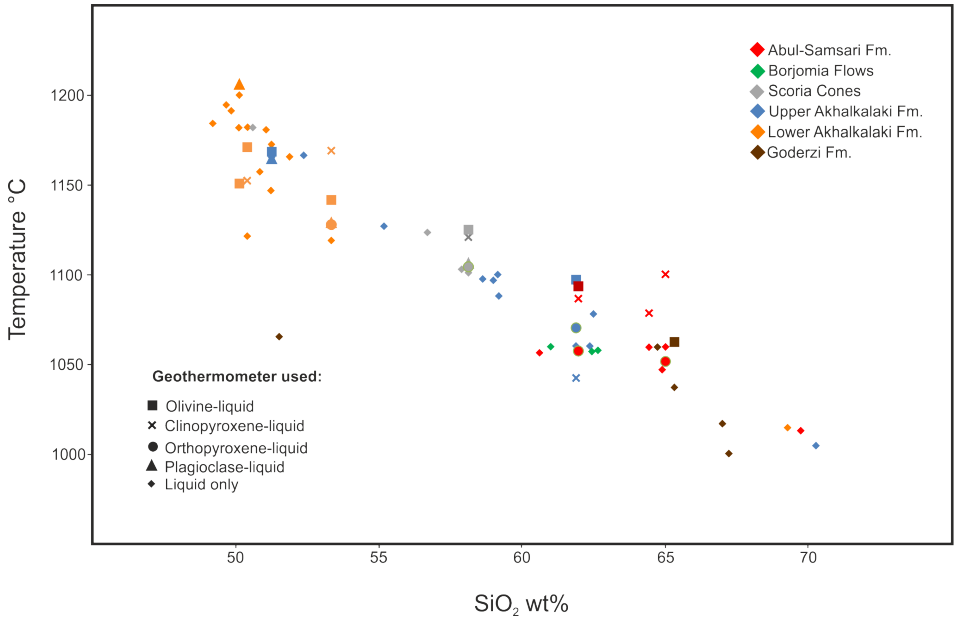

FIGURE 4.13: Plot of temperature with SiO_2. Where available mineral-liquid thermometers used. Also shown are the simple liquid thermometer results based on bulk rock MgO content only.

4.3 Bulk-Rock Geochemistry Results

Full details of the whole-rock major and trace element chemistry can be found in Appendix C.

4.3.1 Sample Freshness

Samples of volcanic rock were monitored for freshness using loss-on-ignition (LOI) values. Samples had LOI values between -0.47 and 1.55 wt.%, although most were below 0.5 wt.%. Two samples from the Paravani section had an LOI of 2.14 and 5.80 wt.%, which is due to the presence of carbonate in the rock. LOI broadly forms a positive trend with SiO_2 (Fig. 4.14), suggesting the higher values may be from the presence of hydrous phases such as amphibole, which typically crystallises in more evolved melts, and agrees with observed mineralogy. Trends consistent with magmatic processes are observed in plots of SiO_2 against elements that are easily mobilised during surface alteration (i.e. CaO, Na_2O, Ba: Figs 4.18 and 4.20), rather than the scattered patterns expected after alteration, whilst there is no correlation between these elements and oxides with LOI. In thin section mafic minerals and feldspars rarely show evidence of weathering and lack typical minerals, such as sericite and chlorite, related to alteration.

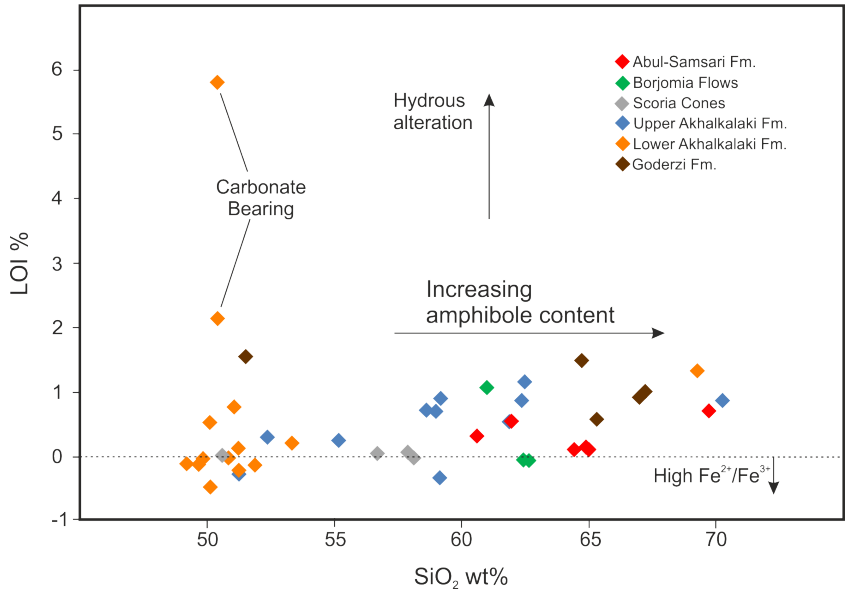

FIGURE 4.14: Variation of LOI with SiO_2 for Lesser Caucasus volcanics. Increasing trend likely represents fractionation of hydrous phases, such as amphibole, rather than alteration. Negative LOI caused by oxidation of Fe^{2+}. Two very high LOI points both contain carbonate. 2SE errors are within the symbol size.

4.3.2 Major-element Geochemistry

On major-element plots, samples from the Lesser Caucasus define a single array. On a total alkali versus silica plot compositions range from basalts to rhyolites (Fig. 4.15). The more mafic compositions fall on the sub-alkalialkali dividing line of Irvine and Barragar (1971), whereas compositions with SiO_2 >52 wt% plot well below the line on the sub-alkaline side. Lavas from other post-collisional settings often show an alkaline nature (e.g. Pearce et al., 1990; Allen et al., 2004). No samples are nepheline-normative (using the CIPW norm). Samples from the Lower Alkhalkalaki Fm. are all silica saturated (Fig. 4.16). The three most mafic samples of the Upper Akhalkalaki Fm. also contain normative olivine, whereas the rest are silica oversaturated. The young Abul-Samsari and Borjomi rocks are all silica-oversaturated with normative quartz. The older Gudauri Fm. is also quartz normative, but lack diopside, along with one sample from the Abul-Samsari ridge, although this is likely to be due to them being the most evolved. Unlike many other volcanics from continental-collision zones (Pearce et al., 1990; Turner et al., 1996; Williams et al., 2004), these rocks are not high-K or even potassic, and mostly plot as a calc-alkaline series on the plot of Ewart (1982), although the more evolved samples plot as high-K calc-alkaline (See Fig. 4.17).

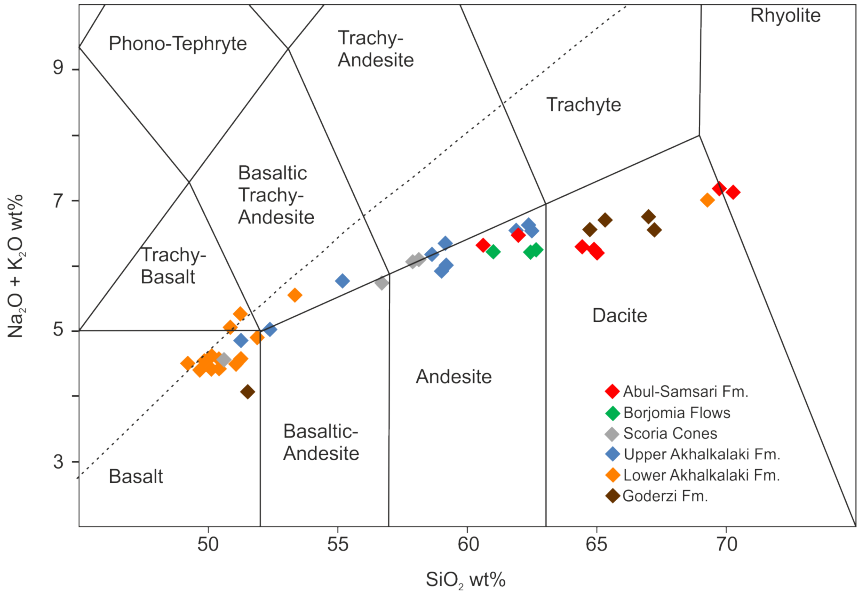

FIGURE 4.15: Total alkalis vs silica diagram for Lesser Caucasus volcanics, based on plot from Le Bas et al. (1986). 2SE errors are smaller than the symbol size. Line of silica saturation (dashed line) taken from Irvine and Barragar (1971).

Trends for major-elements against SiO_2 are well defined by the volcanics rocks of various ages (Fig. 4.18). Data from this project is very similar to published data covering the same area (Tutberidze, 2012). The rocks of the Gudauri Fm. tend to be of quite evolved compositions (SiO_2 = 64.74–67.23 wt.%), however one sample, collected just below the base of the Alkhalkalaki Fm. is basaltic, although does have a much lower Mg# (2.71%) than samples of a similar silica content. The Lower Alkhalkalaki Fm. are the most primitive of the lavas sampled in the Lesser Caucasus. They are typically basaltic with SiO_2 ranging from 49.21 to 53.35 wt.%, MgO contents of 9.81–4.75 wt%, and MgO# of 50–59. A more evolved sample, 13-086, is from a small, isolated volcanic dome, rather than the typical plateau forming flows of this age. It is likely to be from an event at the termination of Stage I or II (Lebedev et al., 2008a) however this is the only one sampled in this investigation. For the purposes of understanding the origin and evolution of volcanism in this area, this sample will not be used as it defines an isolated event rather than the main volcanic activity, however, interestingly it has a higher Mg# (41) for its low MgO (0.78 wt.%) than other similarly evolved samples. Stages III and IV are chemically similar, and shall be considered as the Upper Akhalkalaki Fm. henceforth. They are compositionally basalts to andesites (SiO_2 = 51.26–62.50 wt.%). FeOT (9.80–5.09 wt%) and MgO (2.51–6.51 wt%) decrease linearly, with no inflections,

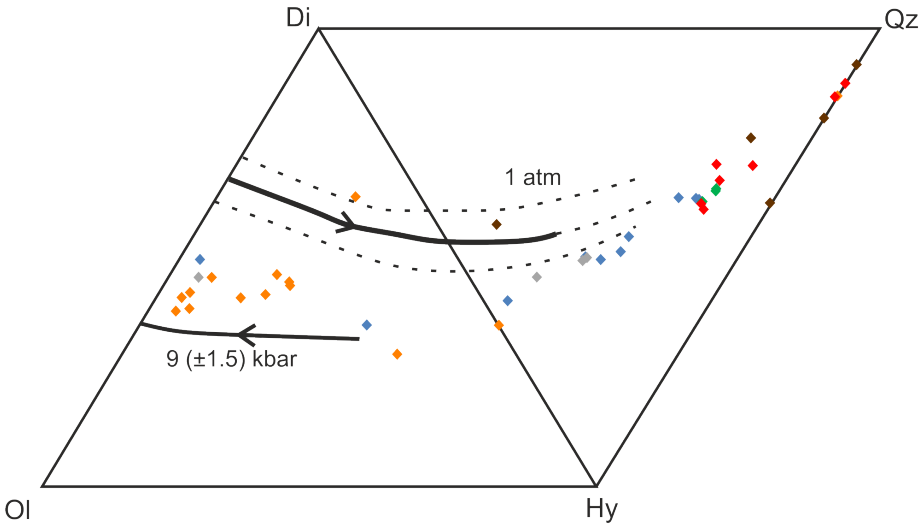

FIGURE 4.16: CIPW normative compositions for Lesser Caucasus volcanics, plotted using $Fe_2O_3/FeO = 0.15$. The 1 atm and 9 (± 1.5) kbar cotectics from Thompson et al. (2001) are shown, with arrows in direction of cooling temperatures. Symbols same as those in Fig. 4.14

with increasing SiO_2. However, they have a almost constant Mg# (54–59). The Lower Akhalkalaki Fm. extends to more SiO_2 rich compositions, whilst the Upper extends to lower SiO_2 to overlap when data from Tutberidze (2012) is included, although the general trend of the younger rocks being more evolved remains.

The youngest centres — Borjomi and Abul-Samsari — are geochemically similar. They are andesites and dacites (60.62–65.02 wt.% SiO_2), with FeOT (4.46–5.67 wt%) and MgO (2.37–2.50 wt%) concentrations that lie at the more evolved end of the trend defined by all Lesser Caucasus volcanics. Mg# (45–53) is slightly lower than the Alkhalkalaki Fm. Two Abul-Samsari samples are rhyo-dacites (69.74–70.27 wt% SiO_2), with corresponding low FeOT (2.55–2.60 wt%) and MgO (0.40–0.72 wt%), and low Mg# (24–35). Variations with TiO_2 (1.69–0.32 wt%) and MnO (0.16–0.02 wt%) are similar to FeO_T.

CaO shows a strong overall negative trend with SiO_2. The Goderzi Fm. has low CaO (4 wt% CaO). The Lower Akhalkalaki Fm. samples show significant variation (9.92–7.53 wt% CaO), without correlation with SiO_2. The Upper Akhalkalaki Fm. samples decrease with SiO_2 (9.38–5.00 wt%). The Abul-Samsari and Borjomi samples have a near constant 5.1–5.2 wt% CaO over a 5 wt% SiO_2 range, with the two most silicic Abul-Samsari samples also containing the lowest CaO of the Lesser Caucasus (~3 wt%). Al_2O_3 shows very little correlation with SiO_2, or discernible variation between rocks of different ages. The range of Al_2O_3 varies from 15.41–17.18 wt%, except for a single, more

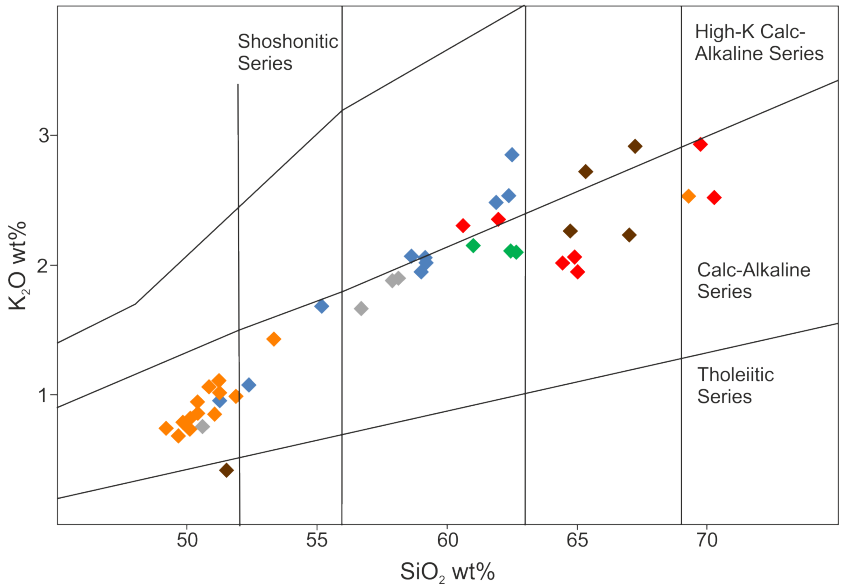

FIGURE 4.17: SiO_2 vs K_2O diagram for Lesser Caucasus volcanics, based on plot from Ewart (1982). 2SE errors are smaller than the symbol size. Symbols used are same as in Fig. 4.15.

aluminous, sample from the Goderzi Fm. with 18.59 wt% Al_2O_3. The Lower Akhalkalaki samples range from 3.56–4.12 wt% Na_2O with very little change in SiO_2. The Upper Akhalkalaki Fm. have consistently higher Na_2O (3.90–4.28 wt%), with a slight positive correlation with SiO_2. The young samples show a stronger trend with SiO_2, ranging from (4.01–4.60 wt%). The opposite is seen with K_2O, where the Lower and Upper Akhalkalaki Fm. show strong positive correlation with SiO_2 (0.68–2.54 wt% K_2O), whilst the younger Abul-Samsari and Borjomi rocks show a slight negative correlation (1.95–2.35 wt%). P_2O_5 is the only major element to show a significant inflection when plotted against SiO_2. The Lower Akhalkalaki show a positive trend (0.26–0.46 wt%), whereas all samples with >55 wt% SiO_2 define a negative trend (0.43–0.13 wt%). Stage III of the Akhalkalaki Fm. plot of both sides of the inflection.

4.3.3 Minor and Trace Elemental Composition

Minor elements (Mn, Sc, V, Ni) act compatibly (Fig. 4.19), showing negative correlations with SiO_2, mirroring FeO, MgO and CaO, and other elements compatible in early crystallising phases, such as olivine and pyroxenes.

Large ion lithophile element (LILE) concentrations are enriched relative to primitive mantle and show positive correlations with SiO_2 (Fig. 4.20). The Lower Akhalkalaki Fm. has Ba 27–42 times enriched to primitive mantle, whilst the Abul-Samsari has

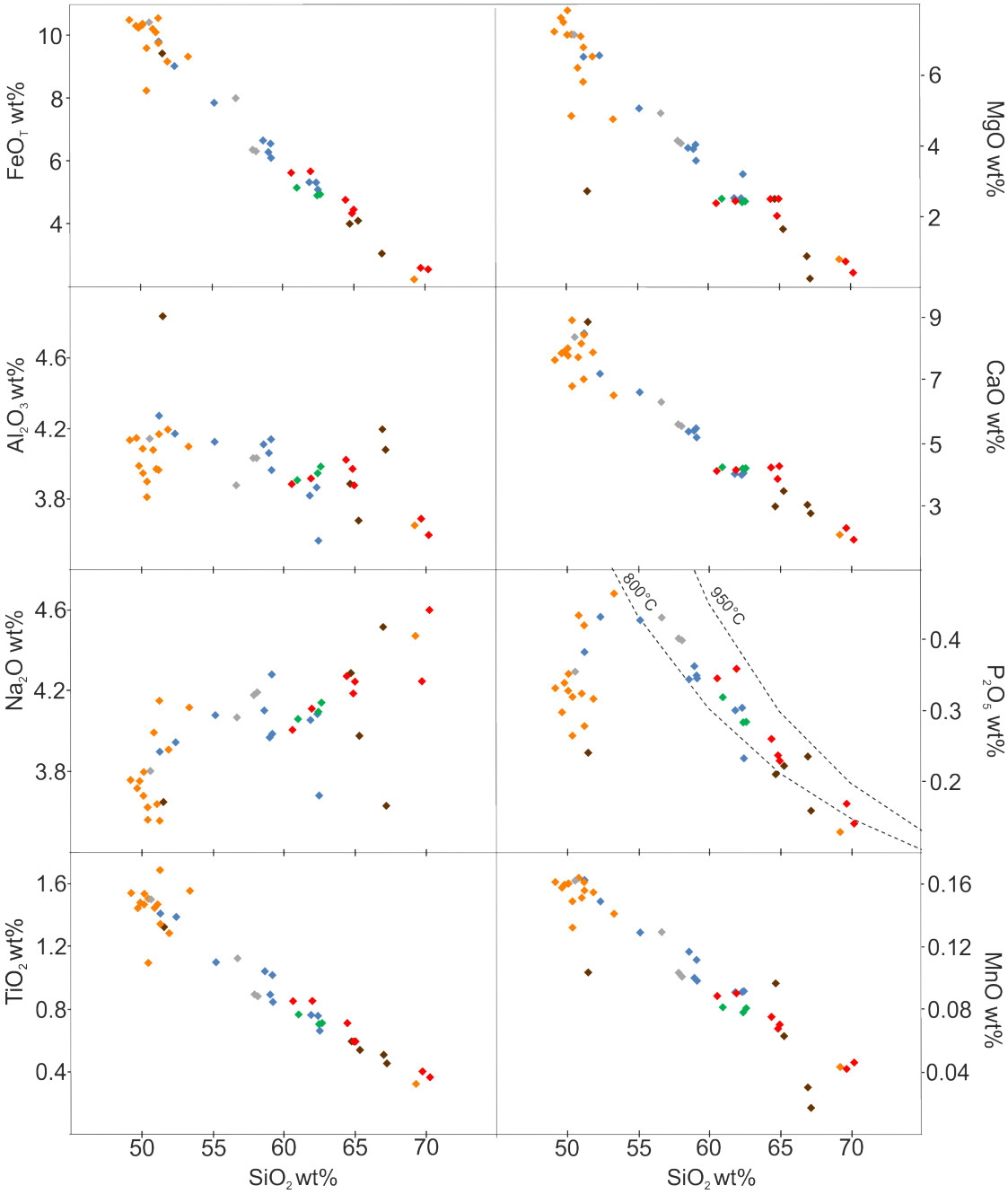

FIGURE 4.18: Major-element variation with SiO_2, as an index of evolution. Symbols used are the same as in Fig. 4.15. 2SE errors are smaller than the symbol size. Strong correlation seen between most elements, reflecting crystallising phases. Isotherms on P_2O_5 plot are from Green and Watson (1982). Errors are within the size of data points.

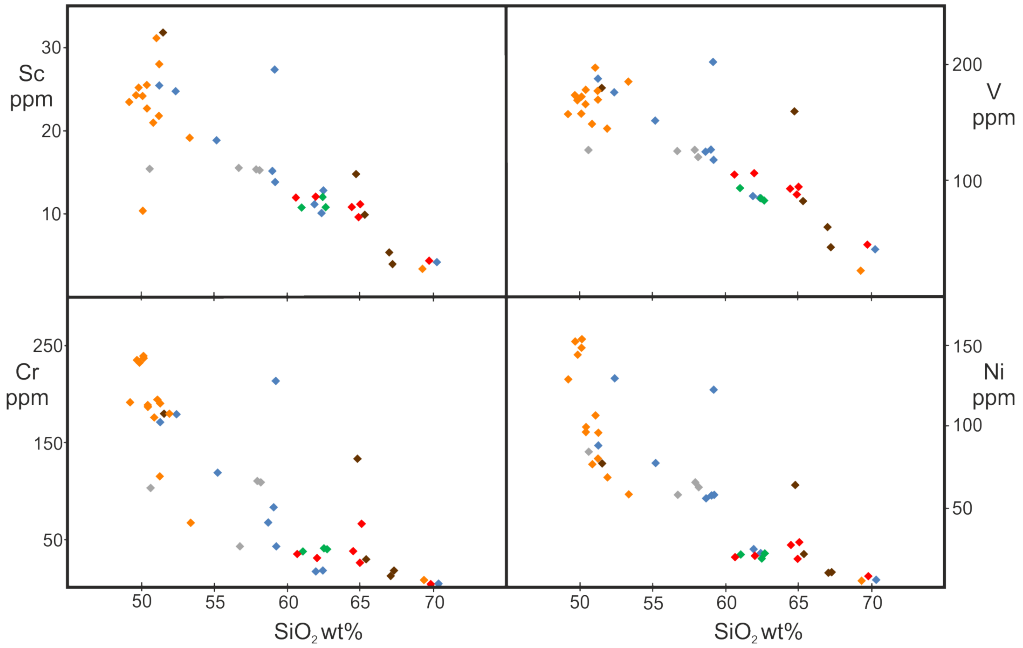

FIGURE 4.19: Minor-element (Sc, V, Ni, Cr) variation with SiO_2, as an index of evolution. 2SE errors are smaller than the symbol size. Symbols used are the same as in Fig.4.15.

Ba concentrations enriched 78–100 fold. In general there is significantly less variation within the Abul-Samsari and Borjomi volcanics compared to the older formations. On multi-element plots large Pb pikes are seen in all but the Lower Akhalkalaki Fm. (Fig. 4.21).

High field strength element (HFSE) concentrations are also enriched relative to primitive mantle, with the Lower Akhalkalaki Fm. showing the least enrichment and most variation, whilst the Abul-Samsari Fm. the greatest enrichment and smallest variation (Fig. 4.21). They generally form weakly positive correlations with SiO_2 (Fig. 4.20), expected for their incompatible behaviour. Large negative anomalies are seen at Nb and Ti on multi-element plots, although they are much smaller in the Lower Akhalkalaki Fm., which across the whole plot show a flatter pattern (Fig. 4.21).

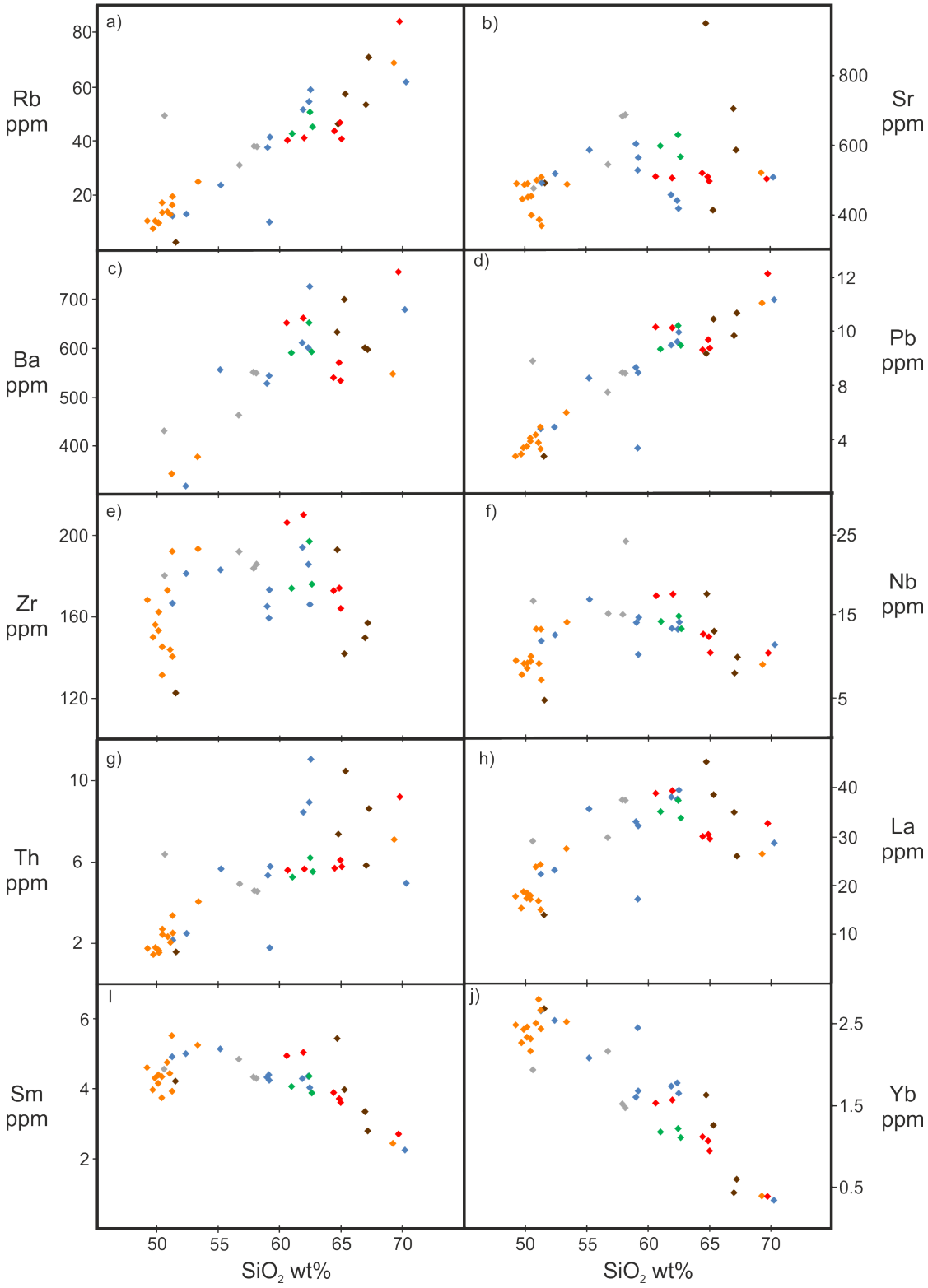

FIGURE 4.20: Trace-element variation with SiO_2, as an index of evolution. a–d) LILEs, e–g) HFSEs, h–j) REEs. Symbols used are the same as in Fig4.15.

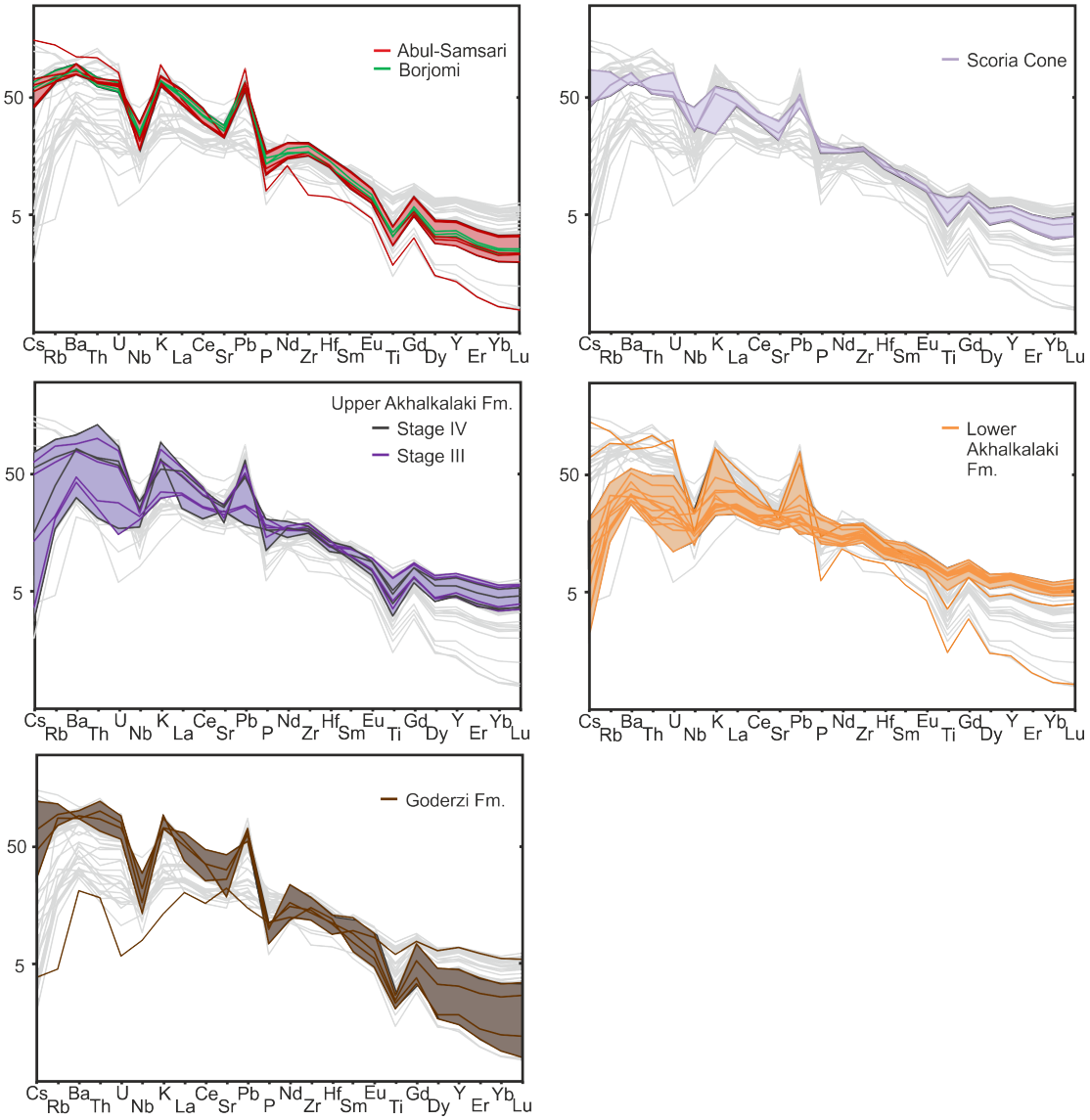

FIGURE 4.21: Multi-element variation diagram, normalised to primative mantle (Palme and O'Neill, 2014). Pale grey lines represent full range of compositions from the Lesser Caucasus (this study) as a comparison to the highlighted patterns for each centre. Upper Akhalkalaki and Abul-Samsari have been split into Stage II and IV, and Abul-Samsari and Borjomi respectively to show the similarity between the two, and why they have been grouped (along with age).

Variations across the REEs are shown in Fig. 4.22. The Lower Akhalkalaki Fm. have the lowest concentration of LREE, yet highest HREE, and therefore the flattest REE patterns ($(La/Yb)_N$ = 4.08–7.39). The most evolved samples of the Goderzi and Abul-Samsari volcanics have extreme $(La/Yb)_N$ (29–67), probably due to contamination of LREE. The Upper Akhalkalaki Fm. has slightly steeper patterns ($(La/Yb)_N$ = 3.53–14.36) due to being more enriched in LREE, as they have similar slopes in the HREE. The Abul-Samsari and Borjomi samples have the steepest slope ($(La/Yb)_N$) = 17.00–21.13), as well as having the steepest slope in the HREE ($(Dy/Yb)_N$ = 1.34–1.42, whereas Akhalkalaki samples are all below 1.32). The REE patterns of the Lower Akhalkalaki Fm. cross those of the other formations around Nd and Sm. Significant Eu-anomalies are not seen (Fig. 4.22), samples with SiO_2 between 53–65 wt% from all ages show Eu/Eu* <0.95, but nothing exceeds 0.89.

4.3.4 Isotopic Composition

19 samples were analysed for Sr-isotopic composition, 20 samples for Nd-isotopes, and 18 for DS Pb-isotopes. Details of the analytical techniques and quality of the data can be found in Appendix B, whilst Table 4.1 presents a summary of accuracy and precision of isotopic analyses based of similar standard rock samples. Values presented are not age-corrected as these samples are so young, any correction is within the error of the measurement. Older basement samples have also not been age corrected as they are being treated as contaminants of the younger lavas, therefore the current, rather than the initial isotopic ratio is of importance.

Isotopic Ration	Published Value	This Study	Reference
$^{87}Sr/^{86}Sr$	0.703996±20	0.704006±9	Weis et al. (2006)
$^{144}Nd/^{143}Nd$	0.512784±18	0.512758±15	Weis et al. (2006)
$^{206}Pb/^{204}Pb$	18.9420±20	18.9442±34	Baker et al. (2004)
$^{207}Pb/^{204}Pb$	15.6580±20	15.6597±28	Baker et al. (2004)
$^{208}Pb/^{204}Pb$	38.5690±60	38.5735±78	Baker et al. (2004)
$^{176}Hf/^{177}Hf$	0.282979±6	0.282983±10	Weis et al. (2007)

TABLE 4.1: Summary of accuracy and precision of isotopic analyses in this study. All values are shown for AGV-1 as the bulk rock composition is close to rocks from this study. Full details of analytical techniques is shown discussed in Appendix B.

Samples of the Lower Akhalkalaki show very little variation in $^{87}Sr/^{86}Sr$ (0.70392–0.70415) or *varepsilon*Nd (4.40–4.98: Fig. 4.23a). Abul-Samsari rocks define a similar cluster of little variation ($^{87}Sr/^{86}Sr$ = 0.70408–0.70428), *varepsilon*Nd = 2.38–3.39).

Together these form an array sub-parallel to the mantle array. The Upper Akhalkalaki samples plot at intermediate $^{144}Nd/^{143}Nd$, and cover a wider range of $^{87}Sr/^{86}Sr$ (0.70391–0.70461). Literature data for the Akhalkalaki Fm. (Lebedev et al., 2007a) agree with the divisions seen in our data. Due to the limited number of analyses it is unclear whether the Upper Akhalkalaki trends at a shallower angle, or is part of the larger trend of Lesser Caucasus volcanics. Data from Armenia (Neill et al., 2015) form a parallel trend, often overlapping the Georgian samples, but with slightly more radiogenic $^{87}Sr/^{86}Sr$.

Variation in the Hf-isotopic data is again very limited ($^{176}Hf/^{177}Hf = 0.28299$–$0.28305$, $\varepsilon Hf = 7.7$–9.7), forming a positive correlation with Nd-isotopes (Fig. 4.23b). Compositions are similar to those of a similar age in Armenia (Neill et al., 2015).

In Pb-isotope space, two different trends are clearly distinguishable (Fig. 4.23c and d). The Lower Akhalkalaki Fm. form an array from the Northern hemisphere reference line (NHRL) to more radiogenic values ($^{206}Pb/^{204}Pb = 18.81$–$18.99$, $^{207}Pb/^{204}Pb = 15.50$–$15.63$, $^{208}Pb/^{204}Pb = 38.61$–$38.99$). The Upper Akhalkalaki and younger volcanics for a second array at a much shallower angle to the NHRL, but elevated in $^{207}Pb/^{204}Pb$ and $^{208}Pb/^{204}Pb$. The Upper Akhalkalaki Fm. forms the more radiogenic part of the trend extending to the most radiogenic Lower Akhalkalaki values, while the Abul-Samsari rocks form the less radiogenic end ($^{206}Pb/^{204}Pb = 18.66$–$18.92$, $^{207}Pb/^{204}Pb = 15.61$–$15.63$, $^{208}Pb/^{204}Pb = 38.66$–$38.95$). Armenian rocks of similar age to the Upper Akhalkalaki Fm. share a similar Pb-isotope composition (Neill et al., 2015).

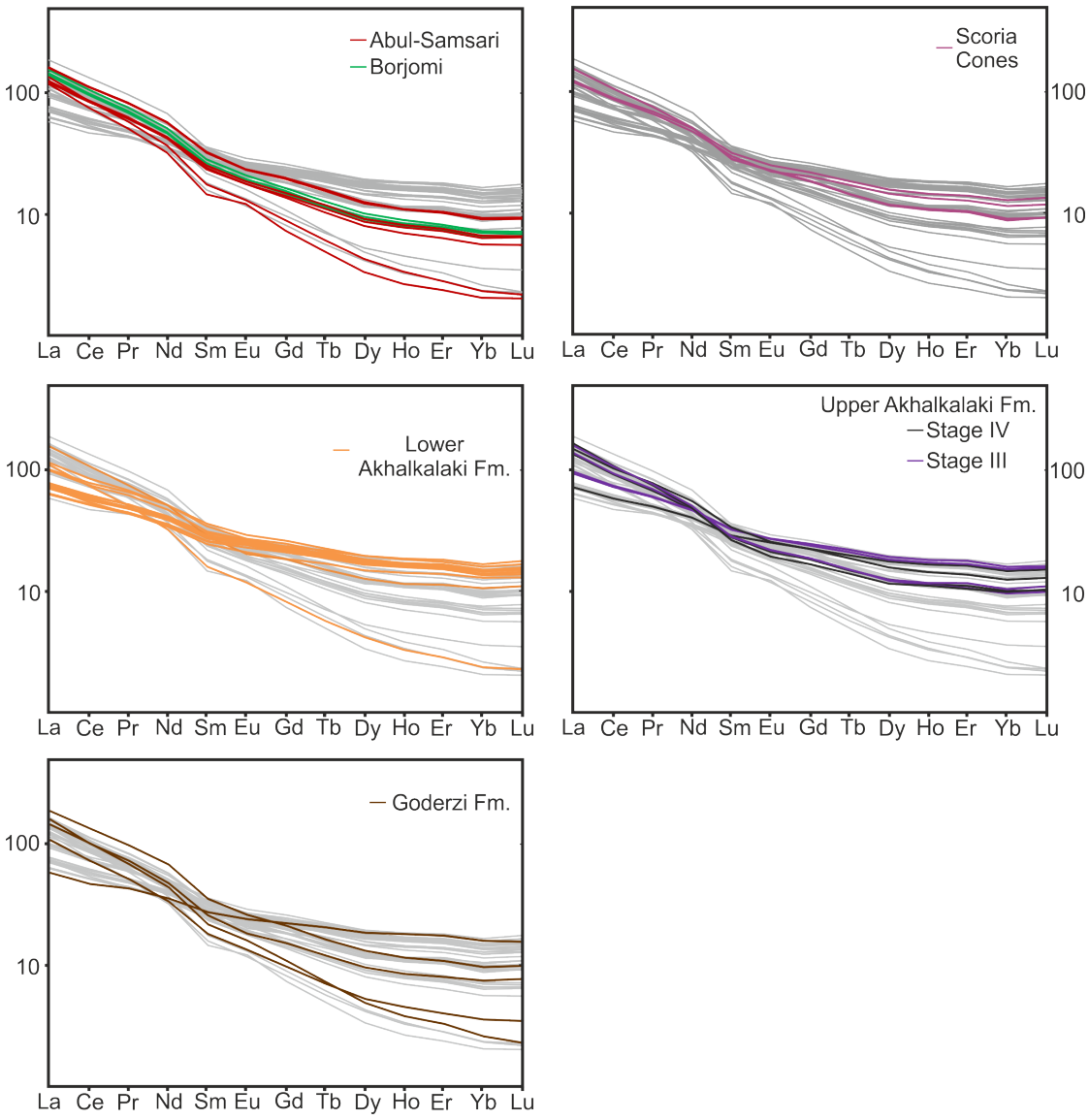

FIGURE 4.22: Rare earth element variation diagram, normalised to CI-chondrite (Palme and O'Neill, 2014). Pale grey lines represent full range of compositions from the Lesser Caucasus as a comparison to the highlighted patterns for each centre.

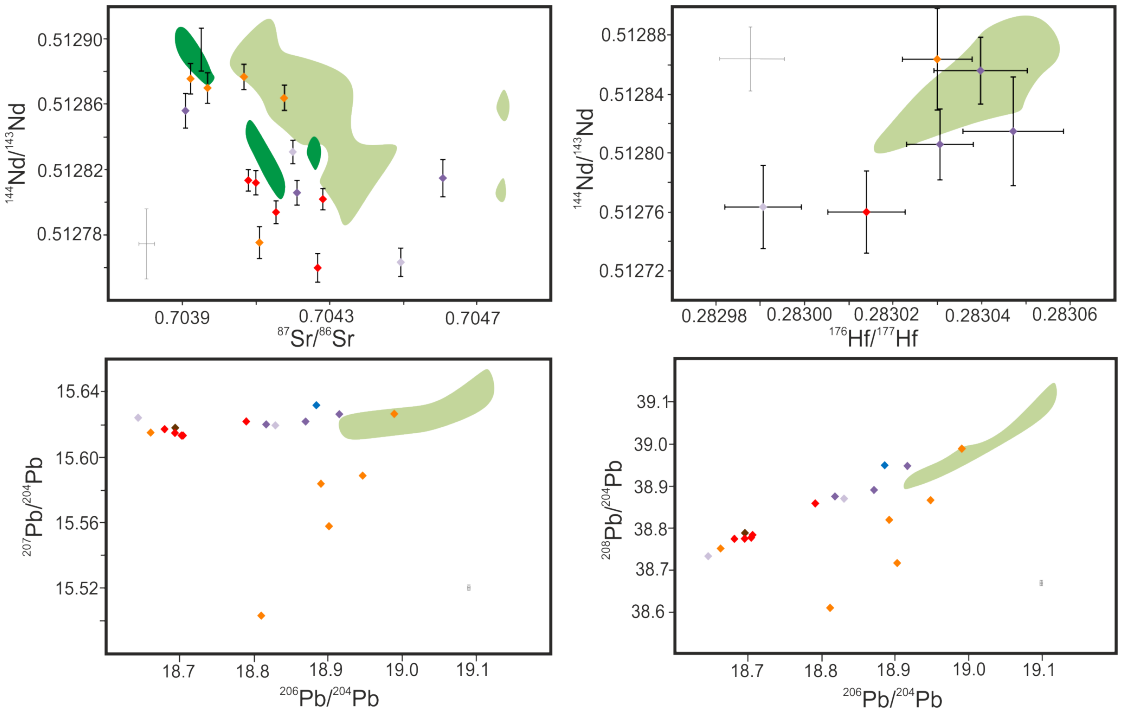

FIGURE 4.23: Isotopic variation in lavas from the Lesser Caucasus. a) $^{87}Sr/^{86}Sr$ vs $^{144}Nd/^{143}Nd$ plot. b) $^{144}Nd/^{143}Nd$ vs $^{176}Hf/^{177}Hf$ plot. c) $^{206}Pb/^{204}Pb$ vs $^{207}Pb/^{204}Pb$ and d) $^{206}Pb/^{204}Pb$ vs $^{208}Pb/^{204}$. Data from this study compared to literature data for the same area (Dark green Lebedev et al., 2007a) and Armenian Lesser Caucasus (Pale green: Neill et al., 2013, 2015) Error bars on data points show 2se. For Pb data error is same as, or smaller than symbol size. Pale grey error bars display 2sd standard reproducibility.

4.4 Discussion

The characteristics of the major and trace elements, and Sr-Nd-Pb-Hf isotope compositions of the full suite of volcanic rocks in the Lesser Caucasus can help constrain the source region, partial melting and crustal level processes during magmatic evolution, and variations over the time-scale of the volcanic activity in the area. This can be related to the geodynamic setting, and onto the linking the petrogensis of these rocks to the collision of Arabia with Eurasia. The large variations between rocks of different age, and the spread within these groups, reflect variation in source composition and conditions of magma residence, including depth and time-scale. This will in turn affect the fractionation history and the impact of assimilation of local crust. The following discussion will concentrate on the variation between groups of different ages to understand the evolution of the region, rather than variations within individual groups.

4.4.1 Fractional Crystallisation

A primary mantle melt (one in equilibrium with mantle olivine of Fo_{90}) is expected to have Mg# of ~73. All Lesser Caucasus samples have Mg# ¡60, suggesting that all these lavas have previously undergone extensive fractionation, or are derived from a previously depleted source. Major elements (particularly CaO, FeOT, MgO) show strong negative correlation with indices of fractionation (SiO_2 and Mg#: Fig. 4.18), that can be reconciled with the crystallisation of the observed phenocryst assemblage (olivine, cpx, opx, Fe-Ti oxide). Plagioclase fractionation does not seem to play an important role in controlling the chemistry, as no correlation is seen with Al_2O_3, Na_2O, or Sr (Fig. 4.18). Despite this suite of volcanoes representing a broad stratigraphic sequence covering the last 3 Ma, it is difficult to know whether these trends represent true liquid lines of descent due to the temporal gaps between eruptive episodes, and various volcanic styles making it less than certain that these are the product of a single evolving magma chamber. There are two compositional ranges conspicuous due to the lack of samples plotting there: 53–58 wt% SiO_2 and 65–69 % SiO_2.

These are often recognisable as calc-alkaline suites. On an AFM diagram the data forms a broad calc-alkaline trend too, however the Lower Akhalkalaki Fm. shows a rapid decrease of 3 wt% MgO in the space of less than 5 wt% SiO_2, which could be considered typical of a tholeiitic trend.

The Abul-Samsari volcanics show a peculiar trend of increasing MgO and Mg-number between 60–65 wt% SiO_2. This requires a low Mg phase (<2 wt% MgO) crystallising. Feldspar would be one possible phase. If plagioclase was crystallising, CaO, Al_2O_3 and

Na_2O should act compatibly, when in fact the concentration (especially Na_2O) show the opposite and increase.

The trends of FeO and TiO_2 with SiO_2 are linear, with no significant inflections that would be indicative of Fe-Ti oxides appearing on the solidus. However, the Abul-Samsari volcanics possibly show an inflection between 61–64 wt% SiO_2. This is quite an evolved composition for an Fe-Ti Oxide phase to appear, and likely represents ilmenite, rather than magnetite, which would be expected to appear earlier. The inflection is also seen in plots involving Sc and V (Fig. 4.19), which are both compatible in ilmenite.

Variations of Y relative to Rb have been used in the East Anatolian Plateau (Pearce et al., 1990) and Armenia (Neill et al., 2013) to distinguish anhydrous and hydrous fractionating assemblages. The decreasing trend of the Abul-Samsari magmas (Fig. 4.24) likely reflect the crystallisation of amphibole (along with more the more compatible nature of Y in more evolved cpx; Pearce et al., 1990). This trend is also seen in rocks from the Armenian Javakheti plateau (Neill et al., 2013) and East Anatolia (Pearce et al., 1990). This is consistent with the petrography as amphibole is only seen as a phenocryst phase in these youngest rocks. It appears an anhydrous assemblage can explain the Akhalkalaki Fm., however an increase in Y would be expected, whereas Y remains constant (23–28 ppm) over a wide range of Rb (7–25 ppm) for the Lower Akhalkalaki Fm. This could be a result of the increasing partition coefficient of Y in more evolved rocks (Pearce et al., 1990), or a minor role for amphibole or apatite. The role of amphibole can also be understood using the compatibility of MREE which should cause a decrease Dy/Dy* if amphibole was on the solidus (Davidson et al., 2013). The only systematic decrease in Dy/Dy* with increasing SiO_2 is seen in the Lower Akhalkalaki Fm. at SiO_2 ¡55 wt% (Fig. 4.25a), which is more likely due to cpx crystallising where MREE are also relatively compatible compared to LREE and HREE. However the younger volcanics do have a consistently lower Dy/Dy*, suggesting the source may have already been depleted by amphibole, cpx, or apatite crystallisation, or has experienced an enrichment in the LREEs that has not affected the HREEs (Fig. 4.25b). In watersaturated conditions, at depths of 25–85 km (a sensible depth range of crust and top of lithosphere beneath the Javakheti Plateau), amphibole is expected to be a liquidus phase, and dominate the crystallising assemblage, even in basaltic-andesite melts (Pearce et al., 1990). As the melt rises the fractionating assemblage would become dominated by cpx, opx and plagioclase, and any pre-existing amphibole would be resorbed. This can explain the geochemical characteristics that suggest amphibole crystallisation, but the lack of amphibole phenocrysts, and where the phenocrysts are present, the highly resorbed nature of them.

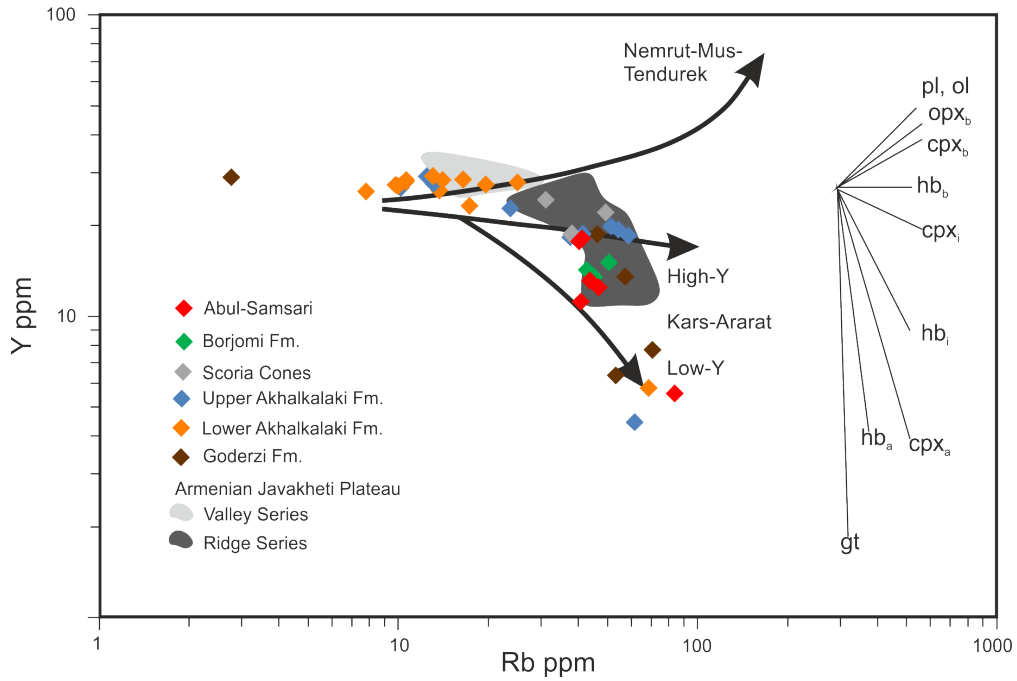

FIGURE 4.24: A plot of Rb against Y. Data in grey shaded fields from Neill et al. (2013) for the Armenian Lesser Caucasus. Three fractionation trends from East Anatolia from Pearce et al. (1990). 50% fractional crystallisation vectors from Pearce et al. (1990). Mineral abbreviations: ol = olivine, pl = plagioclase, hb = hornblende, gt = garnet. Subscripts represent generalised composition of mineral, b = basic, i = intermediate, a = acidic. Symbols used are same as Fig. 4.15.

Phosphorus acts incompatibly until ~53 wt% SiO_2, when concentration peaks at 0.46 wt% P_2O_5, before decreasing. The only significant host of phosphorus in this suite of rocks is apatite. In these rocks phosphorus becomes saturated at a low concentration, and apatite appears on the solidus relatively early (55 wt% SiO_2). Experimental work (Watson, 1980; Green and Watson, 1982) has shown that P_2O_5 becomes saturated at lower concentrations in cooler melts, higher pressures, and in the presence of volatiles. Figure 4.18 shows that data from the Lesser Caucasus plots parallel to the 800^{circ}C, 7.5 kbar curve of Green and Watson (1982). As the water content of the melt and depth of crystallisation are unknown, this gives a lower estimate of saturation temperature, as both water and increased depth will suppress the temperature at which saturation occurs (Watson, 1980), and it is clear that the data also plots parallel to curves of hotter temperatures too, but obviously well below normal asthenospheric values. Apatite may also play a role in decreasing concentrations of MREE, which are relatively compatible in the minerals structure compared to LREEs and HREEs. In samples with ¿54 wt%

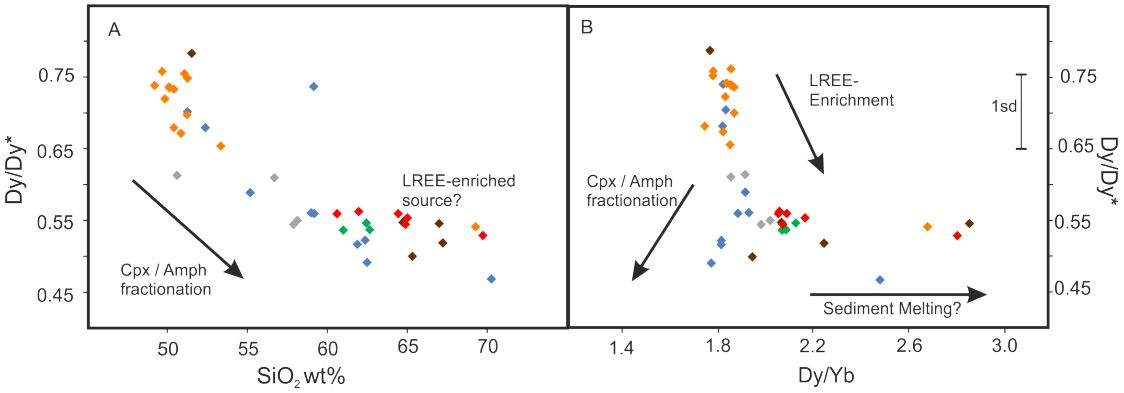

FIGURE 4.25: Dy/Dy* variations, based of variable from Davidson et al. (2013). a) Variation of Dy/Dy* with SiO_2. Arrow showing general direction of amphibole and cpx fractionation. b) Dy/Dy* against Dy/Yb. Enrichment in LREE drives down Dy/Dy* with very little change in Dy/Yb. Most enriched samples in Dy/Yb are also some of the most evolved. Symbols same as those used in Fig. 4.15.

SiO_2 (saturated in P_2O_5), Dy/Dy* is consistently lower.

4.4.2 Magma Mixing

Petrographic evidence for magma mixing is plentiful, be it zoned plagioclase, sieve textures, reaction rims, embayed olivines and pyroxenes or quartz and potassium-feldspar xenocrysts. These observations need to be reconciled with the geochemical data. In a crystallising melt it would be expected to see curved or kinked patterns on major-element plots against SiO_2 (an index of fractionation) as various minerals come onto the solidus, or solid-solution changes the composition of the crystallising phases. The data from the Lesser Caucasus tends to plot as very straight lines, particularly MgO, CaO, and TiO_2, where kinks would be expected from plagioclase, cpx, and Fe-Ti oxides respectively. Straight lines are often interpreted to represent mixing between a mafic and felsic melt.

Petrographically the Lower Akhalakalaki Fm. shows the least evidence of mixing, and major-element plots tend to show the most scatter and least linear patterns. This lends support to these melts not having undergone mixing. However the Abul-Samsari samples contain plenty of evidence of mixing, yet these do show an inflection suggestion the fractionation of Fe-Ti oxides, although the compositional range of these magmas is quite limited and quite evolved.

Mixing may play an important role in the Upper Akhalkalaki Fm. Rocks of this age lie on top of the more evolved Goderzi. Fm. (which itself seems to be a melt with a complex history of magma mixing) which it could have mixed with. They also lie above

the more mafic Lower Akhalkalaki Fm., with very little time between the eruption of the two formations, giving rise to the possibility of mixing or hybridisation of the two (still possibly molten) melts at depth, producing the two formations.

4.4.3 Crustal Contamination

As these volcanics have erupted through >40 km of crust, it is fair to assume that there may have been some interaction with crustal lithologies. Quartz xenocrysts in the Upper Akhalkalaki Fm. may be evidence of these interactions. Before trying to understand the chemistry of the source region, signatures inherited from this contamination must be considered. In other studies from the region, Keskin et al. (1998) suggested significant AFC occurred in East Anatolia, whereas on the thicker crust of Armenia contamination played a very minor role, except in the later stages of magmatic evolution (Neill et al., 2015).

Crustal lithologies beneath the volcanics are highly variable, including JurassicPalaeogene volcanic arc series, Hercynian granites and Early Palaeozoic schists, gneisses and amphibolites. Due to the large range of chemical characteristics and ages, they cover a wide range of Sr-Nd-Pb-Hf isotopic compositions (Fig. 4.26), that can be used to investigate contamination.

Variation in isotopic composition is modest in the post-collisional volcanism, but does form trends towards crustal end-members (Figs. 4.26 and 4.27). Less than 20% crustal input is needed to produce the variation shown assuming bulk-mixing (Fig. 4.27). However trends are not consistently towards a single crustal composition. Isotopic variation also forms trends with SiO_2, suggesting assimilation fractional crystallisation (AFC) processes are likely to be occurring (Fig. 4.28), rather than bulk mixing.

Assimilation fractional crystallisation (AFC) processes are suggested by observing isotopic variation also forms trends with SiO_2 (Fig. 4.28). Plots of isotope ratios against trace elements, such as Sr (Fig. 4.29) show that the amount of contamination does not have to be too great, and fractionation causes most of the spread of data.

The Lower and Upper Akhalkalaki Fms. show increasing $^{87}Sr/^{86}Sr$ with SiO_2 (Fig. 4.28), which can be explained by contamination with radiogenic crust. The Abul-Samsari rocks have relatively constant, to slightly decreasing $^{87}Sr/^{86}Sr$ during fractionation. It is unclear whether this is mixing with a less radigenic melt, assimilating less radiogenic crust (e.g. Mesozoic arc magmas) or just natural variation. All samples show a negative trend of $^{144}Nd/^{143}Nd$ with SiO_2 (Fig. 4.28).

Pb-isotopes show most clearly that more than a single trend is present (Figs. 4.23

and 4.27). This can also be seen on Fig. 4.28 where the Lower Akhalkalaki Fm. shows rapidly increasing $^{206}Pb/^{204}Pb$ with SiO_2, whilst the Upper Akhalkalaki Fm. remains constant, and the Abul-Samsari rocks decrease. The same trends are also seen with $^{207}Pb/^{204}Pb$ and $^{208}Pb/^{204}Pb$. The increasing trend points towards contamination by granitic crust, whilst decreasing trends suggest mixing with metabasic crust (Figs. 4.26 and 4.27).

The Lower Akhalkalaki Fm. forms a trend from the NHRL towards local granitic crust (Figs. 4.26 and 4.27). The least radiogenic sample (14-027) resembles an asthenospheric component, with flat multi-element plots and REE diagrams, low SiO_2, and the least contaminated $^{87}Sr/^{86}Sr$ and $^{144}Nd/^{143}Nd$. Therefore this will be used as an end-member for modeling the Lower Akhalkalaki trend. The trend formed by the remaining volcanics runs sub-parallel to the NHRL, suggesting a source already enriched by metasomatism or small-degree partial melting. They may be similar to the most contaminated Lower Akhalkalaki sample. Assuming this to be the case, contamination must be by a low $^{206}Pb/^{204}Pb$ lithology, such as the meta-mafic schists, amphibolites and diorites, which likely represent the oldest and deepest crust in the region. To model this suite, 14-045 has been chosen as the initial 'least contaminated melt, as it has the lowest SiO_2 of the samples that do not significantly overlap the older rock, and has isotope ratios at the extremes of the trends observed. A second interpretation could suggest the Abul-Samsari rocks form a separate cluster to the the Upper Akhalkalaki Fm., that has undergone contamination in the source region, and does not form a continuum from a single source. This is less clear when considering other isotope systems.

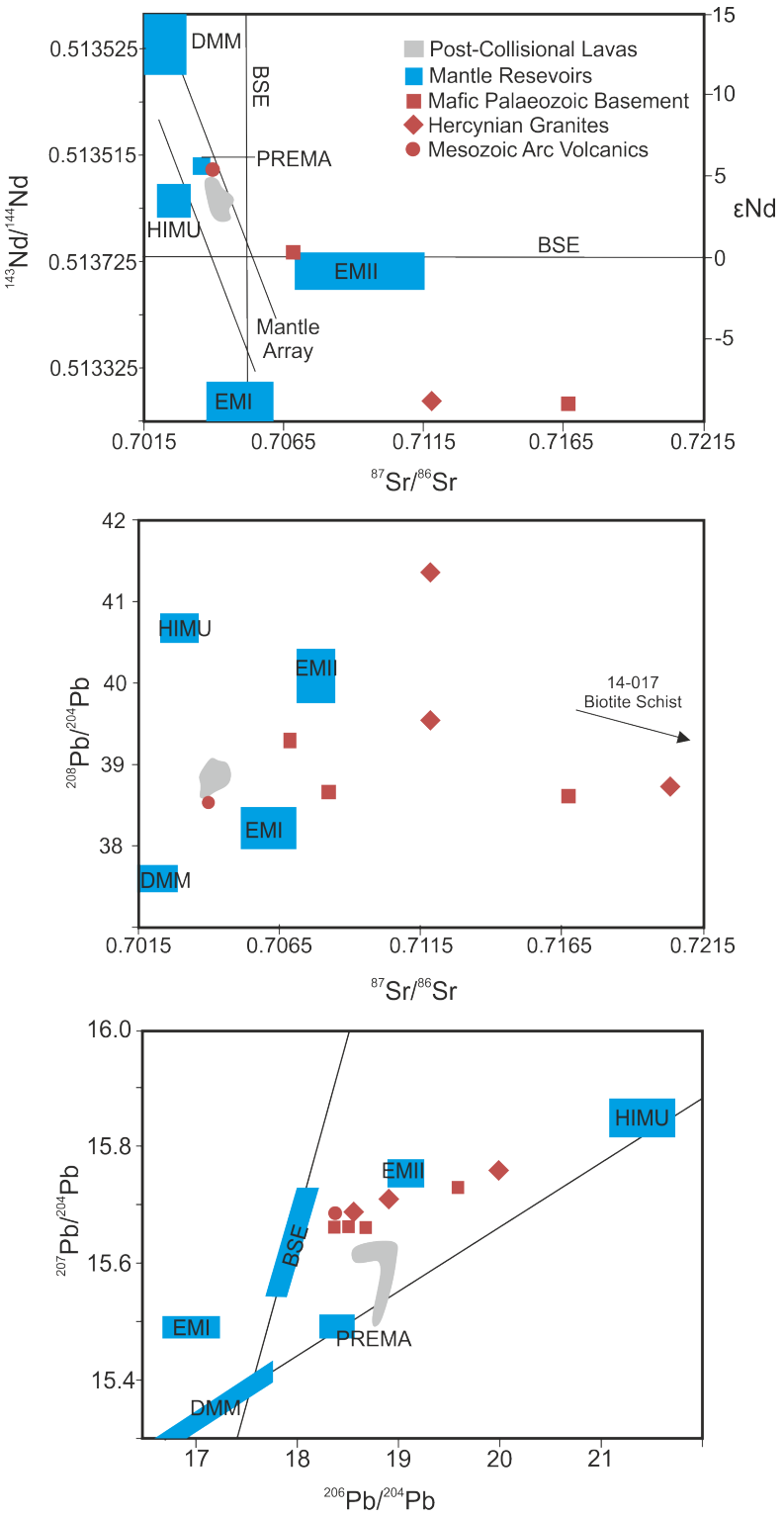

FIGURE 4.26: Range of crustal compositions observed in the Lesser Caucasus separated into three groups: Mafic Palaeozoic basement (Gneisses, amphibolites, schists, diorites), Hercynian granites and Mesozoic Arc volcanics. Total range of compositions observed in the post-collisional volcanics shown as a grey cloud. Mantle resevoir compositions taken from Faure and Mensing (2005), Sr-Nd mantle array taken from Wilson (1989), NHRL from Hart (1984). Uncertainties on measurements are well within the symbol size.

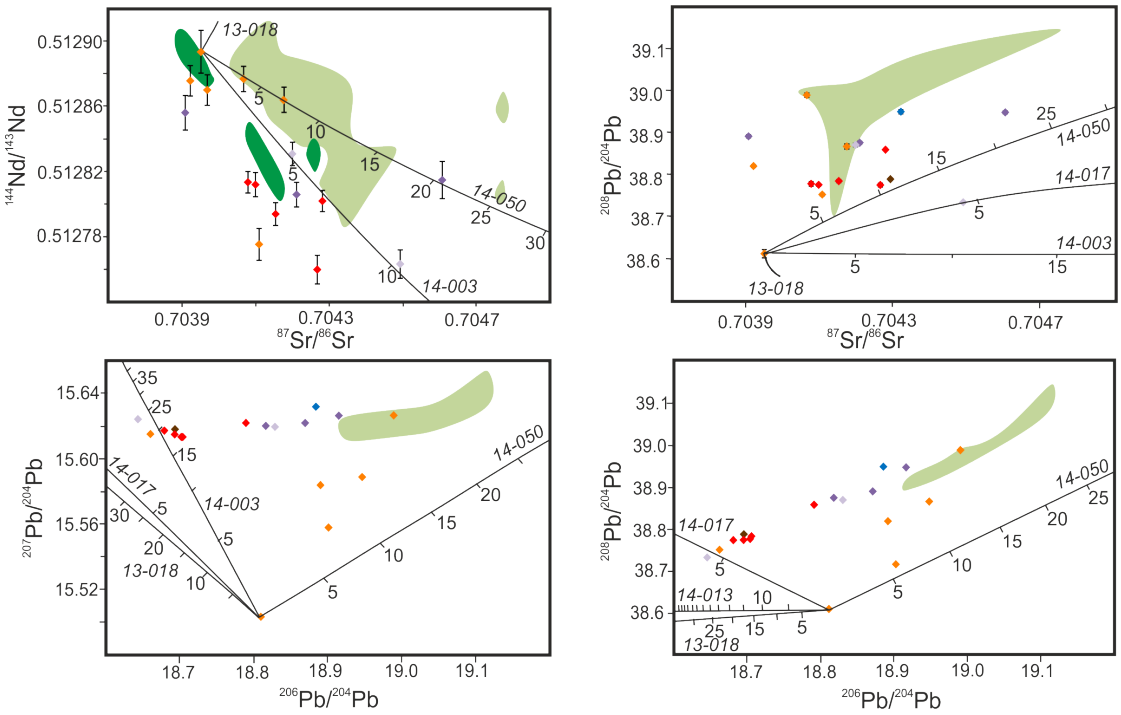

FIGURE 4.27: Bulk-mixing curves to explain trends seen in the Lesser Caucasus data for $^{87}Sr/^{86}Sr$ vs $^{144}Nd/^{143}Nd$, $^{87}Sr/^{86}Sr$ vs $^{208}Pb/^{204}Pb$, $^{206}Pb/^{204}Pb$ vs $^{207}Pb/^{204}Pb$ and $^{206}Pb/^{204}Pb$ vs $^{208}Pb/^{204}Pb$. Green fields are literature data (See Fig. 4.23 for details). Tick marks on mixing curves represent 5% mixing. Endmembers chosen are Early Palaeozoic siliminite bearing biotite schist (14-017) and migmatite (14-003), Hercynian granite (14-050) and Mesozoic arc volcanic (13-018). Symbols used are same as Fig. 4.15

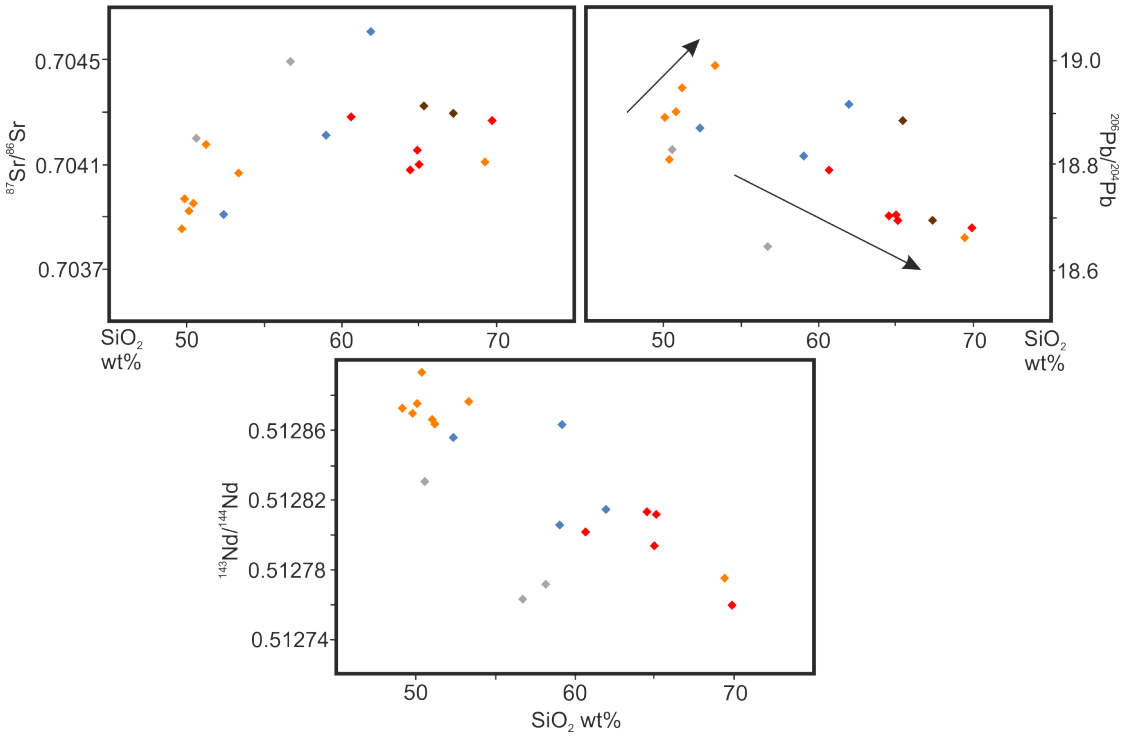

FIGURE 4.28: Variation of isotopic composition with SiO_2 acting as an index of fractionation. Two separate trends on the Pb-isotope plot, with arrows representing the trends. The distinction is more clearly displayed in Fig. 4.23. Symbols used are same as Fig. 4.15.

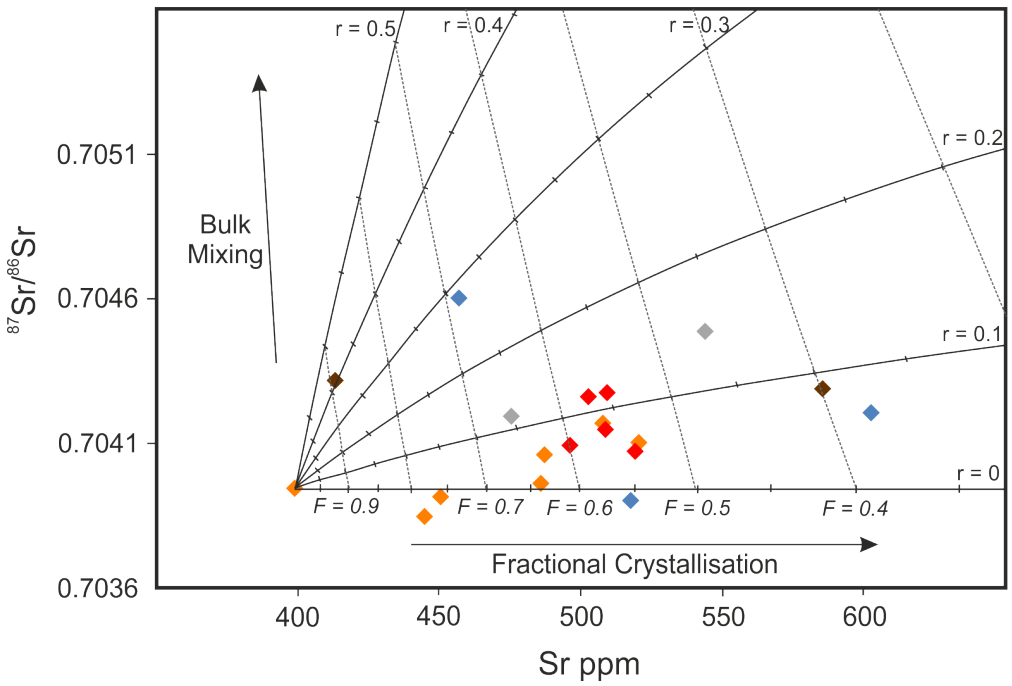

FIGURE 4.29: Isotope and trace element variation, with AFC model. Spread in Sr with relatively constant $^{87}Sr/^{86}Sr$ can be explained by increasing fractionation, with limited input from crust. Starting composition is rock 14-027, Sr = 399 ppm, $^{87}Sr/^{86}Sr$ = 0.70395. Contaminant is 14-003, Sr = 149.9, $^{87}Sr/^{86}Sr$ = 0.716727. Fractionating assemblage is same an anhydrous assemblage in Table 4.3. Symbols used are same as Fig. 4.15.

AFC processes are harder to distinguish with trace elements because of the very wide range of crustal compositions, and effect of source variation and melting in their composition. Figure 4.30 shows two separate models of AFC with an anhydrous and amphibole-bearing crystallising assemblage. Details of parameters used in the modelling is shown in Tables 4.2 and 4.3. The Lower Akhalkalaki Fm. trend can be explained by an anhydrous assemblage. The range in Nb/Zr is difficult to explain by pure fractional crystallisation, as it produces such little variation (as shown by the 50% fractionation mark on r = 0 on Fig. 4.30). However some crustal contamination helps produce the linear array. The contaminant chosen in the model shown is a migmatite, although the other crust types all show a similar trend. Despite the Pb-isotopes suggesting granite as being the key contaminant, it was not chosen here due to uncertainties on the Zr content, because of poor dissolution of zircon.

The elevated $(La/Yb)_N$ of the younger rocks can be explained by small degrees of partial melting (¡1%), however Nb/Zr and $(La/Yb)_N$ would both be expected to increase with decreasing degree of melting (See inset of Fig. 4.30), so the negative trend cannot be explained by this, or the same fractionating assemblage as the Lower Akhalkalaki Fm. A model with amphibole crystallising can replicate the observed trends, contaminated with mafic basement (in agreement with Pb-isotopes). This assemblage is supported by the observed amphibole phenocrysts. Only limited contamination is needed to explain the variation (r <3), however this model also requires what are likely unrealisticly high amounts of fractionation (Over 50%).

The Abul-Samsari lavas require the most contamination, which supports contamination on Fig. 4.27 towards lower $^{206}Pb/^{204}Pb$. However the model shown requires unrealistically high amounts of contamination, based off this source composition. I believe this rules out the Upper Akhalkalaki Fm. and Abul-Samsari rocks being related by fractionation or contamination, and they are derived from separate sources.

4.4.4 Chemical Nature of the source region

Variations in isotopic compositions give an insight into the source of the Lesser Caucasus volcanics, as fractional crystallisation and partial melting should not affect isotopic ratios. Used in combination with trace elements, a picture of the geochemistry, mineralogy, and melting conditions can be established. On mantle-normalised trace-element plots (Fig. 4.21) and Pb-isotopes (Fig. 4.23), samples from the Lower Akhalkalaki Fm. show very different patterns to all younger volcanics. The Upper Akhalkalaki Fm., scoria, and Holocene volcanics all show large negative Nb and Ti anomalies, large positive Pb

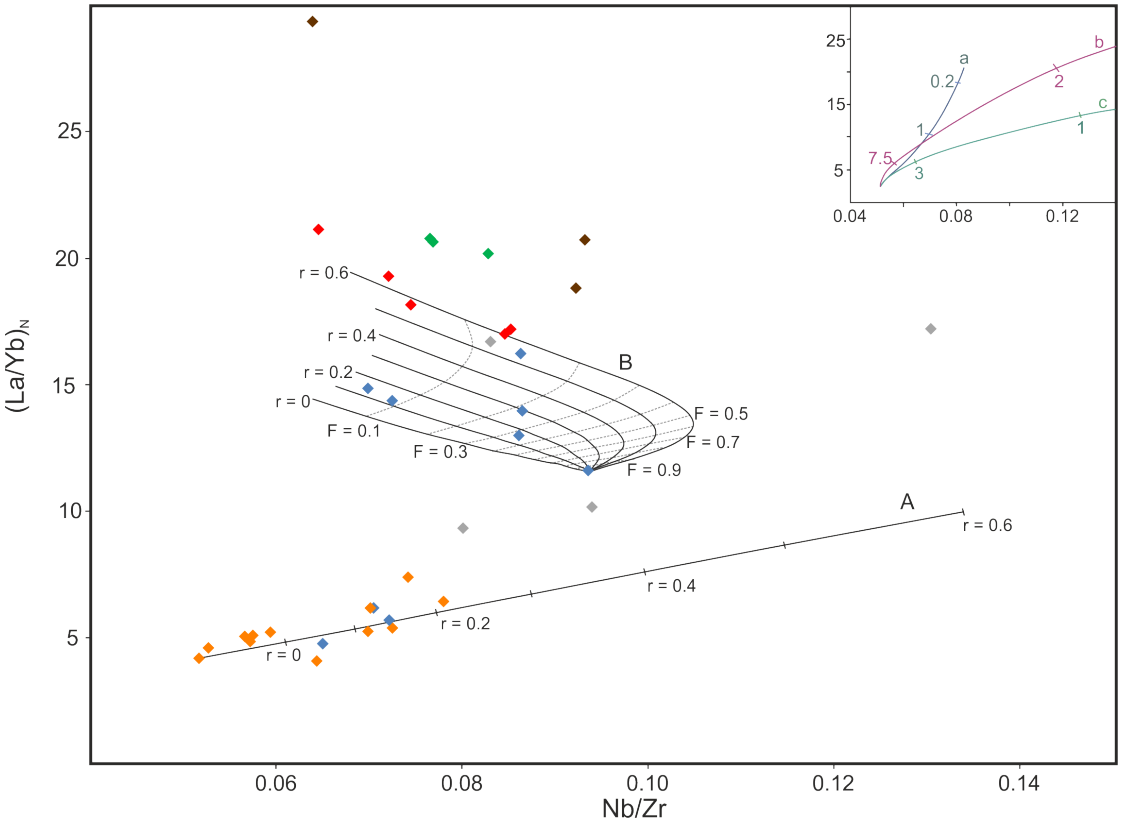

FIGURE 4.30: Trace element variation within the Lesser Caucasus explained by AFC processes. Two models are shown. Model A represents an anhydrous fractionating assemblage. Tick marks represent F = 0.5, for the variaious r-values. r-value increases by 0.1 at each tick. At higher F-values the models fan out, however at this scale they all overlap, forming the single trend seen in this data set. Model B is an amphibole bearing assemblage. Solid black lines show 0.1 variations in r-value, whilst the gray dashed lines represent equal F-values for various r-values. Both models use migmatite 14-003 as the contaminant. The inset graph has the same scales, but shows melting curves for a) amphibole-bearing, b) garnet-bearing and c) spinel bearing assemblages, with numbers representing degree of partial melting. For details on the model parameters used, see Tables 4.2 and 4.3. Symbols used are same as Fig. 4.15. Chondrite normalising values for $(La/Yb)_N$ are from Palme and O'Neill (2014).

anomalies, LILE are enriched by over 50 times primitive mantle and significant enrichment of LREE relative to HREE. These features are lacking in the Lower Akhalkalaki Fm. The flat REE pattern, which cross the younger volcanics around Nd, are difficult to explain with anything but a non-cogenetic comparison of the two sets of data. Differences are also seen in Pb-isotopes where the Lower Akhalkalaki Fm. trends towards the NHRL, whereas the other volcanics plot on a sub-parallel array. This difference is likely to have originated from two separate source regions.

TABLE 4.2: Partition coefficients used in AFC modelling. Kd values taken from GERM database for reasonable composition minerals. Starting compositions for the Lower Akhalkalaki fm. (NS-PhD-5), Upper Akhalkalaki Fm. (14-045) and migmatite contaminant (14-003).

	Element				
	Zr	Nb	La	Dy	Yb
Partition Coefficient					
Olivine	0.12	0.01	0.0004	0.0017	0.0015
Orthopyroxene	0.032	0.0013	0.02	0.022	0.049
Clinopyroxene	0.1	0.05	0.54	0.33	0.28
Plagioclase	0.12	0.01	0.27	0.055	0.031
Spinel	0.045	0.15	0.1	0.1	0.01
Amphibole	0.156	0.8	0.17	0.78	0.59
Starting composition (ppm)					
NS-PhD-5	140.7	7.275	15.09	4.353	1.227
14-045	183.2	17.15	35.67	4.353	2.447
14-003	122.2	22.08	43.12	5.443	2.163

TABLE 4.3: Fractionating assemblage for AFC models. Anhydrous assemblage used to model the Lower Akhalkalaki FM. whilst the hydrous assemblage is used for the Upper Akhalkalaki Fm. Assemblages based on petrographic observations

	Fractionating Assemblage					
	Ol	Opx	Cpx	Plag	Sp	Amph
Anhydrous assemblage						
For Lower Akhalkalaki Fm.	0.13	0.15	0.45	0.25	0.2	
Hydrous assemblage						
For Upper Akhalkalaki Fm.		0.3	0.15	0.03	0.02	0.23

4.4.4.1 Asthenosperic Component

The clearest indication of a normal asthenospheric mantle component, (i.e. one that has not been affected by subduction related activity) is seen in the Lower Akhalkalaki Fm. The relatively flat multi-element variation and REE patterns suggest a low-pressure melt from a slightly depleted source. However it is unlikely to be pristine MORB-like source. It shows enrichment in Sr- and Nd- isotopes, without trending back to values typical of MORB, unlike with Pb-isotopes where the trend extends to the NHRL. Figure 4.31 shows that even though the trend is towards the NHRL, at mantle like $^{207}Pb/^{204}Pb$, $^{208}Pb/^{204}Pb$ is still enriched, suggesting this mantle-like source already has elevated Th, a sign of previous subduction-like (sediment-dominated) contamination. This is consistent with trace-element patterns (Fig. 4.21) which are still strongly enriched relative to primitive mantle. This is also expected in a geodynamic context, where significant subduction has occurred prior to this volcanism. This component underwent crustal

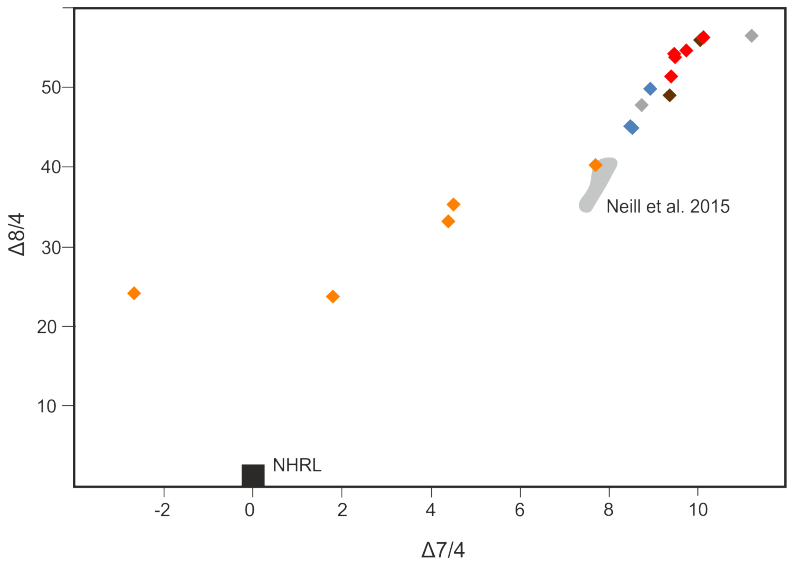

FIGURE 4.31: Variation in Pb-isotopes shown by Δ7/4 vs Δ8/4, representing deviation from the NHRL based on equations of Hart (1984).

contamination (Fig. 4.27) to produce a potential source for the younger volcanics.

4.4.4.2 Enrichment of the source

On mantle-normalised trace-element plots (Fig. 4.21) elements are ordered in increasing compatibility in a spinel lherzolite mantle mineral assemblage. Melting of this source would give a smooth decreasing trend as the least compatible elements get most enriched. This is not the case with the magmas from the Lesser Caucasus, where that trend has been superimposed by negative anomalies reflecting HFSEs depletion relative to LILEs and LREEs, and other elements, such as Pb, show positive anomalies. This pattern is typical of arc lavas, and reflects the nature of the source region.

The depletion of the HFSEs, particularly Nb-Ta and Ti, has received much attention in the literature. Typical explanations involve metasomatism of the mantle wedge by LILE- and LREE-rich slab-derived aqueous fluids, depletion of the mantle wedge by earlier melt extraction, and residual accessory phases in the slab and wedge preferentially holding back HFSEs.

Although the data shows large negative anomalies, HFSEs remain significantly enriched relative to primitive mantle (by a factor of 12–30 for Nb, and 1.5–8 for Ti). This rules out previous depletion events as a cause for the anomalies, as even the lavas that show the flattest patterns (largest degree of partial melt) still show significant enrichment. Continental crust also typically shows this pattern, therefore crustal anatexis

is another potential source of the chemistry. Local crust can be ruled out a source of the rocks of this study as the isotopic compositions of the volcanics are irreconcilably different to the local crust. Crustal contamination could explain the enrichment in some elements, however the concentration of the Sr, Zr-Hf and HREEs are lower than that of the magmas, and therefore contamination would have a depleting effect, rather than the required enrichment. The data also show fractionation of HFSEs. Zr/Hf of 42–49 is well above the chondritic value of 34.3 (Pfänder et al., 2007). Lower and Upper Akhalkalaki Fms. have consistently higher ratios than the Abul-Samsari rocks (46–49, compared to 42–46, respectively). Where available, Nb/Ta values are sub-chondritic values (<19.9; Pfänder et al., 2007), which is in agreement with data from Armenia (16–22; Neill et al., 2013), however the reliability of the Ta data is questionable (standard analyses resulted in very poor reproducibility), so this ratio has not been used for further investigation. Fractionation of clinopyroxene and amphibole only causes a small increase in Zr/Hf (Pfänder et al., 2007), and no increase of Zr/Hf is observed with SiO_2. Zr/Hf remains constant over a wide range of Zr concentrations, suggesting fractionaction of titanium-rich phases (such as rutile and ilmenite, which both have $D_{Zr/Hf}$1; Pfänder et al., 2007) is also ruled out, where increasing Zr/Hf would correlate with decreasing Zr. Accumulation of zircon can also be ruled out by the lack of correlation between Zr/Hf and Zr. Zr/Hf also does not correlate with $^{87}Sr/^{86}Sr$, suggesting crustal contamination is also not the cause. Therefore metasomatism of the source region remains the most likely explanation of the pattern seen.

The nature of the metasomatic fluids typically fall into three categories: Aqueous fluid from dehydration of a subducting slab, slab-derived hydrous silicic melt, and carbonatitic melt (Hermann et al., 2006). Hermann et al. (2006) also note a solute-rich fluid existing at conditions transitional between the aqueous fluid and hydrous melt (P >30 kbar, and a peak temperature of 700 °C). At depths of over 55 kbar a super-critical liquid with melt-like solubilities is formed (Kessel et al., 2005), although Mibe et al. (2011) suggest that the critical endpoint where the melting temperature of the subducting crust cannot be defined (and therefore a super-critical fluid produced) may be as low as 35 kbar (and 770 °C).

Carbonatitic fluids/melts have the necessary high HFSE/LILE (Ionov et al., 1993) and increase Zr/Hf (Ionov et al., 1993), and would be a source for the CO_2 required for the carbonate mesostasis seen in some samples. However elevated CaO/Al_2O_3 (Yaxley et al., 1991), high concentrations of Sr and high Sr/Sm and La/Nb (Ionov et al., 1993) would also be expected, but are lacking. The carbonate minerals are only observed in the samples with the lowest HFSE/LILE. Therefore carbonatitic melts seem an unlike

candidate for the metasomatic fluid.

Slab derived fluids are left as the most likely source of enrichment. Residual minerals in the slab host HFSEs producing the observed negative anomalies. This could be the result of the dehydration process, or as a relict of the dehydrating sediment (Hermann and Rubatto, 2009). Aqueous fluids only transport limited amounts of LILE, Sr and Pb, and do not have a significant role in the transport of LREE, U and Th (Hermann et al., 2006). The enrichment in all elements, instead of just the LILEs, must therefore be the result of small-degrees of partial melting in the slab or deep super-critical fluids, which can transport significant amounts of all the elements, including fluid-immobile elements (Kessel et al., 2005). Melting of the slab is likely to be facilitated by dehydration of deeper basaltic and ultra-mafic parts of the slab (Hermann et al., 2006).

It is clear from Fig. 4.21 that the Lower Akhalkalaki Fm. only shows a very minor slab component. This may be due to a different metasomatic event, such as a carbonatitic event, or the Lower Akhalkalaki Fm. sampling a remnant enriched source. Cs/Nb ¡1 is not consistent with slab fluids. Another clear difference between the Lower Akhalkalaki Fm. and the younger rocks is seen in the fractionation of Rb and Cs. Both are LILEs and their concentrations in supra-subduction settings is thought to be controlled by residual phengite in the slab (Bebout et al., 2007; Hermann and Rubatto, 2009). The Lower Akhalkalaki Fm. shows a typical MORB-like signature, with very low concentrations of Cs relative to Rb, which is less obvious in the younger rocks. Cs is expected to be the least compatible element in the slab, so should be the most enriched in the metasomatic fluid, however this is not the case here. At lower temperature prograde P-T paths for a slab, both Cs and Rb are relatively compatible in phengite (Bebout et al., 2007), whereas at higher temperatures phengite retains Rb, whilst Cs is incompatible. This may suggest that devolatisation of the slab in this region occurred at low temperatures for the Lower Akhalkalaki Fm., whereas later higher temperature, and deeper, dehydration resulted in the source of the younger rocks, which is consistent with a sinking slab.

4.4.4.3 Melting the source

Metasomatic enrichment and contamination by crustal material can go a long way to explain the trace element patterns and concentrations observed in these rocks. However melting of rocks within the source region will also have left its own signature on the these rocks, such as the variably fractionated LREE/HREE. To improve understanding on the source mineralogy and degree of melting the source has undergone, melting is modelled using an equation for non-modal fractional melting (Shaw, 1970).

Due to their range of compatibilities, the rare earth elements can provide an insight into the melting conditions of the melts. Figure 4.32 shows the data for the various ages of Lesser Caucacus volcanism, along with three models varying in source mineralogy and melting modes. On this plot, the large difference between the highly incompatible La and smaller, more compatible Yb allow $(La/Yb)_N$ to be used as a proxy for degree of melting, whereas $(Dy/Yb)_N$ shows the fractionation of MREE/HREE, typically caused by the presence of garnet, therefore being a proxy for depth of melting.

Neill et al. (2015) noted the complex history of the source region beneath Armenia (and therefore the Georgian Lesser Caucasus too), involving depletion through melting in the Mesozoic/Early Cenozoic arc phase of the history, and the re-fertilisation by slab-derived metasomatic fluids. It is clear from the trace elements patterns (Fig. 4.21) that this has played an important role (to variable degrees) in the chemistry of the Georgian Lesser Caucasus samples. This complicates the choice of starting composition. The composition has clearly been changed from depleted MORB-source mantle (DMM). Other authors have chosen mixtures of DMM with Tethyan sediments (Allen et al., 2013), enriched primitive mantle (Özdemir and Güleç, 2014), and ultramafic xenoliths representing metasomatised mantle (Allen et al., 2013; Neill et al., 2015).

We also compare three different melting assemblages and modes (Table 4.3). The spinel model represents shallow, anhydrous melting. The garnet model represents a deep melt (>70 km), where garnet is now the stable host of Al. The final model includes amphibole, and represents melting of a hydrous source.

In the spinel model assemblage, La, Dy and Yb are all of similar incompatibilities (particularly Dy and Yb), so only a limited range of compositions would be expected. The wide spread in $(La/Yb)_N$ values can only be produced in this model from very small degrees of partial melting (<0.5 %), which is unrealistic for the volume of lava erupted. Some fractionation is produced in $(Dy/Yb)_N$ in this model, as a result of cpx hosting Dy. This fractionation is similar to that observed in the Abul-Samsari volcanics, however is too fractionated for most other rocks of the Lesser Caucasus.

The second model includes garnet instead of spinel in the source. As HREEs are compatible in garnet, this model readily fractionates MREE/HREE and produces a wide range of $(La/Yb)_N$ and $(Dy/Yb)_N$ values. This model reproduces $(La/Yb)_N$ values close to those observed in the samples at >2% melting, which would be realistic for the amount of volcanism in the region. However, the presence of garnet produces significantly more fractionation in $(Dy/Yb)_N$ than is observed in the Lesser Caucasus samples. Therefore garnet is unlikely to be in the source, constraining the depth of melting to shallower than 70 km.

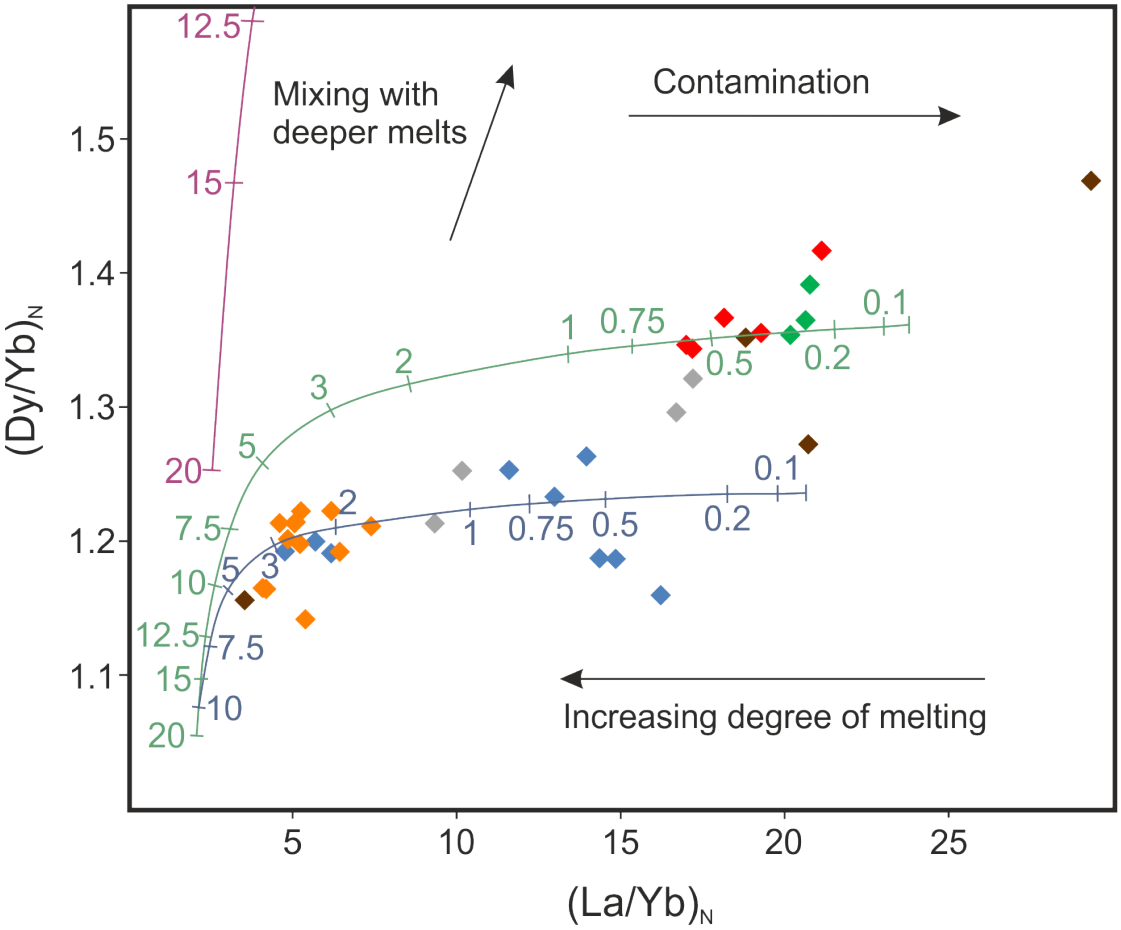

FIGURE 4.32: Partial melting curves for models involving garnet- (purple), amphibole- (green) and spinel- (blue) bearing source regions, and melting modes. Numbers on the curves represent degree of partial melting. Details of the models and parameters used are discussed in section 4.4.4.3 and Tables 4.4 and 4.5. Symblos used are same as Fig. 4.15. Chondrite normalising values used are from Palme and O'Neill (2014).

The third model is based on one proposed by Neill et al. (2015), and represents a hydrous source region, with amphibole present in the melting assemblage. Based on the mineralogy and trace element geochemistry, a hydrous source is a fair assumption for all but the Lower Akhalkalaki Fm. This model fits the Lesser Caucasus data the best. Slight MREE/HREE is observed, but less than that of the spinel model, as residual amphibole acts as a host for Dy, preventing it from entering the melt.

It is also clear from this model that the various phases of magmatism seem to require different degrees of melting. The Lower Akhalkalaki Fm. requires the highest degree of melting. The trace element chemistry suggests an anhydrous source, therefore the spinel

TABLE 4.4: Source and melt modal compositions for three melt models. Model 3 is based off model by Neill et al. (2015). See text for details of the models.

	Mineral Assemblage					
	Ol	Opx	Cpx	Amph	Sp	Gt
Model 1: Spinel						
Source Mode	0.578	0.27	0.119		0.033	
Melt Mode	0.1	0.27	0.5		0.13	
Model 2: Garnet						
Source Mode	0.598	0.211	0.076			0.115
Melt Mode	0.05	0.2	0.3			0.45
Model 3: Amphibole						
Source Mode	0.794	0.123	0.03	0.042	0.011	
Melt Mode	0.15	0.15	0.22	0.42	0.06	

model is likely to be most realistic. The data is reproduced by degree of melting of 3–10 %. This corresponds well to field observations where this formation has long lived centres, producing large stacks of plateau forming flows. Slight variation in source composition and melting modes can shift the curve to better fit the data. The Upper Akhalkalaki Fm., requires a smaller degree of partial melting, and by this stage plateau forming volcanism had ceased, and valley-filling flows had become the norm. The presence of amphibole in the source is suggested by trace-element chemistry, and explains the relatively low $(Dy/Yb)_N$. The Abul-Samsari rocks require the smallest degree of partial melting, and these are the least widespread, and are typically monogenetic cones, without associated expansive flows. The high $(Dy/Yb)_N$ can either be explained by melting in an anhydrous assemblage without residual amphibole, or by mixing with small degrees of partial melts from the garnet stability field. In the spinel model 0.2–0.8% melting is required, which is rather small. Larger degrees of melting can reproduce this data, if mixed with very small amounts of deeper melts that would have a highly fractionated $(La/Yb)_N$.

The Upper Akhalkalaki Fm. forms a negative trend on this plot, which cannot be explained by melting, or mixing of melts. Assimilation of local crust (granite, gneiss or amphibolite) causes $(Dy/Yb)_N$ to decrease (Fig. 4.33). The two models represent an anhydrous assemblage for the Lower Akhalkalaki Fm. and hydrous assemblage for the Upper Akhalkalaki Fm. These curves suggest that a single melt composition that has undergone AFC can produce the variation observed for each formation. It also clearly shows that three different melts are required throughout the region, confirming the non-genetic relationship of the Upper Akhalkalaki Fm. and Abul-Samsari volcanics.

TABLE 4.5: Distribution coefficients use in melt modelling. Starting composition of modelling also shown, based off Shirak and Lori starting composition from Neill et al. (2015).

	Kd Value						**Starting composition**
	Ol	Opx	Cpx	Amph	Sp	Gt	**(ppm)**
La	0.0001	0.0002	0.054	0.086	0.0004	0.01	0.5869
Dy	0.0014	0.0261	0.442	0.707	0.0004	1.06	0.317
Yb	0.00364	0.0986	0.427	0.683	0.00053	4.03	0.202
Zr	0.004	0.005	0.13	0.156	0.005	0.5	7
Nb	0.0002	0.0005	0.0077	0.2	0.001	0.03	0.3635

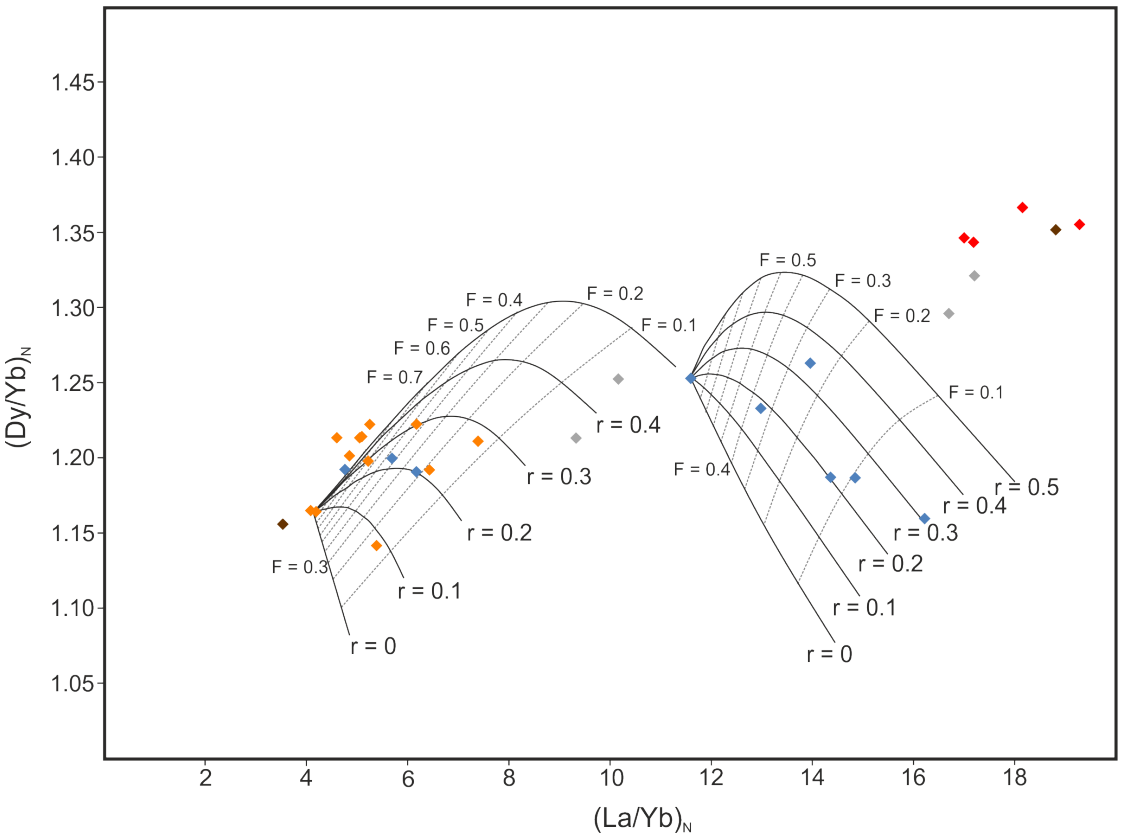

FIGURE 4.33: Same plot as Fig. 4.32, showing AFC models rather than melting models. Two separate models to show spread in Lower (anhydrous) and Upper (Hydrous) Akhalkalaki Fms. Solid black lines show 0.1 increments in r-value, dashed grey lines show 0.1 increments in F-value. See Tables 4.2 and 4.3 for the model parameters. Both models use migmatite 14-003 as the contaminant. Symbols used are same as Fig. 4.15. Chondrite normalising values used are from Palme and O'Neill (2014).

4.5 Summary of Results

Near continuous volcanism has been present in the Georgian Lesser Caucasus for over 3 million years, and as recent as early human times. Any model to explain the origin of this magmatism, and the geodynamics of the Caucasian section of the Eurasian-Arabian collision, needs to be able to explain the observed outcrop styles, petrography and geochemistry.

Bulk-rock and mafic mineral Mg# are too low for an asthenospheric melt, and isotopes of even the most uncontaminated samples plot well away from mantle end-members. Isotope data also show that crust only played a role as a contaminant, rather than the magmas being crustal melts themselves. This constrains the source region to the mantle lithosphere. REE ratios show that melting did not occur in the garnet stability field, constraining the depth of melting to between 40 km (base of crust) and 70 km (where garnet becomes stable). This is a requirement for all post-collisional magmas investigated. However, trace elements and Pb-isotopes suggest that more than a single source is required.

The Goderzi Fm., although not investigated in detail, is a precursor to the main phase of volcanism, and may be classed as syn-collisional. Mineralogy suggests a complex source, with multiple refertilising events, and a long period of relatively shallow (8–12 km) fractionation before eventual eruption. Due to lack of fresh outcrop, and being covered by younger volcanics, it is difficult to make any further suggestions about the source of these rocks.

The Lower Akhalkalaki Fm. requires a source that looks the most asthenospheric. It has undergone only minor contamination by slab-derived fluids, with some influence from carbonatitic melts. However it is still enriched in the full range of trace-elements, and has Sr- and Nd-isotope ratios more radiogenic than would be expected for a 'MORB-source melt. Eruption of these mafic melts formed large plateaus, by relatively large degrees of partial melting (up to 10%) of the source situated just below the base of the crust (~40–50 km based on the carbonate bearing samples). Before eruption there was interaction with the crust, clearly seen in Pb isotopes and trace elements. This may suggest a shallower magma chamber situated in the deeper crust (~16–30 km), where the hot magma (the hottest in the Georgia) interacted with Hercynian granites, and to a lesser extent, mafic Palaeozoic lower crust.

The Upper Akhalkalaki Fm. seems continuous with the Lower Akhalkalaki Fm. in the field, however is chemically quite different. The clearest difference is a source which has undergone much more metasomatism from slab-derived fluids (creating enrichment in

LILEs), and a source that has already undergone some form of contamination (based on Pb-isotpes). It is possible the crustal storage of the Lower Akhalkalaki Fm., rejuvenated by a pulse of metasomatised lithosphere melt became the source of these younger magmas, which formed from a smaller degree of melting than the older part of the formation. These melts also underwent a greater degree of fractionation, and more contamination than the older magmas. The cooler magma chamber, and smaller degree of melting changed the eruption style from plateau forming events, to more isolated valley forming flows.

The Abul-Samsari Fm. and Borjomi flows seem to be chemically similar. After a brief hiatus in volcanism these two regions became active. The emplacement may have been controlled by the disputed Borjomi-Kazbek fault, explaining the N-S orientation of the Abul-Samsari ridge. They erupted from a source similar to that of the Upper Akhalkalaki Fm., the influence of a metasomatism in the source seems even greater. The mineralogy points to the source having a complex history with multiple pulses of melt creating complexly zoned plagioclase, and reverse zoning in mafic minerals, as well as strongly altered amphiboles. Fractionating of amphibole played an important role in their formation. It is likely they formed from smaller degrees of partial melts (<1%), possibly with an input from deeper melts. Storage in the crust was also deep (up to 30 km), and contamination was predominantly by the older (therefore presumably deeper) meta-basic crust. Eruption must have been relatively rapid for the amphibole phenocrysts no the be resorbed into the melt. The young scoria cones may be genetically linked to the volcanism of this age, and represent deep explosive eruptions, with clasts that resemble rocks of this age. The hot springs of Borjomi suggest that there is still some heat at depth, an this area may not have finished being active yet.

These constraints will be put into a geodynamic model for the region, including the related rocks in Armenia, the East Anatolian volcanics, and the contemporaneous volcanics in the Greater Caucasus in Chapter 5.

Chapter 5

Petrogenesis of the Greater Caucasus Volcanics

5.1 Introduction

Volcanism in the Greater Caucasus is focused primarily at two large stratovolcanos, Mt. Elbrus (Russia) and Mt. Kazbek (Georgia). The chapter focuses on Mt. Kazbek, which has only been active in the past 800 ka (contemporaneously with the youngest pulse of volcanism in the Lesser Caucasus; Lebedev et al., 2007b, 2008a). The large stratovolcano, and surrounding monogenetic peaks and satellite cones erupted through up to 60 km of crust (Adamia et al., 2011).

Using a combined approach of petrography, mineral chemistry, major and trace elements and Sr-Nd-Pb isotope data, the roles of asthenosphere, lithosphere and the thickened crust will be investigated, with respect to the source region of the magmatism. The processes of melt generation, fractional crystallisation and crustal assimilation en route to the surface will be considered. The interpretations will be used to create a tectonic and geodynamic framework, reaching to the Greater Caucasus at the far north of the Arabian-Eurasian collision zone in Chapter 6.

5.2 Petrography

Lavas throughout the Mt. Kazbek volcanic region are all porphyritic to varying degrees. Plagioclase and orthopyroxene are almost ubiquitous across all samples with amphibole also a very common phenocryst phase (Fig. 5.1). Clinopyroxene, olivine and a high-Al pyroxene (>5 wt % Al_2O_3) occur as a major phenocryst phase in some some samples,

whilst apatite and an Fe-Ti oxide are common accessory phases. Throughout the following section percentages represent either estimated modal abundances in the whole rock (in regards to amount of phenocrysts) or modal abundance as part of the phenocryst assemblage (where the percentage is given after an individual phase).

The magmas of the Gudauri formation contain 5–30 % phenocrysts in an aphanitic groundmass composed of plagioclase and orthopyroxene (Fig. 5.1A). Plagioclase microphenocrysts define a pilotaxytic texture (Fig. 5.1A). Orthopyroxene (25–70 %) and plagioclase (15–75 %) make up the majority of the phenocryst assemblage, with clinopyroxene (5–15 %) present in all but the most evolved sample. The high-Al pyroxene phase is common in this formation (5–15 %), however it is often strongly altered and pseudomorphed by an aggregate of opaque phases (Fig. 5.1A). Small amounts of olivine are also present in the more mafic samples. One sample (H4) shows a very different texture, being holocrystalline with a coarse plagioclase and opx dominated assemblage with small phenocrysts of plagioclase, cpx and olivine. Glomerocrysts of opx and plagioclase ± cpx ± amphibole are common in these rocks, often enclosing trapped glass (Fig. 5.1A and B).

Rocks from the Qabarjina formation are strongly porphyritic (30–65 %), with a glassy groundmass (Fig. 5.1C). In some samples plagioclase microphenocrysts (0.1–0.2 mm) define a weak trachytic texture. Where the groundmass is slightly coarser, plagioclase and an oxide phase are identifiable. Plagioclase is the most abundant phenocryst phase (60–80 %), followed by amphibole (15–35 %) and opx (5–15 %). Some samples also contain biotite (Fig. 5.2). Recrystallisation of plagioclase can be seen in some sections. Glomerocrysts of plagioclase and amphibole or plagioclase and opx are relatively common. Some sample are vesicular, with broken up pyroxenes (Fig. 5.1C), related to the more evolved and explosive nature of eruptions from this volcanic centre.

The single sample representing stage I of the Mt. Kazbek eruptions is contains 65% phenocrysts. The assemblage is plagioclase (65%), cpx (25%), opx (10%) and trace amounts of amphibole. Microphenocrysts of plagioclase define a tracytic texture within a fine to glassy groundmass, with identifiable plagioclase and oxide phase.

Stage II eruptive products are also strongly porphyritic (30–60 %, Fig. 5.1D). Plagioclase is the dominant phenocryst phase (40–75 %), split into two groups of large (0.3–1 mm) and small (0.05–0.2 mm) grains (Fig. 5.1D). Plagioclase is often very rounded, and shows significant amounts of sieve and other disequilibrium textures (Fig. 5.1D and section 5.5.4). Opx (5–35 %) and amphibole (5–25 %) are present in all samples. Amphiboles are often very strongly rimmed or totally opacitised. Cpx and olivine are present in the more mafic samples (up to 20 %) and the high-Al pyroxene phase is also

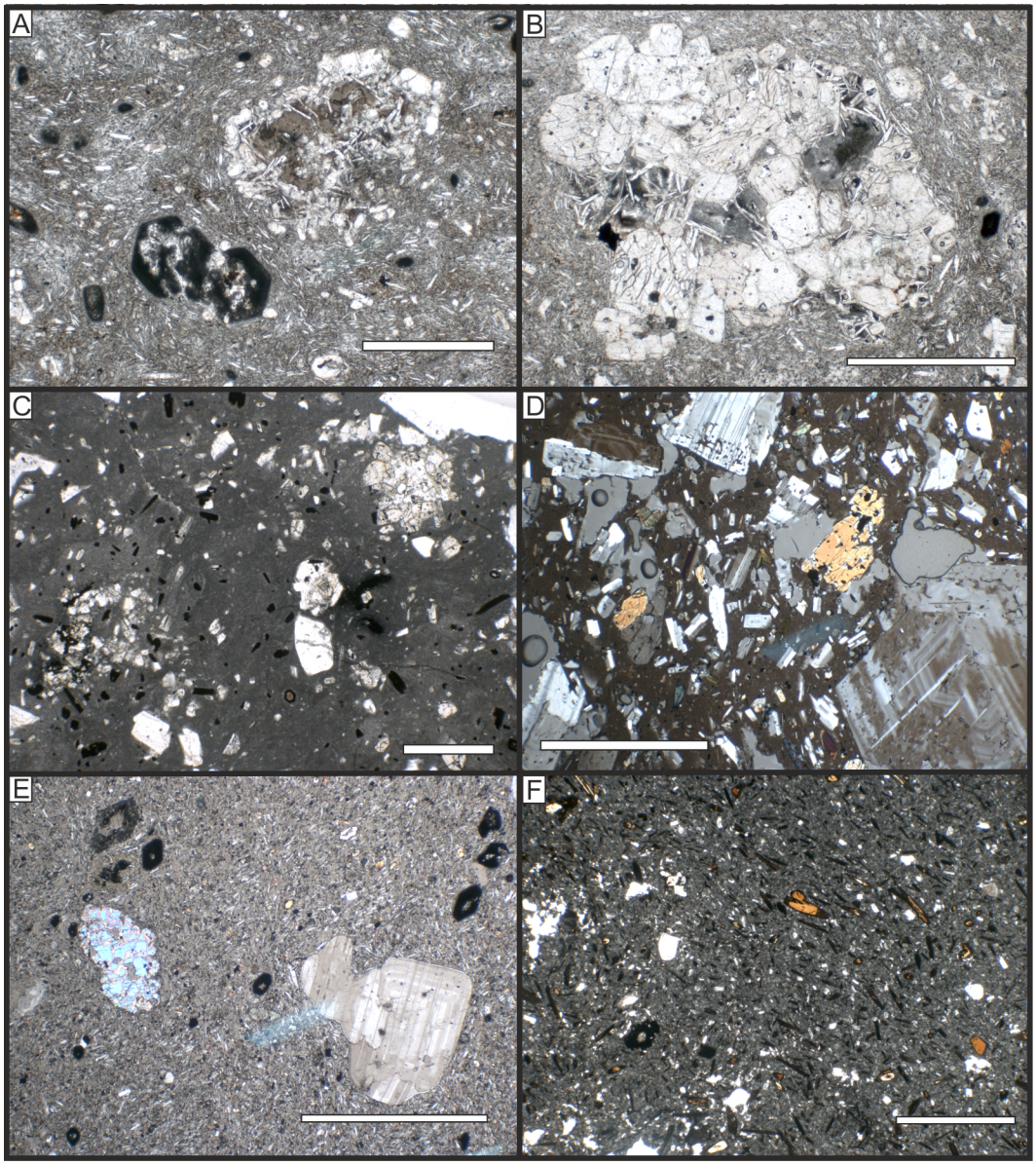

FIGURE 5.1: Microphotographs showing textures observed in volcanic rocks of the Greater Caucasus. A) Pilotaxytic groundmass in the Gudauri Fm. Two euhedral, but opacitised high-Al pyroxenes. An opx dominated glomerocryst is present, with plagioclase laths protruding into a trapped melt. B) Large glomerocryst from the Gudarui Fm., dominated by opx and cpx, with minor plagioclase, and trapped glass phase. C) Glassy groundmass of the Qabarjina Fm. Small amphibole phenocrysts strongly altered, but larger plagioclase remain fresh. Pyroxene grains are broken up, and a pyroxene dominated glomerocryst in seen in the top right corner. D) Phenocryst rich Stage II of Mt. Kazbek, with two groups of plagioclase grains in disequilibrium. Glassy groundmass, cpx and vesicles also present. E) Phenocryst poor Stage III of Mt. Kazbek. The groundmass in coarser than other rocks from the area. Amphiboles are strongly altered and cpx is rounded and embayed. F) Stage IV of Mt. Kazbek. Phenocrysts are small, and amphibole laths form a trachytic texture. White scale bar is 0.5 mm long.

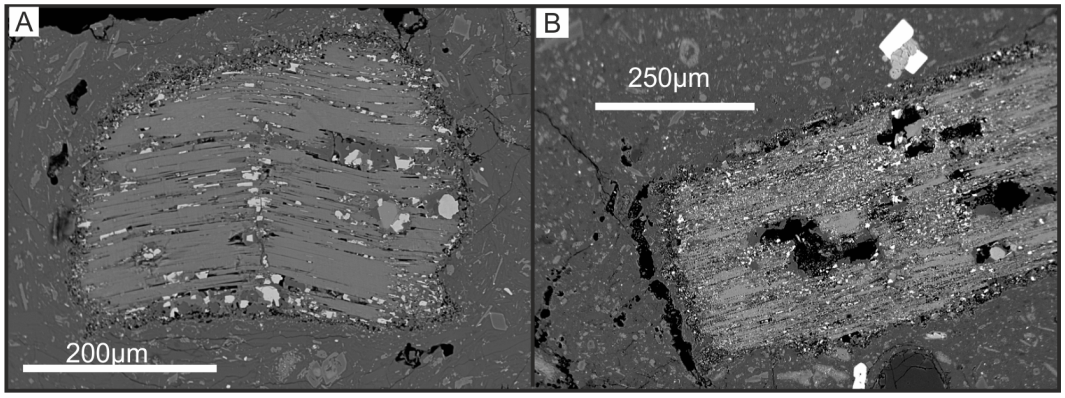

FIGURE 5.2: Alteration of phlogopite in sample KZ1, from Stage IV of Mt. Kazbek. A) Fine grained reaction rim, with coarser alteration along parallel cleavage planes, and ever coarser oxides along the crack cutting across the cleavage. B) Oxides pseudomorphing a phlogopite grain, with alteration focussed along cleavage planes. The reaction rim is maintained.

present. The groundmass is typically glassy or very fine. Small Fe-Ti oxide phenocrysts can form up to 5 % of a sample. In some sections plagioclase microphenocrysts show a trachytic textures, although this is not seen in all samples.

Stage III volcanics contain 15–25 % phenocrysts. Plagioclase, amphibole and cpx each form 20–30 % of the assemblage, with opx (10–15 %) and the high-Al pyroxene also present. Unlike the other lavas, the groundmass of these volcanics is quite coarse (Fig. 5.1E), with plagioclase, orthopyroxene, and Fe-oxide all present. One sample shows a weak tractytic texture in the groundmass. Disequilibrium textures are common, including rounded plagioclase, opacitised amphiboles, and recrystallisation of cpx. Plagioclase-opx-cpx glomerocrysts are common.

Stage IV volcanics generally have a glassy or very fine groundmass, with plagioclase, amphibole and Fe-oxide identifiable (Fig. 5.1F). Microphenocrysts of plagioclase and amphibole laths are present, often showing some alignment. Phenocrysts form 10–30 % of the rock. Plagioclase (45–60 %) and amphibole (30–50 %) are the most abundant phases. Opx, high-Al pyroxene, biotite and quartz make up the remainder of the assemblage. Plagioclase phenocrysts are often rounded.

5.3 Results

Full details of the whole-rock major and trace element chemistry, and isotopic ratios, can be found in Appendix C.

5.3.1 Analytical Techniques

Sixty-five whole rock samples were prepared for geochemical analysis using the methods described in Appendix B. Major elements concentrations were determined by X-ray florescence (XRF). Trace elements concentrations were measured by inductively coupled plasma mass-spectrometry (ICP-MS). Analytical procedure and standard data for these procedures can be found in Appendix B.3 and B.4 respectively.

Thirty-two samples were selected for isotopic analyses. All the isotope systems used (Sr-Pb-Nd-Hf) were measured at the Open University, using a Neptune multi-collector (MC)-ICP-MS. Analytical procedures and standard data can be found in Appendix B.

5.3.2 Sample Freshness

Samples of volcanic rock were monitored for freshness using loss-on-ignition (LOI) values. Samples had LOI values varying between -0.26 and 1.21 wt.%. The highest values correspond to samples containing hydrous minerals such as amphibole and biotite. Trends consistent with magmatic processes are observed in plots of SiO_2 against elements easily mobilised during surface alteration (i.e. CaO, Na_2O, Ba, Sr), rather than the scattered patterns expected after alteration. Whilst there is no correlation between these elements and oxides with LOI. In thin section mafic minerals and feldspars rarely show evidence of weathering and lack typical minerals related to alteration, such as sericite and chlorite.

Samples of the older basement crust have LOI between 0.4 and 2.5 wt.%. This reflects both hydrous phases and sub-solidus alteration. In thin section, sericitisation of feldspars is common, and many samples contain significant amounts of chlorite.

5.3.3 Major-element Geochemistry

Flows from all three centres (Mt. Kazbek, Qabarjina Fm. and Gudauri Fm.) fall on similar arrays on major-element geochemical plots. All rocks have intermediate, and sub-alkali composition (Fig. 5.3) The most basic samples collected were basaltic-andesites from the Gudauri flow (56.71–57.49 wt.% SiO_2). Two dacitic samples were also sampled from this centre, one at the base of the largest flow, and the second from a separate flow assumed to be associated with the same volcanic centre (although the edifice is not observed). Samples from the Qabarjina centre were the most evolved in the region, with compositions that ranged from andesite to dacite (62.65–67.27 wt.% SiO_2). Samples from Mt. Kazbek covered a wide range of compositions from trachy-basaltic-andesites to dacites (55.83–65.39 wt.% SiO_2). This range corresponds well with data from Lebedev

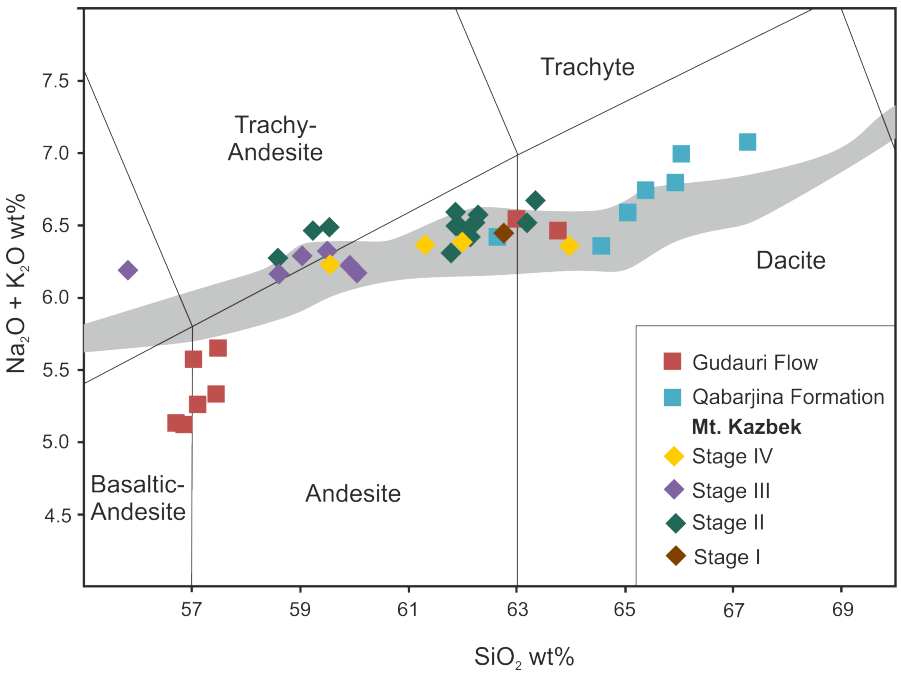

FIGURE 5.3: Total alkalis vs silica diagram for Greater Caucasus volcanics, based on plot from Le Bas et al. (1986). 2SE errors are smaller than symbol size. Grey shaded area represents total extent of compositions from the Georgian Lesser Caucasus (this study).

and Vashakidze (2014). All samples are quartz normative (as expected for these evolved compositions). They follow a calc-alkaline trend on an AFC diagram (not shown), although this is not fully clear as there are no low silica samples. Samples are not potassic (Na_2O/K_2O), plotting in the low-K, calc-alkaline field on Figure 5.4, the classification diagram of Ewart (1982).

Trends in major elements are well defined by the three centres (Fig. 5.5). Strong negative linear trends are formed by plots of MgO, CaO, $Fe_2O_3^{Tot}$, and TiO_2 against SiO_2. Within the overall trend, the Gudauri Fm. typically forms a cluster at the more mafic end, rather than showing any trend within the group. The Qabarjina Fm. and Stage IV Kazbek volcanics show the most well defined trends. The Kazbek and Gudauri samples all have higher Mg# than similarly evolved Lesser Caucasus rocks. Mt. Kazbek Stage IV rocks show a flat MgO pattern, with MgO concentration increasing in the most evolved sample.

No trend is observed across the whole suite between Al_2O_3 and SiO_2. The most mafic Gudauri rocks shows high- and low- Al_2O_3 groups, with the more evolved rocks sharing the high Al_2O_3. Stage III volanics have a slight positive correlation, whilst the Qabarjina Fm. and Stage IV volcanics both show strong negative trends. The Stage IV volcanics

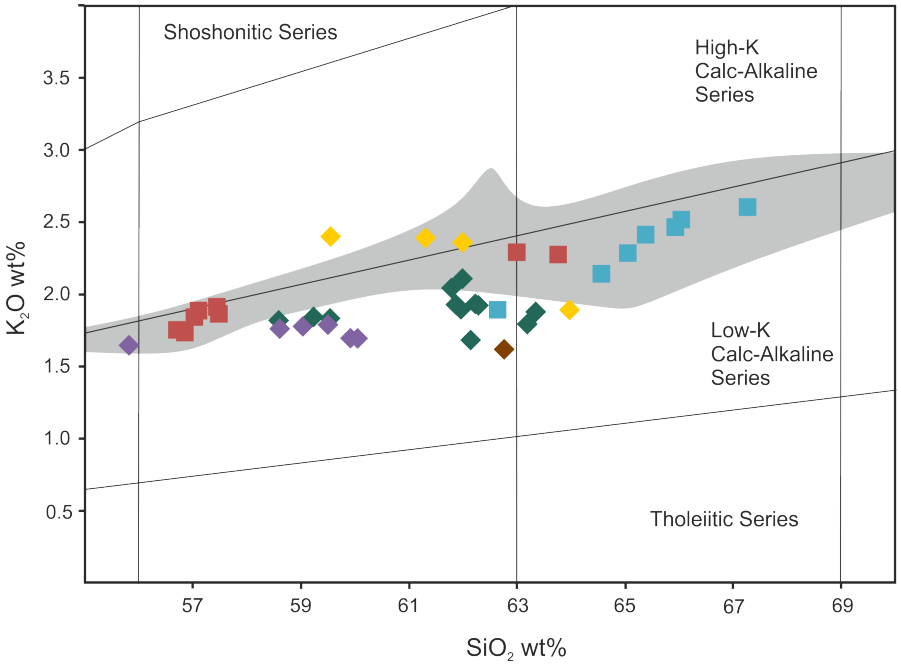

FIGURE 5.4: SiO_2 vs K_2O diagram for Greater Caucasus volcanics, based on plot from Ewart (1982). Grey shaded area represents total extent of compositions from the Georgian Lesser Caucasus (this study).

show high Al_2O_3, similar to the Gudauri Fm.

Concentrations of K_2O are relatively constant across the range of SiO_2 concentrations (Fig. 5.4), particularly for stages II and III of Mt. Kazbek. The Qabarjina Fm. shows a positive trend, whilst Mt. Kazbek Stage IV decreases with increasing SiO_2. Concentrations are similar to those of the Lesser Caucasus. Na_2O forms a positive trend with SiO_2 (Fig. 5.5). The Gudauri Fm. has lower Na_2O concentrations than the other centres (Na_2O = 3.37–3.79 for Gudauri, 3.83–4.83 wt.% for the others). Two parallel trends can be distinguished, a low-Na_2O one involving the Gudauri Fm., Qabarjina Fm. and stage IV volcanics of Mt. Kazbek, and a high-Na_2O one involving the other three stages of Mt. Kazbek. A broadly negative trend is shown between SiO_2 and P_2O_5, although the Gudauri samples form a positive trend with the inflection point ~58 wt.% SiO_2.

5.3.4 Trace-element Geochemistry

Moderately compatible trace elements (Ni, Cr, V) show negative correlations with SiO_2 (Fig. 5.6). The Gudauri formation typically shows the highest concentrations (up to

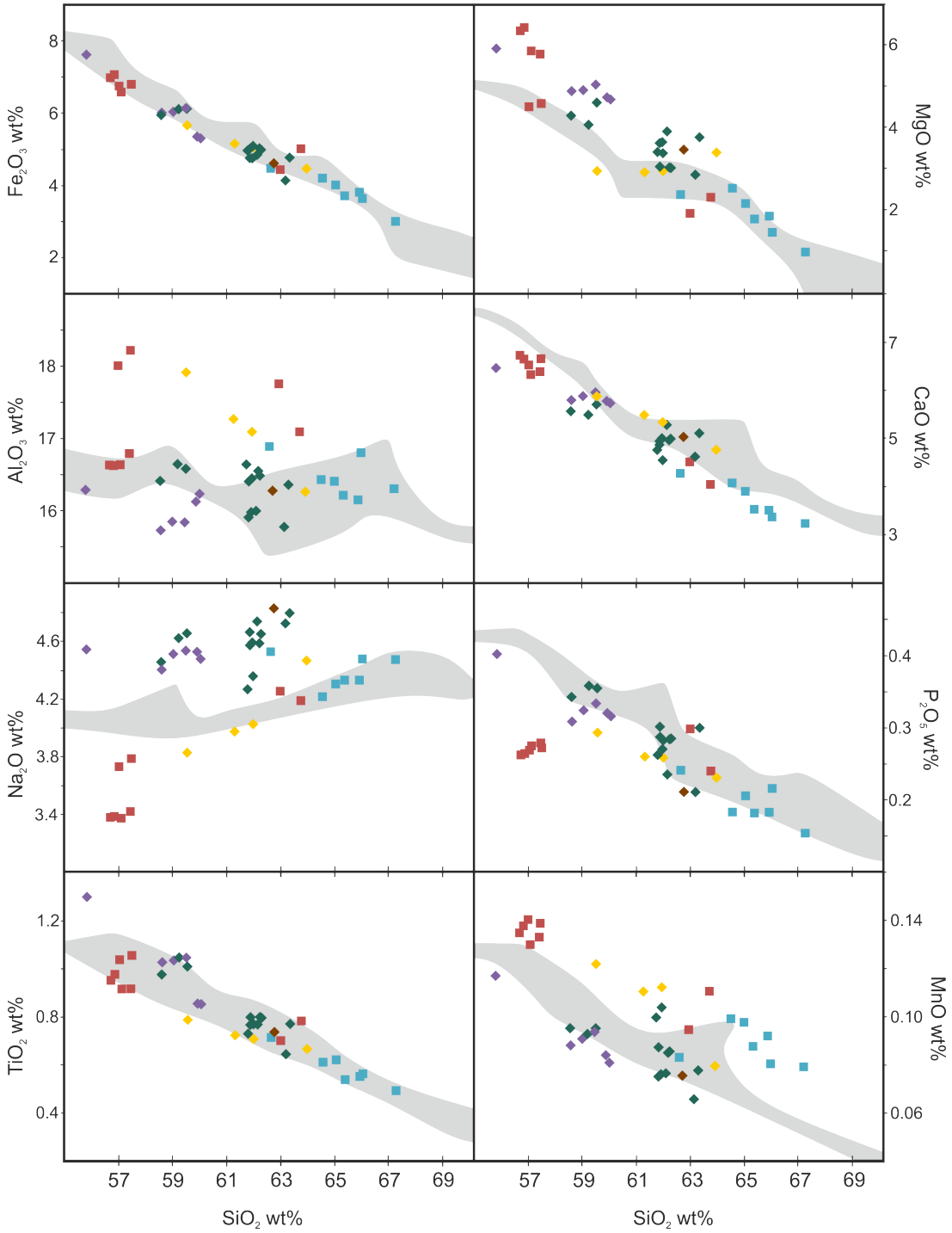

FIGURE 5.5: Major-element variation with SiO_2, as an index of evolution. Symbols used are the same as in Fig. 5.3. Strong correlation seen between most elements, reecting crystallising phases. Grey shaded area represents total extent of compositions from the Georgian Lesser Caucasus (this study). Errors are within the size of data points.

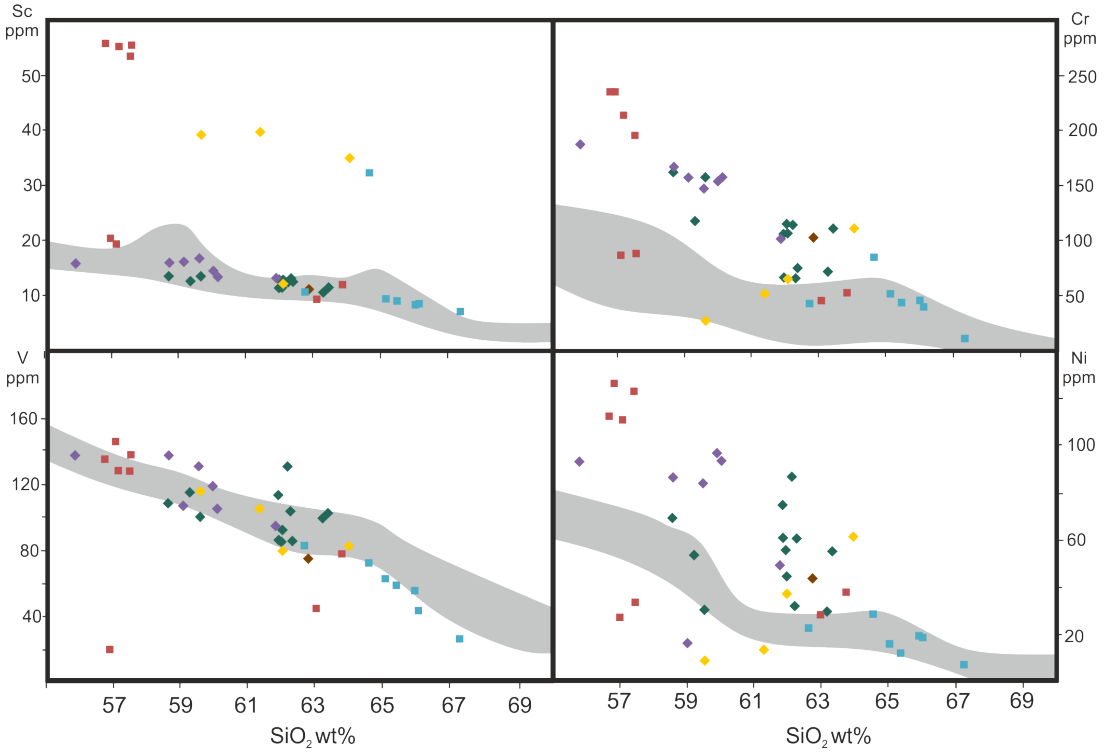

FIGURE 5.6: Minor-element (Sc, V, Ni, Cr) variation with SiO_2, as an index of fractionation. Symbols used are same as in Fig. 5.3. Grey shaded area represents total extent of compositions from the Georgian Lesser Caucasus (this study). Symbol size is larger than 2se error on measurements.

135 ppm Cr), with the Kazbek flows having intermediate values (28–188 ppm Cr), and the Qabarjina formation the lowest (85.4–11.6 ppm Cr). Two samples from the Gudauri formation (H4 and 13-005) and one from Mt. Kazbek (H6), show anomalously low Ni and Cr.

Concentration of trace-elements, and variation with SiO_2 is shown in Figure 5.7. On primitive-mantle normalised variation plots all three centres show similar patterns (Fig. 5.8). All elements show enrichment relative to primitive mantle. Large ion lithophile elements (LILEs) are enriched relative to high field strength elements (HFSEs), with large negative Nb anomalies, although anomalies in Zr-Hf and Ti are less clear. There is a positive Pb anomaly.

Enrichment in LILEs is typically in the order of 55–153 (for Rb and Ba), relative to primitive mantle. The greatest enrichment is seen in the Qabarjina formation, although this may be related to them also being the most fractionated. The largest Pb anomaly is also found in the Qabarjina Fm. The Gudauri formation typically shows a smaller

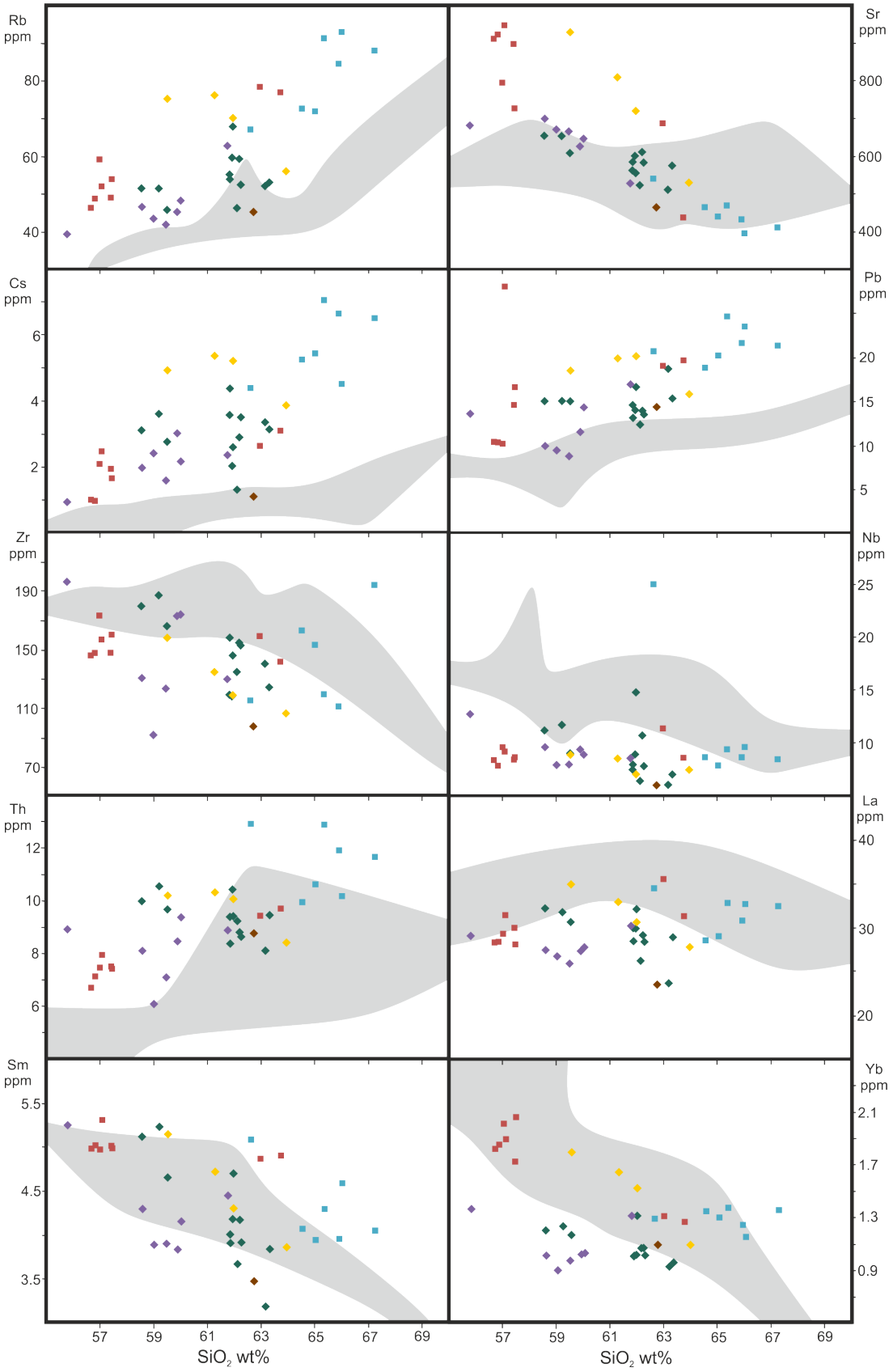

FIGURE 5.7: Trace-element variation with SiO_2, as an index of fractionation. Variation in LILEs demostrated by Rb, Sr, Cs and Pb. HFSEs represented by Zr and Nb. REEs shown by La, Sm and Yb. Symbols used are same as in Fig. 5.3. Grey shaded area represents total extent of compositions from the Georgian Lesser Caucasus (this study). Symbol size is larger than 2se error on measurements.

negative Nb anomaly (Nb/Nb* >0.2) than the Qabarjina (0.135–0.201) and Mt. Kazkek centres (0.135–0.297). The Mt. Kazbek samples show the widest variation in trace element compositions. Stage II tends to have the least enrichment overall, and smallest Pb, Nb and Ti anomalies, whilst Stage IV shows the most enrichment. The Greater Caucasus samples show greater enrichment the contemporaneous Abul-Samsari lavas of the Lesser Caucasus for most elements.

Chondrite-normalised plots of rare earth elements (Fig. 5.9) again show similar patterns between all three centres (Fig. 5.9). All samples lack a significant Eu-anomaly (Eu/Eu* = 0.79–1.03, although most are >0.9). Light REE (LREEs) are enriched relative to heavy REEs (HREEs). Concentrations of LREE show a very limited range, fanning out to a wider range in the HREE. Stage IV of Mt. Kazbek shows the greatest enrichment in LREE (La up to 145 times enriched relative to chondrite). However it also shows significant enrichment in the HREEs, so along with the Gudauri centre shows the flattest slope ($(La/Yb)_N$ = 9.25–13.60). Stage II and III show the steepest slope, and the Qabarjina Fm. plot at intermediate values. The slope of the HREEs was monitored by $(Dy/Yb)_N$. Stage II and III of Mt. Kazbek again show the steepest slope ($(Dy/Yb)_N$ = 1.35–1.65). The Gudauri and Qabarjina Fms., and Stage IV of Mt. Kazbek have virtually flat patterns ($(Dy/Yb)_N$ = 1.23–1.33). $(Dy/Yb)_N$ lacks correlation with modal abundance of cpx and amphibole phenocrysts,trace elements such as Ba, Cr and V, or ratios such as Dy/Dy*.

5.3.5 Isotopic composition

24 samples were analysed for Sr-isotopic composition, 15 for Nd-isotopes, 24 for double spike Pb analyses, and 3 for Hf-isotopes. All volcanic samples are <800 ka (Lebedev et al., 2008c), no age-correction has been done, as the correction would have been smaller than the analytical uncertainty.

Variations in composition are small (Fig. 5.10). $^{87}Sr/^{86}Sr$ and $^{143}Nd/^{144}Nd$ form a negative correlation. The Gudauri and Mt. Kazbek samples have overlapping $^{87}Sr/^{86}Sr$ (0.70415–0.70456). For a given $^{87}Sr/^{86}Sr$, the Gudauri Fm. has lower $^{143}Nd/^{144}Nd$ (Mt. Kazbek: 0.51274–0.51280, εNd = 0.48–3.18, Gudauri Fm: 0.51268–0.51274, εNd = 0.87–1.93). The Qabarjina Fm. plots with more radiogenic Sr and Nd ($^{87}Sr/^{86}Sr$ = 0.70487–0.70495; $^{143}Nd/^{144}Nd$ = 0.512660.51269, εNd = 0.411.02). Within the Mt. Kazbek samples Stage II is more radiogenic than Stage III, whilst Stage IV shows a displacement to lower $^{143}Nd/^{144}Nd$, comparable to that of the Gudarui Fm. The Greater Caucasus samples overlap slightly, but extend to more radiogenic values than the Lesser

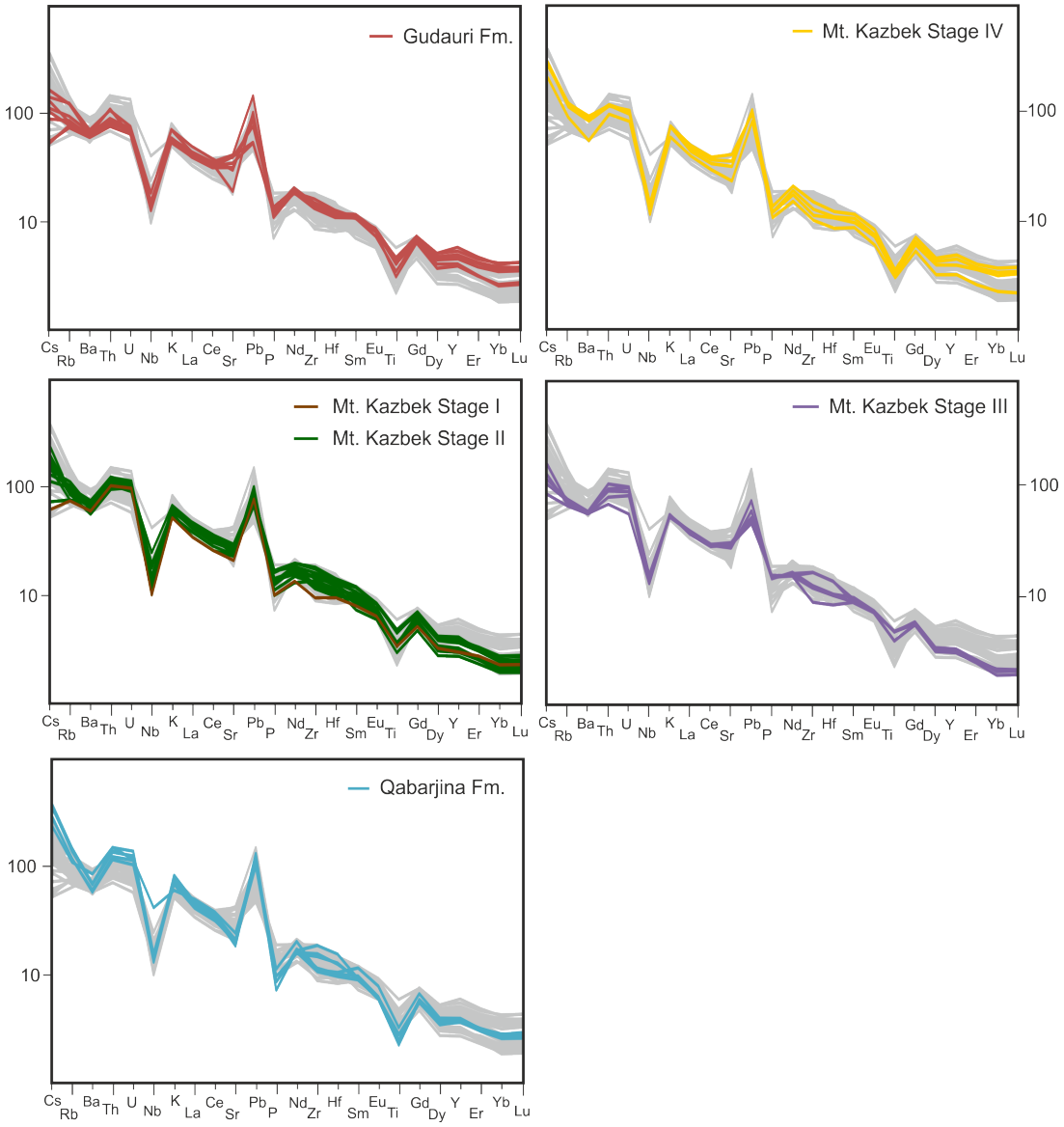

FIGURE 5.8: Multi-element variation diagram, normalised to primitive mantle (Palme and O'Neill, 2014). Pale grey lines represent full range of compositions from the Greater Caucasus as a comparison to the highlighted patterns for each centre.

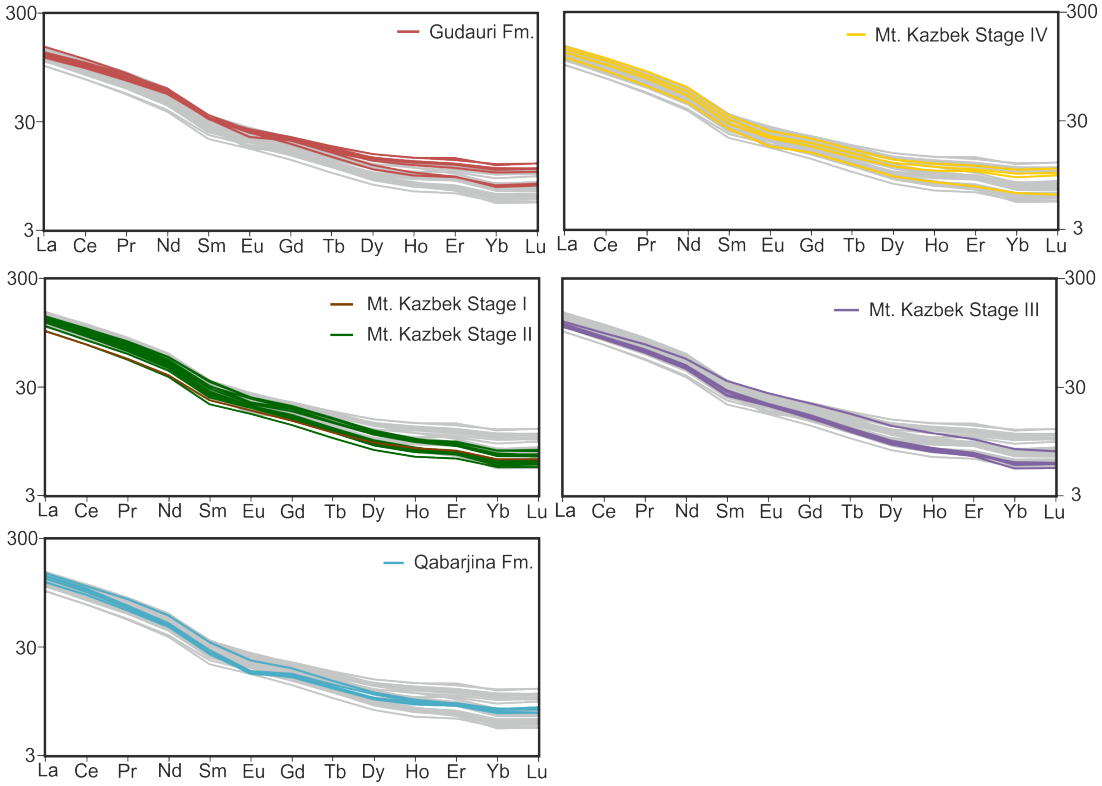

FIGURE 5.9: Rare earth element variation diagram, normalised to CI-chondrite (Palme and O'Neill, 2014). Pale grey lines represent full range of compositions from the Greater Caucasus as a comparison to the highlighted patterns for each centre.

Caucasus.

Pb isotopes also show small variations. Positive trends are formed between $^{206}Pb/^{204}Pb$ and $^{207}Pb/^{204}Pb$ or $^{208}Pb/^{204}Pb$. Similarly to Sr- and Nd-isotopes, the Gudauri Fm. form the least radiogenic part of the trend ($^{206}Pb/^{204}Pb$ = 18.59–18.61), Mt. Kazbek extends to the most radiogenic values ($^{206}Pb/^{204}Pb$ = 18.59–18.67), while the Qabarjina Fm. plots at intermediate values ($^{206}Pb/^{204}Pb$ = 18.59–18.63). $^{207}Pb/^{204}Pb$ has a very restricted composition ($^{207}Pb/^{204}Pb$ = 15.614–15.626), while $^{208}Pb/^{204}Pb$ ranges from 38.65–38.76. The trends run sub-parallel to the northern hemisphere reference line (NHRL: $\Delta 7/4$ = 10.4–11.4; $\Delta 8/4$ = 54.6–58.8). A single sample from the Qabajina Fm. plots off the trend closer to the NHRL ($^{207}Pb/^{204}Pb$ = 15.60 and $^{208}Pb/^{204}Pb$ = 38.62). The Mt. Kazbek samples overlap with the contemporaneous Abul-Samsari rocks in the Lesser Caucasus, whilst extending to lower $^{206}Pb/^{204}Pb$, $^{207}Pb/^{204}Pb$ and $^{208}Pb/^{204}Pb$, and plotting slightly further from the NHRL.

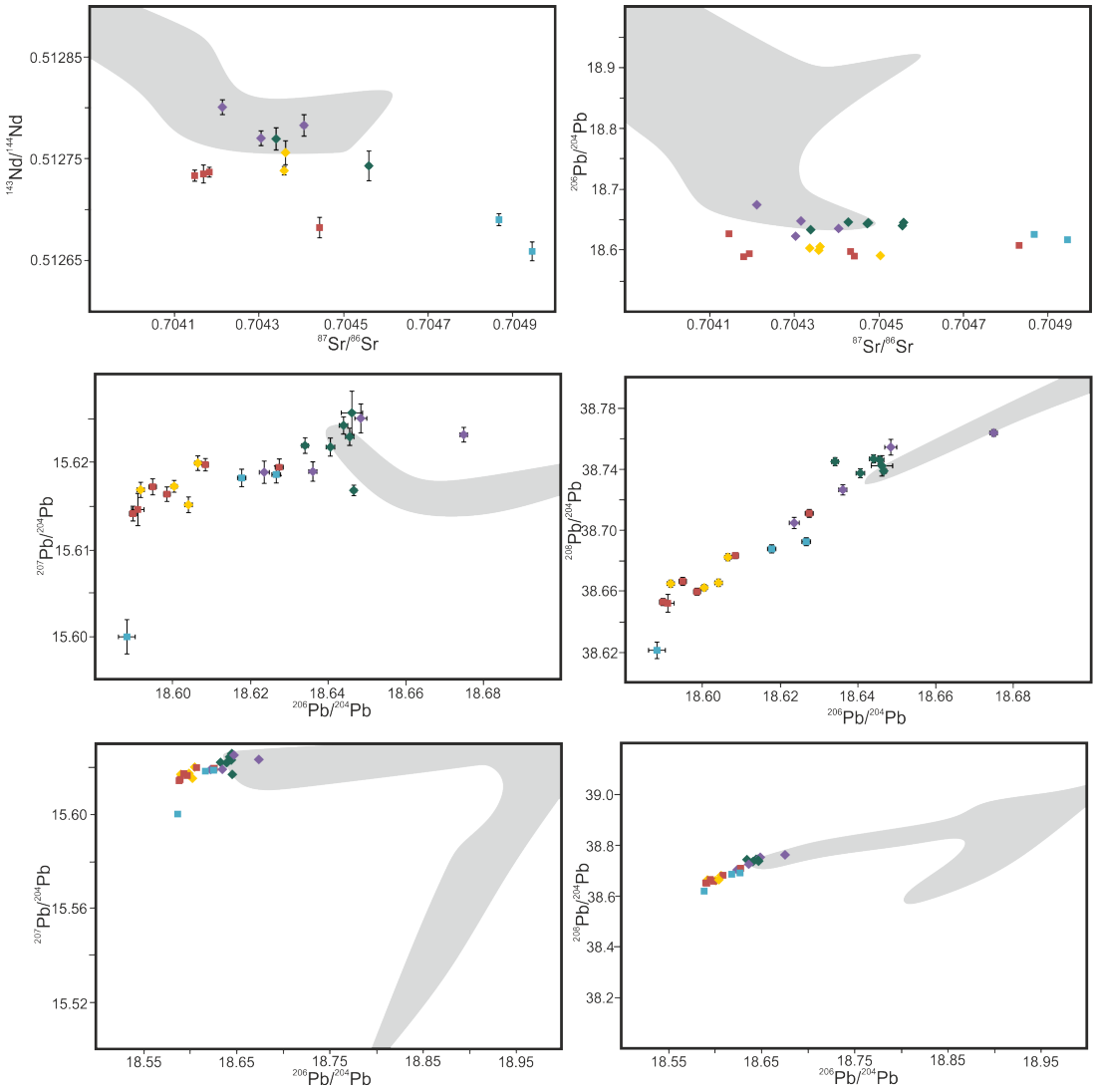

FIGURE 5.10: Isotopic variation in lavas of the greater Caucasus. a) $^{87}Sr/^{86}Sr$ vs $^{144}Nd/^{143}Nd$ plot. b) $^{87}Sr/^{86}Sr$ vs $^{206}Pb/^{204}Pb$ plot. c and e) $^{206}Pb/^{204}Pb$ vs $^{207}Pb/^{204}Pb$ and d and f) $^{206}Pb/^{204}Pb$ vs $^{208}Pb/^{204}$. Data from the Greater Caucasus compared to that of the Lesser Caucasus (grey shaded areas). c) and d) show variation within the greater Caucasus, whilst e) and f) show a comparison with the full Lesser Caucasus data set, as well as demonstrating the very limit range of compositions in the Greater Caucasus. Error bars on data points show 2se. In cases where error bars are not present, 2se is smaller than symbol size. See Appendix B.5 for reproducibility and machine accuracy.

5.4 Mineral Chemistry

5.4.1 Olivine

Olivine is a relatively uncommon phase in the volcanic rocks of the Kazbek region. It is present in the Gudauri flow, and in smaller proportions in volcanics of stage I and III of Mt. Kazbek. It may be found in other stages of the volcanism, and the limited amounts seen is just a sampling bias.

Olivine is typically seen as small (0.3–1 mm), sub-angular grains with little alteration to iddingsite along grain boundaries and cracks. In the Gudauri flow compositions range from Fo_{61}–Fo_{79}. The total range can be seen in a single thin section. Some grains show normal compositional zoning with cores ($Fo_{78–76}$) being more primitive than rims ($Fo_{71–63}$). These olivine compositions are significantly more differentiated than the host bulk rock, with no grains in equilibrium with the bulk rock (Fig. 5.11). This may be due to these olivines crystallising in a more evolved melt, and then mixing with a more mafic melt, producing a more magnesian bulk rock. The slight rounding may be a relic of this mixing.

In the Mt. Kazbek samples, olivine crystals tend to be small (0.1–0.5 mm), subangular to sub-rounded crystals, occasionally showing some resorption features. The range in compositions is more limited than the Gudauri Fm., as well as being more magnesian ($Fo_{82–86}$). Only two olivine grains were found in 13-008, the single example of a Mt. Kazbek stage I flow. One of these was more forsteritic than expected for the bulk rock composition (Fig. 5.11). This grain could suggest olivine removal has occurred, or magma mixing. However the presence of so few olivine crystals, and the evolved nature of the bulk-rock, may point to this just being a xenocryst. Olivine is much more common in stage III of Mt. Kazbek. The majority of these are in equilibrium with the bulk rock ($Fo_{85–83}$, bulk-rock calculated assuming 10% of total iron is ferric iron), extending to more differentiated values (Fig. 5.11). Many olivines are normally zoned, with cores having a very limited compositional range ($Fo_{84.8–85.8}$). The cores in equilibrium with the bulk rock suggest a closed system, whilst the differentiated olivine crystallised in equilibrium with a fractionating melt.

5.4.2 Plagioclase

As is typical in many andesitic and dacitic lavas, plagioclase phenocrysts show a wide variety of compositions, zoning and textures. These textural and compositional variations can preserve details of the magmatic evolution within this complex system due to the

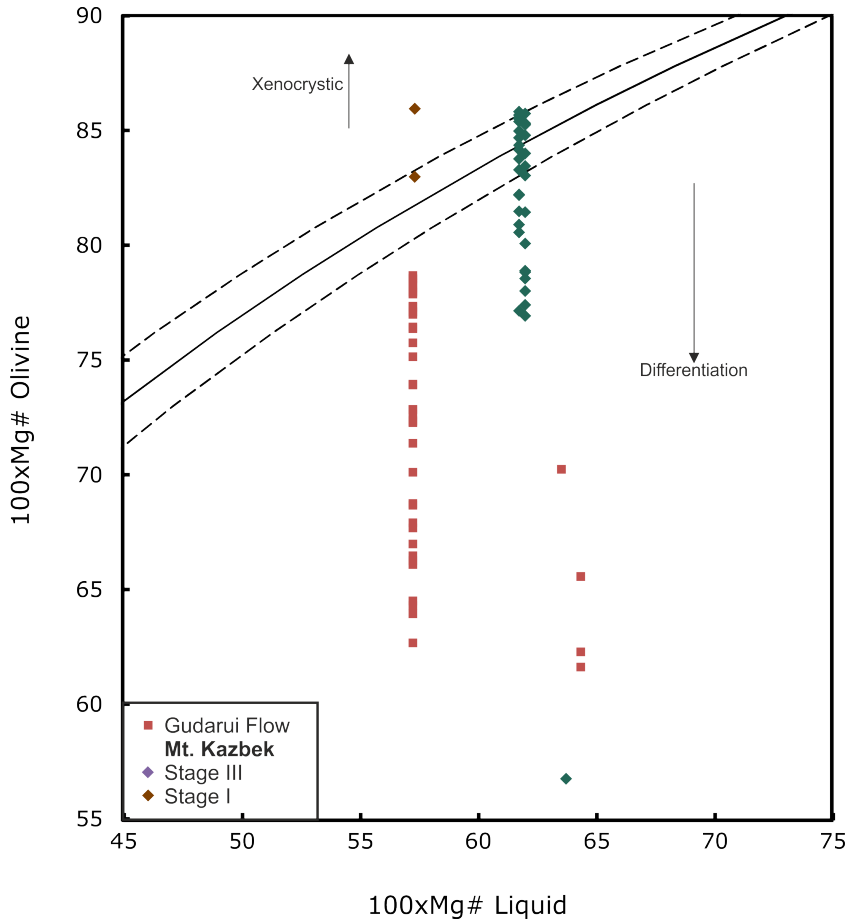

FIGURE 5.11: Rhodes diagram (Rhodes et al., 1979) comparing measured olivine composition with those predicted based on Mg# of bulk rock. Solid curve, with dashed error bounds, represents Fe-Mg exchange coefficient of 0.3±0.03 (Roeder and Emslie, 1970). Analyses which plot in these bounds are considered in equilibrium with the bulk-rock.

very slow diffusion of the major components within plagioclase crystals (Cashman and Blundy, 2013). Textures, and related compositional variation will be covered in detail in section 5.5.4.

The range of compositions of plagioclase is shown in Fig. 5.12. The Qabarjina Fm. assemblage is mostly andesines and labradorites (25–50 % An). Stage I of Mt. Kazbek covers a similar range, but is dominated by andesine end. Stage II also covers the same range as the Qabarjina Fm. Also present in Stage II are some more potassic feldspars, possibly crustal xenocrysts. Stage III has a slightly more disperse range of compositions (20–60 % An). Again a couple of K-felspars are present. Also present in this formation, and absent in any older, are high-K labradorites. At low pressures, and low temperatures

(800–900°C), K_2O in plagioclase with >50% An should be low (see solid isotherms in Fig. 5.12). The grains that plot with high potassium for their given X_{An} contain >1 wt% K_2O. They could represent higher pressure (>5 kbar), higher temperature (>1000°C), or both. Stage IV volcanics show a wide range (25–70% An), overlapping with the compositions of older centres. A greater number of grains in this formation are of the higher potassium variety, with some labradorites containing >2 wt% K_2O. Plagioclase from the Gudauri Fm. tends to be more calcic, containing a significant proportion of bytownite grains. Andesine and labradorite grains are noticeably different from the other formations by the higher K_2O content. Assuming these crystallised at higher temperatures than the Mt. Kazbek and Qabarjina rocks is consistent with the Gudauri host rocks also being the most mafic, so likely hottest. There are also some plagioclase grains with significantly higher K_2O, more similar to that of the high-K plagioclase in Stage III and IV rocks, which may point towards higher pressures as well as temperatures, and potentially a common source, or crystallisation region, that was not present before Stage III. This may also be related to the caldera forming event that occurred between Stage II and III.

5.4.3 Pyroxene

Three varieties of pyroxene are found in these rocks, orthopyroxene, clinopyroxene, and an Al-rich sub-calcic pyroxene (Fig. 5.13). All of these are found in all volcanic centres of Mt. Kazbek region, except the explosive Qabarjina Fm. lacking cpx.

5.4.3.1 Orthopyroxene

Orthopyroxene is the second most common phenocryst phase across the region (behind plagioclase), covering a very wide range of compositions (Mg# = 48–90: Fig. 5.14). The most magnesian grains are found in the Gudauri flows, which are also the most mafic melts. Where zoning is observed, the cores are in equilibrium with the bulk rock (Mg# = 85–88), or in one case, even more magnesian than expected (Fig. 5.14). Compositions extend to Mg# = 64 towards to the rims of grains, which in a similar way to the zoned olivines, reflects the continued growth in an evolving melt.

Stage I of Mt. Kazbek typically shows more evolved compositions (Mg# <70), with some more enstatitic grains in equilibrium with the bulk rock (Fig. 5.14). This could just be a relict of fortuitous mixing, however a similar pattern is also seen with the two olivine grains). The opx compositions are more differentiated than the bulk rock, possibly pointing towards mixing with a more mafic melt and open-system behaviour.

The two samples analysed from Stage II show very different compositions (Fig. 5.14).

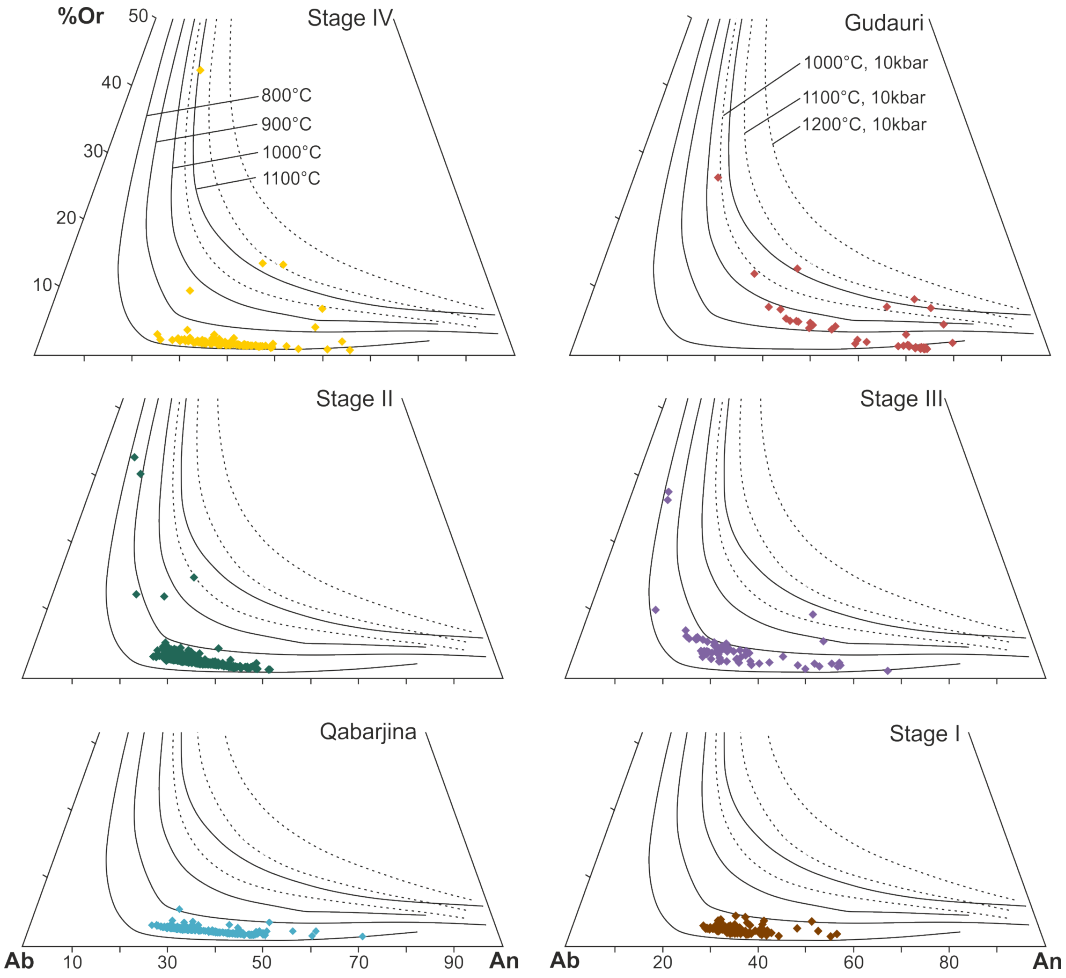

FIGURE 5.12: Composition of plagioclase grains in the different volcanic centres of Greater Caucasus, on An-Ab-Or ternary plots. Isotherms based on calculations from Fuhrman and Lindsley (1988).

13-026 has enstatite-rich opx (Mg# = 84–87), in equilibrium with the bulk rock. 13-059 is much more differentiated opx (Mg# = 65–70). This may suggested heterogeneity within a very short time frame, variations in petrogenesis on a local scale, or be a relict of sampling.

Stage III of Mt. Kazbek is very similar to the Gudauri flow. Cores are magnesian and in equilibrium with bulk rock, whilst rims extend to more differentiated compositions (Fig. 5.14). For the most part, these opx's are the most enstatite-rich from the Mt. Kazbek centre. Being in equilibrium with the host lava, this suggests a second pulse of mafic magma enriching the source beneath the volcano.

Stage IV, apart from a couple of potentially xenocrystic enstatitic grains, contain the

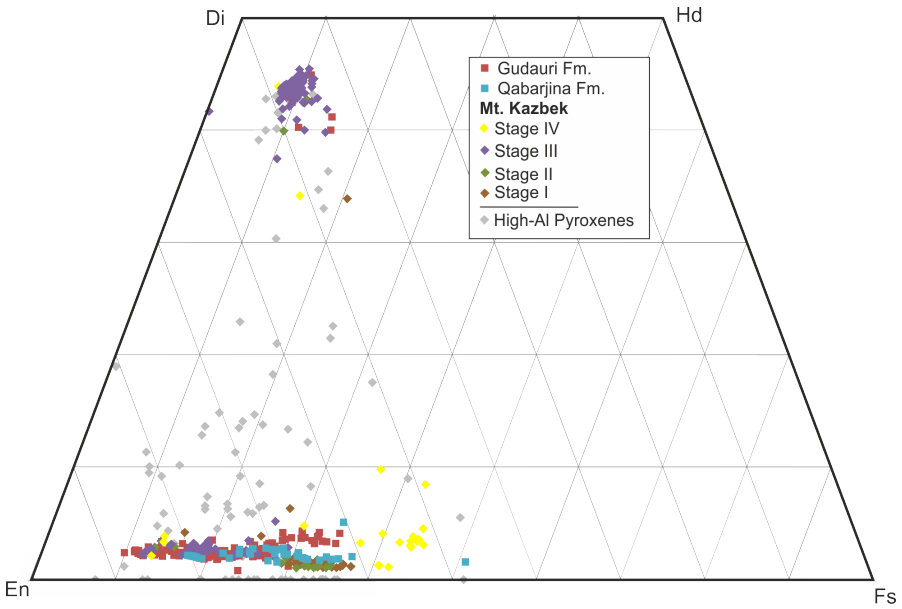

FIGURE 5.13: Composition of pyroxene grains in the different volcanic centres of Greater Caucasus, on the quadrilateral for typical opx-cpx solid solutions. Grey diamonds represent high-Al pyroxenes (see text for details) are contain significant amounts of non-quadrilateral components.

most ferrous opx in the region (Mg# = 53–61). These are significantly more differentiated than the host melt (Fig. 5.14). They also tend to have slightly higher CaO contents (Fig. 5.13), and in some cases noticeable concentrations of alkali metals. The Qabarjina formation contains mostly quite evolved opx compositions (Mg# = 62–72: Fig. 5.14). Some grains show reverse zoning, with rims in equilibrium with the bulk rock (Mg# ~81), pointing towards magma mixing.

5.4.3.2 Clinopyroxene

Clinopyroxene is found in all four stages of Mt. Kazbek's evolution, and also in the Gudauri flow, however is only common in Stage III. The compositions from all centres overlap, forming a rather restricted range ($En_{44–56}$, $Fs_{7–21}$, $Wo_{23–45}$: Fig. 5.13). Grains show very little zoning. The Gudauri Fm. define the low CaO, high FeO end of the array (Fig. 5.13).

5.4.3.3 High-Al Sub-Calcic Pyroxene

The high-Al sub-calcic pyroxene phase has been classified as any pyroxene with over 4 wt% Al_2O_3. This phase is quite abundant in the Kazbek region, particularly in the Gudauri

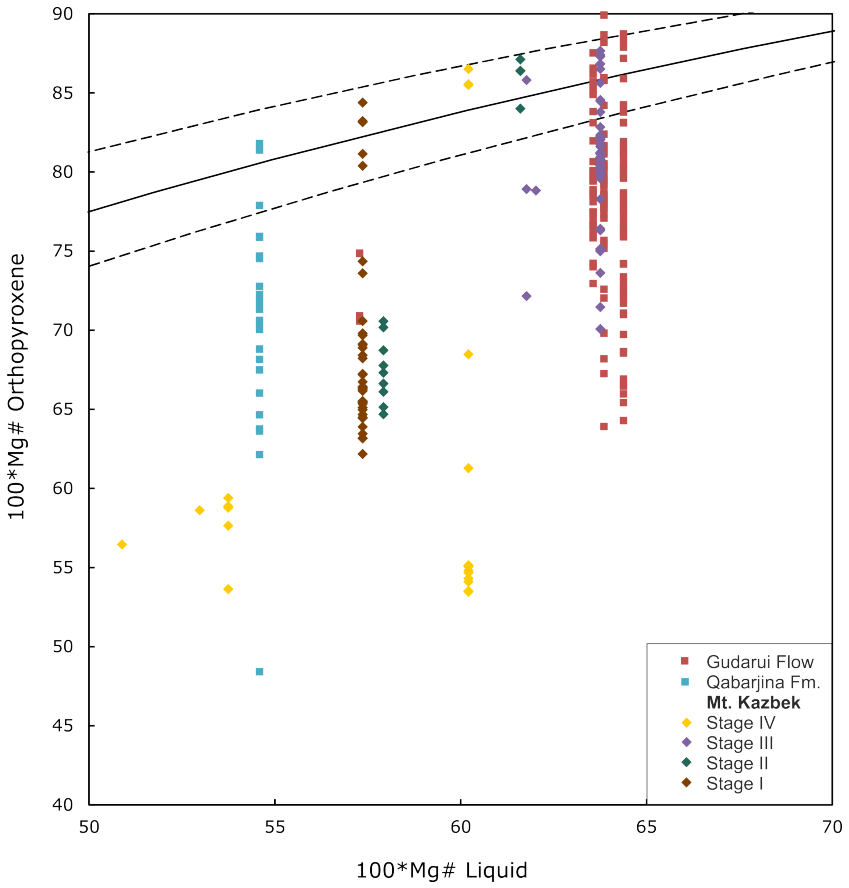

FIGURE 5.14: Rhodes diagram (Rhodes et al., 1979) comparing measured orthopyroxene composition with those predicted based on Mg# of bulk rock. Solid curve, with dashed error bounds, represents Fe-Mg exchange coefficient of 0.29±0.06 (Putirka, 2008). Analyses which plot in these bounds are considered in equilibrium with the bulk-rock

flow. A similar pyroxene was also found in older rocks in the Lesser Caucasus. On Fig. 5.13 these pyroxenes plot between typical fields for opx and cpx. This is due to their composition having significant amounts of Ca residing in non-quadrilateral end-members, rather than the diopside-hedenbergite solid solution. Representative chemical analyses are shown in Table 5.1.

There is a variety of molecules that can host Al. It can be assumed jadeite ($NaAlSi_2O_6$) is present in these pyroxenes, based on the high Na_2O (0.31–3.36 wt%) compared to the opx and cpx. Similarly, these pyroxenes contain much more TiO_2 (0.33–4.50 wt%). In the classification schemes of Cawthorn and Collerson (1974) and Morimoto et al. (1988), Ti is attributed to a Ti-Tschermak molecule ($CaTiAl_2O_6$), whilst more recent studies into high-Al pyroxenes (Pertermann and Hirschmann, 2003; Gerke et al., 2005) have placed

Ti in an alumino-buffonite molecule ($Ca(Mg,Fe)_{0.5}Ti_{0.5})AlSiO_6$). The two schemes also differ in how they deal with Fe^{3+}, which also is related to Al. Fe^{2+}/Fe^{3+} is not measured by EMPA. Gerke et al. (2005) place Fe^{3+} in buffonite ($Ca(Mg,FeFe^{2+})_{0.5}Ti_{0.5}Fe^{3+}SiO_6$), however all of the pyroxenes in this suite of rocks have excess Al for the T-site (assuming a pyroxene formula of $M^1M^2T_2O_6$, Si + Al is always greater than 2, therefore filling the T-site. Buffonite hosts Ti and Fe^{3+} in the T-site along with Si, therefore ruling it out as a constituent molecule in the pyroxenes in this study which require Ti and Fe^{3+} to sit in the M^2 site.) Pertermann and Hirschmann (2002) work with the assumption that all Fe is Fe^{2+}, and if the sum of the cations (when normalised to 6 O's) is less than 4, it is due to the presence of Ca-Eskola molecules ($Ca_{0.5}[]_{0.5}AlSiO_6$). In many of the analyses in this report, when normalised to 6 O's, the sum of cations is above 4 (up to 4.10), suggesting significant amounts of Fe^{3+}. Morimoto et al. (1988) suggest Fe^{3+} can be calculated stoichiometrically, then being placed in essenite ($CaFe^{3+}AlSiO_6$). Ca-Eskola remains as an end-member for compositions with cation totals below 4. The final major host of Al is the Ca-Tschermak component ($CaAl_2SiO_6$).

In this report, the scheme of Pertermann and Hirschmann (2002) has been adapted to calculate end-members. If the sum of cation (S) is less than 4, the mole fraction for Ca-Eskola (Ca-Esk) is calculated using 2·(4-S). If S>4, then Fe^{2+}/Fe^{3+} is calculated using the method of Droop (1987), where the number of Fe^{3+} ions (F) per X oxygens (6 for pyroxene) is caluculated by F = 2X·(1-T/S), where T is the ideal number of cations (4 in the case of pyroxene). All Na is assigned to jadeite (Jd), Fe^{3+} is assigned to essenite (Ess), and Ti is assigned to alumino-buffonite (Al-Bf). All Al not already assigned to Ca-Esk, Jd, Ess and Al-Bf, goes to form Ca-Tschermak molecules (Ca-Ts). The remaining Ca (if any remains), Mg, Mn and Fe^{2+} are assigned to the quadrilateral components, wollastonite (Wo), enstatite (En) and ferrosilate (Fs) respectively. A constant Mg# is assumed when calculating the Al-Bf component, and the En and Fs molecules.

Figure 5.15 shows that three groups of high-Al pyroxene can be identified: low-Al and low-Ca (Group A), low-Al and high-Ca (Group B), and high-Al and medium-Ca (Group C). Typical compositions of these groups is shown in Table 5.1. Group A has 4.0–7.7 wt% Al_2O_3 and <5 wt% CaO, and is mostly found in the Gudauri Fm., with two grains from Stage IV of Mt. Kazbek. Figure 5.16 shows the main host compositions for aluminium in each formation. The major Al-hosts are Ca-Esk (up to 20%), Jd (5–16%, with one grain having 33%), and up to 10% in Ca-Ts. Al-Bf and Ess are a very minor components. All Ca resides in aluminous components, rather than the diopside-hedenbergite solid solution (0% Wo). Most pyroxenes from Stage III of Mt. Kazbek belong to Group B have 5–7 wt% Al_2O_3 and 16–21 wt% CaO. The Ca-Esk component is absent in these samples, with Fe^{3+}

TABLE 5.1: Typical compositions of the three groups of high-Al pyroxene identified in this study. See text for end-member calculations.

	Group A			Group B			Group C				
	H2_16	H3_13c	H5_1c	H3_6b	13-008_8	13-073_35b	13-008_18	13-025_8	13-073_20a	13-012_11	H2_3a
Fm.	Gudauri	Gudauri	Stage IV	Gudauri	Stage I	Stage III	Stage I	Stage II	Stage III	Stage IV	Gudauri
Oxide wt%											
SO_3	0.00	0.00	0.00	0.00	0.01	0.02	0.02	0.04	0.00	0.04	0.00
P_2O_5	0.15	0.04	0.00	0.04	0.05	0.03	0.02	0.05	0.08	0.07	0.03
SiO_2	55.55	51.71	56.32	51.14	47.26	50.60	52.72	42.90	49.64	46.12	43.55
TiO_2	0.18	0.32	0.63	0.71	1.99	0.59	0.56	3.04	1.98	2.26	3.02
Al_2O_3	4.39	5.75	5.61	5.08	6.92	6.56	8.36	9.81	16.08	14.87	16.30
Cr_2O_3	0.05	0.11	0.01	0.26	0.30	0.44	0.02	0.13	0.02	0.01	0.13
MgO	25.54	19.26	16.44	14.55	14.45	16.37	13.11	14.15	6.56	10.27	14.20
CaO	1.62	2.41	1.80	20.19	19.79	20.18	11.61	14.16	9.61	10.12	11.69
MnO	0.34	0.41	0.44	0.27	0.14	0.15	0.27	0.17	0.18	0.31	0.18
FeO	11.51	17.49	15.79	5.26	4.64	4.08	10.90	5.31	12.37	14.76	8.73
Fe_2O_3	0.00	0.00	0.00	2.98	3.18	1.86	0.00	9.51	0.00	0.00	2.07
NiO	0.01	0.02	0.00	0.01	0.03	0.06	0.01	0.02	0.02	0.00	0.05
Na_2O	0.85	0.89	1.82	0.95	0.53	0.39	1.96	1.13	3.66	2.13	1.15
K_2O	0.27	0.03	0.86	0.04	0.00	0.00	0.15	0.02	0.25	0.31	0.09
Cl	0.06	0.00	0.01	0.01	0.00	0.01	0.01	0.00	0.03	0.01	0.02
Total	100.51	98.43	99.75	101.48	99.29	101.33	99.69	100.43	100.49	101.28	101.20
APFU (Based on 6 Os)											
S			0.00	0.00	0.00	0.00	0.00	0.00		0.00	0.00
P	0.01	0.00	0.00	0.00	0.00	0.00	0.00	0.00	0.00	0.00	0.00
Si	1.96	1.92	2.04	1.86	1.76	1.82	1.92	1.60	1.80	1.70	1.58
Ti	0.00	0.01	0.02	0.02	0.06	0.02	0.02	0.09	0.05	0.06	0.08
Al	0.18	0.25	0.24	0.22	0.30	0.28	0.36	0.43	0.69	0.64	0.70
Cr	0.00	0.00	0.00	0.01	0.01	0.01	0.00	0.00	0.00	0.00	0.00
Mg	1.34	1.07	0.89	0.79	0.80	0.88	0.71	0.79	0.36	0.56	0.77
Ca	0.06	0.10	0.07	0.79	0.79	0.78	0.45	0.57	0.37	0.40	0.45
Mn	0.01	0.01	0.01	0.01	0.00	0.00	0.01	0.01	0.01	0.01	0.01
Fe2+	0.34	0.54	0.48	0.16	0.14	0.12	0.33	0.17	0.38	0.45	0.26
Fe3+	0.00	0.00	0.00	0.08	0.09	0.05	0.00	0.27	0.00	0.00	0.06
Ni	0.00	0.00	0.00	0.00	0.00	0.00	0.00	0.00	0.00	0.00	0.00
Na	0.06	0.06	0.13	0.07	0.04	0.03	0.14	0.08	0.26	0.15	0.08
K	0.01	0.00	0.04	0.00	0.00	0.00	0.01	0.00	0.01	0.01	0.00
Cl	0.00		0.00	0.00	0.00	0.00	0.00	0.00	0.00	0.00	0.00
Total	3.97	3.97	3.91	4.00	4.00	4.00	3.95	4.00	3.93	4.00	4.00
End-members											
Ca-Esk	0.05	0.05	0.17				0.10		0.15		
Jd	0.07	0.07	0.16	0.07	0.04	0.03	0.15	0.08	0.28	0.17	0.08
Ess				0.09	0.10	0.06		0.25			0.06
Al-Bf	0.01	0.02	0.03	0.04	0.11	0.03	0.03	0.16	0.11	0.12	0.16
CaTs	0.03	0.06		0.01	0.03	0.08	0.05		0.09	0.17	0.19
Wo				0.34	0.29	0.31	0.15	0.12	0.02	0.05	0.03
En	0.67	0.53	0.42	0.38	0.37	0.43	0.36	0.33	0.17	0.27	0.35
Fs	0.17	0.27	0.22	0.08	0.07	0.06	0.17	0.07	0.18	0.21	0.12

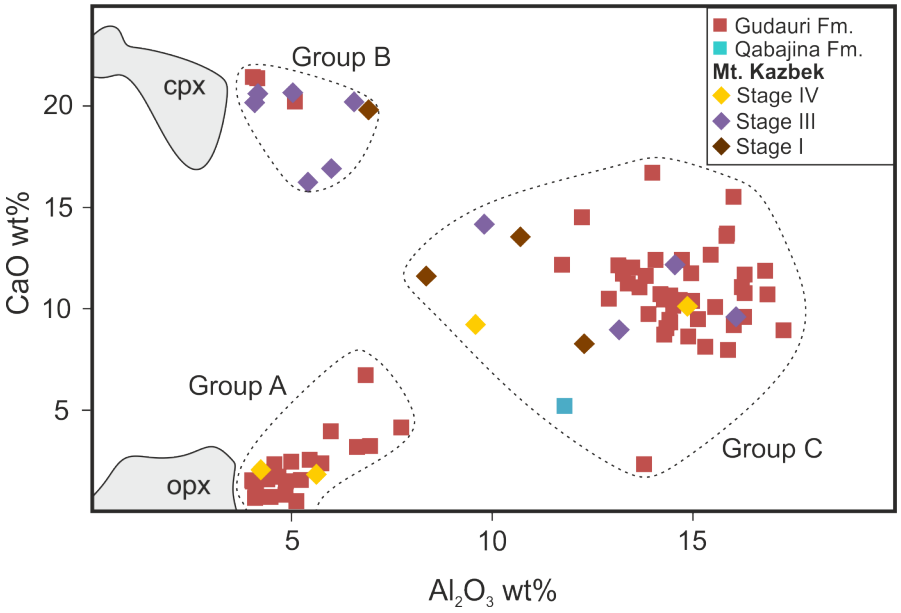

FIGURE 5.15: Three groups of high-Al pyroxene distinguished by their Al_2O_3 and CaO compositions.

always present (5–10 % Ess component). Other aluminous components are relatively minor (<5%). The high-Ca is hosted in the diopside-hedenbergsite solid solution (29–37 % Wo). Group C is the most common group (although this may be sampling bias), containing 10.0–17.5 wt% Al_2O_3 and 8–17 wt% CaO. Some pyroxenes plot between the groups, but have been included in this all inclusive group. All the Gudarui Fm. and Stage IV pyroxenes of this group have no Ca-Esk component, whereas it is a significant host (4–17 %) in Stage I and III Kazbek samples. The Kazbek samples also show a larger Jd component (15–28 %) compared to the Gudauri pyroxenes (<15%). Essenite, Al-Bf and Ca-Ts are the main hosts of Al in the Gudauri Fm. As CaO concentration increases, so does the Wo component. For any given CaO, the Wo component is greater in Stage I Kazbek samples than any other.

5.4.4 Amphibole

Amphibole is a common phenocryst in almost all samples with over 60 wt% SiO_2 (all centres apart from the mafic Gudauri Fm.). They are typically euhedral-subhedral, showing strong brown pleochroism (or green in the freshest crystals). The cores are usually quite fresh, and surrounded by dark reaction rims.

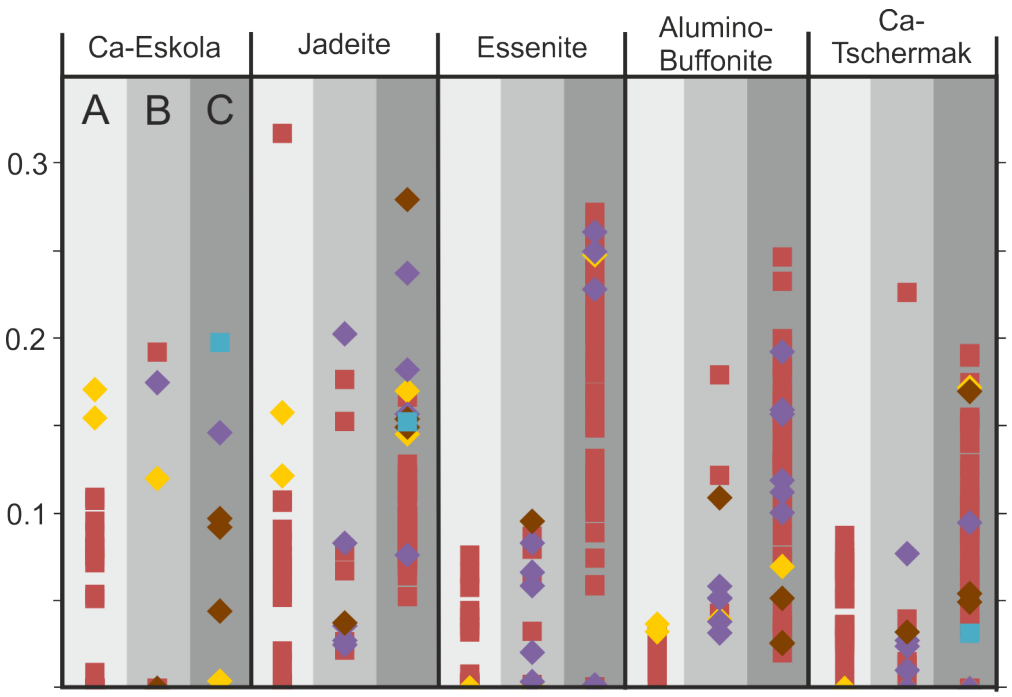

FIGURE 5.16: Composition of the high-Al pyroxenes belonging to group A, B and C. Potential Al-bearing hosts are shown, with the y-axis showing the proportion of each component present in each analysis. See text for details of calculation of end-members. Symbols used are same as Fig. 5.15.

5.4.4.1 Composition

Classification of amphiboles has been carried out using the recalculation and classification scheme of Leake et al. (1997), with the general formula $A_{01}B_2^{VI}C_5^{IV}T_8(OH)_2$ assuming 23 O atoms per formula unit. Fe^{2+}/Fe^{3+} was estimated assuming $\Sigma 13$ cations, except for Mg-Fe-Mn-Li amphiboles where $\Sigma 15$ cations was used (this is only applicable for the cummingtonite grains in these samples). The most common amphiboles belong to the calcic-group (Fig. 5.17).

Stage I of Mt. Kazbek shows two distinct compositions, magnesio-hornblende and pargasite. It is unlikely these are cogenetic, and based on composition may be xenocrystic. Due to the rarity of amphibole in these sample it is difficult to make any further conclusions. Stage II shows a limited range of compositions, mostly being ferri-magnesio-hornblendes (Fe^{3+} >1), suggesting quite oxidising conditions. These are distinguishable from other amphiboles in the region by their relatively low Al contents (<8.5 wt% Al_2O_3). Stage III contains more aluminous tschermakites, and lowish-Al (<13 wt% Al_2O_3) magnesiohastingsites and edenitic hornblendes. Most amphiboles of this age

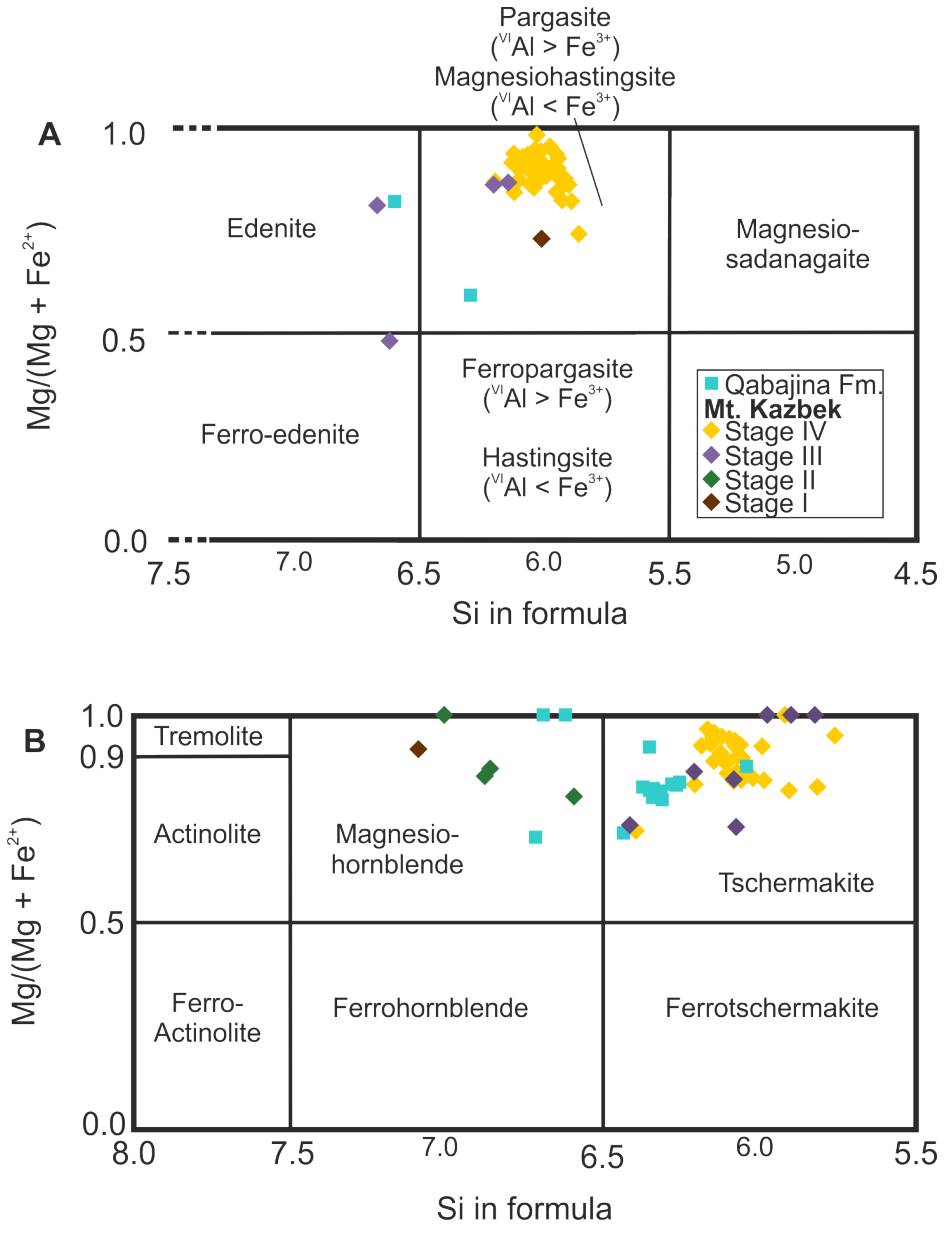

FIGURE 5.17: Range of calcic amphibole compositions from the Greater Caucasus based of classication diagrams from Leake et al. (1997). Diagram parameters are a) ^{B}Ca $\geq$ 1.5; ^{A}(Na + K) $\geq$ 0.5; Ti $<$ 0.5 b) ^{B}Ca $\geq$ 1.5; ^{A}(Na + K) $<$ 0.5; Ca $<$ 0.5 (where the number represents cations pfu, based on O=23).

contain significant amounts of titanium (>2.5 wt% TiO_2). They also have a lower X_{Mg} (Mg/[Mg+Fe^{2+}]) than stage II, as would be expected for an evolving system. However the high X_{Mg} in Stage II may be a result of most iron being found as Fe^{3+}. Some grains show zoning from a hornblende core to a tschermakite rim, with a marked decrease in Mg# (Mg/Mg+Fe^{Tot}100), ^{A}(Na +K) and Si (Fig. 5.18). However positive correlations of ^{T}Al with ^{A}(Na + K) or Ti are not strong, suggesting the zoning may be the result of changing melt composition rather than the temperature and pressure dependent edenite and tschermakite-exchanges Bachmann and Dungan (2002).

Stage IV hosts the widest range of compositions, found in three tight clusters. The (ferrian- titanian-) tschermakites are the most aluminium rich in the region (Al_2O_3 >13 wt%), and have a higher X_{Mg} than Stage III (0.86–0.96), suggesting a more mafic magma. The second group is the (titanian-) magnesio-hastingsite. Their composition reflects the tschermakites in having the highest Al_2O_3 (>12.6 wt%), and being the most magnesian (X_{Mg} >0.84) in the region. Zoning is common in the hastingsites. Mg# increases from core to rim (Fig. 5.18). This change does not correspond to a concurrent change with elements related to variations in P-T, such as Ti, Na and K. Therefore this zoning is likely to reflect changes in magma composition, rather than crystallisation conditions. The rims must have crystallised from a more mafic melt, suggesting at least two pulses of magma formed the magma chamber that these rocks erupted from. Further evidence for this can be seen from the optical zoning within the grain. Figure 5.19D shows a zoned grain, in which the core is rounded, and has clearly been resorbed by the second melt it is in disequilibrium with, whereas the rim maintains a euhedral shape. One sample does show normal zoning (higher Mg# in the core), but this has a tschermakite rim, rather than a hastingsite core and rim like the reverse zoned grains. A pair of neighbouring amphiboles go further than this, and show more that just the simple core-rim relationship seen in other crystals. The cores are high-X_{Mg} tschermakite-hornblendes, gradually zoning to a lower-X_{Mg} magnesio-hastingsite zone, similar to the normally zoned grains (Fig. 5.18). However a third thick rim of high-X_{Mg} (0.84–0.92) magnesio-hastingsite is observed, reflecting the common reverse zoned grains. It is possible that hornblende cores were present in the reverse zoned grains, but have been fully resorbed by the new melt. The grains has a thin rim of Ca-Na amphiboles (richterite-winchite).

The most common compositions in the Qabarjina Fm. range from (ferri- titanian) tschermakite to sub-calcic magnesio-hornblendes. In the few examples where these amphiboles are zoned, core compositions are relatively constant (tschermakitic hornblende: Fig. 5.18), but with very different rim compositions. This needs variable melt conditions and compositions interacting with an initial homogeneous melt (unless the similarity in

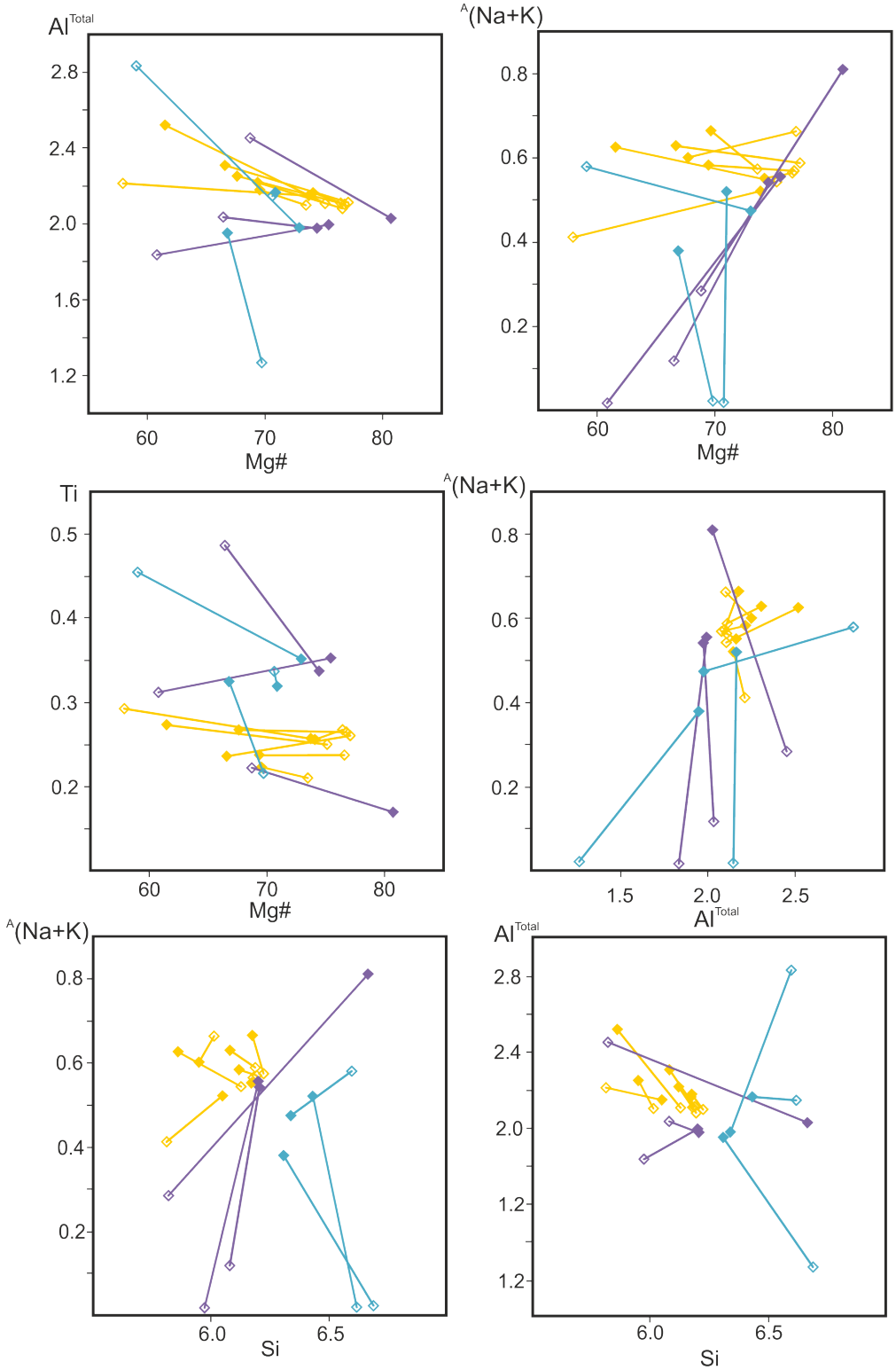

FIGURE 5.18: Core-rim relationships in amphiboles. Pairs are joined with a tie-line between two measurements taken, the core (filled diamond) and rim (open diamond), colours are same as those used in Fig. 5.17. All values are based on cations per formula unit, based on 23 O's, except Mg# which is 100·Mg/(Mg + Fe).

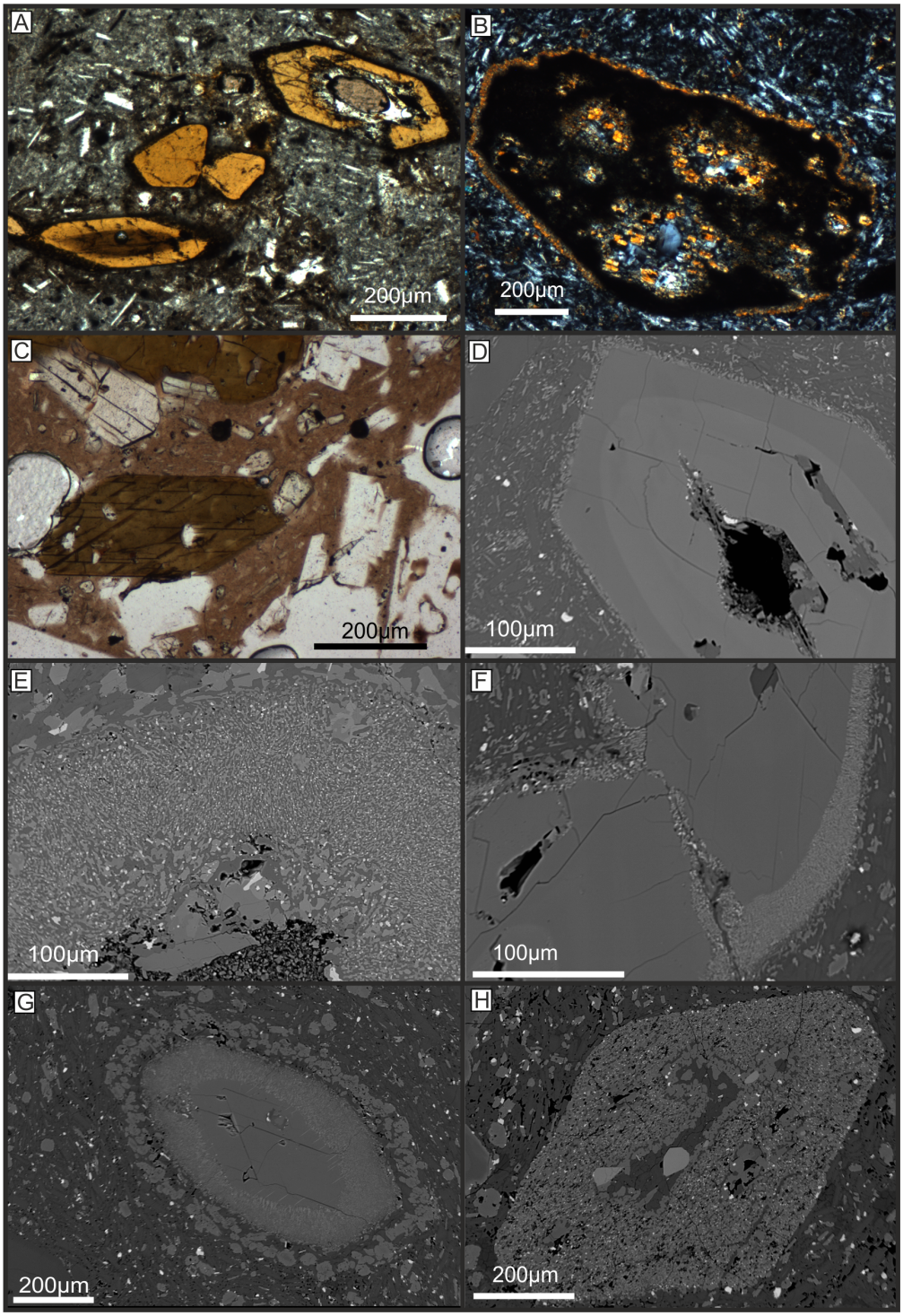

FIGURE 5.19: Variety of reaction texture observed in amphiboles in the Kazbek region. A) Opaque reaction rim on amphibole phenocrysts in ppl. Textures within grains vary from zoned, unzoned, and embayed. Smaller groundmass amphiboles are totally altered to ne opaque material. B) Amphibole phenocryst pseudomorphed by fine pyroxene-oxide aggregate. Coarser pyroxene dominates along rim, and cracks. C) Unrimmed amphibole in 13-059. Brown glassy groundmass, and large vesicles are also visable in ppl. D) BSE image of an amphibole with no significant reaction rim. Thin pyroxene rich rim is present, and pyroxene-oxide aggregate is present in central crack. Core is also clearly rounded. E) Close-up of the symplectite texture, getting coarser towards the rim of the crystal. F) Contrasting habit of the symplectite, in contact with the melt, and the coarse cpx-oxide aggregate cutting across the symplectite and cracks between grains. G) Euhedral amphibole with symplectite rim. Pyroxene exsolution lamelae can be seen in the core of the grain, controlled by cleavage planes. The grain has a corona of pyroxene, possibly as a result of metasomatic processes described by Plechov et al. (2008). H) Euhedral amphibole, pseudomorphed by a cpx-oxide aggregate. The core is plagioclase, rimmed with cpx, with an included apatite crystal.

core composition is just coincidental), and then mixing and erupting as a single melt. Hastingsites are rare, and have low ^{A}(Na + K).

5.4.4.2 Textural Features

A wide variety of textures can be observed both in samples of different age and volcanic centre, and within a single thin section. The vast majority of amphiboles show some sort of reaction or breakdown texture. These textures are typically opaque rims in thin section, or alteration along cracks and between grains (Fig. 5.19). The breakdown comes in three varieties: fine-grained granular opx-cpx-plag-Fe-oxide rims (Fig. 5.19A), pyroxene-amphibole symplectite (Fig. 5.19E-G), and coarse pyroxene-oxide-plagiogclase aggregates (Fig. 5.19B, F and H). These textures can be seen in a single crystal (Fig. 5.19F). The range of textures observed is similar to those seen in other currently active andesitic-dacitic volcanoes, such as Soufriere, Monserrat (Buckley et al., 2006), Mt. St. Helens (Rutherford and Hill, 1993), and Bezymyannyi, Kamchatka (Plechov et al., 2008). Green, near pristine, euhedral to sub-angluar amphibole phenocrysts are rare, but present in flows of Stage II of Mt. Kazbek (Fig. 5.19C). These are particularly associated with sample 13-059, which is different from many other samples by having a very glassy groundmass, no plagioclase microphenocrysts, and being quite vesicular.

Mineralogically the fine-grained aggregates and symplectites are the same, and correspond to the 'gabbroic-type rims of (Garcia and Jacobson, 1979)). This reaction rim only occurs where the crystal is in contact with melt, rather than another crystal. This supports the idea that this is a dehydration reaction during ascent to the surface, involving exchange of elements with the melt (Rutherford and Hill, 1993; Buckley et al., 2006; Plechov et al., 2008). This idea is consistent with the unrimmed amphiboles in sample 13-059, where the glassy matrix and vesicular nature shows the melt kept its volatiles until very soon before eruption, and this exchange did not have time to occur. In some samples it can be seen that the fine-grained aggregate occurs on the melt side on the symplectite, reflecting the increased time contact with the melt to dehydrate and crystallise.

The reaction can be generalised by equation 5.1. It has been debated whether this is reaction with the melt (Rutherford and Hill, 1993), a bimetasomatic exchange with the melt (Plechov et al., 2008) or a near-isochemical reaction (Buckley et al., 2006). It seems likely that some exchange with the melt is necessary to supply SiO_2 to the amphibole, and volatiles will be released into the melt, but without detailed investigation it is difficult to say exactly what is going on in these samples.

$$AmphCpx + Opx + Plag + Fe - TiOxide \tag{5.1}$$

The symplectite texture is only present in samples from Stage III of Mt. Kazbek, suggesting their formation is unique to the eruption conditions of this age. This seems to be an uncommon texture in amphibole breakdown, with the only other examples found in andesites from Mt. Bezymyannyi (Plechov et al., 2008). The width of the rim is consistent within the grain (Fig. 5.19G), and a function of eruption rate (Rutherford and Hill, 1993). They can be up to 100μm wide, significantly thicker than the more common granular version of the breakdown (5–40 μm; Rutherford and Hill, 1993; Murphey et al., 2000). The symplectite texture suggests a very rapid ascent, not allowing time for crystals to form. Individual interlacing strands in the symplectite are rarely wider than 1–2 μm wide, often showing a coarsening away from the center of the grain (Fig. 5.19E). Outside of the symplectite, the granular product of this alteration is sometimes seen, usually as a rim no wider than 10 μm. As this has the greatest interaction with the melt it is no surprise the reaction has the longest to occur here. Most of the oxides are concentrated in this rim, rather than the symplectite. The amount of oxide decreases rimwards, as does plagioclase, leaving a pyroxene rim at the very outside of the rim (Fig. 5.19G), following the same sequence as observed in amphiboles of Mt. Bezmyannyi (Plechov et al., 2008). The contact with the melt is sharp, and maintains the euhedral shape of the grain (Fig. 5.19G). This is in agreement with (Rutherford and Hill, 1993) who observed that this breakdown reaction occurs at the grain surface and proceeds inwards. The boundary with the unaltered core of the grain is also very sharp, but rounded or very irregular, not following any crystallographic boundaries (Fig. 5.19F-G). Another common feature in the inside boundary are exsolution lamelae of pyroxene (Fig. 5.19G). These are most common when looking down the c-axis, and are controlled by the cleavage planes.

The second type of breakdown is not constrained to areas when the grain is in contact with the melt. It can cut across the symplectite rim, fill voids and cracks in the grain, form at the contact with a second grain (Fig. 5.19F), or in extreme cases pseudomorph the whole amphibole (Fig. 5.19H). It is much coarser than the 'gabbroic-type. The reaction product is dominated by cpx, with major oxides and minor plagioclase. The pyroxene is in optical continuity with the amphibole. This reaction is the result of thermal decomposition of amphibole, rather than decompression (Buckley et al., 2006). Influx of hotter mafic melts could cause this type of decomposition. Some samples show this texture rimmed by the 'gabbroic-type, meaning it occurred deeper than the decompression rim.

5.4.4.3 Geothermobarometry

Due to the wide range of compositions observed in calcic amphiboles, they have been assumed to be good at recording magmatic temperatures and pressures (Putirka, 2016). Regarding pressure, Al-in-hornblende barometers have received the most attention (e.g. Hammarstrom and Zen, 1986; Johnson and Rutherford, 1989; Schmidt, 1992; Ridolfi et al., 2010; Ridolfi and Renzulli, 2012). The Ridolfi et al. (2010) and Ridolfi and Renzulli (2012) models produces lower pressures than those of the older models. Despite consistency of pressures resulting from the older barometers, the more recent models will be used in this discussion as they were calibrated for volcanic systems, rather than granitic systems (e.g. Hammarstrom and Zen, 1986). The barometer from Ridolfi and Renzulli (2012) has been used to calculate pressures due to the relatively low errors associated with it over the range of pressures associated with these amphiboles. Throughout the region pressures range from 0.8–7.2 kbar (2.5–25 km: Fig. 5.20). Amphiboles from Mt. Kazbek produce higher pressures the younger they are. Stage II has the lowest pressures (<1.5 kbar), stage III are at intermediate depths (2.8–3.5 kbar), whilst the youngest stage IV has minimum pressures of 3.5 kbar and extend to the 7.2 kbar. The Qabarjina Fm. overlaps with Stage III. The large pressure difference between Stage II and IV suggests a different, deeper source for the younger volcanics. However the reliability of Al-in-hornblende barometers has recently been brought into question (Erdmann et al., 2014; Putirka, 2016). The barometers are potentially temperature dependent (Blundy and Holland, 1990), and may reflect changes in melt composition and mixing rather than variations in depth of crystallisation (Erdmann et al., 2014). With this in mind, along with analytical uncertainties from EMPA measurements, and systematic errors in the barometer calibrations, these pressures should be taken with a pinch of salt. Without solid constraints on the melt composition that the amphiboles crystallised from (due to lack of fluid/melt inclusions, and evidence of disequilibrium and magma mixing making bulk-rock compositions very different from original melt), amphibole-liquid barometers (e.g. Putirka, 2016) cannot be used to verify the Al-in-hornblende results. However it can be assumed that crystallisation was crustal (crust is >55 km beneath Mt. Kazbek), and there is certainly a significant difference between crystallisation conditions between Stage II and Stage IV of Mt. Kazbek's volcanism.

Geothermometry in amphiboles is far more reliable Putirka (2016). The thermometer from Ridolfi et al. (2010) was used. Similarly to the pressure calculations, a pattern can be seen with age in the Mt. Kazbek samples (Fig. 5.20). Stage II has by far the coolest crystallising temperatures (790–871°C). Stage III produced a narrow range of hotter

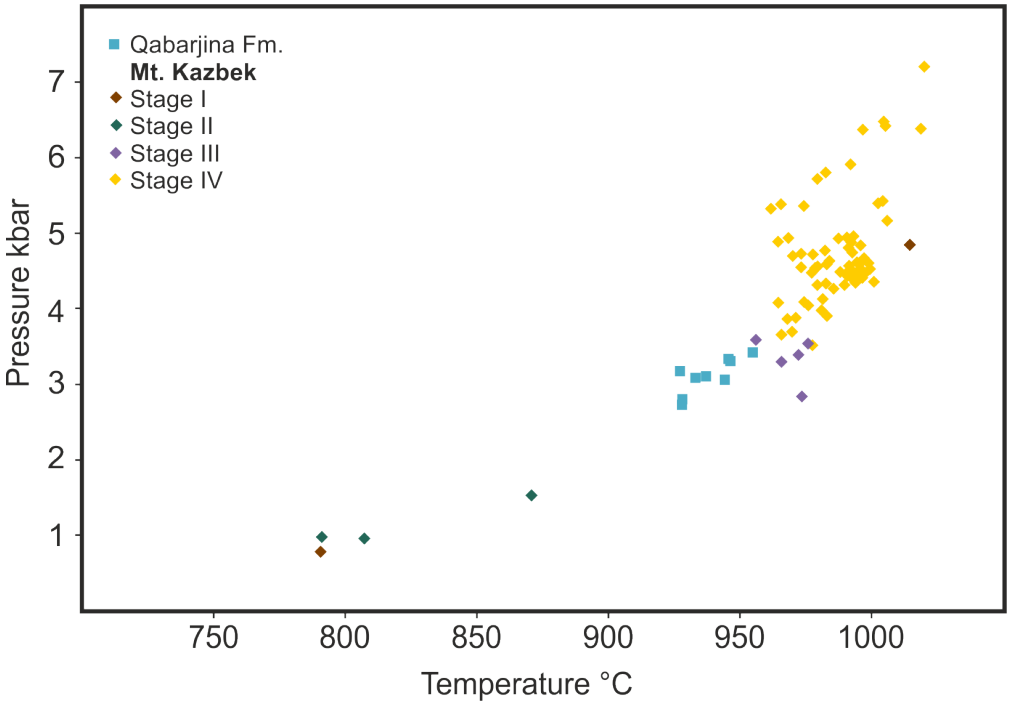

FIGURE 5.20: Estimate pressure and temperatures based on amphibole mineral chemistry. Estimates measured using equations from Ridolfi et al. (2010).

temperatures (956–976°C), while Stage IV extended to the warmest temperatures in the region (962–1020°C). The Qabajina Fm. again plots close to the Stage III volcanincs (927–956°C), although at slightly cooler temperatures. These temperatures add some strength to the pressure data, assuming a relatively normal P-T gradient in the region. Therefore variations in the Al concentration may be related to pressure, rather than just melt composition.

5.4.5 Minor and Accessory Phases

Along with the major phenocryst phases, mica, oxides, apatite, quartz and potassium feldspar all occur as rare phenocrysts or microphenocrysts, usually making up less than 1% of the phenocryst assemblage.

5.4.5.1 Mica

Biotite is a relatively common phase in the rocks of Stage IV, with a few grains present in most thin sections (although relatively insignificant, $< 5\%$, modally). It is not seen in any other age, or formation.

Biotite occurs as strongly-pleochroic red-brown grains, up to 1 mm across. Compositionally the micas are phlogopites. They have relatively low Mg/(Mg+FeO$^{T}otal$), reflecting the acidic nature of the host rocks. They are also similar to coexisting amphiboles by having high Ti and Al (this is likely due to tschermaks substitution, which may also decrease the Mg/(Mg+FeO$^{T}otal$) by increasing Fe^{3+}). Texturally biotites are also similar to the amphiboles, showing opaque reaction rims. Under the back-scattered electron light, alteration can be seen occurring as a rim, and along parallel cleavage planes, and occasionally pseudomoprphing the grain (Fig. 5.2).

5.4.5.2 Oxides

Under reflected light, only a single opaque phase is identifiable, which is a Fe-Ti oxide. EMPA analyses show this is ilmenite, and is ubiquitous across the region. Fe-rich spinel has also been identified, but is very rare, often incorporating >5 wt% TiO_2. Quartz is present in Stage IV volcanics only, reflecting the acidic bulk-rock composition, and is probably not xenocrystic. Zircon is not observed in thin section, but after ICP-MS analyses Zr and Hf gave very low totals (much lower than analyses on the same rock by XRF), suggesting zircon is present and was not dissolving. This is only seen in Stage IV and the Qabarjina Fm., the most evolved compositions. Apatite also occurs in all rocks, in small amounts.

5.5 Discussion

The volcanic products of Mt. Kazbek, since the oldest eruptions 800 ka ago, have almost entirely been andesite to dacitic lavas. The following discussion explores whether these are the most primitive compositions produced, the products of fractionation from a more mafic parent or crustal melts. The role contamination from crustal material played in affecting the chemistry will be considered, before attempting to unravel the source region, mineralogy and composition, and how melting produced the lavas we see at the surface today. To produce a comprehensive story, based on temporal and spatial differences, variations between the different centres and ages will be predominantly considered, rather than variation within a single centre or time period.

5.5.1 Fractional Crystallisation

No lava collected from the Mt. Kazbek region represents a primary magma from a peridotitic mantle source. The most primitive compositions (from the Gudauri Fm.) are

SiO_2 rich basaltic-andesites, with Mg# ~64. All other centres have MgO <5 wt%. It can therefore be assumed that all lavas from the Greater Caucasus have previously undergone significant fractionation of olivine and spinel, or are derived from a non-peridotitic source.

Overall, strong negative correlations are seen between CaO, $Fe_2O_3^T$, MgO, MnO and TiO_2 with SiO_2. This can be explained by fractionation of the observed mineral assemblage (olivine, opx, cpx, Fe-Ti oxide). Al_2O_3 concentrations are restricted to a limited range, with no trends, apart from in Stage IV of Mt. Kazbek, where a strong negative correlation is seen (as well as a corresponding trend in Sr), which is missing from the other groups. It therefore seems plagioclase fractionation only plays an important role in these youngest volcanics. However Na_2O acts incompatibly for all groups, especially Stage IV. Plagioclase crystals from Stage IV are not particularly Ca-rich, so cannot explain this. K_2O shows very little variation, except for an inflection to act compatibly in Stage IV at ~62 wt% SiO_2, and acting incompatible in the Qabarjina Fm. All samples lack a significant Eu-anomaly ($Eu/Eu^* > 0.9$), again suggesting a limited role for plagiocalse. Amphiboles from Stage IV are typically the most potassic, so this phase coming onto the solidus could explain this inflection, and similar infections seen with Rb and Ba. P_2O_5 acts compatibly due to apatite crystallising except in the Gudauri Fm. (<58 wt% SiO_2), before it reaches saturation.

Complex zoning in plagioclase and amphiboles suggest multiple pulses of magmatism, making it unlikely that trends on the Harker plots (Fig. 5.5) are representative of liquid lines of descent. The majority of trends are very linear, which may imply mixing rather than crystallisation where inflections would be expected, especially for $Fe_2O_3^T$ and TiO_2, when oxides joined the solidus. In fact these show the two strongest linear correlations with SiO_2. Trends within a group are more likely to be representative of liquid lines of descent, and the lack of inflections due to the limited range of SiO_2 these rather restricted groups cover. The Qabarjina Fm. shows good linear trends, as does Stage IV (and inflections), however the other groups do not.

Trace elements may be useful in determining fractionation trends. Figure 5.21 uses MREEs to decipher fractionating trends involving cpx and amphibole. Both cpx and amphibole preferentially host MREEs significantly over LREEs, and to a lesser extent over HREEs (Davidson et al., 2007), producing concave down REE profiles (Dy/Dy^* <1; Davidson et al., 2013). Fractionation of both cpx and amphibole have a similar effect, but as $Kd_{REE}^{amph} > Kd_{REE}^{cpx}$ (Davidson et al., 2007), amphibole is likely to be the dominant cause of variation in hydrous rocks. Figures 5.21A and B show Dy/Yb and Dy/Dy^* decreasing during fractionation for Stage II and III of Mt. Kazbek and the Qabarjina Fm. This suggests that for these rocks variation is not due to source variation,

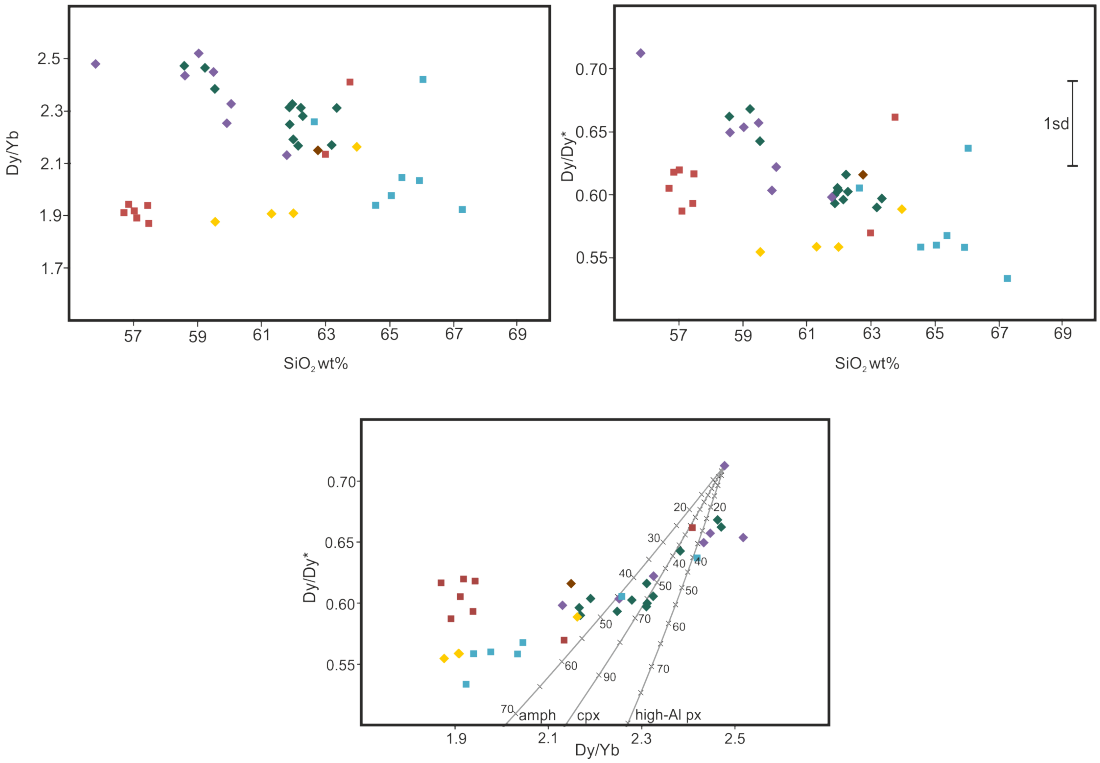

FIGURE 5.21: Top two graphs show variation of Dy/Yb and Dy/Dy* with SiO_2 (i.e. with fractionation). Decreasing trends are present in Stage II and III, and the Qabarjina Fm., but not in Stage IV and the Gudauri ows. Bottom plot shows variation of Dy/Yb with Dy/Dy*. Fractional crystallisation curves are shown for amphibole, cpx and high-Al Px, using 13-056 as the least fractionated sample as a starting composition. Numbers represent percentage of fractionation, with tic marks every 5%. Distribution coefficients used are from McKenzie and O'Nions (1991) for cpx (Kd: La = 0.54, Dy = 0.33, Yb = 0.28) and amphibole (Kd: La = 0.17, Dy = 0.78, Yb = 0.59), and Lofgren et al. (2006) for the high-Al pyroxene (Kd: La = 0.2124, Dy = 0.7986, Yb = 0.7444. Symbols used are same as Fig. 5.3.

and related to petrogenesis of each suite.

If each formation is treated as a separate group, it can be generalised that the Gudauri Fm. has undergone the least fractionation, whilst the Qabarjina Fm. has undergone the most. Stage III of Mt. Kazbek has undergone less fractionation than Stage II, whilst Stage IV has undergone similar amounts to Stages II and III. The single sample from Stage I makes it difficult to interpret. The Stage I andesite collected on the southern flank of Mt. Kazbek is very different from the trachy-basalt samples of Stage I collected from the northern flanks in Russia (Lebedev and Vashakidze, 2014), making the picture of this early formation even less clear. The Gudauri Fm., Stage II and Stage III show the poorer correlations on major element diagrams against SiO_2 diagrams than the Qabarjina

Fm. and Stage IV (Fig. 5.5). It can be assumed that fractional crystallisation played a more important role in controlling the chemistry of the Qabarjina Fm. and Stage IV than the other formations, where other processes have overprinted the fractionating trends.

If the formations are treated as a cogenetic suite, then a single, simple liquid line of decent can be ruled out as age and degree of fractionation do not correlate. Other processes, such as magma mixing and crustal contamination, must have occurred between each discreet phase crystallised.

5.5.2 Crustal Contamination

The lavas in this region lie on >60 km of crust. It seems unlikely that they could have passed through this without any interaction. Crustal xenoliths are rare, but were present in a flow from Stage II. This xenolith looked very similar to local Hercynian granite exposed <20 km away. Crustal contamination has been suggested to play a role in the Lesser Caucasus (Section 4.4.3; Keskin et al., 1998; Neill et al., 2015) and Mt. Elbrus (Lebedev et al., 2010a; Chugaev et al., 2013). Sr-Nd-Pb-isotope ratios trend towards crustal values, albeit the range of values is very limited. Even the least radiogenic volcanic samples (the Gudauri Fm. samples) have isotope ratios far more radiogenic than MORB-style mantle melts, suggesting a source that must have undergone enrichment with a radiogenic end-member, such as Palaeozoic crust. Correlation between isotope ratios and SiO_2 are not clear (Fig. 5.22), potentially suggesting only a limited role of assimiliation of crust during fractional crystallisation. In the case of the more mafic crust (diorites, schists, amphibolites, rather than granites) the SiO_2 content of the crust and the magma are very similar, so trends on these plots may not be expected to be clear. Figure 5.23 instead uses Sr as an indicator of fractionation. Whilst crystallisation should not affect the $^{87}Sr/^{86}Sr$ ratio, a marked decrease in Sr would be observed (based on Fig. 5.7, particularly if plagioclase is crystallising).

Figure 5.23 shows models for AFC based of the least evolved and contaminated sample (H2: high Sr, low $^{87}Sr/^{86}Sr$) as a starting composition, with assimilating granitic material, similar to the xenolith observed (very similar trends are observed with migmatites, which have similar SiO_2 to the magmas). This starting composition is not meant to represent the actual starting composition of the parent melt, but rather just as a guide to the minimum amount of assimilation and fractionation needed to produce the range of compositions observed in the Greater Caucasus. Models have been plotted with different assimilation/crystallisation rates (r = 0, 0.1, 0.25, 0.5, 0.75) and bulk mixing.

The Gudauri Fm. plots in two clusters, one that requires very little crust, and

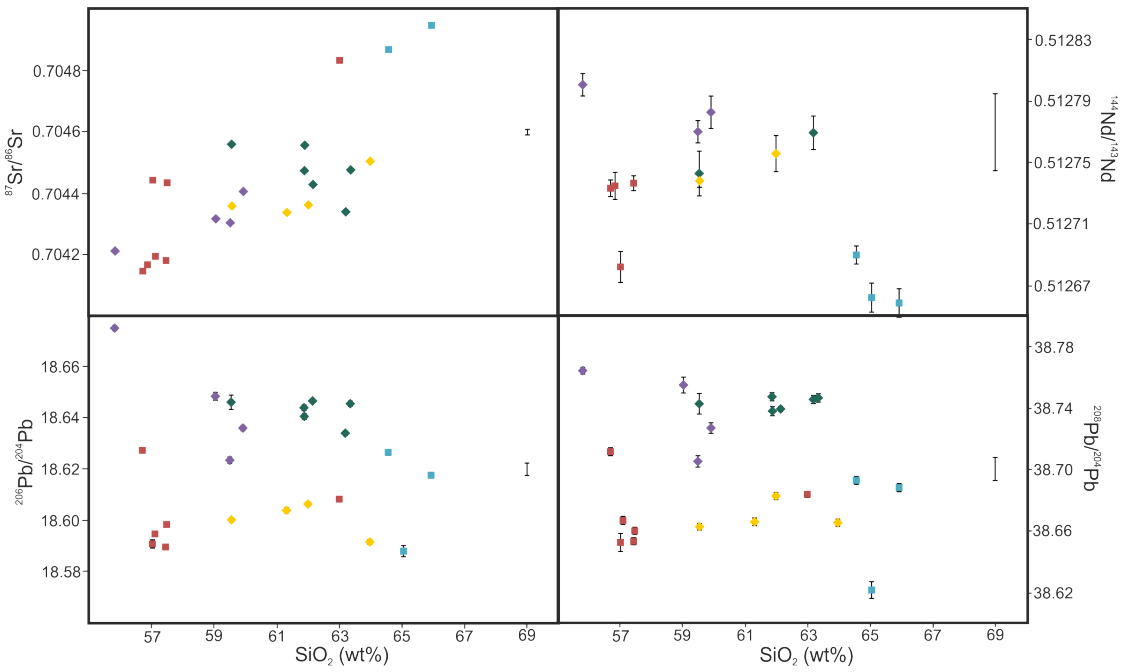

FIGURE 5.22: Various isotopic ratios plotted against SiO_2. Fractionation should not alter isotopic ratios, therefore variation of these plots can be due to AFC or mixing. Symbols used are the same as Fig. 5.3.

one which requires AFC with a high assimilation/crystallisation rate. It is seen with SiO_2 that is a more fractionated group as well, and this possibly resided in the crust longer. Stage IV of Mt. Kazbek also shows high Sr concentrations, but also slightly more radiogenic $^{87}Sr/^{86}Sr$. Stages II seems to require more crust than Stage III, suggesting the assimilation is not just increasing with time as a result of crustal storage. The Qabarjina Fm. is both the most evolved and the most contaminated. In Pb-isotope space, the Gudauri Fm. is the least radiogenic. This suggests contamination is with a more radiogenic contaminant, likely to be the local granite. This is in contrast with the Lesser Caucasus volcanics that share a similar Pb-isotope composition, but have been contaminated with less radiogenic Palaeozoic mafic material.

5.5.3 Role of Magma Mixing

There is some of evidence to suggest magma mixing played an important roles in the formation of these magmas. Petrographically, complexly zoned plagioclase, amphibole and pyroxene show evidence for mixing with more mafic melts. Disequilibrium features, such as embayed pyroxenes, reaction rims, sieved plagioclase and rounding of grains are

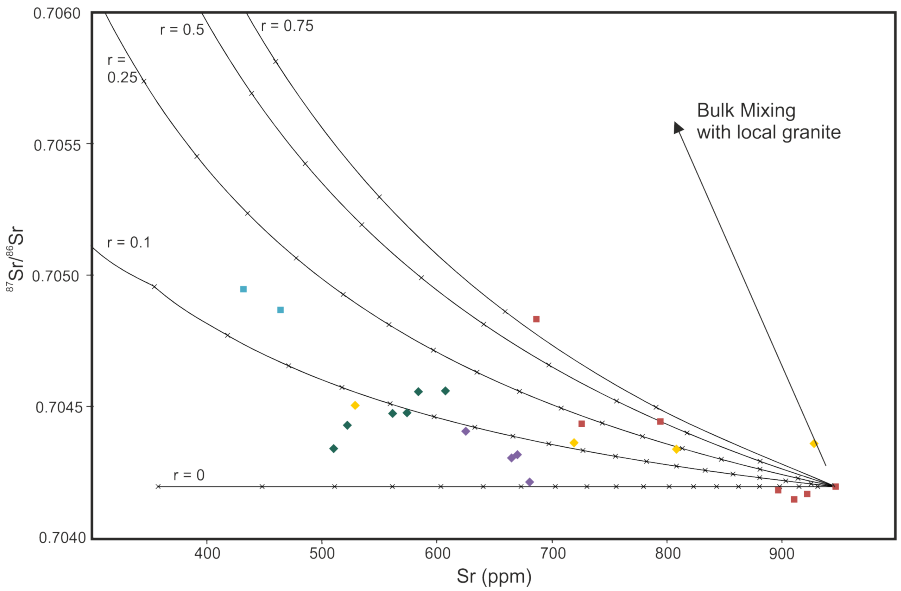

FIGURE 5.23: Isotope and trace element variation, with AFC model. Decrease in Sr with relatively constant $^{87}Sr/^{86}Sr$ can be explained by fractionation, with limited input from crust. Starting composition is rock H2, Sr = 946 ppm, $^{87}Sr/^{86}Sr = 0.70420$. Contaminant is local granite 13-020, Sr = 226 ppm, $^{87}Sr/^{86}Sr = 0.71184$. Fractionating assemblage is a plagioclase rich, hydrous assemblage, as used by Jweda (2014) in the Andes: 10% opx, 65% plag, 5% sp and 20% hbl. Partition coefficients used were $K_{Sr}^{opx/melt} = 0.07$, $K_{Sr}^{plag/melt} = 2$, $K_{Sr}^{sp/melt} = 0.002$ (McKenzie and O'Nions, 1991) and $K_{Sr}^{hbl/melt} = 0.12$ (Ewart and Griffin, 1994). Symbols used are same as Fig. 5.3.

more visual features to support this. The linear patterns in major-element plots (Fig. 5.5) could also be due to mixing. In the field small mafic enclaves were occasionally observed, particularly in flows from Stage II and III of Mt. Kazbek. Mineralogically these were similar to the erupted melt, and may be mixing of similar pulses of magma.

5.5.4 Zoning in Plagioclase

Along with fractional crystallisation and assimilation of wall-rock, magma chamber replenishment and mixing are also important processes in the evolution of a magmatic system. Zoning in plagioclase phenocrysts can record changes in the temperature and composition of the magma in which they grew, were stored, and eventually erupted in (e.g. Ginibre et al., 2002; Humphreys et al., 2006; Ruprecht and Wörner, 2007; Cashman and Blundy, 2013). By looking at textures within the grain (Fig. 5.24), zone boundaries, and concentration of major-elements (e.g. anorthite, X_{An}) and minor-elements (e.g. Fe), it is possible to distinguish open-system magma-mixing behaviour (e.g. Humphreys

et al., 2006; Ruprecht and Wörner, 2007) and closed-system behaviour, such as thermal mixing and decompression crystallisation (Ruprecht and Wörner, 2007).

Two common textures were observed within grains: oscillatory zoning and sieved zones. In many cases both textures are observed within a single grain. Sieve texture is often observed in the core of crystals, however can also form zones nearer the rim, with oscillatory or unzoned areas both inside and outside of it (Fig. 5.24D and E). In some cases the whole grain exhibits a sieve texture. Oscillatory zoning is the most common of all textures, occurring in the vast majority of plagioclase phenocrysts (Fig. 55.24A, B and C), however is absent in groundmass microlites. Two types can be observed. The first is high-frequency, narrow (<20 μm) zones, with small variation in X_{An} (<5 mol% An, Fig. 5.24A and E), whereas the second is characterised by larger jumps in X_{An} (>8 mol% An, Fig. 5.24A and B), and much wider zones (50–200 μm). The finer zones can be superimposed on the larger zones, and both can be superimposed upon a general normal (decreasing X_{An} rimwards) or reverse (increasing X_{An} rimwards) composition zoning pattern. The contact between zones near the rim of a grain are typically sharp, often following a euhedral morphology, whereas contacts nearer the core are more diffuse, following a rounded morphology (Fig. 5.24B). This is also observed with composition changes across these boundaries (Fig. 5.24B). In the core, variations tend to be more gradual, whereas boundaries nearer the rims have a characteristic asymmetry, with a steep increase in X_{An} followed by a more gradual decrease. This is consistent with diffusion and partial re-equilibration occurring in the core, due to the long residence time in the magma chamber relative to the rims (Humphreys et al., 2006). Evidence of resorption can be observed at some boundaries.

5.5.4.1 X_{An}-Fe systematics

Variations of minor elements in plagioclase, such as Fe, have been used in conjunction with X_{An} to help constrain conditions during the plagioclase growth process (e.g. Humphreys et al., 2006; Ruprecht and Wörner, 2007; Shcherbakov et al., 2011). Fe is incompatible in the plagioclase structure, not taking part in substitution reactions, and is mainly incorporated into the crystal structure because it is a major component of the melt. Therefore the melt composition is the main control over concentration of Fe in plagioclase (Ginibre et al., 2002). Temperature, An-content, and oxygen fugacity also affect the partitioning of Fe to a lesser extent (Bindeman et al., 1998; Aigner-Torres et al., 2007).

Figure 5.25 shows the relationships between X_{An} and Fe across major resorption zones in plagioclase. In the majority of cases there is very little variation in Fe content

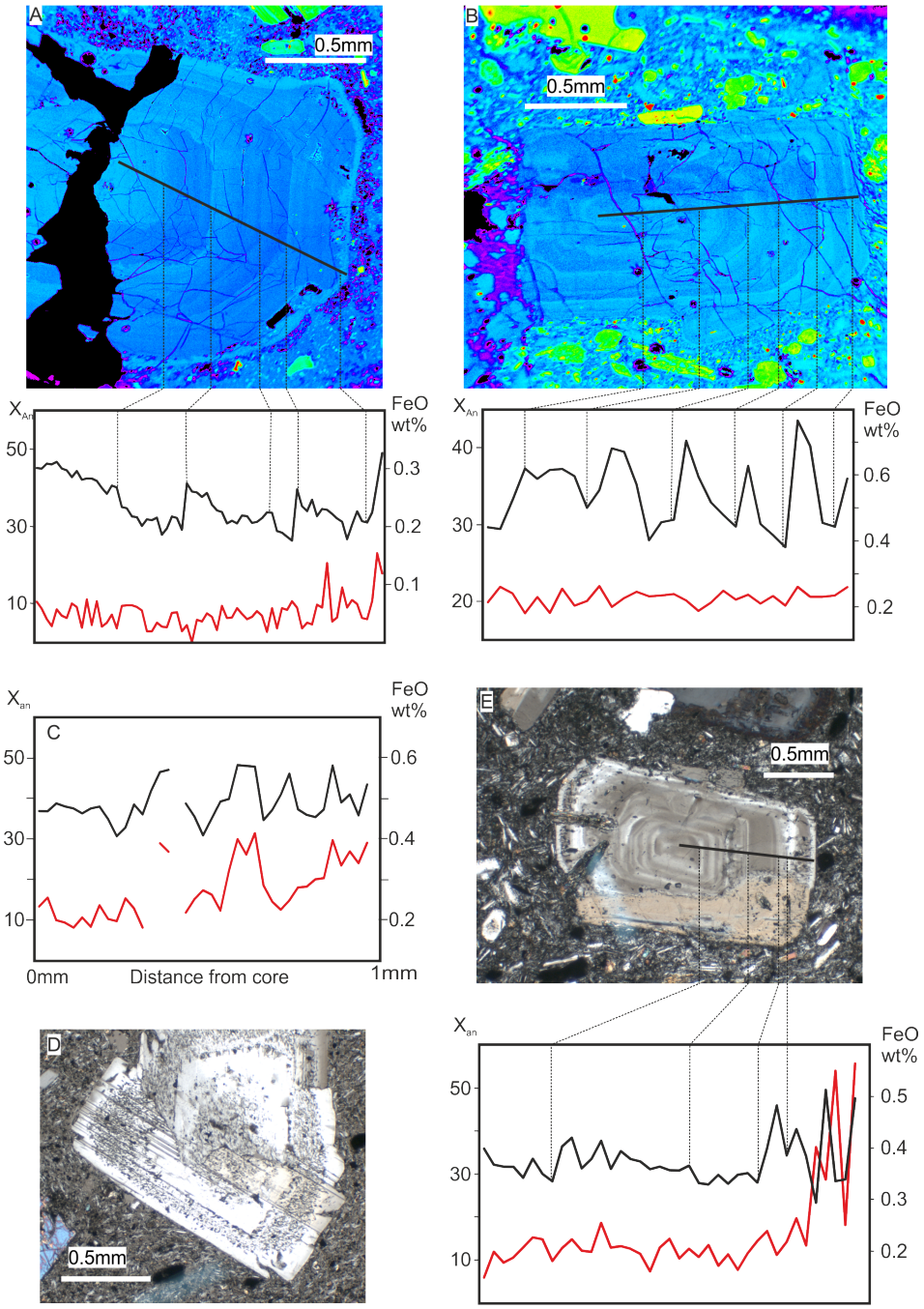

FIGURE 5.24: A) False coloured BSE image. Asymmetric zoning observed in XAn (black line), with no correlation with FeO content (red line). Zone boundaries of the inner zones are clearly zoned, within a sub-hedral grain. Small-scale oscillations in X_{An} superimposed on main trend. B) False coloured BSE image. Large changes in An content, with clear rounding of inner zones corresponding to decreasing asymmetry of chemical zoning towards the core of the grain. C) Chemical profile, with no image. Variation in XAn correspond to those in FeO%. Gaps in the trends are due to analyses hitting inclusions or cracks in the grains. D) Photomicrograph of a plagioclase grain with a sieved core, and sieved outer zone, with clear middle zones and rim. E) xpl image of a grain. Variations in X_{An} not relating to FeO in the core of the grain. The dirty, inclusion-rich rim shows much more variation in both X_{An} and FeO%.

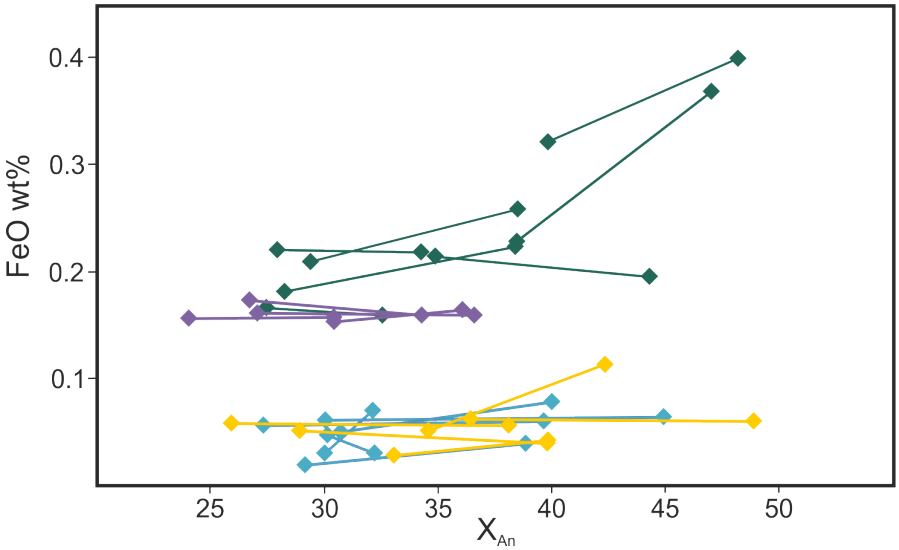

FIGURE 5.25: An-Fe relationship across plagioclase resorption boundaries. In all cases the analysis closer to the core has the lower An, with the higher-An analysis on the rimward side of the resorption zone, with the two analyses connected by a solid line. Colours used are the same as those used throughout the chapter.

across the resorption zone and associated jump in X_{An}. The Qabarjina Fm. and Stage IV of Mt. Kazbek are characterised by low FeO content. The Qabarjina Fm. is dacitic, and has low bulk-rock FeO content, which is likely reflected in the plagioclase. Stage IV volcanics typically have Al-rich bulk-rock compositions, possibly saturating the rock in Al, thus not allowing significant exchange with Fe^{3+} in the plagioclase.

Stage II and III have more Fe-rich bulk-rock compositions, and more Fe-rich plagioclase. Stage III is characterised by having horizontal An-Fe trends, similar to those of Stage IV and the Qabarjina Fm. Closed-system behaviour typically produces this type of relationship (Ruprecht and Wörner, 2007). If crystallisation occurs as a result of slow decompression of a hydrous magma, the latent heat release will cause an increase in the temperature of the melt, and the resulting An-content of the plagioclase (Blundy et al., 2006). If this decompression or magma ascent happens in discreet steps, jumps in An-content of plagioclase, like those seen in these plagioclase, will appear (Ruprecht and Wörner, 2007). If cooling, or storage, occurs after the ascent, a gradual decrease in An-content should be seen, which is consistent with the asymmetrical An-profiles across resorption zones (See Fig. 5.24A and B). A second potential cause is thermal mixing within the magma chamber (Ruprecht and Wörner, 2007). Underplating, but not recharge and mixing, of the magma chamber by a hotter magma results in convection occurring. This causes variation in temperature within the chamber, and therefore temperatures at

which plagiocalse will crystallise, affecting the An-content. This could be a mechanism to explain small-scale, high-frequency variation occilatory zoning, but would not explain the asymmetric profiles seen. Small variation in FeO with An is observed (<0.02 wt% FeO), these can be the result of changes in fO_2 that can occur as a result of changing temperature and water content caused by these close-system behaviours (Ruprecht and Wörner, 2007).

Stage II, as well as having the highest Fe-content, also shows An-Fe relationships that are not horizontal. Large increases in FeO (0.04–0.14 wt%) across resorption boundaries associated with jumps in X_{An} (Figures 5.24C and E, and Fig. 5.25). This implies open-system behaviour (Ruprecht and Wörner, 2007). Magma mixing/recharge causes changes in both temperature, composition and fO_2 of the melt, which would affect both the X_{An} and FeO contents, which would crystallise a composition reflecting the new hybrid magma. 13-059, a vesicular sample with glassy matrix and unrimmed amphiboles, shows large variations in both An and FeO. If the An increases were due to decompression, it is unlikely this texture would have been preserved, supporting magma mixing. The increase in FeO is most strongly seen nearer the rim of the grains, often with a core that has little variation in An (Fig. 5.24C and E). It has often been suggested that magma recharge events can trigger large explosive eruptions (Murphey et al., 2000; Hernando et al., 2016), and the X_{An}-Fe correlation near the rims in this grains may be evidence of one of these events that triggered the caldera forming eruption suggested by Lebedev et al. (2014), that occurred between Stage II and III.

5.5.5 Origin of the High-Al pyroxenes

In nature, pyroxenes with Al_2O_3 contents as high as these rocks (up to 16 wt%) are rare. They are typically associated with alkali volcanic rocks e.g. basanites from Mt. Erebus, Antarctica (Kyle et al., 1992; Gerke et al., 2005), post-collisional potassic lavas (Turner et al., 1996), anorthosites (e.g. Charlier et al., 2010; Bybee et al., 2014) and pyroxenites (e.g. Orejana et al., 2006; Borghini et al., 2016). Cpx with Al_2O_3 up to 6.7 wt% has been found in Andean andesites (Samaniego et al., 2005), which is the most comparable host rock to these Greater Caucasus samples.

Major-element and trace element bulk-rock data show these rocks are silica-saturated, and show only very small influence, if any, of garnet in the source. The presence of garnet in the source or fractionating assemblage should deplete the bulk rock of HREEs, however the Gudauri Fm., where these pyroxenes are most common, has the lowest $(Dy/Yb)_N$ in the Mt. Kazbek region. Therefore these pyroxenes are unlikely to be associated with

garnet-bearing xenoliths. These melts do not exhibit particularly high K_2O contents, and are not be classified as potassic. This leaves anorthosites and pyroxenites as containing the most likely analogous pyroxenes.

As well as the high concentration of Al, the sub-calcic nature also needs to be explained. Natural high-Al pyroxenes related to pyroxenites tend to contain Ca concentrations expected for a typical cpx (~20 wt%; Chapman, 1975; Orejana et al., 2006; Borghini et al., 2016). These look similar to the group B pyroxenes, associated with stage III of Mt. Kazbek. High-Al pyroxenes related to anorthosites can be classified as opx (CaO <2.5 wt%; Charlier et al., 2010), which looks similar to the lower Al_2O_3 group A pyroxenes. The variation in CaO content suggests that the sub-calcic nature of the more common Group C, is not necessarily a function of the high-Al content.

One mechanism to obtain the sub-calcic CaO concentrations observed in the dominant group C pyroxenes involves the early separation of Ca-rich plagioclase (similar to anorthosite formation), therefore depleting the melt in the Ca-Tschermaks component, driving the pyroxene to sub-calcic compositions (Muir and Mattey, 1982), however this will not produce the high-Al contents observed. Sub-calcic compositions could be formed by exsolution of Ca-poor pyroxene from a Ca-rich host (Wilkinson, 1976), as the solubility decreases at higher pressures (Thompson, 1974). However obvious exsolution features are not seen in these grains. Thompson (1974) note that Ca (and Na) decreases with increasing pressure and temperature, with a corresponding rise in Si, Mg and Fe, and it is this that pushes compositions towards a sub-calcic nature. They notice that this effect only occurs at intermediate pressures of 10–20 kbar. Higher pressure experiments (20–30 kbar; Pertermann and Hirschmann, 2003) show CaO and Al_2O_3 increasing with temperature, and TiO_2 and Na_2O decreasing (although the later increases with pressure). CaO seems to decrease with increasing pressure, extending the range observed by Thompson (1974), and produces sub-calcic compositions (Table 5.1). It therefore seems sensible to assume the Ca content in these pyroxenes is controlled by pressure (and bulk-rock composition).

High-Al in pyroxenes has also often been linked to high pressures (e.g Thompson, 1974; Wenk and Weiss, 1982), and may be used to constrain the depth of crystallisation of this phase. Many barometers involving pyroxene require the melt composition to be known (Putirka, 2008). These are not applicable to these rocks as the pyroxenes are not in equilibrium with bulk-rock composition. Barometers that use just the pyroxene composition (e.g. Nimis, 1995) yield pressures of 5.0–19.7 kbar (mean = 10.8 kbar) for the lower Al_2O_3 (Groups A and B), and 11.4–25.5 kbar (mean = 18.5 kbar) for the higher Al_2O_3 pyroxenes (Type C). Despite worse precision and systematic errors in hydrous experiments (Putirka, 2008), these pressures are comparable to pressures constrained by

11.2

TABLE 5.2: Compilation of high-Al pyroxenes from the literature, to compare with pyroxenes from the Greater Caucasus. For classification of the groups in this study see 5.4.3.3. Pressure data for this study estimated using pyroxene-only barometer of Nimis (1995).

Publication	Host	Concentration (wt.%)		Pressure (kbar)
		Al_2O_3	CaO	
Borghini et al. (2016)	Clinopyroxenite	6.21–10.21	19.32–22.26	12–15
	Cpx Neoblast	3.16–6.62	21.84–22.38	3–7
	Orthopyroxenite	4.33–7.56	0.52–1.19	12–15
Orejana et al. (2006)	Clinopyroxenite	7.50–9.34	20.31–21.32	7.7–11.7
	Hornblenditic Xenolith	5.00–9.14	19.65–21.28	6.8–8.7
	Orthopyroxenite	7.43–7.75	0.70–1.10	10.8
Chapman (1975)	Clinopyroxenite	9.19–12.75	19.02–20.92	>18
Wilkinson (1976)	Clinopyroxenite	7.57–8.26	15.0–15.5	∼20
Upton et al. (2001)	Pyroxenite	3.80–8.36	18.94–23.54	5–10
Best (1970)	Basanite	6.29–9.98	17.10–20.92	>10
Thompson (1974)	Alkali-transitional basalt	5.64–13.2	6.01–14.5	18–20
	Tholeiite	4.91–12.0	10.7–13.4	17–25
Turner et al. (1996)	Shoshonite	1.86–4.60	18.33–20.80	
Pertermann and Hirschmann (2003)	Experimental	14.1–15.1	12.8–15.6	20–30
This Study	Andesite^{GpA}	4.02–7.74	0.54–4.16	6.7–19.7
	Andesite^{GpB}	4.03–6.92	16.69–21.41	6.0–13.7
	Andesite^{GpC}	11.75–16.87	7.99–14.51	14.2–30.2

literature values (Table 5.2).

It is clear that the pyroxenes of this study are most analogous to those produced by the experimental work of Pertermann and Hirschmann (2003), which is based on melts from a pyroxenite source. This is also consistent with the common association of high-Al pyroxenes being found in pyroxenites (Chapman, 1975; Orejana et al., 2006; Borghini et al., 2016). In the adiabtic melting experiments of Pertermann and Hirschmann (2003), the staring composition approximated subducted oceanic crust, and can represent a slab in the Caucasus situation. The Al is hosted by the pyroxene because of the low pyroxene:garnet modes at the solidus (18 wt% garnet; Pertermann and Hirschmann, 2003). As these are the two major crystallising phases, simple mass balance would show

that the composition of the pyroxene would approach the composition of the melting pyroxenite. As temperature increases, garnet preferentially melts, increasing the Al_2O_3 of the melt, again forcing more Al into the pyroxene. The compositions obtained in the experiements were at 30 kbar, where solidus temperatures were 1310±12°C, therefore potentially putting melting in the asthenosphere (assuming a mantle lithosphere thinner than 30 km), beneath the Greater Caucasus. Dehydration melting experiments of slab crust (basaltic amphibolites) yield much higher garnet modes at the solidus at 27–32 kbar (40 wt% garnet; Rapp and Watson, 1995). With this much garnet, the garnet would be the host of the Al. Therefore it seems more likely that these pyroxenes are associated with asthensophere rising from depths, with pockets of pyroxenite preferentially melting.

5.5.6 Chemical Nature of the Source Region

The magmas collected at the surface are not a simple reflection of the source region. The primary melt or melts have undergone a long history involving bulk-mixing, magma chamber recharge, fractional crystallisation and crustal contamination and assimilation. These processes have significantly altered the major- and trace-element signature of the primary melt, as well as the isotopic signature. Isotope ratios should only record the effects of AFC and magma mixing, and when used in combination with trace-element ratios should start to produce a picture of the geochemistry, mineralogy and melting conditions in which these melts were formed.

5.5.6.1 Enrichment of the Source

Figure 5.8 shows multi-element variation diagrams for the various centres of the Greater Caucasus. Elements are ordered with increasing compatibility in a spinel lherzolite mantle mineral assemblage. Melting of this MORB-source mantle would result in a smooth curve, decreasing towards the HREEs, with the most incompatible elements becoming more enriched with smaller degrees of partial melting. This is the general trend seen in all the rocks, but is superimposed by significant anomalies. All show negative anomalies in HFSEs (Nb and Ti) relative to LILEs and LREEs, and positive anomalies in fluid-mobile elements such as Pb and Cs. Every element is significantly enriched relative to primitive mantle (even the least enriched/most compatible elements, such as Yb and Lu are >2 times more enriched than primitive mantle), meaning previous source depletion, which can also give the negative HFSE anomalies, is not a possible causes for these patterns. Partial melting, even small degrees, is unlikely to produce the enrichment in all elements, and would likely give a smoother curve. This pattern is consistent with those of typical

arc lavas, and is likely to be a signature inherited from the source.

This pattern would also be expected of a crustal melt, as the local crust has a similar trace-element pattern. For most elements the enrichment is of a similar magnitude. However the isotopic ratios of the melts and the crust are so wildly different, crustal anatexis can be ruled out. Mixing with a crustal melt could lead to some of the observed enrichment, but elements such as Sr and P are less enriched in all crustal samples compared to the melts, so cannot in itself be the sole explanation of the pattern.

Fractionation within the HFSEs is seen in the Zr/Hf ratio. Most values are super-chondritic, ranging from 38 to 44 (Chondritic value of 34.3; Pfänder et al., 2007), with one Qabarjina sample plotting lower (which may be a remnant from zircon remaining during the dissolution process). This range is similar to that of the contemporaneous Abul-Samsari volcanics in the Lesser Caucasus (Zr/Hf = 42–46). There is no distinction of Zr/Hf with volcanic centre (Fig. 5.26). Fractionation of cpx and amphibole can fractionate Zr and Hf (Pfänder et al., 2007), however no correlation is seen with SiO_2 (Fig. 5.26a), which would be expected if this were the case. Lack of correlation with $^{87}Sr/^{86}Sr$ or $^{206}Pb/^{204}Pb$ rules out crustal contamination. Residual garnet would result in increased fractionation of Zr/Hf at smaller melt fractions (Pfänder et al., 2007), although lack of correlation between Zr/Hf and Dy/Yb rule this out (Fig. 5.26c). Fractionation of Ti-bearing phases (rutile, ilmenite, phlogopite) may be expected from the phenocryst assemblage and major-element chemistry. Zr behaves in a similar way to Ti, so fractionation of these minerals can increase Zr/Hf (as they all have $D_{Zr/Hf} < 1$; Pfänder et al., 2007). This would be associated with a marked decrease in bulk-rock concentration of Zr, whereas a positive correlation between Zr and Zr/Hf is observed (Fig. 5.26d). Zr/Hf increases strongly with Zr, suggesting the increase in the ratio is controlled by the preferential addition of Zr over Hf.

Metasomatism of the source is the most likely explanation of this, with slab derived fluids the most likely metasomatic agent. The overall enrichment of all elements can be the result of small-degree partial melting, or source enrichment prior to melting. Slab-derived silicic melts, or super-critical fluids at depth, result in enrichment of all elements, even HFSEs and HREEs which are not enriched by simple water-rich dehydration, and the production of aqueous fluids (Kessel et al., 2005). The super-critical fluids refer to fluids released after the critical endpoint as which the melting temperature of the subducting crust can no longer be defined (Mibe et al., 2011). This may occur as shallow as 100 km (Mibe et al., 2011) or as deep as 180 km (Kessel et al., 2005). However, water released from dehydration in the deep basaltic and ultra-mafic portions of the slab, can trigger fluid-present partial melting within the trace-element enriched, sedimentary part

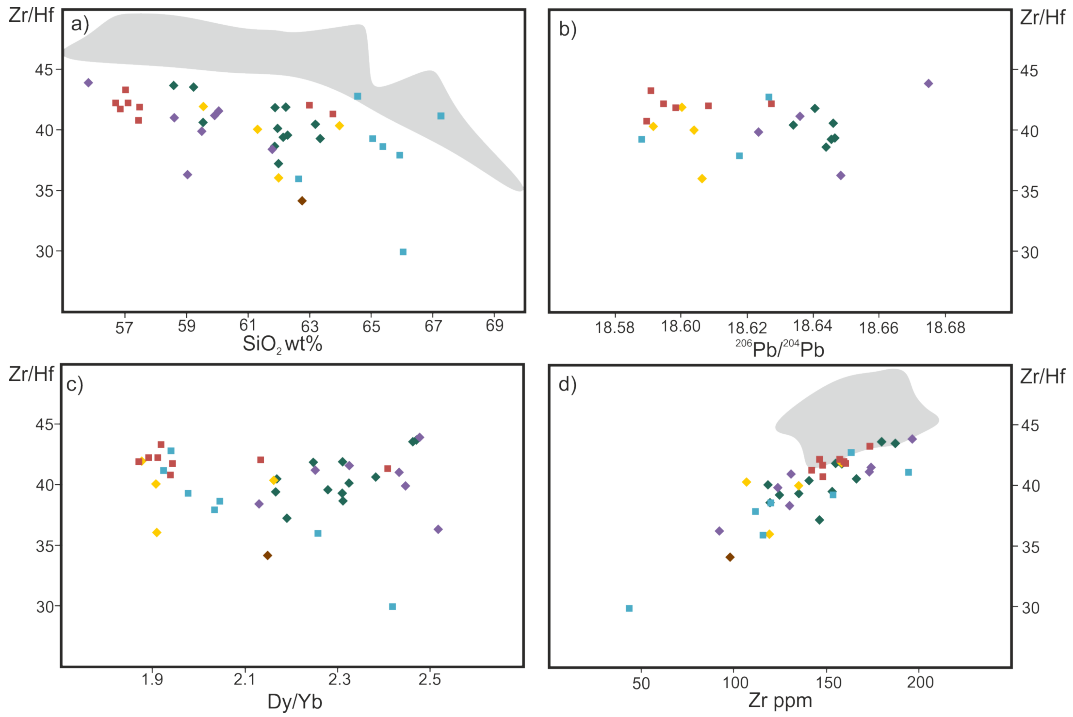

FIGURE 5.26: SiO_2 vs Zr/Hf. No signicant varation in Zr/Hf during fractionation of cpx and amphibole. Grey shaded area shows values for the Lesser Caucasus (this study) being higher than the Greater Caucasus. b) 206Pb/204Pb vs Zr/Hf. No correlation of Zr/Hf with an index of crustal contamination (assuming more radiogenic values are more contaminated), although crustal Zr/Hf is highly variable. c) Dy/Yb vs Zr/Hf. Residual garnet would be expected to significantly fractionate Dy/Yb as well as Zr/Hf to a lesser extent, however no correlation is seen. d) Zr vs Zr/Hf. Strong correlation suggesting Zr controls the Zr/Hf ratio. Same correlation is not observed in the Lesser Caucasus (grey shaded area).

of the slab (Hermann et al., 2006), which can produce a similar signature as seen in these rocks, without the need to very deep processes. Negative HFSE anomalies can be the result of residual HFSE-bearing minerals left in the slab after dehydration processes, or as relics of dehydration sediment (Hermann and Rubatto, 2009).

The low Zr and Zr/Hf can be caused by zircon being a residual phase. The low abundance of Zr in mafic slab lithologies, and the relatively soluble nature of zircon in silicate melts, restrict the importance of residual zircon to relatively low, sub-solidus temperatures, and the dehydration of subducted sediments (Klimm et al., 2008). The high concentration of Zr and super-chondritic Zr/Hf both point to the source being already be enriched in Zr, before being held back to create the observed patterns. The positive correlation may the result of mixing between a low Zr-Zr/Hf (shallow, fluid-dominated metasomatism) and high Zr-Zr/Hf (deeper slab-melt dominated metasomatism)

endmembers.

Isotopically, rocks from the Greater Caucasus volcanic region plot with ratios more radiogenic than would be expected for typical mantle melts (such as MORB and the NHRL, see Fig: 5.10). This can be the result of crustal contamination or enrichment of the source region. Figure 5.22 shows that variation in isotopic composition with SiO_2 is very limited, suggesting AFC only played a minor role and isotopic enrichment of the source (relative to DMM) must have occurred prior to crystallisation and storage in the crust. As the range of isotopic compositions is so restricted, multiple sources with very different compositions can be ruled out, however mixing and re-homogenisation prior to fractional crystallisation can not. It is widely agreed that sediments play an important role in modifying sub-arc mantle (Elliott et al., 1997; Plank and Langmuir, 1998; Plank, 2005). In an attempt to recreate the least radiogenic compositions observed in the volcanics, mixing models have been calculated with sediments (Fig. 5.27). For the modelling, two compositions have been chosen, an average depleted MORB mantle (DMM) and an enriched DMM (E-DMM; Workman and Hart, 2005). Unlike in active arcs, where marine sediments can be directly associated with their corresponding arc for modelling (e.g. Plank, 2005), the composition of sediments beneath the Greater Caucasus is unclear. Therefore two possible compositions have been chosen: GLOSS (Plank and Langmuir, 1998) as a rough estimate, and a Tethyan sandstone flysch sample (Prelević et al., 2008) to obtain a composition possibly more relevant to the region (and also used in calculation involving Iranian post-collisional volcanics by Allen et al., 2013). Sediment could be transferred into the wedge via bulk-mixing, or as a sediment melt from the slab. To model the second scenario, melts have been calculated assuming batch-melting of the two sediment types, using experimentally determined bulk distribution coefficients calculated for 850°C, 3 GPa, and corrected for 7% H_2O (Skora and Blundy, 2010). These partition coefficients take into account the important role of accessory minerals, such as monazite and rutile, in controlling the movement of LREEs and Th (Hermann and Rubatto, 2009).

The various mixing scenarios are shown on Figure 5.27. The black curves represent mixing with sediment-melts. Both models A and B (10% partial melts of the GLOSS and Tethyan flysch respectively) are convex upwards curves, producing compositions further from the Greater Caucasus values. Degrees of partial melt lower than 10% push compositions even further away. Curve C (50% partial melt of Tethyan Flysch) is convex downwards, so can produce compositions closer to the values observed. Less than 1% mixing is required to produce $^{87}Sr/^{86}Sr$ of the lavas, however $^{143}Nd/^{144}Nd$ remains far too high. Using E-DMM as the starting composition produces a composition closer

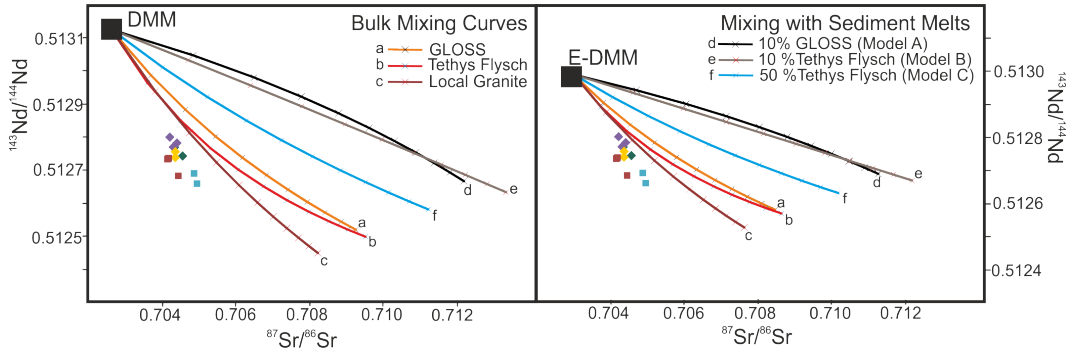

FIGURE 5.27: Two plots showing the same data from the Greater Caucasus. Red curves show mixing of original composition with sediment and crust, whist black lines show mixing with sediment melts. Tick marks on the model curves are at 0.5% melt intervals, and total curve length is 10% melting. For details of the sediment melting models, and sediment, crust and melt compositions, see Table 5.3. Symbols are the same as those used in Fig. 5.3.

to the lavas, with even less mixing. Increasing the degree of partial melting results in compositions closer to the Mt. Kazbek values, however these seem unrealistically high, and the partition coefficients used would no longer be valid as the accessory minerals also start to melt. Changing the trace-element composition of the sediment to be have a lower Sr/Nd (more enriched in LREEs), closer to that of the schists and gneisses of the basement outcrops in the Main Range Zone, increases the curvature of the convex downwards shape, resulting in compositions more similar to the lavas. Rather than mixing with a sediment melt, bulk-mixing with the sediment is another possibility. This scenario is shown by the red curves in Fig. 5.27. These can produce compositions much closer to those of the lavas, and require just 1–2% sediment input. Due to the uncertainty of the sediment composition, it would be purely guesswork to say which of the three curves shown is most likely to represent what is truly occurring. However one feasible scenario, that can result in bulk-mixing of lower crustal material or slab sediment, is a zone at the base of crust, where the density contrast between crust and lithosphere causes rising melts to pool. Melting, and assimilation of the lower crustal material, followed by storage and homogenisation would create a MASH zone, and be the parent magma that supplies the complex crustal plumbing system above. Rather than melting of lower crustal material, subduction erosion, scraping sediments off the down-going slab, which then assimilates with the mantle wedge material, creating a similar effect.

The REEs can also be used to investigate the source (Fig. 5.28). Figure 5.21 showed that the range of compositions for Stages II and III of Mt. Kazbek can be produced by crystallisation of cpx and amphibole. For this to be the case, the source composition must

TABLE 5.3: Source compositions and contaminants used in Fig. 5.27. DMM and E-DMM are source end-members taken from Workman and Hart (2005). Sediment compositions used in bulk mixing curves are GLOSS (Plank and Langmuir, 1998), Serbian Tethyan flysch (Prelević et al., 2008) and local granite, 13-020 (this study). Sediment melt compositions have been calculated using the composition, and percentage melt shown in column title, and bulk partition coeffiecients in column $D^{Sed/Melt}$. Distribution coefficients from Skora and Blundy (2010).

	Source Composition		**Sediment/Crust Composition**		
	DMM	E-DMM	GLOSS	Flysch	Granite
Sr (ppm)	7.664	9.718	120	83	226.2
$^{87}Sr/^{86}Sr$	0.70263	0.70307	0.71730	0.72161	0.71184
Nd (ppm)	0.581	0.703	20	25.3	29.0
$^{143}Nd/^{144}Nd$	0.51313	0.51300	0.51218	0.51222	0.51219
	Melt Composition			**$D^{Sed/Melt}$**	
	10% GLOSS	10% Flysch	10% Flysch		
Sr (ppm)	272	188.2	120.4	0.379	
$^{87}Sr/^{86}Sr$	0.71730	0.72161	0.72161		
Nd (ppm)	10.5	13.3	16.9	2	
$^{143}Nd/^{144}Nd$	0.51218	0.51222	0.51222		

have elevated Dy/Yb and low Dy/Dy* compared to both primitive mantle, and MORB compositions. The Dy/Yb is similar to Andean continental arc volcanics (Fig. 5.28; Davidson et al., 2013), whilst the lowed Dy/Dy* may be the result of significant LREE enrichment, which is consistent for what is required of the source by Sr- and Nd- isotopes. The enrichment in Dy/Yb may be the result mixing with sediments melts (in the presence of residual garnet). Whilst this is consistent with the isotope data for the majority of the lavas, how the Gudauri Fm. fits into the story is less clear. Major-elements show the Gudauri Fm. is the least fractionated, so should plot closest to the source, but plots furthest from it (Lowest Dy/Yb, highest Dy/Dy*) on Fig. 5.28. This suggests a different source, possibly shared with the Stage IV volcanics that plot close to the Gudauri Fm. samples. This source still requires the LREE enrichment, which can be supplied by fluids. These samples also have high Zr/Hf, so can be related to the slab melt end-member, with little interaction with the shallow sediment-derived fluids, which have high Dy/Yb, but low Zr and Zr/Hf.

5.5.7 Depth of melting

Contamination of the source region, and further interaction with crust and fractionation alter the chemistry of the magmas. These will have over-printed a signature left by

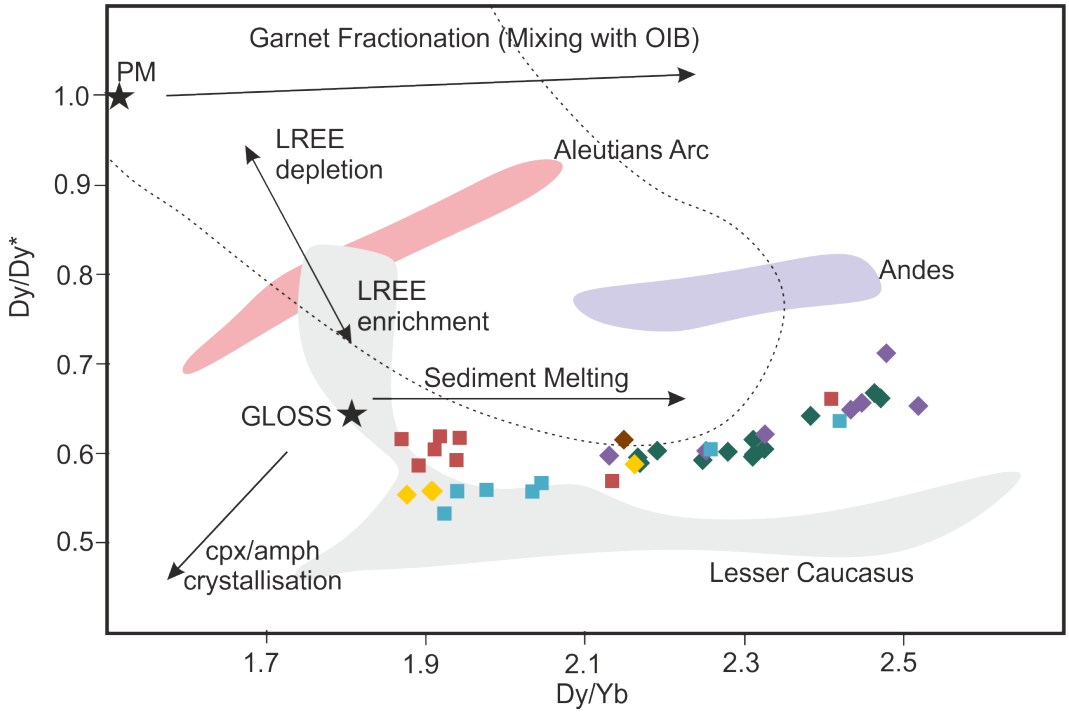

FIGURE 5.28: Dy/Yb vs Dy/Dy* to show source enrichment. Dotted line defines the MORB field, pink (Aleutian Arc) and purple (Andes) fields shows range of values for other oceanic and continental arcs respectively. Arrows show generalised vectors or enrichment and mixing. Fields and arrows taken from Davidson et al. (2013)). Further details of cpx and amphibole fractionation are modelled in Fig. 5.21c. Grey eld shows Lesser Caucasus data from this study. Symbols used are the same as Fig. 5.3. Primitive mantle (PM) from Palme and O'Neill (2014).

melting of the source. Fractionation within the REEs has commonly been used to investigate the melting signature. Being incompatible in most mafic minerals, and the main phases that compose the Greater Caucasus volcanics, fractionation probably had little effect on their ratios. Increasing compatibility with atomic number (and decreasing ionic radius) should result in a steeper slope in the REE patterns (measured using La/Yb) with decreasing degrees of partial melting. HREEs are compatible in garnet, which would fractionate them on a REE plot (measured using Dy/Yb), and can give an insight into the depth of melting.

Figure 5.29 uses these ratios, and shows melting models of different assemblages. The model curves are just there as a guide to expected variations under different conditions, not to replicate the true conditions the lavas were derived from. Models A-C are all peridotitic sources. Model A shows melting of an anhydrous, garnet-bearing source, representing deep melts (>70 km). Model B represents a shallow, spinel-bearing, anhydrous assemblage.

Model C contains amphibole, representing a hydrous assemblage, based on a model from Neill et al. (2015). The starting composition is that of an ultramafic xenolith, thought to represent a metasomatised mantle (Neill et al., 2015). This has been chosen as it is likely to be somewhat similar to the metasomatised mantle beneath the Greater Caucasus, and enriched in REEs, and also for consistency and easy comparison with Lesser Caucasus models (this study, section 4.4.4.3, and Neill et al., 2015). However, multi-element plots (Fig. 5.8), trace-element ratios (Fig. 5.28), and isotopes (Fig. 5.10) suggest a larger sediment-derived input, which may mean an even more enriched source, especially in MREEs (which would increase $(Dy/Yb)_N$, Fig. 5.28). Despite this the shape of the model curves remains largely unchanged. Model D uses an anhydrous pyroxenite assemblage, although including amphibole in that model changes very little. The starting composition and modal mineralogy is that of an upper mantle cpx-pyroxenite, from the Italian Appenines (Borghini et al., 2016). Introducing garnet into model D produces very high $(Dy/Yb)_N$ ratios.

The Greater Caucasus volcanics plot at much lower $(Dy/Yb)_N$ than the garnet curve, ruling out a single deep source. A non-garnet bearing pyroxenitic source will not change $(La/Yb)_N$ much due to the very small La/Yb of the starting composition. Dy is most compatible in cpx, compared to other minerals in the starting assemblage. Cpx is the last phase to be consumed during melting (Lambart et al., 2009), therefore hosting most of the Dy (and Yb), meaning at relatively low degrees of melting (<20%), there will be very little increase in $(Dy/Yb)_N$.

The data plot closest to models B and C, both representing relatively shallow melting. This agrees with the geothermobarometry, where there is no evidence for deep, asthenospheric-type temperatures or deep crystallisation, and the olivine and opx compositions being less magnesian than those expected for crystallising in equilibrium with these types of melts. It is also clear that the data does not plot along the melting curves (with the exception of the Gudauri Fm.), and the Qabarjina Fm. and Stage IV of Mt. Kazbek form linear trends. This suggests mixing of more than one melt, potentially between a small-degree, deeper asthenospheric, and larger degree hydrous, metasomatised, shallower melt. The linear trend in the Gudauri Fm. could also be mixing between a shallow melt and a pyroxenitic melt. With such variation in compositions, and lack of constraints of most of the variables, it is not possible to confidently suggest what is mixing with what. Stage II and III form clusters rather than linear trends. This may be the result of mixing multiple pulses of magmas, of shallower processes altering the composition. They plot at higher $(Dy/Yb)_N$ than the models, which may be mixing with a deeper melt, or mixing with a sediment-rich melt/altered lithology.

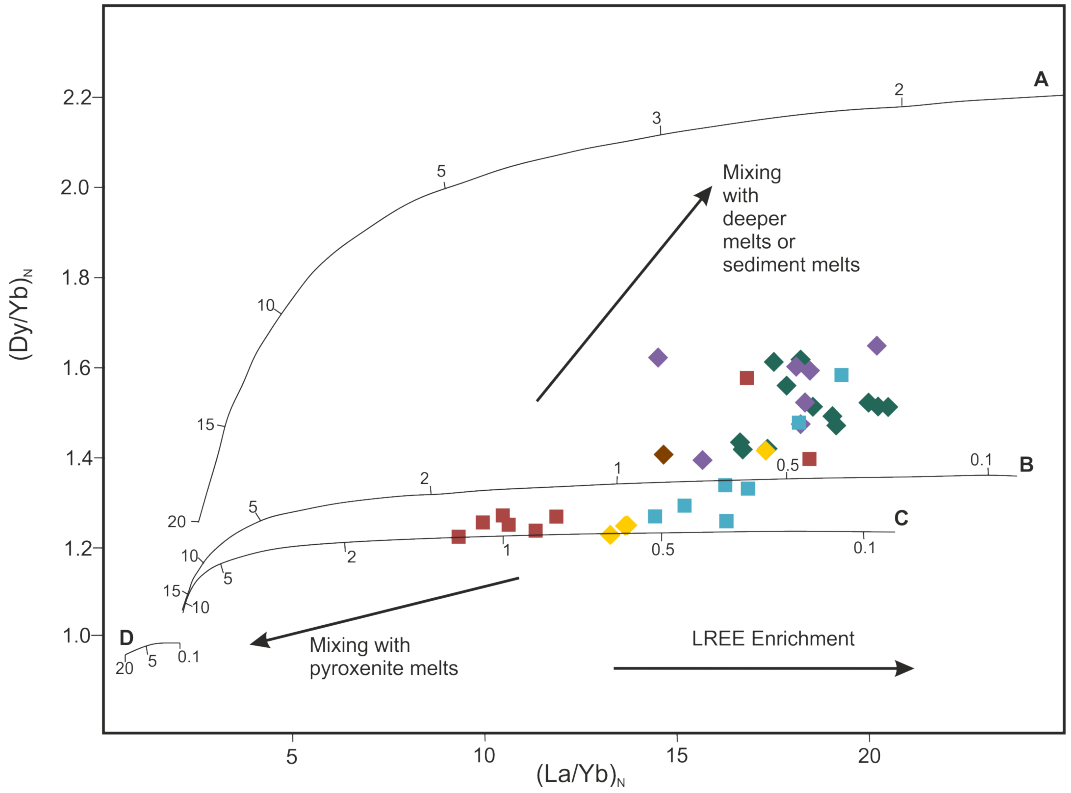

FIGURE 5.29: Partial melting curves for models garnet- (A), spinel- (B) and amphibole- (C) bearing peridotites and pyroxenites (D). Numbers on the curves represent percentage degree of partial melting. Details of the models and parameters used are discussed in the text and tables 5.4 and 5.5. Symbols used are same as Fig. 5.3. Chondrite normalising values used are from Palme and O'Neill (2014).

What can be said with relative confidence from Figure 5.29 is that the Greater Caucasus volcanics are relatively small degree partial melts. Even with a source that has undergone further LREE-enrichment than the source used in the models, they are unlikely to be more than 1–2% partial melts of a shallow source. The Gudauri Fm. was formed from slightly larger degrees of melting, and this manifests itself at the surface by forming the thickest flow (~200 m), whereas other volcanics tend to be smaller, thinner flows. However, the low $(La/Yb)_N$ and $(Dy/Yb)_N$ may also be the result of mixing between an anhydrous peridotite melt (there are no hydrous phenocryst phases in the Gudauri Fm. and the flattest patterns are shown on Fig. 5.8) and a pyroxenite melt.

TABLE 5.4: Source and melt modal compositions for the four melt models of Fig. 5.29. See text for details of the models.

	Mineral Assemblage					
	Ol	Opx	Cpx	Amph	Sp	Gt
Model A						
Source Mode	0.598	0.211	0.076			0.115
Melt Mode	0.05	0.2	0.3			0.45
Model B						
Source Mode	0.578	0.27	0.119		0.033	
Melt Mode	0.1	0.27	0.5		0.13	
Model C						
Source Mode	0.794	0.123	0.03	0.042	0.011	
Melt Mode	0.15	0.15	0.22	0.42	0.06	
Model D						
Source Mode	0.1	0.26	0.63		0.01	
Melt Mode	0.05	0.75	0.1		0.1	

TABLE 5.5: Distribution coefficients used in melt modelling. Starting composition of modelling also shown. Models A-C based off Shirak and Lori starting composition from Neill et al. (2015). Model D based on clinopyroxenite (BG5) from Borghini et al. (2016).

	Kd Value						Starting composition (ppm)	
	Ol	Opx	Cpx	Amph	Sp	Gt	Models A-C	Model D
La	0.0001	0.0002	0.054	0.086	0.0004	0.01	0.5869	0.43
Dy	0.0014	0.0261	0.442	0.707	0.0004	1.06	0.317	1.92
Yb	0.00364	0.0986	0.427	0.683	0.00053	4.03	0.202	1.93

5.6 Summary of Results

Mt. Kazbek, and the surrounding area, was volcanically active for much of the last 800,000 years. As well as forming a major stratovolcano, satellite cones and eruptive centres have produced their own flows of varying styles. Along with the field observations and volcano geomorphology, the petrography and geochemistry discussed in this chapter needs to be explained in any petrogenetic and geodynamic model.

The intermediate nature of the lavas, and the low Mg# cores of mafic opx and olivine suggest these are not asthenospheric melts. The zoning in plagioclase and amphibole, abundance of disequilibrium textures, and lack of inflections in major-element plots all point towards significant mixing occurring, rather than simple cooling from a single pulse of melt, in a single magma chamber. Within the magma chambers, early crystallisation of olivine and opx produced the evolved compositions, and low concentrations of elements such as Ni. Cpx, amphibole, Fe-Ti oxides and apatite all were involved in the crystallising assemblage later, with some evidence of plagioclase being an important phase in Stage

IV.

Zoning in plagioclase reflects minor changes in conditions, heating from below, or mixing with similar magmas. This points towards a complex plumbing system. Only between Stage II and III does mixing with a more mafic pulse of magma occur. This is also where amphibole record a change to deeper crystallising conditions. This may represent a deep mafic melt infiltrating the shallow chamber (<5 km), causing the caldera forming eruption. The emptying of the shallow chamber resulted in crystallisation moving to the deeper chamber (7–10 km). Continued addition of hotter magma beneath the magma chamber, or mixing with melts of similar composition, kept the turbulent conditions through Stage III and into Stage IV, where crystallisation occurred at greater depths (10 km). The Gudauri Fm. shows many similar features to Stage III and IV. Transport to the surface seems to be very rapid, based on rim textures in amphiboles.

The source that fed the crustal plumbing system is likely a MASH zone at the base of the crust. Either melting of lower crust, or erosion of subducted sediment passed on their enriched isotopic signature. As little as 1% assimilation is required. This would also add to the trace-element signature. Melting in this zone is consistent with REE data showing melting predominantly being in the spinel-stability field. The magmas formed from small degrees of partial melting (<2%).

At least two source signatures for this MASH zone can be distinguished. One has been significantly altered by fluids derived from dehydration of subduction sediments at sub-solidus temperatures. This holds back Zr, producing low Zr/Hf ratios, as well as enrichment in LILEs. This will have created an enriched lithosphere beneath the thickened crust, that may have been trapped for up to 15 Ma, since the end of subduction. There is also evidence of deeper slab derived melts, that were likely a mixture of peridotite and pyroxenites, which underwent adiabatic melting whilst rising through the mantle wedge. The rising of hot, deeper melts, may have caused melting of the lithospheric material.

The high-Al pyroxenes are likely remnants from the deeper melt. The source of the Gudauri Fm. seems to be the most unique in the region. It is least enriched in LILEs, has the highest Zr/Hf, least radiogenic, and contains the most high-Al pyroxenes. This suggests that it came from the least hydrous source, or interacted with the shallow, sediment-derived fluids the least, and came from a deeper, pyroxenite bearing source. It is possible this represents a broken part of the slab, or small-scale delaminated material, that has sunk. Heating of this, either by asthenospheric upwelling, or heating as it sinks deeper, produced a source that rose and melted adiabatically, mixing with the more common source beneath Mt. Kazbek.

It seems that the source of magmatism in the Greater Caucasus is, in general, distinct from that in the Lesser Caucasus. However there are specific geochemical similarities between Mt. Kazbek and the contemporaneous Abul-Samsari rocks (Lesser Caucasus). The thermal activity in both Borjomi (Abul-Samsari area) and beneath the Mt. Kazbek region, suggests in both areas a system is still cooling, with potential for future eruptions. The constraints that the geochemistry and petrology have provided will be used to produce a geodynamic model of the region in Chapter 6.

Chapter 6

Post-Collisional Geodynamic Interpretation and Implications

This chapter will consider various geodynamic models that have been applied to the post-collisional volcanism of the Eurasia-Arabia collision zone. By combining existing geophysical data with the geochemical data from this study, a preferred model will be proposed for the Lesser and Greater Caucasus, thus placing them in the larger context of the entire collision zone.

6.1 Lesser Caucasus Geodynamics

Recent geophysical and tectonic studies have improved understanding of the lithospheric structure beneath the Caucasus (See Fig. 6.1; Koulakov et al., 2012; Skobeltsyn et al., 2014; Mumladze et al., 2015; Zabelina et al., 2016). However the timing of slab break-off events in the region are poorly constrained (Skobeltsyn et al., 2014). The most southerly slab, the north-dipping Neo-Tethys slab beneath the Taurides is most commonly assumed to have broken off during the Eocene (e.g. Sosson et al., 2010). This pre-dates the volcanism by over 30 Ma, and having a suture situated 400 km south of the volcanism in this region, seems unlikely to have played a role in the source of this magmatism. The second slab, the north-dipping Palaeo-Tethyan slab beneath the Pontides, may have played a more significant role. The suture zone resulting in the subduction of this plate (the Sevan-Akera Suture) is proximal to the volcanism, with volcanic rocks covering the suture in some areas. Break-off of this slab is thought to have occurred during the Miocene (Keskin, 2003; Skobeltsyn et al., 2014), which pre-dates the bulk of the volcanism by just 10–15 Ma. This second slab detachment in a relatively short

period of time beneath the collision zone is likely to have resulted in a turbulent mantle, with hot asthenospheric upwellings replacing the down-going broken off slabs. This hot asthenosphere has been ascribed as a cause of the Miocene onset of volcanism across the whole region (Neill et al., 2015). Rather than slab-breakoff, other authors have suggested the geophysical data represent lithospheric delamination (Zor, 2008; Koulakov et al., 2012). If whole-scale lithospheric delamination occurred, significant melting of the lower crust would be expected. Isotopic and trace element data from the rocks of this study do not show evidence for this. Therefore this is not considered as a likely mechanism. Geophysical studies suggesting a thinned lithosphere is present beneath the region (See Fig. 6.1; Zabelina et al., 2016), adding further evidence for slab break-off, rather than delamination.

A schematic diagram of the proposed geodynamic model is presented in Figure 6.2. Unlike previous models for volcanism in the Lesser Caucasus (e.g. Neill et al., 2013, 2015; Nomade et al., 2016), this model requires multiple sources. Firstly, one for the early Goderzi Fm., then the Lower Akhalkalaki Fm., without a significant subduction component, and finally a source for the younger volcanism, dominated by the strong subduction component.

6.1.1 Enriching the source

Dehydration and melting of the Palaeo-Tethyan slab enriched the over-lying mantle wedge, imparting the subduction-style trace element pattern, and introducing volatiles (H_2O and CO_2) into the system, prior to both continental collision and slab-breakoff (top section of Fig. 6.2). When this slab broke-off, it did not trigger the bulk of the magmatism observed at the surface today. As shown by the >10 Ma delay between break-off and the onset of volcanism. Slab breakoff is also likely to produce a narrow zone of upwelling asthenosphere (Davies and von Blanckenburg, 1995), whereas volcanism here is dispersed over a large area, and shows a migration of source from W to E (Lebedev et al., 2008b). The thickness of crust in this area (~45 km; Zor, 2008; Koulakov et al., 2012), may have suppressed melting at the time of breakoff, and pathways to the surface for any melts that had formed, may not have been present at this time, especially as N-S compression was the dominant stress regime.

The Goderzi Fm. may post date the break-off by just a few million years, and is the only volcanism that could be directly related to the break-off event. The phenocrysts assemblage, especially plagioclase, shows a complex history for this formation, with a magma chamber that has undergone enrichment by multiple pulses of mafic magma,

whilst the evolved nature of the rocks suggest a relatively long residence time. If melt formed, but could not migrate through the crust, it may have been stored near the base of the crust, mixing with pulses of mafic magma whilst fractionating, before a route to the surface opened. With so few samples from this formation, this is only one possibility.

For subsequent volcanism, a process is required to retain the subduction signature, and hydrated mantle, beneath the region for 10–15 Ma after subduction has ceased, and slab-breakoff had occurred. Neill et al. (2013) propose that the slab stalling in the mantle, prior to break-off, would refrigerate the system, and allow the enriched mantle wedge to rapidly cool, forming an enriched lithosphere beneath the Lesser Caucasus. Assuming an initially thin mantle lithosphere, which is likely beneath the accretionary part of the orogen, north of the Palaeo-Tethys slab, the cooling to an enriched lithosphere can occur within 15–20 Myr (Holt et al., 2010). This provides a relatively stable source region for the enriched magmas observed at the surface. It also places the source just below the Moho, and assuming a mantle lithosphere <30 km (or the source being in the shallow part of a thicker lithosphere), this is consistent with REE ratios, which constrain the source to be shallower than the garnet stability field.

6.1.2 Trigger of volcanism

The trigger of significant magmatism at ~3 Ma is likely to be related to the shift in tectonic regime at ~5 Ma (Allen et al., 2004). The region is still experiencing compressional stresses, so a shift to predominantly strike-slip faulting is unlikely to have caused significant decompression melting, even if it has controlled the shallow level placement of volcanism into strike-slip basins (Avagyan et al., 2005). Although not triggering the volcanism, this transition may have opened new pathways for melts to reach the surface.

As the broken remnants of the slab sunk and were recycled into the mantle, it will have continued de-watering, keeping the solidus depressed, and adding an enriched subduction signature to the asthenosphere below the enriched lithosphere (middle section of Fig. 6.2). Importantly this also adds water into the underlying asthenosphere. Kaislaniemi et al. (2014) show that viscosity contrasts caused by even small amounts of water in the asthenosphere (a few hundred ppm H_2O) can result in small-scale convection. This results in small delamination events (or drips) at the base of the lithosphere every few million years. These drips will produce space for asthenosphere to rise into (bottom section of Fig. 6.2). This is likely to produce small volumes of asthenospheric decompression melts. More importantly it will provide a heat source to melt the enriched lithosphere. The lithosphere will preferentially melt over the asthenosphere due to the higher water content,

and its more fusable amphibole-rich mineralogy. It is possible the change in tectonic regime caused disturbances in the asthenosphere and lithosphere beneath the region, encouraging drips to form, and delaminate, producing intensive volcanism at ~3.5 Ma (the Lower Akhalkalaki Fm.) This initial intense pulse involved a larger proportion of asthenospheric melts, rising to the surface with little fractionation in the crust, and assimilation of local crust. Fractional crystallisation occurred in shallow, crustal, magma chambers (<15 km).

In the lithosphere, melting continued, caused heating from the asthenosphere below. Melts ponded in the crust, forming deeper magma chambers (~20 km), where fractionation occurred. Mixing occurred with more mafic melts, fed from the lithosphere, which erupted as the more evolved, porphyritic Upper Akhalkalki Fm., displaying the more enriched trace element patterns, inherited from the refrigerated lithosphere. Further fractionation occurred in a second, shallower magma chamber, where amphibole became unstable and broke down. This was erupted as the Abul-Samsari and Borjomi volcanics. Rapid eruption of these magmas resulted in the glassy groundmasses. Concomitantly with the Abul-Samsari volcanoes, scoria cones were formed from the eruption volatile-rich melts.

6.2 Greater Caucasus

Lying further north than the Lesser Caucasus, it seems even less plausible that the Neo-Tethys slab played a role in the petrogenesis of the Great Caucasus volcanics. The suture for the Palaeo-Tethyan slab is situated between 150–200 km south of Mt. Kazbek, and may have had some influence of the sub-crustal geochemistry. However, between the Lesser and Greater Caucasus is the rigid Trans-Caucasusian block, currently associated with a thickened lithosphere (Fig. 6.1; Zabelina et al., 2016). This potentially acts as a barrier between the two volcanic regions covered in this study.

The lithospheric structure beneath the Greater Caucasus is strongly debated. The thickened crust seems to be underlain by a relatively thin lithospheric mantle (<30 km; Zabelina et al., 2016), giving a total lithospheric thickness of <100 km. However, tomographic studies show the northern anks of the eastern Greater Caucasus are underlain by a seismic high-velocity zone, extending to depths of up to 250 km (Skobeltsyn et al., 2014), which is associated with deep seismic events (Mellors et al., 2012; Mumladze et al., 2015). Therefore, it is unlikely to represent a cold lithospheric root, and more likely represents subduction or under-thrusting of the Kura back-arc basin lithosphere beneath the Greater Caucasus (Skobeltsyn et al., 2014; Mumladze et al., 2015). The clear differences between the western and eastern Greater Caucasus (e.g. Forte et al.,

2014), seem to support the models of Forte et al. (2014) and Mumladze et al. (2015), in which subduction is occurring beneath the eastern Greater Caucasus, but the slab has broken off beneath the western half. It is difficult to reconcile the seismic event at a depth of 250 km with under-thrusting, where events are likely to occur at the base of the Greater Caucasus crust, along the under-thrusting boundary. The scarcity of these deep events, and predominance of seismic at events at depths of <60 km, means that the under-thrusting scenario can not be ruled out entirely, and the 250 km event may be related to a small delamination event from the base of the under-thrusting Trans-Caucasian lithosphere.

6.2.1 Enriching the source

The arc-like geochemical signature in the Greater Caucasus volcanics require the source to have been enriched by fluids derived from a subducting slab. The Palaeo-Tethyan slab is a potential source of these fluids: however this requires the signature to have migrated laterally over 150 km from the slab, and to have remained in the lithosphere for over 15 Ma after subduction ceased, and slab break-off occurred. It is possible this slab caused an enriched background signature beneath the back-arc that would close to become the Greater Caucasus (Fig. 6.3), but it is unlikely to have provided the main source of enrichment. However, if the back-arc crust was itself subducting, this would be a much more proximal source for the enrichment (middle section of Fig. 6.2).

The data set presented in Chapter 5 showed that a MASH zone at the base of the crust is likely to have provided the source of the volcanic rocks. This zone required input from two different sources. The first involved fluids released during sub-solidus dehydration of the subducting crust, which would impart the arc-like signature observed in the volcanic of the Mt. Kazbek region. As the slab descended and broke-off, further dehydration and/or melting of the slab occurred. This later and deeper event produced a less hydrous melt, which interacted with pyroxenitic material, and rose adiabatically through the mantle wedge, which would produce the high-Al pyroxenes. The Moho beneath the Greater Caucasus is at depths of 55–60 km, well within the spinel-stability field, so no garnet-signature, such as fractionation of MREE/HREE, would be seen. This is also shallower than the back-bend in the amphibole peridotite solidus, that Allen et al. (2013) invoked to explain volcanism beneath the thick crust, and compressional regime of NW Iran. Break-off also caused upwelling of hot asthenosphere, which could provide a necessary source of heat to melt the already hydrous lithosphere. It may also have acted as a further source of enriched melt as it interacted with the metasomatised mantle wedge.

In the under-thrusting model of Niu et al. (2013) for Himalayan syn-collisional volcanism during the collision between India and the Lhasa block (South Tibet), dehydration and fluid release accompanied hydrous melting of the under-thrusting crust. If the fluids for this are provided from breakdown of amphibole, it places the melting too deep for the Caucasus model, as that melting occurs at the contact between the two crusts, and therefore proximal to the required MASH zone. Moreover, hydrous melting can not produce the high-Al pyroxenes observed in the Greater Caucasus, as the under-thrusting model does not allow any significant adiabatic melting. Therefore, subduction, and slab-breakoff seems the most plausible mechanism to enrich the source, as well as being supported by seismic data. Enrichment by a subducting slab is also supported by the similar isotopic compositions of Mt. Kazbek and Mt. Elbrus volcanics (Fig. 6.3), suggesting a common origin. It can be assumed the radiogenic Sr-Nd values for Mt. Elbrus are caused by contamination from the older, and thicker crust that underlies the region (<60 km of Palaeozoic granites and metamorphic core complex), compared to Mt. Kazbek (~55 km of Mesozoic flysch).

It therefore seems likely that although both the Lesser and Greater Caucasus volcanics share many geochemical similarities, they do not share a common source. However they do share a background mantle signature (Fig. 6.3), and the sediment that supplied the basins that went on to subduct came from broadly similar lithologies (based on the similarities between the basement of the Greater Caucasus and Trans-Caucausian massifs). The sediment plays a key role in enriching the mantle, and the similarities in the sedimentary compositions may help produce the similar geochemistry of the volcanic rocks.

6.2.2 Triggering of volcanism

The geochemistry and mineralogy of Greater Caucasus volcanics suggest that crystallisation of the lavas occurred within magma chambers in the crust, and was part of a complex plumbing system, fed from the MASH zone. The structure of the crust in the Greater Caucasus is likely to be complex, lying in a collision zone, with major thrust faults over-printed by more recent strike-slip faults. These can provide pathways for melt to migrate within the crust, pooling to form the magma chambers. The earliest lavas were erupted from a shallow magma chamber (~2 km depth). Zoning of plagioclase provides evidence for this magma chamber being refertilised by a more mafic melt. This may be the trigger of the large caldera forming eruption, around 200,000 years ago (Lebedev and Vashakidze, 2014), emptying this magma chamber. Mt. Kazbek began to grow again,

being fed from a deeper crustal reservoir. It is also significant that, following the caldera forming event, a stronger influence is seen from the deeper melts feeding the MASH zone. This is reasonable as the dehydration of sediments would occur during subduction and early break-off, whereas the slab melts and asthenospheric upwelling would occur later, possibly constraining the timing of the break-off to within the past 800,000 years, the timespan of activity of Mt. Kazbek. This is consistent with the observations of Mumladze et al. (2015), who propose an active tear in the slab, roughly beneath Mt. Kazbek itself. If this is the case, future volcanism may be predicted to the east of Mt. Kazbek.

6.3 Structural Controls

In regions such as Iran, volcanics centres show alignment to the Zagros Suture (Allen et al., 2013), implying the regional tectonic fabric has some effect on the distribution of magmatism. Volcanism in Eastern Anatolia and the Lesser Caucasus seem to show a more random distribution (Kaislaniemi et al., 2014). In the Greater Caucasus, volcanic centres are too sparse to make any conclusions, although both Mt. Kazbek, and Mt. Elbrus lie close to the main axis of the Greater Caucasus mountain belt (Fig. 6.4). Across the Turkish-Iranian plateau and Caucasus region, there is no evidence of late-stage, or post-orogenic extension, which has been suggested to be the structural control in volcanism in the Eastern Mediterranean (Prelević et al., 2008), and other regions of post-collisional magmatism, such as the Sierra Nevada (Colgan et al., 2006). Strike-slip faulting is clearly active in the region, and has been since the 5 Ma tectonic regime change (Allen et al., 2004). In the Armenian Lesser Caucasus, pull-apart basins related to this have been shown to control the distribution of volcanism (Avagyan et al., 2005). In the Javakheti Highlands, faults seem to circumscribe the volcanism to the north and south (Nomade et al., 2016), whilst Lebedev et al. (2007b) showed that volcanism throughout the Akhalkalaki Fm. migrated eastwards, which could be attributed to en-eschelon, pull-apart basins. However, no clear evidence of this was seen in the field. The extensive lava ows covering surface structures combined with poor exposure, except in river valleys, means this can not be ruled out, and does seem to provide a logical explanation.

The young Abul-Samsari and Borjomi volcanics do not fit into the same pattern as the Akhalkalaki Fm. The N-S trend of the Abul-Samsari range is likely to have been controlled by strike-slip faults (Fig. 6.4), which are now covered by volcanics (Nomade et al., 2016). The Borjomi flows seem to provide a continuation of the broadly N-S trending ridge. This trend also cuts across major E-W trending structures relating to the main Arabia-Eurasia collision, suggest that it post dates this event. No evidence

was observed in the field of a N-S fault connecting the two areas of magmatism. It has been suggested (Philip et al., 1989), that Mt. Kazbek lies on a continuation of this linear feature (the Borjomi-Kazbek Fault, Fig. 6.4), and this fits well with the geography and timing of the volcanism. Faulting is present in the Mt. Kazbek region, associated with hydrothermal alteration, and is in a location consistent with the Borjomi-Kazbek Fault. However, given a distance of 150 km between Mt. Kazbek and the Abul-Samsari ridge, and a further 100 km south to the Kars Plateau, Turkey, the lack of surface expression of any connecting structure is surprising. However it may be present at depth, requiring that smaller, previously active faults acted as pathways for the magma to the surface. It may also be related to a northern extension of the East Anatolian Fault, or the western edge of the Dagestan arcuate indenter (Fig. 6.4).

As a final comment on structural control, Mt. Kazbek is located at the intersection of a major E-W thrust in the Greater Caucasus, and the major strike-slip fault, mentioned above. This is likely to have determined its location, and may be related to the tear in the slab beneath the Greater Caucasus (Mumladze et al., 2015).

6.4 Importance of post-collisional magmatism

This project has focused on classifying the type of volcanism, and the source of magmatism, to better understand the geodynamics of the Arabian-Eurasian collision zone. Two other important aspects to this style of post-collision volcanism are described below.

6.4.1 Role in continental crust formation

It is commonly considered that continental crust is derived from supra-subduction environments (e.g. Rudnick and Gao, 2003; Kelemen et al., 2007). Continental crust shares many geochemical similarities with arc-rocks, particularly the characteristic LILE and LREE enrichments and relative depletion in HFSEs. Other features, such as the andesitic bulk-composition and high Th/La of continental crust, can be produced by modifying the arc-lavas with processes such as delamination and crustal recycling (Plank, 2005; Kelemen et al., 2007; Jagoutz and Behn, 2013). Niu and O'Hara (2009) propose continental collision, rather than arc magmatism, as the producer of new juvenile crust. Late Cenozoic, felsic, collision-related magmatism (both intrusive and extrusive) magmatism on the Tibetan Plateau, share very similar bulk-rock composition to bulk continental crust (Niu et al., 2013), and do not require the later alteration that arc lavas imply, therefore supporting this model. Neill et al. (2013) consider whether the mafic

magmas of the Lesser Caucasus share similar properties. They note that the collision related magmas tend to be more enriched in incompatible elements, than continental crust by up to a factor of 3, whilst the Th/La ratios remain lower than continental crust, in all but the most felsic samples. Therefore it is suggested that post-collisional magmatism can add a component to the incompatible-element signature of continental crust, whilst not affecting the major-element budget. Mechanisms, such as foundering of the lower crust (e.g. Plank, 2005; Jagoutz and Behn, 2013) are still required to alter certain characteristics, such as the high Th/La signature.

The composition of the lavas from this study are also very similar to those of continental crust (Figs. 6.5 and 6.6). An average of all samples across both the Lesser and Greater Caucasus produce a composition most similar to average continental crust (r-squared = 0.99, if Sr is excluded). An average of all samples has been chosen as a rough estimate of a bulk composition of the volcanism. Neither sampling bias caused by flow volume, nor the preservation of specific flows or compositions have been considered. Despite this, the average of the Greater Caucasus and Lesser Caucasus show remarkable similarity to each other and with average continental crust. One aspect that makes it difficult to assess the role of the Caucasus volcanics in continental crust growth, is our lack of knowledge of how primitive the least evolved volcanics were, and how much of their geochemistry is controlled by recycling of pre-existing crustal material. It has been shown (Chapters 4 and 5) that the limited range of isotopic compositions of Caucasus magmatism is due to only a small amount of contamination and assimilation in the crust. Therefore these are likely to be lithospheric melts, that can add to continental crust, but the crust-like signature of the lavas is inherited, at least in part, from recycling of pre-existing crust, before enriching the lithosphere. However, as shown by the two models proposed earlier in this chapter, mantle melts play a key part in producing these magmas, so this tectonic setting is suitable for adding new juvenile material to the crust. In the Lesser Caucasus, the Lower Akhalkalaki Fm. showed the greatest asthenospheric component, and least crustal interaction. Although its geochemistry is the most distinct from bulk continental crust (Fig. 6.6), its lavas played an important role in altering the average Caucasus volcanic composition, to produce an average composition similar to bulk continental crust.

Two key elemental ratios, that crop up in many discussion on continental crust formation, and Th/La and Sr/Sr* (where $Sr/Sr^* = 2Sr_N/(Pr_N + Nd_N)$. e.g. Plank, 2005; Niu and O'Hara, 2009; Niu et al., 2013). Ocean arc volcanics show a similar pattern, but not enough enrichment, and are too basaltic to be the sole producer of continental crust (e.g. Fig. 6.6, and Niu et al., 2013). The rocks from this study have similar Th/La

to bulk continental crust (0.22 for Caucasus average, 0.28 for crust, although the average for the Greater Caucasus is 0.31. Lack of exposure of volcanics in the Greater Caucasus, and potential intrusive rocks not sampled, may mean that the high Th/La of the Greater Caucasus is under-represented in these calculations). However, the positive Sr-anomaly common to all arc-rocks, and this study, is unlike continental crust. The size of the anomaly in the Caucasus is smaller than many arcs ($Sr/Sr^* = 1.3$, island arc basalts have $Sr/Sr^* = 2.72 \pm 1.2$; Niu and O'Hara, 2009).

Although the post-collisional magmatism is not a perfect match for continental crust, it shares more similarities than do island- and continental-arc magmas that are so dominant in most models of continental crust formation. Another interesting aspect of continental crust being formed in collision zones, is the increased potential for preservation (Hawkesworth et al., 2010). Currently, at both oceanic and continental arc settings, addition of arc crust is balanced by losses through subduction erosion, and sediment recycling (e.g. Stern and Scholl, 2010). Accretionary orogens are capable of preserving juvenile continental crust produced at arcs, by accreting material onto the continent during continental collision (e.g. Condie, 2014). It is likely that this has occurred in the Eurasian-Arabian collision zone, with terranes such as the Pontide-Lesser Caucasus Arc. The post-collisional magmatism, which has been shown to be compositionally closer to bulk crust in this study, then adds further juvenile material to the crust, and as it already occurs within the orogen, is highly likely to be preserved.

In most calculations of continental growth/loss, this highly preservable, compositionally 'crustal material, is given very little consideration (e.g. Scholl and von Huene, 2007; Clift et al., 2009). This study has only considered magmatism expressed at the surface. The complex crustal plumbing system feeding this volcanism also has a high chance of preservation. Being associated with continental collision, means this magmatism is also consistent with continental crust formation being associated with the super-continent cycles (e.g. Hawkesworth et al., 2010; Cawood et al., 2012). As this type of magmatism is poorly studied (possibly due to its relative rarity on Earth today), it has not been recognised it in ancient orogens. Therefore, post-collisional magmatism is a mechanism for enhancing continental growth that may be under-estimated by many continental growth models.

6.4.2 Role in mountain building events

It is likely that this post-collisional magmatism is absent from most models of continental crust formation because it is not commonly recognised in other collisional orogens, either

today, or in the geological record. Most importantly, intense, mantle-derived magmatism has not been traditionally recognised in the Himalayas, the archetypal collisional orogen (assuming the small-volume potassic lavas of the Tibetan Plateau are not analogous to the calc-alkaline volcanism of the Caucasus, e.g. Williams et al., 2004). Therefore, the second area of possible importance for this magmatism, is to consider how integral it is to mountain building.

Broadly speaking, the collision of India and of Arabia with Eurasia are similar, so the Caucasus and Himalayas might be expected to be tectonically similar. The Caucasus are a younger orogen, so represent an earlier stage of the collision process. This magmatism may have occurred in the Himalayas already, but never reached the surface, so has not been identified. However, each orogen is unique. Although it would be nice for all continental collision zones to follow a single, simple model, it is also totally unrealistic because the complex mosaic of oceanic crust, island arcs, rigid continental blocks, sea-mounts and back-arc basins, that existed between Arabia and Eurasia before collision, would all affect what collides, what accretes, and what subducts. The presence of the Mediterranean to the west, allowing space for the Anatolian plate to move into after being squeezed out of the collision zone, and the related strike-slip faulting, also alters the local tectonic settings. The shape of the Arabian indenter, the contrasts in lithospheric thickness between Arabia, Eurasia and the Tethys basin, will have all affect mantle flow. It is these unique set of circumstances that have resulted in the intense, post-collisional volcanism of the Caucasus today. Each collision zone will have its own idiosyncrasies, perhaps promoting under-thrusting, or continental subduction, or discouraging slab-breakoff, or pathways for melts to pass through the crust.

This is not to say that the features seen in the Caucasus are a one-off. Compared to mid-ocean ridges, or island arcs, there are significantly fewer examples of active continent-continent collision zones to study today. With so few investigations into current post-collisional volcanism at the core of orogenic belts before the recent studies in the Caucasus (e.g. Neill et al., 2013, 2015; Nomade et al., 2016), it is not surprising that it has not been investigated in ancient collision zones. Recent work from the North Qaidam belt, NW China (Song et al., 2014) suggests a similar tectonic history to the Caucasus. It identifies post-collisional magmatism, post-dating the closure of the oceanic basin, and onset of continental collision, by 10–20 Ma, which is certainly similar to the situation in the Caucasus. Whilst this type of post-collisional magmatism is far from essential to the mountain building process, it is also unlikely to be unique to the Caucasus, and with careful analysis of well preserved sections, may be identified in other ancient collision zones.

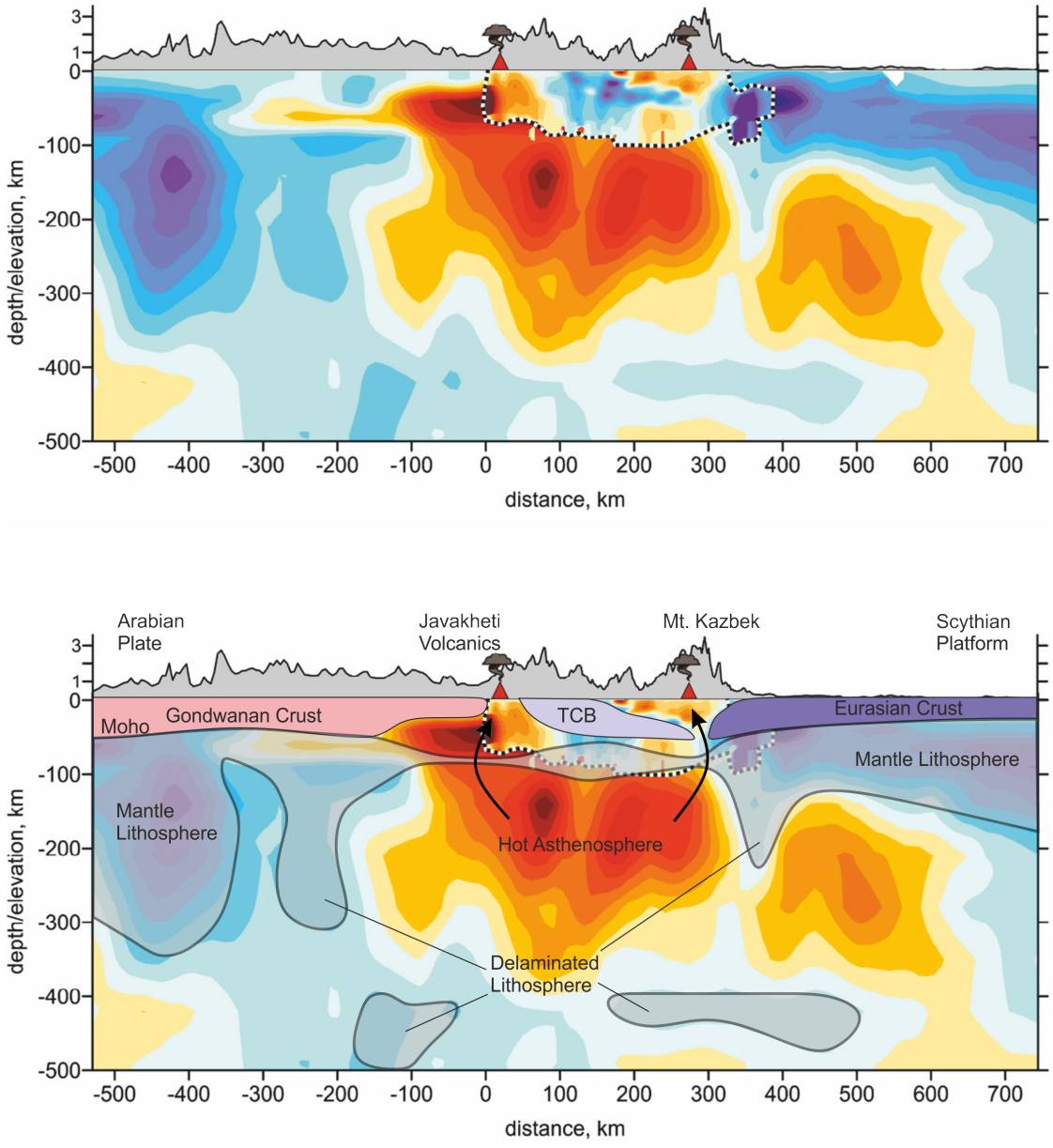

FIGURE 6.1: A regional model of the lithospheric structure beneath the Eurasia-Arabia collision zone, based on work by Koulakov et al. (2012), and the more detailed shallow model, within the dotted line beneath the Lesser and Greater Caucasus, of Zabelina et al. (2016). Blue colours represent cold areas, red areas are hot. The bottom diagram is an interpretation of the crust and lithosphere, based on this study and Zabelina et al. (2016). Three solid, rigid blocks are distinguished; the Eurasian crust, Trans-Caucasus block (TCB), and Gondwanan crust (representing the South Armenian Block, East Anatolian crust and the Arabian Plate). Black arrows show potential path of hot, rising asthenosphere. For details of the location of the section, and of the modelling used, see Zabelina et al. (2016).

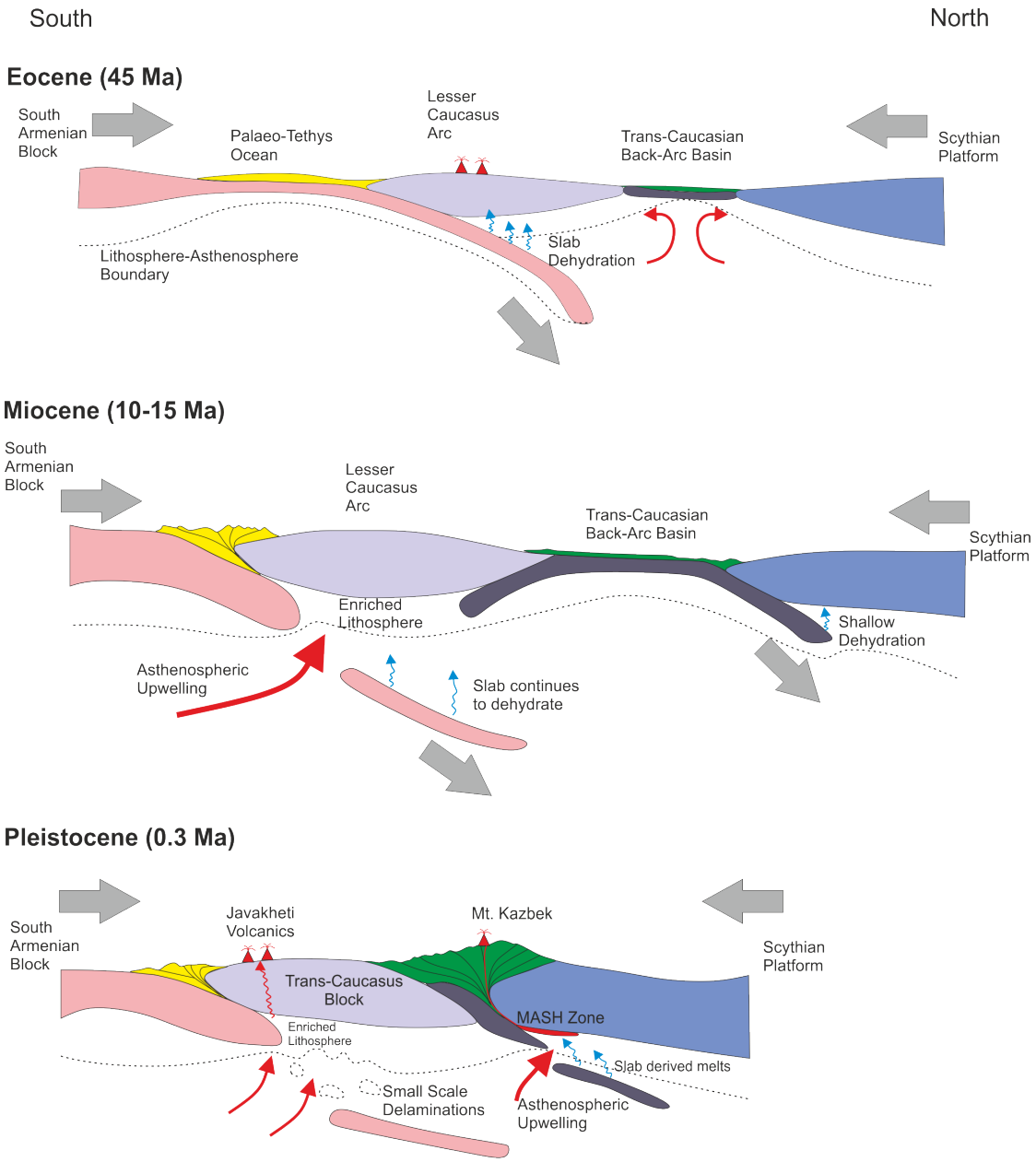

FIGURE 6.2: Sketch cross-sections across the Caucasus to show the development of the collision zone, and initiation of magmatism. Top section represents active subduction of Neo-Tethyan crust prior to collision. The Trans-Caucasian back-arc basin is opening, arc volcanism is erupting in the Lesser Caucasus, and slab dehydration is metasomatising the overlying mantle wedge, that will eventually cool to form an enriched lithosphere. The middle section shows break-o of the Neo-Tethys slab. The back-arc basin is beginning to close, and collision is beginning to occur, without active volcanism. The bottom section shows active volcanism beneath both the Lesser and Greater Caucasus, with break-o of the back-arc crust. Dotted line indicates the estimated base of the lithosphere. Solid coloured blocks are the major, rigid, crustal blocks. From S to N they are the South Armenian Block (and Neo-Tethys crust in the top section), Trans-Caucasian Block and Pontide-Lesser Caucasus Arc, and the Eurasian crust and Scythian Platform furthest north. Sketches are not to scale.

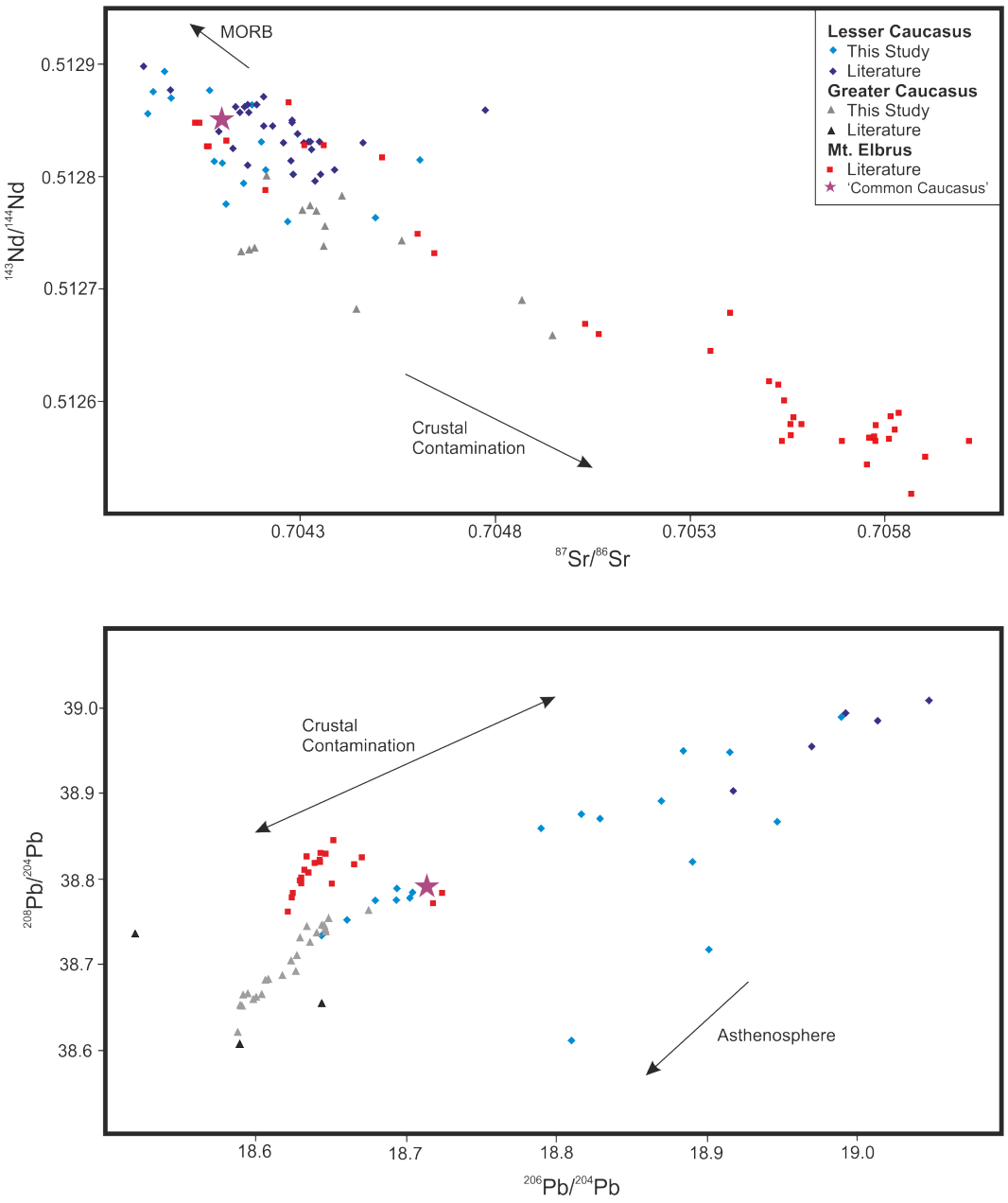

FIGURE 6.3: A comparison of the isotopic compositions of Mt. Elbrus, Mt. Kazbek (both Greater Caucasus) and the Lesser Caucasus volcanics. Literature values for the Lesser Caucasus are from Lebedev et al. (2007a); Neill et al. (2013, 2015), for the Mt. Kazbek region from Lebedev et al. (2014), and for Mt. Elbrus from Lebedev and Bubnov (2006); Lebedev et al. (2010a). Crustal contamination arrows are vectors based on crust collected as part of this study. The pink star represents a 'common Caucasus' mantle source composition suggested by Lebedev et al. (2010a). Their estimate, although based on a rather limited number of analyses, is generally consistent with this much larger compilation.

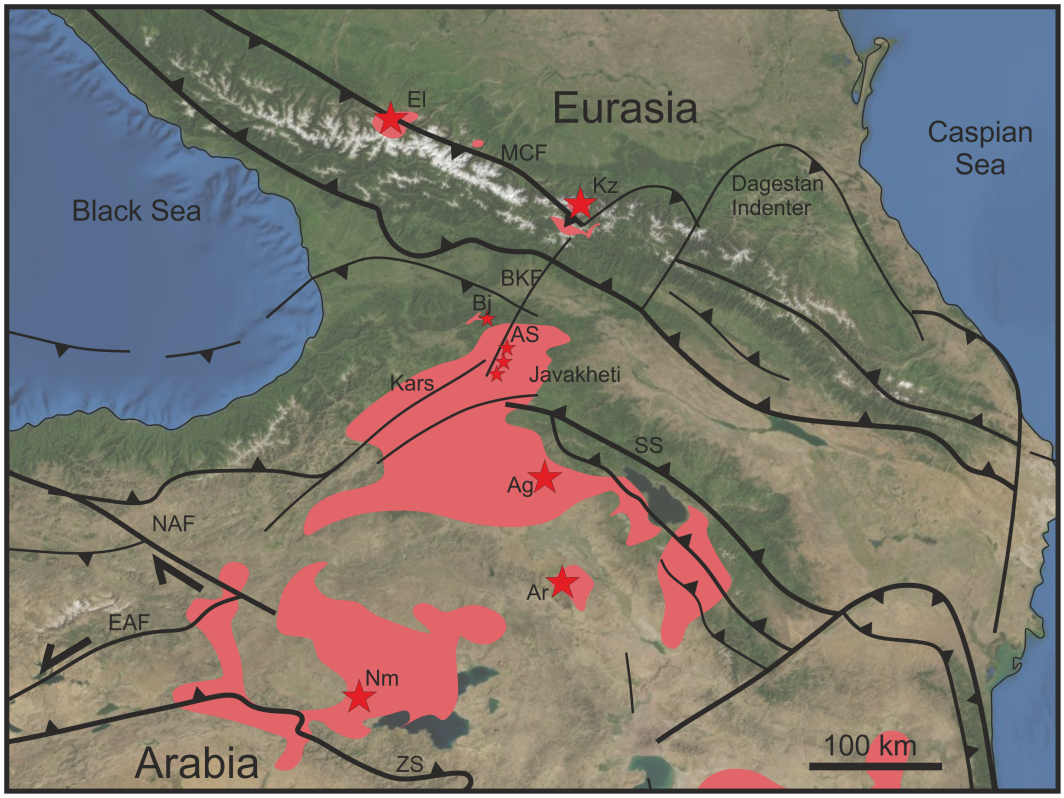

FIGURE 6.4: Map showing distribution of volcanics in the Arabia-Eurasia collision zone, and the relationship with major crustal structures. Red areas show extent of volcanism. Red stars show location of major volcanoes, and the Abul-Samsari and Borjomi formations. El - Mt. Elbrus, Kz - Mt. Kazbek, Bj - Borjomi Fm., AS - Abul-Samsari ridge, Ag - Aragats, Ar Ararat, Nm - Nemrut, MCF - Main Caucasus Thrust, BKF - Borjomi-Kazbek Fault, SS Sevan Suture, NAF - North Anatolian Fault, EAF - East Anatolian Fault, ZS - Zagros Suture. Distribution of volcanism based on (Adamia et al., 2011).

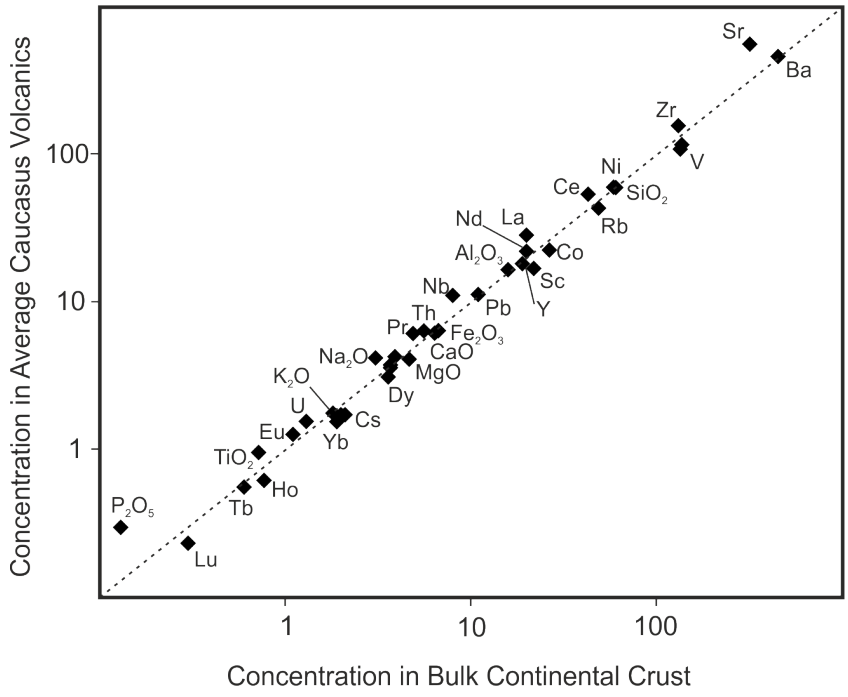

FIGURE 6.5: One-to-one plot for all measured elements of an average of all the post-collisional volcanic samples from this study, against bulk continental crust (Rudnick and Gao, 2003). Log scale is used to show all data with varying abundances. Concentration for trace elements is in ppm, whilst oxides are wt%. Dashed line is a 1:1 line to emphasise similarities.

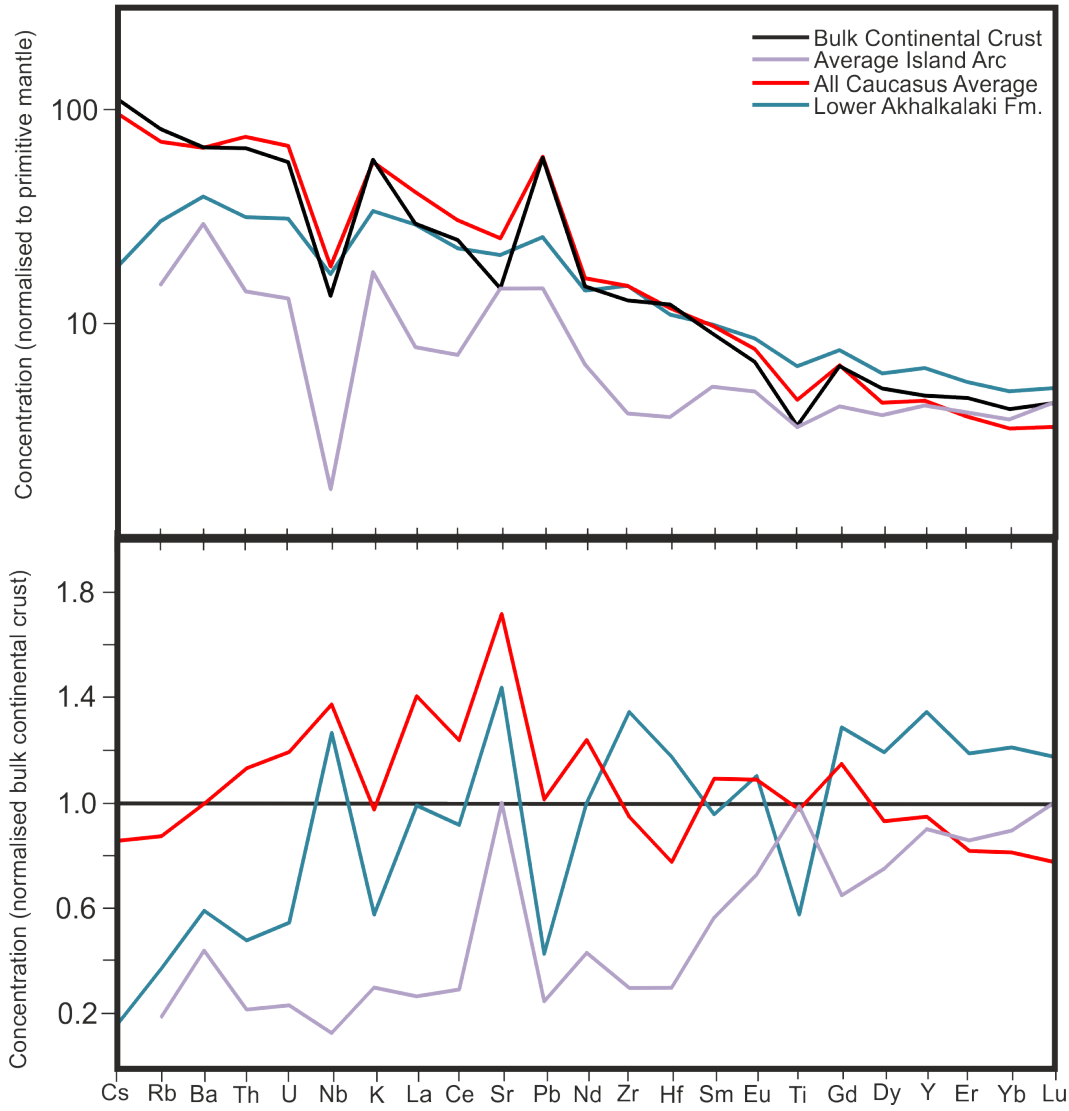

FIGURE 6.6: Top plot is a primitive-mantle normalised, trace-element variation plot comparing the patterns for bulk continental crust (Rudnick and Gao, 2003), an average oceanic arc (Hawkesworth and Kemp, 2006), an average of all post-collisional volcanics from the Caucasus (this study) and the Lower Akhalkalaki Fm. (this study). Normalising values from Palme and O'Neill (2014). Bottom plot shows same data, but normalised to bulk continental crust (Rudnick and Gao, 2003).

Chapter 7

Summary of Findings

This chapter presents a brief summary of the main findings from this study, before going on to consider ways it can be developed in the future.

- Georgia hosts two distinct areas of post-collisional volcanism related to the Arabia-Eurasia collision zone. The Javakheti Plateau in the Lesser Caucasus, composed to the Miocene Goderzi Fm., Pleistocene Akhalkalaki Fm., and Pliocene-Holocene Abul-Samsari Ridge, and Borjomi volcanics, is a northern continuation of volcanics studied in Armenia (Neill et al., 2013, 2015). The second area surrounds Mt. Kazbek in the Greater Caucasus. Mt. Kazbek, and Mt. Elbrus in Russia, are large stratovolcanos that represent the most northerly (and furthest from the main collision front, the Zagros Suture) expression of post-collisional volcanism, and have erupted through up to 60 km of crust.

- Volcanism in the Lesser Caucasus began at a similar time to a regional tectonic rearrangement and change to a more strike-slip style of deformation, rather than the earlier N-S compression. The source of this Goderzi Fm. remains poorly constrained, but seems to have a complex history, with multiple pulses of magmatism.

- The Akhalkalaki Fm. covered much of the Goderzi Fm. and represents the most voluminous phase of volcanism in the region. Pb-isotopes have shown that the large plateau forming, and valley-filling flows required an asthenospheric component. Subsequent volcanism in the region shows a more arc-like signature, with an enrichment of LILEs over HFSEs. However, subduction in the region ceased over 10 Ma prior to the onset of this volcanism. An important part of the model proposed as part of this project, is the refrigeration of the enriched lithosphere beneath the Lesser Caucasus crust, that maintained hydrated for up to 15 Ma. Slab-breako will

have introduced asthenosphere into the source region, but likely occurred well before the volcanism observed at the surface today. Small-scale convection of hydrated lithosphere, and related small-scale delamination events will have had a similar effect, and at the correct time for the Akhalkalaki Fm. Compositions similar to those of the lavas can be modelled by small-degree melting of spinel-peridotite, constraining the source to depths shallower than the garnet-stability field. The shift to strike-slip fault is likely to have played a role in the emplacement of the lavas.

- Whilst the Lesser Caucasus were highly volcanically active, the Greater Caucasus were undergoing significant uplift, but were volcanically quiet. The first magmatism in the Mt. Kazbek area occurred at 800,000 years ago, simultaneously with a final burst of activity in the Lesser Caucasus, along the Abul-Samsari ridge. Although contemporaneous and geochemically similar, separate sources and petrogeneses are proposed. Northward subduction of back-arc crust beneath the Greater Caucasus would have enriched the lithosphere, and give the trace-element patterns observed in the Mt. Kazbek volcanics. Input from sediment dehydration, and pyroxenite bearing slab melts are required, and likely formed a MASH zone at the base of the crust. Tearing and break-off of this slab caused an asthenospheric upwelling, and melting. The plumbing system beneath Mt. Kazbek is complex, and evidence is seen for replenishment of the system after a large caldera-forming event, with crustal storage moving deeper. Movement along the Borjomi-Kazbek strike-slip fault may have triggered both the Mt. Kazbek and Abul-Samsari volcanism, and may be related to the tearing of the back-arc slab. If this model is correct, it implies that the region may still be volcanically active, and eruptions likely to be migrating eastwards along the main ridge of the Greater Caucasus.

- Contamination with crustal material is observed, however contamination of the source with recycled crustal material is preferred in most cases over shallow AFC processes. It is therefore possible to consider the role of this magmatism in the formation of continental crust. Preservation potential is high, as eruptions are occurring within an orogen, and the chemistry more closely resembles bulk continental crust than that of more typical arc-lavas. It is proposed that post-collisional magmatism, such as this seen in the Caucasus, although not present in all collision zones, does impart a signature onto the bulk composition of continental crust, and should be included in future models of crust formation.

7.1 Future work

There are many possible ways in which this work can be taken further. This study covered as many flows and regions as possible within Georgia given logistical constraints. However much of the Abul-Samsari formation was not sampled, and this has proved to be one of the most interesting lithologies to compare with the magmatism of the Greater Caucasus. The other important region not sampled was the Keli Highlands, south of Mt. Kazbek. The Keli volcanics could be of real significance as their eruptive style (monogenetic cones), and timing, seems to match the Abul-Samsari volcanics. However, this region was not accessible due to conflict in South Ossetia.

With the samples collected, a more detailed investigation into the phenocryst phases could shed light onto their evolution in shallow magma chambers. Trace-element and Sr-isotope analysis across the complex zoning shown in plagioclase, predominantly in, but not restricted to, the Greater Caucasus, could give a much clearer picture of magma mixing and rejuvenation within the magma chamber. It may also reveal mixing of magmas with similar bulk-rock compositions, that might have appeared to reflect closed-system behaviour in this study, but actually might have had very different isotopic signature, and so represent open-system behaviour. This could be done quite simply with a combined EMPA, laser-ablation ICP-MS, and micro-drilling and TIMS approach. The composition of trapped melt in glomerocrysts could also be of interest.

Appendix A

Field Localities

In this appendix, the first three tables give the localities of every sample used in this study. Samples not collected in situ are given with the nearest settlement or GPS reading of the area where the float was collected. The final two tables give a very brief sample descriptions for a representative selection of samples.

TABLE A.1: Table of localities in Lesser Caucasus

Location					Location				
Sample	Latitude	Longitude	Altitude (m)	Place name	Sample	Latitude	Longitude	Altitude (m)	Place name
Goderzi Fm.					**Akhalkalaki**				
13-091	N 41° 28.889	E 43° 22.963	1335	Khando	NS-PhD-1	N 41° 30.586	E 44° 32.481	637	Dizveli
13-092				Khando	NS-PhD-2	N 41° 30.545	E 44° 32.554	641	Dizveli
13-094	N 41° 32.422	E 43° 15.63	1076	Atskuri	NS-PhD-3	N 41° 29.838	E 44° 36.465	617	Qosalari
14-023	N 41° 38.031	E 42° 31.864	1929	Goderzi Pass	NS-PhD-4	N 41° 29.834	E 44° 29.838	805	Qosalari
14-025	N 41° 34.277	E 43° 02.489	1341	Tskordza	NS-PhD-5	N 41° 21.046	E 44° 21.532	812	Damanisi
14-054	N 41° 21.172	E 44° 07.001	1450	Shakhmarlo	NS-PhD-6	N 41° 19.406	E 44° 11.870	1249	Damanisi
Scoria Cones					13-076	N 41° 39.647	E 44° 17.412	1717	Imera
13-081	N 41° 17.571	E 43° 43.62	2034	Lake Saghamo	13-077	N 41° 39.647	E 44° 17.412	1717	Imera
13-099	N 41° 22.476	E 43° 46.309	2063	Poka	13-078	N 41° 39.625	E 44° 16.774	1657	Imera
13-100	N 41° 22.476	E 43° 46.309	2063	Poka	13-079	N 41° 17.571	E 43° 43.62	2034	Lake Saghamo
13-101	N 41° 22.476	E 43° 46.309	2063	Poka	13-080	N 41° 17.571	E 43° 43.62	2034	Lake Saghamo
13-102	N 41° 22.476	E 43° 46.309	2063	Poka	13-082	N 41° 20.484	E 43° 29.624	1742	Kulalisi
14-030	N 41° 30.301	E 43° 52.221	2223	Lake Paravani	13-083	N 41° 17.789	E 43° 40.453	1951	Didi Aragiali
14-031	N 41° 30.301	E 43° 52.221	2223	Lake Paravani	13-084	N 41° 17.789	E 43° 40.453	1951	Didi Aragiali
14-032	N 41° 27.807	E 43° 51.841	2158	Lake Paravani	13-085	N 41° 23.903	E 43° 29.775	1782	Akhalkalaki
Borjomi					13-086	N 41° 23.903	E 43° 29.775	1782	Akhalkalaki
13-095	N 41° 50.102	E 43° 23.676	940	Borjomi	13-087	N 41° 24.79	E 43° 28.887	1687	Akhalkalaki
13-096	N 41° 50.51	E 43° 23.587	861	Borjomi	13-088	N 41° 24.63	E 43° 28.772	1673	Akhalkalaki
13-097	N 41° 50.51	E 43° 23.587	861	Borjomi	13-089	N 41° 24.63	E 43° 28.772	1673	Akhalkalaki
13-098	N 41° 50.483	E 43° 23.526	851	Borjomi	13-090	N 41° 25.342	E 43° 28.684	1629	Akhalkalaki
Abul-Samsari					14-027	N 41° 27.985	E 43° 24.802	1415	-
14-035	N 41° 29.427	E 43° 30.454	1737	Aragva	14-028	N 41° 27.840	E 43° 26.550	1497	-
14-036a	N 41° 29.658	E 43° 30.336	1726	Aragva	14-029	N 41° 27.499	E 43° 27.867	1557	Korkhi
14-038	N 41° 41.789	E 43° 42.558	2107	Mt. Tavkvetiki (Pipeline)	14-033	N 41° 26.515	E 43° 50.933	2121	Lake Paravani
14-039	N 41° 39.307	E 43° 41.674	2024	Mt. Shavnabada	14-034	N 41° 19.579	E 43° 23.031	1796	Vachiani
14-040	N 41° 39.397	E 43° 44.832	2012	Mt. Egoisari	14-036	N 41° 37.774	E 43° 33.973	2008	Lake Tabatskuri
14-041	N 41° 39.397	E 43° 44.832	2012	Mt. Egoisari	14-037	N 41° 39.377	E 43° 36.634	2023	Lake Tabatskuri
14-042	N 41° 39.027	E 43° 51.354	1707	Kizilkilisa	14-044	N 41° 35.603	E 44° 07.812	1358	Dashbashi
					14-045	N 41° 35.480	E 44° 07.566	1443	Dashbashi
					14-049	N 41° 30.612	E 44° 32.270	642	Dashbashi

TABLE A.2: Table of localities in Greater Caucasus

	Location					
Sample Name	Latitude	Longitude	Altitude (m)	Place Name	Flow?	Other
Gudauri Fm.						
13-001a	N 42°27.82	E 44°28.397	1651	Gudauri	Gudauri Flow	
13-001b	N 42°27.82	E 44°28.397	1651	Gudauri	Gudauri Flow	
13-002	N 42°26.243	E 44°29.598	1653	Gudauri	Gudauri Flow	
13-003	N 42°26.328	E 44°29.568	1730	Gudauri	Gudauri Flow	
13-005	N 42°28.828	E 44°28.344	2213	Gudauri	Surface flow	
13-006	N 42°29.979	E 44°27.077	2368	Jvari Pass	Surface flow	
13-075			2324	Gudauri	Surface flow	
H1	N 42°27.862	E 44°28.616	1632	Gudauri	Gudauri Flow	
H2	N 42°27.862	E 44°28.616	1641	Gudauri	Gudauri Flow	
H3	N 42°26.327	E 44°29.883	1727	Gudauri	Gudauri Flow	
H4	N 42°29.303	E 44°28.296	1632	Gudauri	Surface flow	
Keli Highlands						
13-009	N 42°34.981	E 44°34.849	2135	Truso Gorge	Truso Gorge	
13-010	N 42°34.842	E 44°28.008	2020	Truso Gorge	Truso Gorge	
Qabarjina Fm.						
13-011	N 42°33.597	E 44°30.739	1989	Kobi	Ukhati Flow	
13-044	N 42°34.568	E 44°34.477	2266		Qabarjina Cirque	Float
13-045	N 42°34.559	E 44°34.481	2285		Qabarjina Cirque	Float
13-046	N 42°34.643	E 44°34.123	2273		Qabarjina Cirque	Float
13-047	N 42°34.643	E 44°34.123	2273		Qabarjina Cirque	Float
13-048	N 42°34.643	E 44°34.123	2273		Qabarjina Cirque	Float
13-049	N 42°34.643	E 44°34.123	2273		Qabarjina Cirque	Float
13-050	N 42°34.643	E 44°34.123	2273		Qabarjina Cirque	Float
13-051	N 42°34.643	E 44°34.123	2273		Qabarjina Cirque	Float
13-052	N 42°34.643	E 44°34.123	2273		Qabarjina Cirque	Float
13-053	N 42°34.643	E 44°34.123	2273		Qabarjina Cirque	Float
13-054	N 42°34.246	E 44°31.677	2258	Kanobi	Agglomerate Flow	
13-055	N 42°35.584	E 44°33.298	1928		Agglomerate Flow	
H7	N 42°33.581	E 44°30.742	1942	Kobi	Ukhati Flow	
Sno						
13-068	N 42°35.442	E 44°39.480	1800	Koseli	Sno Valley	Float
13-069	N 42°35.442	E 44°39.480	1800	Koseli	Sno Valley	Float
Mt. Kazbek						
Stage I						
13-008a	N 42°35.051	E 44°28.44	2063	Kvemo Okrokana	Southern Flow	
13-008b	N 42°35.051	E 44°28.44	2063	Kvemo Okrokana	Southern Flow	

	Location					
Sample Name	Latitude	Longitude	Altitude (m)	Place Name	Flow?	Other
Mt. Kazbek (cont.)						
Stage II						
13-023	N 42°40.05	E 44°37.688	1835	Gergeti	Gergeti Valley	
13-024	N 42°40.063	E 44°37.659	1629	Gergeti	Gergeti Valley	
13-026	N 42°40.001	E 44°38.297	1764	Chkheri Valley	Chkheri Stack	
13-027	N 42°40.025	E 44°38.343	1820	Chkheri Valley	Chkheri Stack	
13-028	N 42°40.036	E 44°38.372	1857	Chkheri Valley	Chkheri Stack	
13-029	N 42°40.114	E 44°38.254	1899	Chkheri Valley	Chkheri Stack	
13-030	N 42°40.114	E 44°38.254	1899	Chkheri Valley	Chkheri Stack	
13-031	N 42°40.111	E 44°38.24	1899	Chkheri Valley	Chkheri Stack	
13-032	N 42°40.068	E 44°38.277	1833	Chkheri Valley	Chkheri Stack	
13-033a	N 42°34.568	E 44°34.477	2264		Chkheri Stack	
13-034	N 42°34.568	E 44°34.477	2264		Chkheri Stack	
13-035	N 42°41.584	E 44°38.151	1768	Tsdo	Tsdo Flows	
13-036	N 42°41.302	E 44°38.139	1737	Tsdo	Tsdo Flows	
13-037	N 42°41.302	E 44°38.139	1737	Tsdo	Tsdo Flows	
13-038	N 42°41.665	E 44°38.501	1609	Tsdo	Tsdo Flows	
13-039	N 42°40.372	E 44°38.275	1610		Tsdo Flows	
13-040	N 42°40.266	E 44°37.842	1884	Chkheri Valley	Chkheri Tuff	
13-041	N 42°40.266	E 44°37.842	1884	Chkheri Valley	Chkheri Tuff	
13-042	N 42°40.266	E 44°37.842	1884	Chkheri Valley	Chkheri Tuff	
13-043	N 42°40.266	E 44°37.842	1884	Chkheri Valley	Chkheri Tuff	
13-059	N 42°37.879	E 44°36.759	1827	Pansheti	Arsha Flows	
13-060	N 42°37.879	E 44°36.759	1827	Pansheti	Arsha Flows	
13-061	N 42°37.879	E 44°36.759	1827	Pansheti	Arsha Flows	
13-062	N 42°37.705	E 44°36.245	1787	Arsha	Arsha Flows	
13-063	N 42°37.369	E 44°35.647	1888	Gaiboteni	Arsha Flows	
13-064	N 42°37.458	E 44°35.583	1951	Gaiboteni	Arsha Flows	
13-065	N 42°37.477	E 44°35.638	1999	Gaiboteni	Arsha Flows	
13-066	N 42°37.523	E 44°35.523	2004	Gaiboteni	Arsha Flows	
13-067	N 42°37.523	E 44°35.523	2004	Gaiboteni	Arsha Flows	
Stage III						
13-025	N 42°40.019	E 44°37.799	1816	Gergeti	Gergeti Valley	
13-056	N 42°39.556	E 44°34.576	2922		Glacier Flows	
13-057	N 42°39.63	E 44°34.496	2938		Glacier Flows	
13-058	N 42°39.984	E 44°36.185	2442		Glacier Flows	
13-070	N 42°40.273	E 44°37.235	1798	Chkheri Valley	Gergeti Valley	
13-071	N 42°40.273	E 44°37.235	1798	Chkheri Valley	Gergeti Valley	
13-072				Chkheri Valley	Gergeti Valley	Float
13-073				Chkheri Valley	Gergeti Valley	Float
13-074				Chkheri Valley	Cumulate	Float
Stage IV						
KZ-1	N 42°36.243	E 44°34.486		Goristsikhe	6000 year flow	
H5	N 42°36.277	E 44°34.457	1641	Goristsikhe	6000 year flow	
H6	N 42°36.344	E 44°34.484	1727	Goristsikhe	6000 year flow	
13-012	N 42°34.571	E 44°34.476	2261	Goristsikhe	6000 year flow	

TABLE A.3: Table of localities of basement samples. All Main Range samples were collected as float. Samples from all other localities were collected in situ.

	Location			
Sample Name	Latitude	Longitude	Altitude (m)	Place name
Main Range (All samples were collected as float)				
14-007	N 43° 07.389	E 42° 35.238	1893	Mazeri
14-008	N 43° 07.389	E 42° 35.238	1893	Mazeri
14-009	N 43° 07.389	E 42° 35.238	1893	Mazeri
14-010	N 43° 07.389	E 42° 35.238	1893	Mazeri
14-012	N 43° 07.389	E 42° 35.238	1893	Mazeri
14-014	N 43° 07.389	E 42° 35.238	1893	Mazeri
14-015	N 43° 07.389	E 42° 35.238	1893	Mazeri
14-016	N 43° 07.389	E 42° 35.238	1893	Mazeri
14-017	N 43° 07.389	E 42° 35.238	1893	Mazeri
14-018	N 43° 06.510	E 42° 44.602	1659	Mestia
14-019	N 43° 06.510	E 42° 44.602	1659	Mestia
14-020	N 43° 06.510	E 42° 44.602	1659	Mestia
14-021	N 43° 06.510	E 42° 44.602	1659	Mestia
14-022	N 43° 06.510	E 42° 44.602	1659	Mestia
Dzirula Massif				
14-001	N 42° 04.185	E 43° 28.815	861	Grigalati
14-002	N 42° 05.189	E 43° 28.007	810	Grigalati
14-003	N 42° 06.194	E 43° 12.706	281	Ubisa
Dizi Fm.				
14-004	N 42° 58.978	E 42° 14.018	428	Lukhi
14-005	N 43° 02.070	E 42° 20.908	921	Dizi
Khrami Massif				
14-043	N 41° 35.597	E 44° 07.634	1338	Dashbashi
14-046	N 41° 32.485	E 44° 07.344	1400	Khramhesi
14-047	N 41° 32.511	E 44° 09.030	1039	Khramhesi
14-048	N 41° 32.611	E 44° 09.223	1030	Khramhesi
Loki Massif				
14-050	N 41° 17.517	E 44° 19.145	972	Saparlo
14-051	N 41° 16.939	E 44° 19.655	1024	Saparlo
14-052	N 41° 15.776	E 44° 22.299	1312	Lokjandari
14-053	N 41° 16.939	E 44° 19.655	1024	Saparlo
Mt. Kazbek (Russian Border)				
13-004	N 42° 28.828	E 44° 28.344	2213	Gudauri
13-007	N 42° 32.774	E 44° 29.443	2065	Alamsiani
13-013	N 42° 41.315	E 44° 38.266	1624	Tsdo
13-014	N 42° 41.315	E 44° 38.266	1624	Tsdo
13-015	N 42° 41.315	E 44° 38.266	1624	Tsdo
13-016	N 42° 43.784	E 44° 37.783	1612	Russian Border
13-017	N 42° 43.784	E 44° 37.783	1612	Russian Border
13-018	N 42° 43.784	E 44° 37.783	1612	Russian Border
13-019	N 42° 43.784	E 44° 37.783	1612	Russian Border
13-020	N 42° 42.62	E 44° 37.638	1607	Gveleti
13-021	N 42° 42.62	E 44° 37.638	1607	Gveleti
13-022	N 42° 42.62	E 44° 37.638	1607	Gveleti

TABLE A.4: Brief sample descriptions for rocks of the Lesser Caucasus

Sample	% Phen	Phenocrysts						Groundmass Texture
		Ol	Cpx	Opx	Plag	Amph	Oxide	
Goderzi Fm.								
14-053	30				80		20	Chloritised
Lower Akhalkalaki Fm.								
14-026	-		30		70			Ophitic
14-027	-		25	5	70			Ophitic. Carbonate bearing
14-028	-	25		15	60			Coarse, holocrystalline, with carbonates
14-044	60	15	4	1	80			Fine grained, plag, oxides, glass
14-049	-	12		8	80			Ophitic
NS-PhD-1	-	15	15	5	65			Ophitic
NS-PhD-2	-	20	15	5	60			Ophitic
NS-PhD-3	-	5	5	15	60		15	Ophitic
NS-PhD-4	-	5	10	10	60		15	Ophitic
NS-PhD-5	-	20	15	5	50		10	Ophitic. Recrystallised px and plag
NS-PhD-6	-	20	10		65		5	Ophitic. Recrystallised px and plag
Upper Akhalkalaki Fm.								
14-030	10		10	20	70			Very fine, trachytic
14-033	15			40	60			30% Vesicles, glassy groundmass
Scoria Cone								
14-031	10		45	5	50			35% Vesicles
Abul-Samsari Fm.								
14-035	40				75	25		Glassy
14-038	5	10	50	40				Glassy, weakly trachytic
14-040	20			5	55	40		Glassy, 20% vesicles
14-041	15				60	30	10	15% Vesicles
14-045	10	5					10	Fine trachytic texture

TABLE A.5: Brief sample descriptions for rocks of the Greater Caucasus

Sample	Formation	% Phen	Phenocrysts								Groundmass Texture
			Ol	Cpx	Opx	Plag	Amph	HAP	Oxide	Bt	
H1	Gudauri	20		5	35	15	30	15			Glassy with plag microphenocrysts, some allignment
H2	Gudauri	25		10	60	20		10	Tr		Pilotaxitic with plag microphenocrysts
H3	Gudauri	20		5	70	15	5	5	Tr		Glassy with plag microphenocrysts, some allignment
H4	Gudauri	5		40	60				Tr		Coarse plag + opx
13-001	Gudauri	30	Tr			72	13	5	Tr		Pilotaxitic with plag microphenocrysts
13-002	Gudauri	15		5	25	70					Glassy with plag microphenocrysts, some allignment
13-005	Gudauri	60	7	13		80			Tr		Pilotaxitic with plag microphenocrysts
H7	Qabarjina	45			15	65	20				Glassy, few plag microphenocrysts
13-048	Qabarjina	35			10	70	20				Glassy, allinged plag microphenocrysts
13-049	Qabarjina	65			5	80	15				Glassy
13-053	Qabarjina	30			10	70	20				Glassy, allinged plag microphenocrysts
13-055	Qabarjina	40			5	60	30			5	Glassy, localised allignment of plag microphenocrysts
13-008	Stage I	65		25	10	65			Tr		Glassy, localised allignment of plag microphenocrysts
13-026	Stage II	50		10	35	40	5		5		Very fine, plag and oxide rich
13-028	Stage II	40			5	75	20		Tr		Glassy, plag microphenocrysts, no allignment
13-030	Stage II	50			15	75	5		5		Very fine to glassy
13-034	Stage II	60		5	25	60	10		Tr		Glassy to fine
13-035	Stage II	40	5	25	10	40	20		Tr		Pilotaxitic with plag microphenocrysts
13-037	Stage II	30	20	15	10	45		10			Glassy, alligned plag microphenocrysts
13-038	Stage II	50			10	65	25		Tr		Glassy, plag microphenocrysts, no allignment
13-043	Stage II	60		5	20	70	5		Tr		Glassy
13-059	Stage II	60		10	2	60	25		3		Very fresh glass
13-025	Stage III	25		20	15	30	30	2	Tr		Quite Coarse: plag-opx-oxide
13-070	Stage III	20		25	10	30	35		Tr		Quite Coarse: plag-opx-oxide
13-073	Stage III	15		60		20	20		Tr		Quite Coarse: plag-opx-oxide
H5	Stage IV	30				60	30	10	Tr		Glassy with plag and oxide microphenocrysts
H6	Stage IV	10			5	45	50				Glassy
KZ1	Stage IV	40									Glassy
13-012	Stage IV	30				55	40		Tr	5	Glassy with plag and oxide microphenocrysts
13-068	Sno	75		2	10	60	20		3	3	Fine, no allignment
13-069	Sno	75			5	65	25			5	Fine, no allignment
13-009	Keli	40	Tr		5	75	20		Tr		Glassy and vesicular

Appendix B

Analytical Techniques

B.1 Sample Preparation

Approximately 0.3–1 kg of the freshest material was collected from the field from each locality. Larger samples were collected of coarser grained rocks to be more representative of the lithology. Weathered surfaces were removed using either a diamond tipped rock saw or a hydraulic rock splitter. A portion of the sample was retained for thin sectioning and petrography. The remaining portion of the sample was placed in a hardened-steel jaw crusher to produced chips <8 mm in size. A random sub-sample of this was powdered for 7 minutes in an agate tema, or until it had a fine, talc-like texture. All equipment was cleaned with distilled water between each sample.

B.2 Laboratory Reagents and Cleaning Procedures

A two step procedure was used for purification of HCl and HNO_3. Quartz distilled (QD) grade acid was produced by sub-boiling analytical grade acid in a quartz still. Thermal distillation of QD grade acid in a Teflon still produced Teflon distilled (TD) grade acid. HF was purified from Aristar grade reagents by thermal distillation in a Teflon still. All water used was purified through a Millipore filtration system (MQ) to a resistivity of >18.4 MΩ. TD grade acids were titrated and diluted with MQ water to the required molarity. Before dissolution, Teflon beakers were cleaned using the following procedure:

- Rinse with MQ H_2O.
- Boil the beaker for 10 minutes in MQ H_2O, then leave to dry.

- Add 1 ml of analytical grade HF and 1 ml QD HNO_3 to each beaker. Seal and leave overnight on a hotplate at 120^{circ}C.
- Discard acid. Rinse three times with MQ H_2O and leave to dry.
- Add 1 ml of TD HF and 1 ml TD HNO_3 to each beaker. Seal and leave on a hotplate at 120^{circ}C overnight.
- Discard acid. Rinse three times with MQ H_2O and leave to dry.
- Add 1.5 ml TD HNO_3 to each beaker. Seal and leave on a hotplate at 120^{circ}C overnight.
- Discard acid. Rinse three times with MQ H_2O and leave to dry.
- Add 1.5 ml TD HCl to each beaker. Seal and leave on a hotplate at 120^{circ}C overnight.
- Discard acid. Rinse three times with MQ H_2O and leave to dry.

HDPE bottles (125 ml and 250 ml) were used to store ICP-MS standard and sample solutions, and isotope standard solutions. Polyprolene centrifuge tubes (15 ml and 50 ml)were used for running Sr isotope standards and samples. Bottles and tubes were cleaned with cold 2% TD HNO_3 both the right way up, and upside down overnight.

Pipette tips and columns were boiled at 120^{circ}C overnight in 2% TD HNO_3, then rinsed twice with MQ H_2O and left to dry. Eppendorf 1.5 ml and 2 ml safe-lock tubes were used for running Pb, Nd and Hf isotope samples, and were cleaned by boiling at 80^{circ}C overnight in 2% TD HNO_3, then rinsing twice with MQ H_2O and leaving to dry.

B.3 Major Element Analysis

B.3.1 X-Ray Florescence (XRF)

XRF was used to analyse 119 samples for major element composition and loss on ignition (LOI). Glass disks for major element analyses were made by mixing 0.700 g of dried rock powder with dried lithium metaborate-tetraborate flux (Spectraflux 100B) in a ratio of 1:5 by weight, and then fused in a mue furnace for 15–20 minutes at 1100^{circ}C, based on the method of Ramsey et al. (1995).

XRF analysis was undertaken at the Open University using an ARL 8420+ dual goniometer wavelength-dispersive XRF spectrometer. Element intensity data were

corrected for background and significant peak overlap interferences. See Ramsey et al. (1995) for details regarding conditions of element determination. Two rock standards, WS-E and OU-3, were used to correct for instrumental drift. External reproducibility of WS-E and OU-3 is better than ±2.5% (2 s.d.) for oxides with a concentration greater than 0.25 wt%. See Table B.1 for details. LOI was calculated by heating the sample at 1000^{circ}C for approximately 40 minutes, and measuring the percentage mass loss of volatiles (H_2O, CO_2, F, Cl, S)

B.4 Trace Element Analysis

B.4.1 X-Ray Florescence

Pressed powder pellets analysed by XRF spectrometry at the Open University were used to determine trace element abundances (Sc, V, Cr, Co, Ni, Cu, Zn, Ga, As, S, Rb, Sr, Y, Zr, Nb, Mo, Ba, Pb, Th, U). Pellets were made by mixing 9–10 g of rock powder with 0.7–0.9 ml of polyvinylpyrrolidone-methylcellulose binding solution using the method of Watson (1996). The mixture was compressed at approximately 0.79×10^6 kPa, and then dried overnight at 100^{circ}C. Analyses were carried out using the method outlined in B.3.1, with further details in Ramsey et al. (1995). Instrumental drift and precision were monitored using standards BHVO-1, QLO-1, DNC-1, W-2 (Table B.2).

	SiO_2	TiO_2	Al_2O_3	Fe_2O_3	MnO	MgO	CaO	Na_2O	K_2O	P_2O_5	LOI	Total
WS-E												
13/05/2013	51.18	2.43	13.87	13.19	0.17	5.59	8.99	2.44	1.00	0.31	0.85	100.02
13/05/2013	51.25	2.43	13.91	13.19	0.17	5.58	9.01	2.45	1.00	0.31	0.85	100.15
08/11/2012	51.09	2.42	13.91	13.14	0.17	5.54	9.02	2.41	1.00	0.30	0.85	99.85
08/11/2012	51.14	2.43	13.89	13.16	0.17	5.59	9.06	2.44	1.01	0.30	0.85	100.02
23/09/2013	51.27	2.43	13.87	13.16	0.17	5.59	8.97	2.45	1.01	0.31	0.85	100.09
23/09/2013	51.33	2.42	13.82	13.12	0.17	5.55	8.91	2.43	1.00	0.30	0.85	99.89
13/11/2013	51.14	2.42	13.90	13.16	0.18	5.56	8.99	2.41	0.99	0.30	0.85	99.90
13/11/2013	51.19	2.41	13.91	13.15	0.17	5.58	8.97	2.41	0.99	0.30	0.85	99.95
13/12/2013	51.17	2.42	13.96	13.14	0.17	5.56	9.01	2.48	1.00	0.31	0.85	100.07
13/12/2013	51.14	2.44	13.93	13.16	0.18	5.59	9.02	2.43	1.00	0.30	0.85	100.04
15/08/2014	51.14	2.41	13.80	13.13	0.17	5.53	8.97	2.40	1.00	0.30	0.85	99.70
15/08/2014	51.06	2.41	13.83	13.12	0.17	5.54	8.94	2.39	0.99	0.30	0.85	99.61
17/10/2014	51.29	2.43	13.95	13.18	0.17	5.60	9.09	2.45	1.01	0.31	0.85	100.34
17/10/2014	51.24	2.44	13.95	13.20	0.17	5.55	9.11	2.45	0.99	0.30	0.85	100.26
Average	51.19	2.42	13.89	13.16	0.17	5.57	9.00	2.43	1.00	0.30	0.85	100.00
2 s.d.	0.16	0.02	0.10	0.05	0.003	0.05	0.11	0.05	0.007	0.01		
2 r.s.d.%	0.31	0.86	0.72	0.37	1.99	0.86	1.24	2.03	1.08	2.17		
Recommended	51.10	2.42	13.78	13.15	0.17	5.55	8.95	2.47	1.00	0.30	0.85	99.75
OU-3												
13/05/2013	74.06	0.22	10.98	3.84	0.09	-	0.21	3.70	4.55	-	1.82	99.51
13/05/2013	74.09	0.22	10.98	3.85	0.09	-	0.20	3.71	4.56	-	1.82	99.56
08/11/2012	74.10	0.23	11.10	3.86	0.09	-	0.20	3.72	4.58	-	1.82	99.74
08/11/2012	74.12	0.23	11.06	3.86	0.09	-	0.21	3.73	4.58	-	1.82	99.74
23/09/2013	74.18	0.23	10.99	3.86	0.09	-	0.21	4.01	4.58	-	1.82	100.02
23/09/2013	74.15	0.22	10.98	3.86	0.09	-	0.21	4.04	4.54	-	1.82	99.98
13/11/2013	74.05	0.23	11.13	3.88	0.09	-	0.21	3.72	4.54	-	1.82	99.71
13/11/2013	74.04	0.22	11.14	3.87	0.09	-	0.21	3.71	4.55	-	1.82	99.70
13/12/2013	73.93	0.23	11.09	3.85	0.09	-	0.21	3.72	4.55	-	1.82	99.53
13/12/2013	73.89	0.22	11.09	3.85	0.09	-	0.21	3.76	4.56	-	1.82	99.54
15/08/2014	74.29	0.22	11.02	3.85	0.09	-	0.21	3.70	4.57	-	1.82	99.81
15/08/2014	74.25	0.22	10.99	3.85	0.09	-	0.20	3.72	4.54	-	1.82	99.74
17/10/2014	74.07	0.23	11.05	3.85	0.09	-	0.21	3.67	4.54	-	1.82	99.57
17/10/2014	73.99	0.23	11.07	3.87	0.09	-	0.21	3.66	4.53	-	1.82	99.54
Average	74.09	0.22	11.05	3.86	0.09	-	0.21	3.75	4.55	-	1.82	99.69
2 s.d.	0.22	0.01	0.11	0.02	0.002		0.01	0.23	0.03			
2 r.s.d. %	0.30	3.18	1.04	0.57	2.37		3.90	6.21	0.67			
Recommended	74.09	0.224	11.11	3.83	0.09	-	0.20	3.68	4.55	-	1.82	99.59

TABLE B.1: Compilation of major element XRF data for rock standards WS-E and OU-3 for various days of analyses. Values represent wt % oxide. Recommended values from Govinaraju et al. (1994) and Thompson et al. (2000)

	Rb	**Sr**	**Y**	**Zr**	**Nb**	**Ba**	**Pb**	**Th**	**U**	**Sc**	**V**	**Cr**	**Co**	**Ni**	**Cu**	**Zn**	**Ga**	**Mo**	**As**	**S**
L.O.D	*2*	*2*	*2.0*	*2*	*1.5*	*12*	*5*	*4*	*3*	*5*	*5*	*4*	*2*	*3*	*3*	*3*	*3*	*2*	*5*	*50*
BHVO-1																				
Average	9	403	28	176	19	135	-	-	-	32	316	288	46	121	138	108	22	-	-	215
2 s.d	1	4	1	5	2	7				3	9	6	6	4	5	9	1			55
% error	11	1	4	3	8	5				9	3	2	13	3	4	9	6			26
Recommended	11	403	28	179	19	139	3	1	0	32	317	289	45	121	136	105	21	1	0	102
QLO-1																				
Average	74	335	25	190	11	1402	20	6	-	9	50	5	7	5	26	57	17	-	3	76
2 s.d	1	3	1	4	1	20	2	2		2	9	2	2	2	2	1	1		2	22
% error	2	1	3	2	9	1	8	37		21	19	44	23	42	6	2	7		86	29
Recommended	74	336	24	185	10	1370	20	4	1.94	9	54	3	7	5	29	61	17	2	3	30
DNC-1																				
Average	4	148	19	40	3	108	6	-	-	32	147	287	60	238	87	63	15	-	-	477
2 s.d	1	2	1	2	1	11	2			4	8	11	3	4	3	1	1			18
% error	22	1	5	4	31	10	31			12	6	4	5	2	3	2	8			4
Recommended	5	145	18	41	3	114	6	6	0.1	31	148	285	54	247	96	66	15	1	0	392
W2																				
Average	21	201	23	96	8	177	8	-	-	37	261	95	46	69	105	83	19	-	-	263
2 s.d	1	2	1	3	1	12	3			2	6	3	3	2	3	2	2			21
% error	4	1	3	3	11	7	43			6	2	3	7	3	2	2	8			8
Recommended	20	194	24	94	8	182	9	2	0.5	35	262	93	44	70	103	77	20	1	1	79

TABLE B.2: Trace-Element standard data and reproducibility for standards BHVO-1, QLO-1, DNC-1, W2 measured by XRF. Values quoted in ppm. L.O.D. shows the limit of detection. - represents analyses below L.O.D. Recommended values taken from Potts et al. (1992)

B.4.2 Inductively Coupled Plasma Mass Spectrometry (ICP-MS)

B.4.2.1 Dissolution Procedure

117 samples were dissolved and analysed by Inductively Coupled Plasma Mass-Spectrometry (ICP-MS) at the Open University. Samples were dissolved in batches of 20–25, including at least one total procedural blank (TPB) and BE-N as a repeat reference sample. Reference materials were selected based on similarities in composition to those of the samples, as well as covering the whole range of compositions in our samples. The reference materials chosen were BE-N, BHVO-2, AGV-1, BIR-1, DNC-1 and W2. Clean Teflon beakers (see section B.2) were used for dissolution of the rock powder using the following procedure:

- 0.1 g of rock powder is dissolved in 0.5 ml concentrated TD HNO_3 and 2 ml concentrated TD HF. The beaker is then sealed and left on the hotplate at 120^{circ}C for at least 24 hours.
- The solution is dried down, and then taken up in 2 ml 6M cupola grade HCl, sealed and left on the hotplate overnight at 120^{circ}C.
- The solution is dried down, and then taken up in 2 ml concentrated TD HNO_3 and 4 ml MQ H_2O, sealed and left on the hotplate overnight at 120^{circ}C.
- The solution is dried down, and then taken up in 3 ml concentrated TD HNO_3 and 6 ml MQ H_2O, sealed and left on the hotplate overnight at 120^{circ}C.
- The solution is then transferred to a clean 125 ml HDPE bottle and made up to 100 g with MQ H_2O to create a 2% HNO_3 solution with a 1000-fold dilution of the original sample.

B.4.2.2 ICP-MS Analysis

Solutions were analysed using an Agilent 7500a fitted with a standard quartz spray chamber and a Babington nebuliser. Samples were aspirated at ~400 μl.min^1. CeO^+/Ce was used to monitor oxide interferences, and were kept low at less than 0.5 %. Interference from doubly charged species were kept below 1.4 %, usually being less than 1 % (Ce^{++}/Ce^+). Detection limits for the instrument are <10 ppt in solution (equivalent to 10 ppb in the rock, as samples were run at a 1000 fold dilution), for elements with atomic masses greater than 85. For lighter elements, detection limits are between 10 and 100 ppt in solution (10–100 ppb in the rock).

Five reference materials were run at the start of each run, to which the samples were standardised against. Data was corrected for drift using two monitor solutions (BE-N and DNC-1), which were re-run at intervals of every 4–6 samples throughout the run. These two monitor solutions were also used to assess external reproducibility. Accuracy and precision is shown in Table B.3. Precision was typically <3% (2 s.d.), although Th and U were slightly worse (4.5–6.5%). Problems were encountered washing out Ta often giving very poor precision, and very poor accuracy, and varied wildly day to day. Because of this the Ta data has not been used in this investigation.

A total procedural black (TPB) was also measured. When greater than the limit of detection, it typically measured <5 ppb for any given element, which is typically below 0.2% of any given measurement falling well within the precision of the instrument.

DNC-1	Li	Sc	V	Cr	Co	Ni	Cu	Zn	Ga	Rb	Sr	Y	Zr	Nb	Mo	Sn	Sb	Cs	Ba
10 Oct '14 n = 5	5.43	31.8	159	294	58.4	261	96.1	63.6	13.3	3.72	149	18.3	36.0	1.77	0.150	1.62	0.871	0.215	107
2 s.d	0.146	1.40	5.72	7.70	2.25	3.85	1.64	1.34	0.244	0.104	3.63	0.416	0.762	0.308	0.007	0.057	0.019	0.006	0.890
2 s.d. %	2.7	4.4	3.6	2.6	3.9	1.5	1.7	2.1	1.8	2.8	2.4	2.3	2.1	17.4	4.6	3.5	2.2	2.9	0.8
Average	**5.04**	**30.7**	**150**	**280**	**54.8**	**246**	**94.5**	**63.2**	**12.9**	**3.53**	**139**	**17.6**	**34.4**	**4.23**	**0.157**	**1.82**	**0.863**	**0.208**	**101**
Accepted	*5.08*	*31.1*	*157*	*291*	*57*	*264*	*86*	*57*	*13.3*	*3.6*	*141*	*18.0*	*36.4*	*1.56*	*0.121*	*2.46*	*0.87*	*0.213*	*105*
BEN																			
9th July '14 n = 6	14.2	24.3	250	378	60.7	275	74.9	122	17.9	48.4	1335	30.8	276	125	2.50	2.58	0.178	0.78	1104
2 s.d	0.355	1.40	6.72	7.70	2.07	6.55	1.14	1.28	0.480	2.21	60.2	1.21	9.51	3.14	0.061	0.042	0.007	0.024	30.6
2 s.d. %	2.5	5.8	2.7	2.0	3.4	2.4	1.5	1.0	2.7	4.6	4.5	3.9	3.4	2.5	2.4	1.6	3.8	3.0	2.8
Average	**13.3**	**23.2**	**238**	**353**	**56.9**	**251**	**72.2**	**114**	**17.4**	**47.6**	**1328**	**29.8**	**270**	**115**	**2.47**	**2.36**	**0.182**	**0.738**	**1032**
Accepted	*12*	*22*	*235*	*360*	*61*	*267*	*72*	*120*	*17*	*47*	*1370*	*30*	*265*	*100*	*2.51*	*2.4*	*0.23*	*0.8*	*1025*

DNC-1	La	Ce	Pr	Nd	Sm	Eu	Gd	Tb	Dy	Ho	Er	Yb	Lu	Hf	Ta	Pb	Th	U
10 Oct '14 n = 5	3.69	8.16	1.13	4.96	1.44	0.591	2.00	0.393	2.68	0.637	1.93	1.96	0.291	0.972	0.346	5.94	0.263	0.060
2 s.d	0.052	0.095	0.019	0.089	0.029	0.006	0.035	0.009	0.074	0.004	0.035	0.083	0.006	0.034	0.661	0.055	0.013	0.004
2 s.d. %	1.4	1.2	1.7	1.8	2.0	1.0	1.8	2.3	2.8	0.7	1.8	4.3	2.0	3.5	190.8	0.9	4.9	6.2
Average	**3.57**	**7.84**	**1.08**	**4.76**	**1.39**	**0.573**	**1.96**	**0.381**	**2.61**	**0.611**	**1.87**	**1.88**	**0.288**	**0.952**	**7.35**	**6.28**	**0.249**	**0.056**
Accepted	*3.68*	*8.17*	*1.11*	*4.95*	*1.44*	*0.529*	*2.02*	*0.39*	*2.71*	*0.638*	*1.95*	*1.92*	*0.292*	*0.955*	*0.089*	*6.47*	*0.24*	*0.055*
BEN																		
9th July '14 n = 6	85.6	156	18.1	67.3	12.7	3.79	11.1	1.35	6.50	1.11	2.63	1.86	0.250	5.64	5.71	4.15	11.4	2.62
2 s.d	2.13	3.57	0.470	1.80	0.350	0.118	0.302	0.036	0.149	0.026	0.082	0.060	0.003	0.077	0.069	0.197	0.505	0.145
2 s.d. %	2.5	2.3	2.6	2.7	2.8	3.1	2.7	2.7	2.3	2.4	3.1	3.2	1.3	1.4	1.2	4.8	4.4	5.5
Average	**81.9**	**148**	**17.2**	**63.8**	**11.8**	**3.61**	**10.9**	**1.28**	**6.21**	**1.06**	**2.53**	**1.77**	**0.238**	**5.42**	**4.90**	**3.94**	**10.7**	**2.46**
Accepted	*82*	*152*	*16.9*	*70*	*12*	*3.6*	*9*	*1.3*	*6.29*	*1.03*	*2.48*	*1.8*	*0.24*	*5.4*	*5.5*	*4*	*11*	*2.4*

TABLE B.3: Compilation of standard data for rock monitors, DNC-1 and BEN. Values quoted for a typical run on a given day. The bold **average** gives long term average for n = 38. Accepted values taken from Potts et al. (1992)

Figure B.1 shows a comparison of trace element data from volcanic and basement samples from Georgia measured by XRF and ICP-MS. Typically these data sets correlate very well, with r^2 values better than 0.9, although transition metals (Sc, Co, V, Zn, Ga and Cu) are typically much worse. Zr shows good correlation for the volcanic samples, however many basement samples show very poor correlation. This is likely due to the presence of accessory minerals such as zircon which do not dissolve well in the hot plate dissolution used for ICP-MS analysis. For the purpose of this project, trace element data measured by ICP-MS has been used for interpretation due to the larger number of elements measured, better reproducibility and lower detection limits. Zr data measured by ICP-MS has been used despite the poor correlation with XRF (Fig. B.1), for the purpose of consistency, and as the effect of poor dissolution is negligible for volcanic samples. However, where it is clear that an element is a major constituent of an accessory phase that has not dissolved (such as Zr in zircon), the XRF data has been used.

B.5 Isotopic Analysis

Samples were selected for isotopic analysis based on major and trace element chemistry, and to get a suite that covers the most comprehensive range of compositions. 0.05 g of sample was leached in 6M HCl for 1 hour at 120^{circ}C, then centrifuged for 1 minute, after which the leachate was pipetted off. Samples were then rinsed with MQ H_2O twice, pipetting off excess water. Samples were then allowed to dry before being reweighed. The leaching stage is used to remove any potential anthropogenic contaminants. During the leaching process between 15–30% of the powder was lost. To check if the leaching process was only removing contamination, and not altering the isotopic signature of the samples, measurements were taken for a leached and unleached sample of the same rock, following the procedure below. The values measured were within error of each other. However, the rock standards (AGV-1 and BHVO-2) were not leached, as this would cause a shift in the Pb isotopes relative to the expected values (Baker et al., 2004). The remaining powder was dissolved using the following procedure:

- Dried rock powder is dissolved in 0.5 ml concentrated TD HNO_3 and 2 ml concentrated TD HF. The beaker is then sealed and left on the hotplate at 120^{circ}C for at least 24 hours.

- The solution is dried down, and then taken up in 2 ml 6M TD grade HCl, sealed and left on the hotplate overnight at 120^{circ}C.

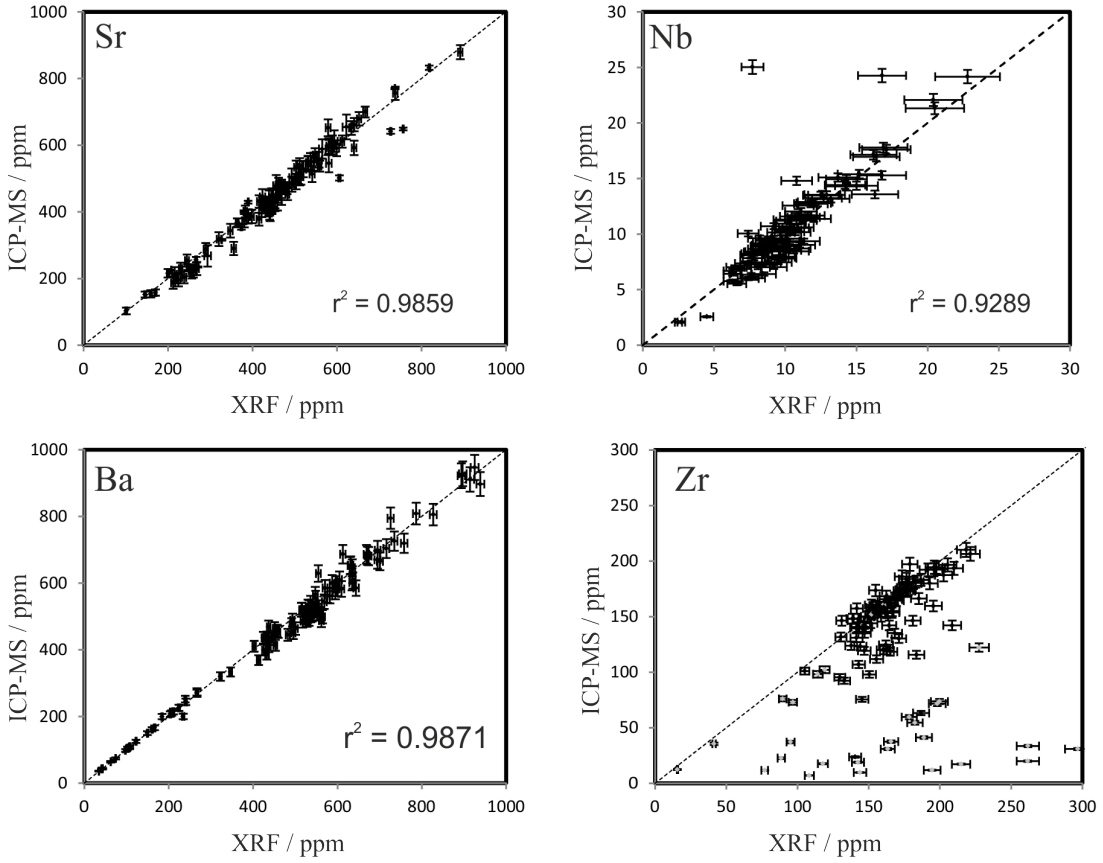

FIGURE B.1: A comparison of trace element data collected by XRF and ICP-MS. Error bars represent 2 s.d. Dashed line is 1:1. Comparisons shown for LILEs (Sr and Ba) and HFSEs (Nb and Zr). For Zr, the grey symbols are for crustal samples.

- The solution is dried down, and then taken up in 2 ml concentrated TD HNO_3, sealed and left on the hotplate overnight at 120^{circ}C.

- Once this solution is fully dissolved it is split into two aliquots of 1 ml each. They are dried down separately, one to be used for Sr and Pb isotope analyses, the other for Nd and Hf isotopic analyses.

- The Sr-Pb cut is taken up in 1 ml 2M HNO_3 and left on the hotplate at 120^{circ}C until completely in solution.

- The Nd-Hf cut is taken up in 2 ml 2.5M HNO_3 : 0.05M HF and left on the hotplate at 120^{circ}C until completely in solution.

B.5.1 Sr and Pb Isotopes

Eichrom Sr-Spec was used for the chromatographic separation of Sr and Pb. The resin was pre-cleaned in batches of 5–7 ml, with 6 cycles of:

- 250 ml 6M HCl
- 250 ml MQ H_2O
- 250 ml 0.05M HNO_3
- 250 ml MQ H_2O

For the first three cycles, QD grade acid is used. TD grade acid is used for the final three cycles. The clean resin was stored for up to 3 months.

All acids used were TD grade, and titrated for accurate molarity. The column procedure, modified from Deniel and Pin (2001), is as follows:

- Clean a fritted 1 ml pipette tip by passing through 1 column volume (CV) of 6M HCl, and then 1 CV MQ H_2O.
- Load 150 l of clean Sr-Spec resin.
- Clean column and resin with 1 CV of 6M HCl, and then twice with MQ H_2O.
- Condition the resin with 1.5 ml 2M HNO_3.
- Load the sample in 1 ml 2M HNO_3, then wash with 0.4 ml of the same acid.
- Wash the column with 1 ml 7M HNO_3, and then 0.2 ml 2M HNO_3.
- Elute Sr with 1 ml 0.05M HNO_3. Collect this cut for Sr isotope analysis.
- Rinse the column wit 0.5 ml 3M HCl
- Elute Pb with 1.5 ml 6M HCl. Collect this cut for Pb isotope analysis.

B.5.1.1 Sr Isotope Analysis

52 samples were analysed for their Sr-isotopic compsition. Sr isotopes were analysed using a Neptune Multi-Collector (MC-) ICP-MS at the Open University in static low-resolution mode, fitted with H-Cones. A standard introduction system (SIS), with an uptake rate of 50 μl.min^1 was used. The cup configuration used is shown in Table B.4, along with

major interferences. 200 or 250 ppb Sr solutions were used depending on the sensitivity of the instrument on any given day. 200 ppb solutions yielded 7.5 - 13.9 V for ^{88}Sr, while 250 ppb solutions yielded 7.2–13.0 V for ^{88}Sr (1 ppm ^{88}Sr = 36.3–79.0 V, average = 56.4 V). On individual runs this allowed an average internal precision (2 s.e.) of 6.8 ppm for the ratio ^{87}Sr/^{86}Sr.

Cup	L4	L3	L2	L1	C	H1	H2	H3	H4
Mass	^{83}Kr	^{84}Sr	^{85}Rb	^{86}Sr	^{87}Sr	^{88}Sr	^{90}Zr	^{91}Zr	^{92}Zr
Interference	-	Kr	-	Kr	Rb	-	-	-	-

TABLE B.4: Cup configuration for Sr analysis by MC-ICP-MS. Major interferences on isotopes of interest are also shown.

Machine gain was measured daily, before each analytical session. An on-peak zero was measured before each sample or standard analysis, and then subtracted from the subsequent measurement. This blank consisted of the same 3% TD HNO_3 that was used to make up the samples and standards, and was measured for 3 blocks of 10 ratios.

Samples were run in 27 blocks of 10 ratios with an 8.389 second integration for each measured ratio. At the beginning of each sample analysis a peak centre was performed. This was not done for the blank measurements. The baseline was measured between each block. Each measurement lasted ~65 minutes, using less than 5 ml of solution. Between each sample or standard measurement the machine and nebuliser were washed with 3% TD HNO_3 for at least 15 minutes, or until the measured blank showed no washout effects or Sr spikes.

Isobaric interferences from Kr and Rb on Sr were monitored using ^{83}Kr and ^{85}Rb (Table B.4). Analyses were corrected for instrumental mass fractionation using the exponential fractionation law. The ^{86}Kr interference on ^{86}Sr was stripped off iteratively assuming an ^{86}Sr/^{88}Sr of 0.1194 and ^{86}Kr/^{83}Kr of 0.6209 (Thirlwall, 1991; de Laeter et al., 2003). ^{87}Rb was corrected from ^{87}Sr using an ^{87}Rb/^{85}Rb of 2.5926 (de Laeter et al., 2003)). Total procedural blanks were negligable (42 pg).

To monitor machine performance over the period of 28 months that analyses were undertaken, the standard NBS 987 was run, and yielded an average ^{87}Sr/^{86}Sr of 0.710276 ± 31 (43.8 ppm, 2 S.D., n=53, Fig. B.2). This is within error of static MC-ICP-MS value of 0.710266 ± 25 reported by Nowell et al. (2003), and the multi-dynamic TIMS value of 0.710248 ± 11 reported by Thirlwall (1991).

During the 28 month period that these measurements were made was an 11 month period (20th February 2014 - 20th January 2015) without any measurements. Figure B.2 clearly shows that after this break there was significant drift in the machine to higher

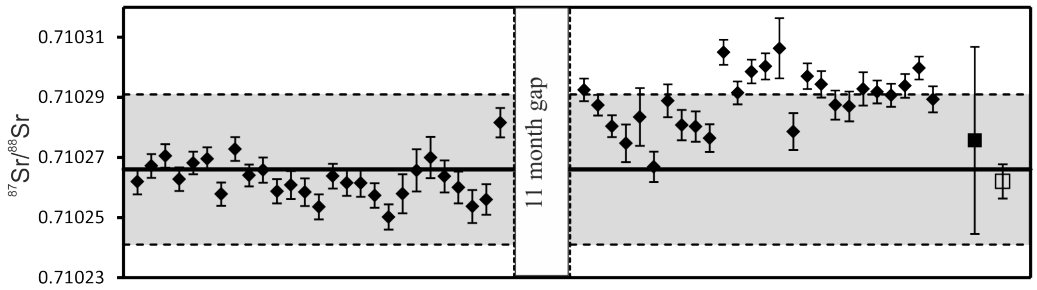

FIGURE B.2: Compilation of $^{87}Sr/^{86}Sr$ ratio for NBS 987. Diamonds represent individual analyses, with internal 2 s.e. error bars. Filled in square represents average and 2 S.D. over the full 28 months analysis period. The open square represents average and 2 S.D. before the 11 month break. The black and dashed lines represent published data of Nowell et al. (2003).

$^{87}Sr/^{86}Sr$ values, and also a decrease in the reproducibility. It is likely this was due to deterioration of the Faraday cups. Since completion of these measurements, a new cup configuration (Table B.5) was tried out, and gave a value $^{87}Sr/^{86}Sr = 0.710226 \pm 3$ (4.5 ppm, 2 S.D., n=5; B. Charlier, pers. comms.) Due to this we normalised our measurements to a preferred value of 0.710266 (Nowell et al., 2003), based on the average value for NBS987 on the day the samples were analysed. This value was close to the average we obtained before the 11 month gap ($^{87}Sr/^{86}Sr = 0.710262 \pm 6$ (8.0 ppm, 2 S.D., n=26). Daily errors were typically 11–19 ppm (2 S.D.). Errors associated with the correction were fully propagated.

Cup	L4	L3	L2	L1	C	H1	H2	H3	H4
Mass	^{82}Kr	^{83}Kr	^{84}Sr	^{85}Sr	^{86}Sr	^{87}Sr	^{88}Sr		
Interference	-	-	Kr	-	Kr	Rb	-	-	-

TABLE B.5: New cup configuration for Sr analysis by MC-ICP-MS following cup degradation. Major interferences on isotopes of interest are also shown.

Two rock standards BHVO-2 and AGV-1 were digested and analysed in an identical way to the rock samples to monitor the effectiveness of the chromatographic separation and machine performance (Fig. B.3). BHVO-2 was digested 4 times, with two of the digestions analysed twice. AGV-1 was digested 5 times, with a single digestion analysed twice. BHVO-2 yielded an average $^{87}Sr/^{86}Sr$ of 0.703498 ± 33 (47.4 ppm, 2 S.D.) before normalisation, and 0.703492 ± 11 (15.0 ppm, 2 S.D.) after, which is within error of the static TIMS values of 0.703479 ± 20 (Weis et al., 2006). AGV-1 yielded an average of 0.704014 ± 30 (42.9 ppm, 2 S.D.) before normalisation, and 0.704006 ± 9 (12.1 ppm, 2 S.D.) after, which is within error of the static TIMS values of 0.703996 ± 20 (Weis et al.,

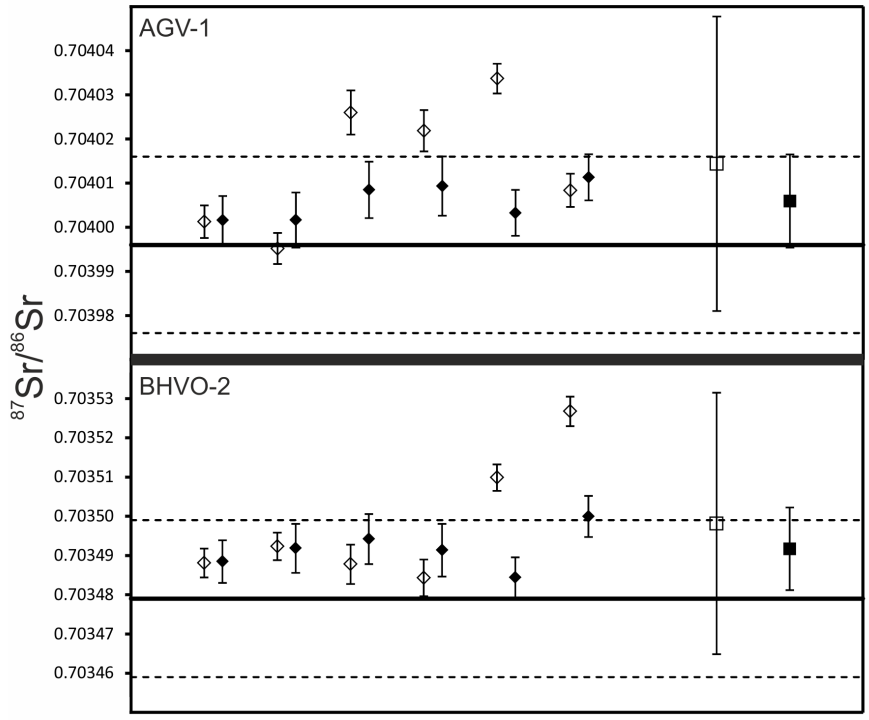

FIGURE B.3: Compilation of analyses of the rock standards AGV-1 and BHVO-2. $^{87}Sr/^{86}Sr$ with 2 s.e. internal precision shown for each measurement by the diamond markers. Open symbols show the raw measurement, whilst the filled in symbols show the data normalised to compensate for drift in the instrument (see text for details). Square symbols represent average of the measurements for raw (open symbol) and normalised data (filled symbol), with 2 s.d. error bars. The thick black lines represent accepted values of Weis et al. (2006), with dashed lines at 2 s.d.

2006)(Weis et al., 2006)

B.5.1.2 Pb Isotope Analysis

54 samples were analysed for Pb isotopes using a ^{207}Pb–^{204}Pb double spike (DS) and a Neptune MC-ICP-MS at the Open University in static low-resolution mode, fitted with H-Cones. A Cetac Aridus II desolvating nebuliser with an uptake rate of $50\mu l.min^{-1}$ was used to introduce the sample into the instrument. Argon was used as a sweep gas, while N2 was used to increase machine sensitivity. The cup configuration and major interferences are shown in Table B.6. Solutions of 20–30 ppb were used depending on the sensitivity of the instrument on any given day. 20 ppb solutions yielded 4.4–11.3 V ^{208}Pb (1 ppm ^{208}Pb = 420–1078 V, average = 727 V), while 30 ppb solutions gave 7.4–10.6 V

^{208}Pb (1 ppm ^{208}Pb = 471–675 V, average = 593 V). On individual runs this allowed an average internal precision (2 s.e.) of 47.6 ppm for the ratio ^{206}Pb/^{204}Pb, on unspiked analyses. Samples and standards were doped with 6 ppb Tl. This allowed a comparison of DS, Tl-normalised, and internally normalised data (Table B.6 and Figure B.4).

Cup	L4	L3	L2	L1	C	H1	H2	H3	H4
Mass	^{198}Hg	^{200}Hg	^{203}Tl	^{204}Pb	^{205}Tl	^{206}Pb	^{207}Pb	^{208}Pb	-
Interference	WO^+	WO^+	ReO^+	Hg	-	-	-	-	-

TABLE B.6: Cup configuration for Pb analysis by MC-ICP-MS. Major interferences on isotopes of interest are also shown.

Machine gain was measured daily, before each analytical session, An on-peak zero was measured before each sample or standard analysis, and then subtracted from the subsequent measurement. This blank consisted of the same 3% TD HNO_3 that was used to make up the samples and standards, and was measured for 6 blocks of 10 ratios.

Samples were run in 6 blocks of 10 ratios with a 4.194 second integration for each measured ratio. At the beginning of each sample analysis a peak centre was performed. This was not done for the blank measurements. The baseline was measured between each block. Each measurement lasted ~15 minutes. Between each sample or standard measurement the machine and nebuliser were washed with 3% TD HNO_3 for at least 20 minutes, or until the measured blank showed no washout effects or Pb spikes.

Internally normalised NBS 981 data were corrected for instrumental mass fractionation using the exponential fractionation law (assuming ^{208}Pb/^{206}Pb = 2.1677; Thirlwall, 2000). Isobaric interference from ^{204}Hg on the isotope ^{204}Pb was corrected for by monitoring ^{200}Hg. A correction was applied assuming ^{200}Hg/^{204}Hg = 2.2766. ^{198}Hg was also measured and used to monitor the correction made. ^{203}Tl and ^{205}Tl were measured and used to correct for instrumental mass fractionation. Data was corrected assuming ^{205}Tl/^{203}Tl = 2.3889 (Baker et al., 2004). Although the Tl-corrected data has a similar accuracy to the internally normalised and DS-corrected data, it is less precise and has larger long-term reproducibility (Table B.7).

The composition of the spike used for the DS-correction is shown in Table B.8. Samples were spiked based on the concentration of Pb in the sample, with the aim to achieve a Q-value as close as possible to the optimum of 0.1 (Q is defined as $^{204}Pb_{spike}/^{204}Pb_{sample}$; Galer, 1999). Natural and spiked runs were deconvolved using the method of Albarede and Beard (2004), and errors propagated using a Monte Carlo simulation. For the samples measured, Q typically varied from 0.09–0.24, which lead to an error magnification for ^{206}Pb/^{204}Pb (γ64) of 1–1.5 from unspiked to spiked sample runs (Galer, 1999).

	$^{206}Pb/^{204}Pb$	$^{207}Pb/^{204}Pb$	$^{208}Pb/^{204}Pb$	N
Internally Normalised	16.9429 ± 25 (147 ppm)	15.5006 ± 18 (117 ppm)	36.7271 ± 54 (147 ppm)	94
Tl-Corrected	16.9420 ± 45 (264 ppm)	15.4994 ± 55 (356 ppm)	36.7233 ± 173 (472 ppm)	94
DS-Corrected	16.9428 ± 24 (144 ppm)	15.5007 ± 28 (184 ppm)	36.7276 ± 75 (206 ppm)	59

TABLE B.7: Comparison of internally normalised, Tl-corrected and DS-corrected Pb isotope data for standard NBS 981, measured over a 30 month period by MC-ICP-MS. Errors stated are 2 s.d.

	^{204}Pb	^{206}Pb	^{207}Pb	^{208}Pb
$n/^{207}Pb$	0.221913	0.065393	1	0.079991

TABLE B.8: Composition of the Pb spike

Machine performance was monitored using unspiked NBS 981. Repeat analyses were run over 30 months with spiked NBS 981 runs used to deconvolve the natural data, and monitor the reproducibility of the DS data. This yielded a $^{206}Pb/^{204}Pb$ of 16.9428 ± 24 (144 ppm 2 s.d., n = 59). Fig. B.4 illustrates the reproducibility of internally normalised, Tl-corrected and DS-corrected data, with data for all used ratios summarised in Table B.7. Figure B.5 shows that our data is within error of published static MC-ICP-MS and TIMS DS-normalised values.

To minimise any memory effects from difficulties washing out the DS, unspiked and spiked samples were run as batches, with several weeks left between analysis of a spiked batch, and the subsequent unspiked batch. Spiked batches could be run on the day after an unspiked batch, as there was no washout effect.

Rock standard AGV-1 was digested and analysed in an identical way to the rock samples to monitor the column procedure and machine performance. AGV-1 was digested 6 times, and yielded an average $^{206}Pb/^{204}Pb$ of 18.9442 ± 34 (181 ppm, 2 S.D.). This is within error of the static MC-ICP-MS values of 18.9420 ± 20 (Baker et al., 2004), as well as other MC-ICP-MS and TIMS measurements (Fig. B.6).

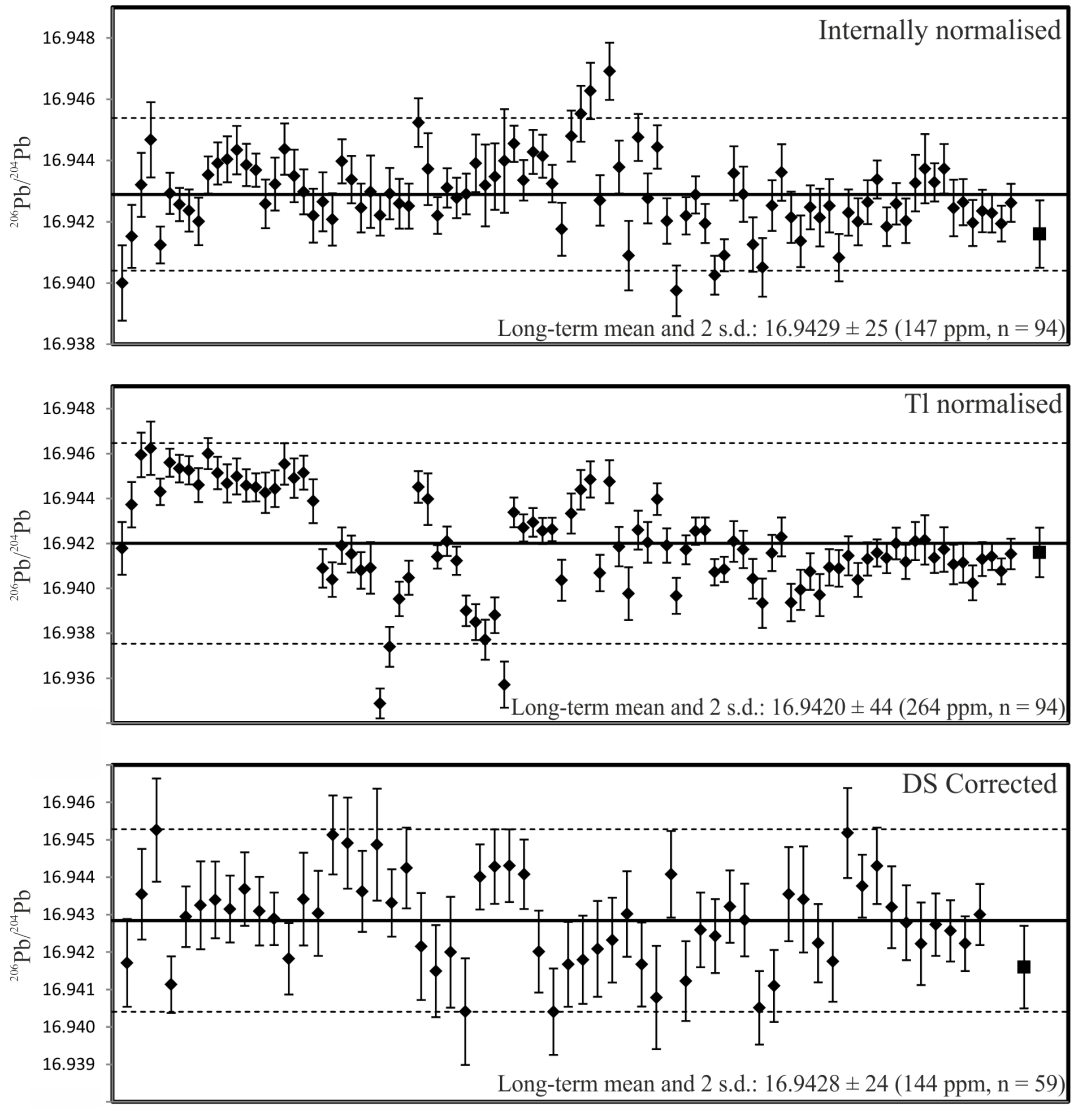

FIGURE B.4: Compilation of NBS981 standard Pb solution, showing reproducibility of $^{206}Pb/^{204}Pb$ for internally, Tl-, and DS- normalised measurements. Diamond markers show individual measurements with 2 s.e. error. Thick black line represents long term average of the data, with dashed lines at 2 s.d. (values also quoted on the plots). Square symbol is accepted DS value from Baker et al. (2004).

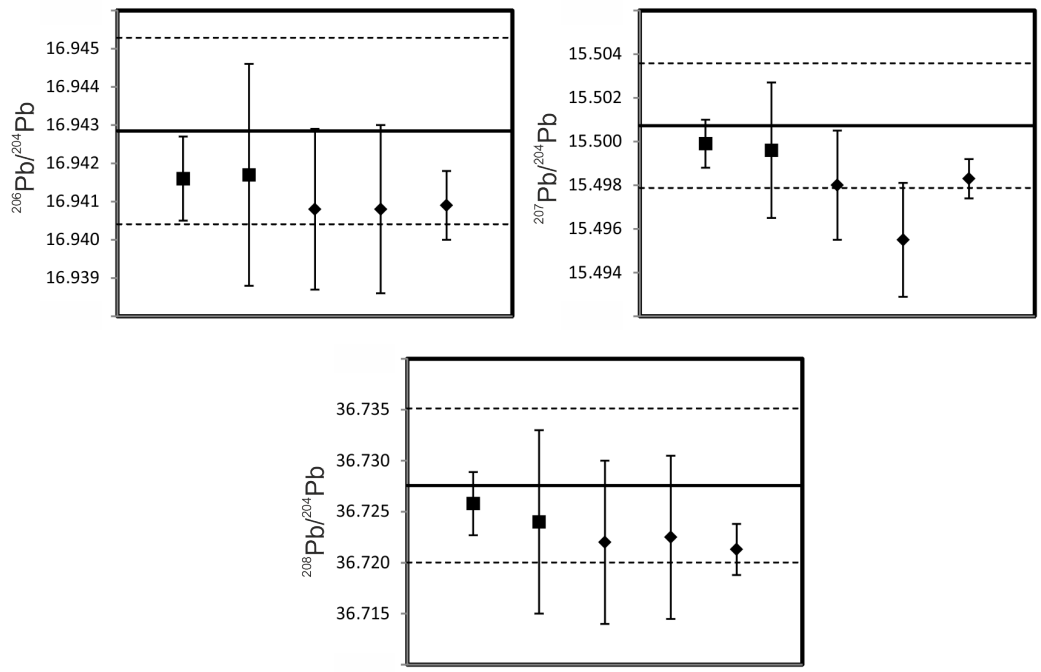

FIGURE B.5: $^{206}Pb/^{204}Pb$, $^{207}Pb/^{204}Pb$ and $^{208}Pb/^{204}Pb$ ratios for NBS981. Thick black line represents average of DS normalised measurements over the course of this project, with dashed lines at 2 s.d. From left to right the square symbols are MC-ICP-MS values of Baker et al. (2004) and Thirlwall (2002), and the diamonds are TIMS values from Thirlwall (2000), Thirlwall (2002) and Klaver et al. (2015).

B.5.2 Nd Isotopes

B.5.2.1 Cation Separation

Nd and Hf was also separated using chromatographic separation. An initial cation separation step was used to reduce the amount of matrix present. Cation resin AG 50W-X8 was used in a clean disposable 10 ml Biorad column. Nd and Hf cuts were collected using the following procedure:

- Rinse the pre-cleaned column with 1 CV MQ H_2O, then 6M HCl, then again with MQ H_2O.
- Load the resin. This resin is reusable, upto around 10 times. If the resin is being reused, the first step and this step is not needed.
- Clean the column and resin with 1 CV 5M HNO_3 : 0.1M HF

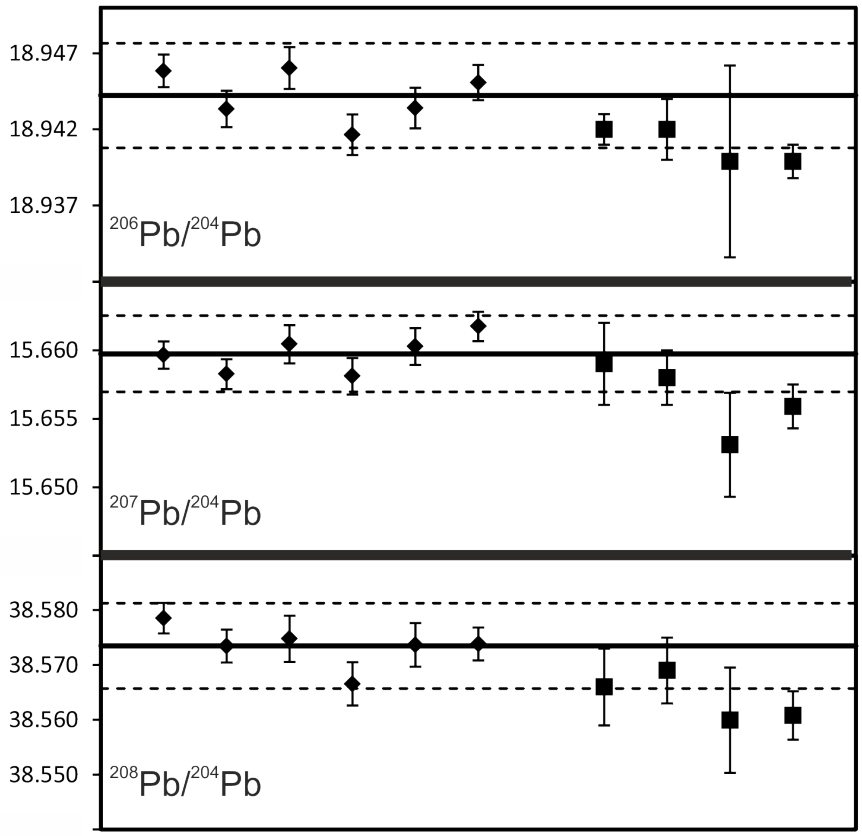

FIGURE B.6: Compilation of analyses of the rock standards AGV-1. Pb isotope ratios with 2 s.e. internal precision shown for each measurement by the diamond markers. Thick black line represents average of measured data, with 2 s.d. marked as the dashed lines. Square symbols represent published data, with 2 s.d. error bars. From left to right the published data is TIMS measurements of Woodhead and Hergt (2000), MC-ICP-MS data of Baker et al. (2004) and Weis et al. (2006) and TIMS data of Klaver et al. (2015).

- Wash the column and resin with 3 ml MQ H_2O, then 2 ml 1.25M HCl, then 2 ml MQ H_2O
- Condition the resin with 2 ml 2.5M HNO_3 : 0.05M HF
- Load the sample as 2 × 1 ml 2.5M HNO_3 : 0.05M HF. Collect this cut for further separation of Hf.
- Further elute with 9 ml 2.5M HNO_3 : 0.05M HF. Collect the first 3 ml for further separation of Hf. Elute the remaining 6 ml.
- Elute REE with 14 ml 5M HNO_3 : 0.1M HF. Collect this cut for further separation

of Nd.

- Elute and clean column and resin with 3 CV 5M HNO_3 : 0.1M HF.
- Store the column in 2 ml 2.5M HNO_3 : 0.05M HF.

B.5.2.2 Nd Separation

From the cation separation, a 14 ml REE cut was collected. This is dried down on a hotplate at 120^{circ}C, and then taken up in 0.5 ml 0.25M HCl, until completely dissolved. For Nd separation, 1 ml Ln-Spec resin is used in a pre-cleaned Savillex column (4 mm I.D.), with the following procedure:

- Rinse and clean the column with 1 CV 6M HCl, and then 1 CV 0.25M HCl.
- Load the resin. This resin is reusable upto 3–5 times. If the resin is being reused the procedure starts from the next step.
- Rinse column and resin with 2 ml 6M HCl, then 4 ml 0.25M HCl.
- Precondition the resin with 1 ml 0.25M HCl.
- Load the sample as 2 $\times$ 0.25 ml 0.25M HCl.
- Elute LREE (La, Ce, Pr) using 3.5 ml 0.25M HCl.
- Elute Nd using 2.5 ml 0.25M HCl. Collect this cut for Nd isotope analysis.
- Elute Sm using 2 ml 0.75M HCl.
- Rinse with 1 CV 6M HCl.
- Rinse with 2 ml 0.25M HCl, and then store in 0.25M HCl.

B.5.2.3 Nd Isotope Analysis

The Nd isotopic composition of 48 samples were analysed. Initially analysis was done on a TIMS, but difficulties were encountered in the loading and filament heating stages, so it was decided to measure the remaining samples using a MC-ICP-MS.

B.5.2.4 TIMS Analysis

Four samples were measured by TIMS, using the ThermoScientific Triton at the Open University in static mode. The dried down sample was taken up in 150 μl of TD HNO_3, and quickly dried back down. 1 μl of sample was loaded onto one side of a double Re filament assemblage, with 1 μl H_3PO_4 acting as an activator, then the filament was flashed at ~1.7 V.

Runs consisted of 270 ratios, with an 8.394 second integration time per measured ratio. A signal between 1.5–6 V was attained. Samples were run at 4550–4820 V on the ionising filament, 1420–1785 V on the evaporation filament, and a pyrometer temperature of 1600–1725 ^{circ}C. Analyses were corrected for instrumental mass fractionation using the exponential fractionation law, assuming a $^{146}Nd/^{144}Nd$ ratio of 0.7219 (de Laeter et al., 2003).

Repeats of standard solution J & M were run, yielding $^{143}Nd/^{144}Nd$ of 0.511821 ± 20, within error of MC-ICP-MS analyses of this project (Fig. B.7).

B.5.2.5 MC-ICP-MS analysis

48 samples were analysed using a Neptune MC-ICP-MS at the Open University in static low-resolution mode, fitted with H-cones. A standard introduction system (SIS), with an uptake rate of 50 μl.min^1 was used. The cup configuration used, and major interferences, is shown in Table B.9. Depending on the sensitivity of the instrument on any given day, and the concentration of Nd in the samples being measured, standard solutions of 100–200 ppb were used. The typical sensitivity of the instrument for these different solutions is shown in Table B.10.

Cup	L4	L3	L2	L1	C	H1	H2	H3	H4
Mass	-	^{142}Nd	^{143}Nd	^{144}Nd	^{145}Nd	^{146}Nd	^{147}Sm	^{148}Nd	^{150}Nd
Interference	-	-	-	Sm		-	-	Sm	

TABLE B.9: Cup configuration for Nd analysis by MC-ICP-MS. Major interferences on isotopes of interest are also shown.

Machine gain was measured daily, before each analytical session. An on-peak zero was measured before each sample or standard analysis, and then subtracted from the subsequent measurement. This blank consisted of the same 3% TD HNO_3 that was used to make up the samples and standards, and was measured for 3 blocks of 10 ratios.

Samples were run in 12 blocks of 10 ratios with an 4.194 second integration for each measured ratio. At the beginning of each sample analysis a peak centre was performed.

Concentration	Typical Signal	Signal for 1ppm ^{88}Sr	Internal precision
100 ppb	0.97 - 1.54 V	40.6 - 64.6 V	16 - 25 ppm
150 ppb	1.78 - 2.32 V	49.9 - 65.0 V	11 - 18 ppm
200 ppb	1.97 - 3.13 V	41.4 - 65.7 V	12 - 20 ppm

TABLE B.10: Sensitivity and precision of signal at different concentrations of Nd in J & M standard solution.

This was not done for the blank measurements. The baseline was measured between each block. Each measurement lasted ~20 minutes, using less than 2.5 ml of solution. Between each sample or standard measurement the machine and nebuliser were washed with 3% TD HNO_3 for at least 15 minutes, or until the measured blank showed no washout effects or Nd spikes. The Isobaric interference of Sm on Nd was monitored using ^{147}Sm (Table B.9). Analyses were corrected for instrumental mass fractionation using the exponential fractionation law. The ^{144}Sm interference on ^{144}Nd was stripped off iteratively assuming an $^{146}Nd/^{144}Nd$ of 0.7219 and $^{147}Sm/^{144}Sm$ of 4.83871 (de Laeter et al., 2003; Weis et al., 2006). A ratio of $^{147}Sm/^{148}Sm = 1.3274$ (de Laeter et al., 2003) was used to correct ^{148}Sm from ^{148}Nd.

To monitor machine performance, the standard J & M was measured over the eight month period of analyses were undertaken. The standard yielded an average $^{143}Nd/^{144}Nd$ of 0.511822 ± 25 (48.2 ppm, 2 S.D., n = 58, Fig. B.7). Our data is within error of long term analysis of J & M on TIMS at the Open University ($^{143}Nd/^{144}Nd = 0.511821 \pm 2$). The TIMS J & M value has been tied to the internationally recognised standard La Jolla with a value of 0.511849 ± 3 for $^{143}Nd/^{144}Nd$, which is within error of published data (Raczek et al., 2003; Weis et al., 2006)

Rock standard AGV-1 was digested and analysed in an identical way to the rock samples to monitor the column procedure and machine performance. It was analysed six times, each from a separate digestion. AGV-1 yielded an average $^{143}Nd/^{144}Nd$ of 0.512787 ± 15 (29.5 ppm, 2 S.D., Fig. B.8). This is within error of TIMS values of Weis et al. (2006), $^{143}Nd/^{144}Nd = 0.512784 \pm 18$.

B.5.3 Hf Isotopes

In this study work has been done to build on the preliminary work of Hunt (2011), to produce a good separation of Hf, and reproducible and accurate values for rock standards.

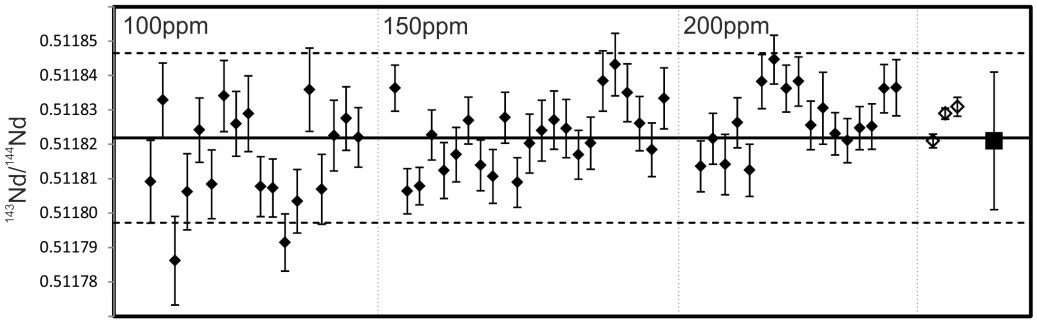

FIGURE B.7: Compilation of analyses of the in house J M standard. $^{143}Nd/^{144}Nd$ with 2 s.e. internal precision shown by the diamond symbols for each measurement at 100, 150 and 200 ppb. Open diamond symbols were measured by TIMS. The thick black lines represent the average measured data by MC-ICP-MS as part of this project, with dashed lines at 2 s.d. Square symbols represent long term average of J & M measured by TIMS at the Open University with 2 s.d. error bars.

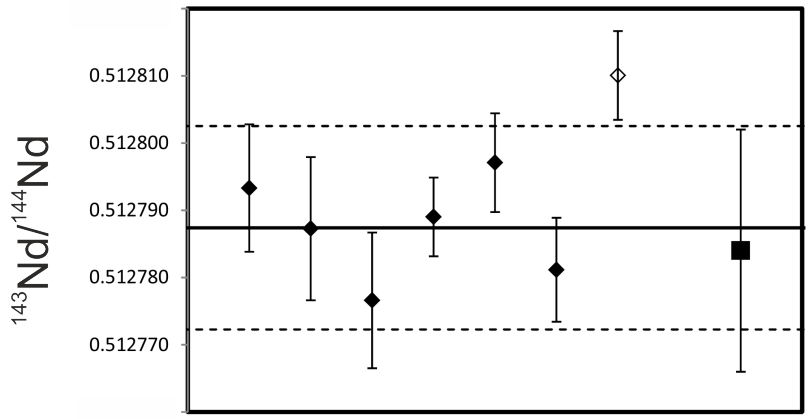

FIGURE B.8: Compilation of analyses of the rock standards AGV-1. $^{143}Nd/^{144}Nd$ with 2 s.e. internal precision shown by the diamond symbols for each measurement. Square symbol represent published data of Weis et al. (2006), with 2 s.d. error bars. The thick black lines represent the average measured data, with dashed lines at 2 s.d

B.5.3.1 Effect of high Zr/Hf

It was first recognised by Blichert-Toft et al. (1997) that the transmission of Hf during mass spectromatic analysis was significantly reduced by a high Ti/Hf ratio. The presence of significant Ti causes deposits of refractory Ti to build up on the sampler-cone orifice, causing an interfering electrical shield across the aperture, as well as matrix effects between Ti and Hf in the ion beam (Blichert-Toft et al., 1997). As Ti/Hf increases, there is a systematic decrease in $^{176}Hf/^{177}Hf$ (Münker et al., 2001). Münker et al. (2001) find

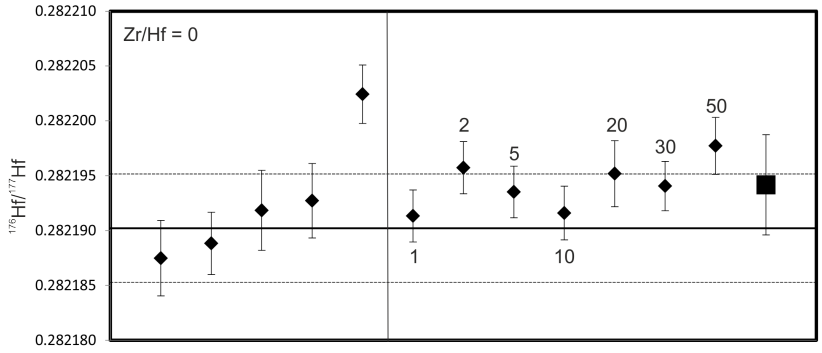

FIGURE B.9: Results for test of doping Hf solution with Zr to see the effect on $^{176}Hf/^{177}Hf$. Diamonds represent single analyses, with the stated Zr/Hf ratios, with 2 s.e. error bars. The solid line represents the average undoped (Zr/Hf = 0, excluding the 5th standard) value with dashed line at 2 s.d. The square symbol represents reproduciblity of all the doped samples

no noticeable offset within error at Ti/Hf <10, although Ulfbeck et al. (2003) suggest a Ti/Hf <1 is required.

Zr shares many properties with Ti and Hf, therefore it is important to understand if a high Zr/Hf has a similar effect to high Ti/Hf. It has been suggested that high Zr/Hf does not affect the $^{176}Hf/^{177}Hf$, even up to chondritic values (Blichert-Toft et al., 1997; Ulfbeck et al., 2003), and therefore some separation methods have found it unnecessary to include a step to separate these two elements (e.g. Le Fèvre and Pin, 2001). Work by Hunt (2011) suggests this may not be the case. It was found that in super-chondritic (Zr/Hf ~50, which is at the upper end of the range of natural ratios found in the samples from this study), the $^{176}Hf/^{177}Hf$ could be increased by more than 1000 ppm.

We tested the effect by doping a Hf standard solution (Alfa Aesar Hf solution A13843) with Zr. We used 50 ppb Hf solution, doping with Zr so we got a range of Zr/Hf ratios from 0 (undoped) to 50 (natural sample). The $^{176}Hf/^{177}Hf$ value stayed constant within error (Fig. B.9). At a Zr/Hf of 50, the $^{176}Hf/^{177}Hf$ had increased by 27 ppm from the average undoped solution, and was the only solution not within error of it. The final undoped solution was significantly higher than the previous undoped, and all the doped solutions, this may suggest that increased Zr can build up reducing reproducibility and accuracy. Zr seems to have much less of an effect than Ti of the $^{176}Hf/^{177}Hf$ ratio, especially for Zr/Hf within the limits of our natural samples. Despite this we developed the method to remove as much Zr as possible, in case there was a long term build up that would have an effect.

B.5.3.2 Hf Column procedure

The 5 ml cut from the cation column (see B.5.2.1) was dried down on a hotplate at 120^{circ}C, and then taken up in 10 ml 3M HCl until fully dissolved. The column procedure used is based on Münker et al. (2001), and uses 1 ml Ln-Spec resin in a 10 ml bio-rad column, and is detailed below:

- Clean a Bio-rad column with 1 CV 6M HCl, then 1 CV MQ H_2O
- Load 1 ml Ln-spec resin
- Clean column and resin with 1 CV 6M HCl, then 1 CV 2M HF
- Neutralise the column with 1 CV H_2O
- Condition the resin with 10 ml 3M HCl
- Load the sample in 10 ml 3M HCl
- Wash out matrix, LREE and MREE with 10 ml 3M HCl
- Wash out matrix and HREE with 40 ml 6M HCl, then neutralise with 4 ml H_2O
- Wash out Ti with ~25 ml 0.4M HNO_3 - 0.09M HCit* - 1% H_2O2 or until the elutant goes clear
- Wash out H_2O2 with 5 ml 0.4M HNO_3 - 0.09M HCit*
- Elute Zr with 50 ml 6M HCl - 0.06M HF
- Elute and collect 12 ml 6M HCl - 0.2M HF
- Clean the column and resin with 1 CV 6M HCl and 1 CV 2M HF
- Store the column in 3M HCl

(*HCit - Citric acid)

To assess the effectiveness of the separation a column calibration was done using a multi-element solution which reflected a typical compositions of the Caucasus volcanic samples. The calibration was measured by ICP-MS, and is shown in Fig. B.10.

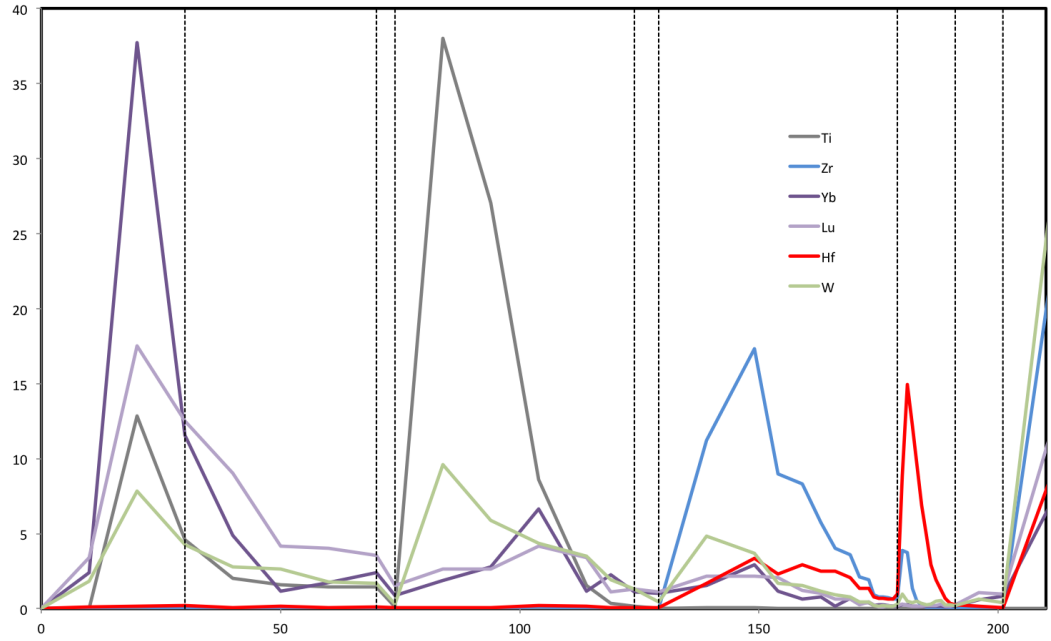

FIGURE B.10: Column calibration for the separation of Hf from the cut taken from the cation column. Curves shown for Hf, major interference elements (Yb, Lu, W) and Ti and Zr which may interfere within the instrument. Shaded area is the cut collected for analysis.

B.5.3.3 Hf Isotope Analysis

15 samples were analysed for Hf isotopes using a Neptune MC-ICP-MS at the Open University in static low-resolution mode, fitted with H-Cones. A Cetac Aridus II desolvating nebuliser with an uptake rate of 50μl.min^1 was used to introduce the sample into the instrument. Argon was used as a sweep gas, while N_2 was used to increase machine sensitivity. The cup configuration and major interferences are shown in Table B.11. Solutions of 37.5 ppb Hf were used, resulting in a signal of 10–11.5 V on ^{178}Hf (1 ppm Hf = 1000–1150 V), resulting in an average internal precision (2 s.e.) of 8.5 ppm on individual runs.

Cup	L4	L3	L2	L1	C	H1	H2	H3	H4
Mass	^{173}Yb	^{175}Lu	^{176}Hf	^{177}Hf	^{178}Hf	^{179}Hf	^{180}Hf	^{181}Ta	^{182}W
Interference	-	-	Yb, Lu	-	-	-	Ta, W	-	-

TABLE B.11: Cup configuration for Hf analysis by MC-ICP-MS. Major interferences on isotopes of interest are also shown.

Machine gain was measured daily, before each analytical session, An on-peak zero

was measured before each sample or standard analysis, and then subtracted from the subsequent measurement. This blank consisted of the same 3% TD HNO_3 that was used to make up the samples and standards, and was measured for 3 blocks of 10 ratios.

Samples were run in either 3 or 5 blocks of 20 ratios, depending on the amount of Hf collected, with an 8.4 second integration for each measured ratio. At the beginning of each sample analysis a peak centre was performed. This was not done for the blank measurements. The baseline was measured between each block. Each measurement lasted ~15 minutes, using less than 1.5 ml of solution. Between each sample or standard measurement the machine and nebuliser were washed with 0.05M HF + 1M HNO_3 for at least 10 minutes, or until the measured blank showed no washout effects or Hf spikes.

The Isobaric interference of Yb, Lu, Ta and W on Hf were monitored using ^{173}Yb, ^{175}Lu, ^{181}Ta and ^{182}W respectively (Table B.11). Analyses were corrected for instrumental mass fractionation using the exponential fractionation law. The ^{176}Yb interference on ^{176}Hf was stripped off iteratively assuming a ^{179}Hf/^{177}Hf of 0.7325 (Patchett and Tatsumoto, 1980) and ^{176}Yb/^{173}Yb of 0.794753 (de Laeter et al., 2003). Mass fractionation cannot be assumed to be the same for Hf and Yb (Choi et al., 2013). Therefore it is assumed f(Yb) = 1.272 × f(Hf) (Choi et al., 2013). ^{176}Lu was corrected from ^{176}Hf using a ^{176}Lu/^{175}Lu of 0.026530 (de Laeter et al., 2003). It is likely that mass fractionation of Lu is also different to that of Hf, but as the correction for Lu is so small, any difference is insignificant within the error of our measurements. ^{180}Ta and ^{180}W were monitored as they interfere with ^{180}Hf. However, as the interference is so small, and we are not interested in ratios involving ^{180}Hf, no correction was made. Total procedural blanks were negligible (5 pg).

To monitor machine performance, the standard JMC 475 was measured over the 9 month period that analyses were undertaken. The standard yielded an average ^{177}Hf/^{176}Hf of 0.282159 ± 7 (26.4 ppm, 2 S.D., n = 21, Fig. B.11). This is within error of published values of 0.282163 ± 9 (Blichert-Toft et al., 1997), 0.282155 ± 9 (Nowell et al., 2003) and 0.282167 ± 5 (Choi et al., 2013).

Rock standard AGV-1 was digested and analysed in an identical way to the rock samples to monitor the column procedure and machine performance. It was analysed six times, from three digestions. AGV-1 yielded an average ^{177}Hf/^{176}Hf of 0.282983 ± 10 (36.5 ppm, 2 S.D.). This is within error of published values of ^{177}Hf/^{176}Hf = 0.282979 ± 6 (Weis et al., 2007).

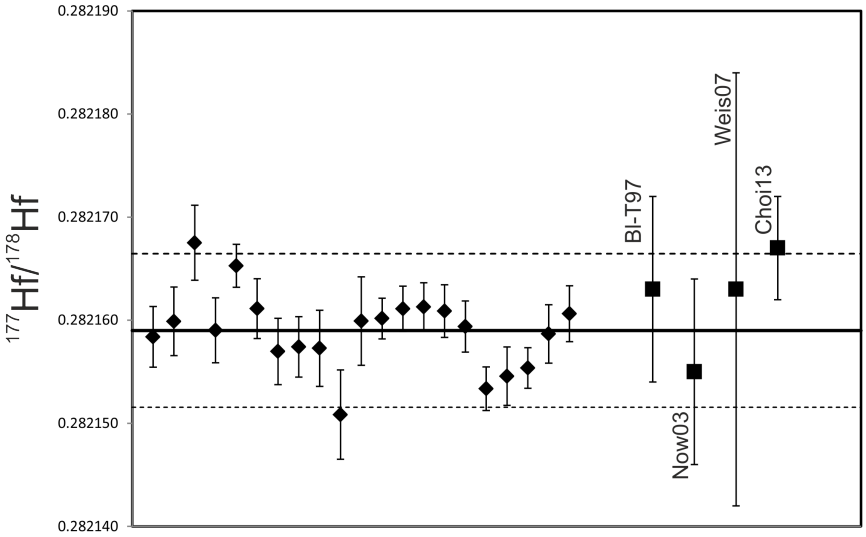

FIGURE B.11: Compilation of analyses for Hf standard solution JMC 475. Black diamonds represent a single analysis, with error bars representing 2 s.e. Solid line represents long term average of the analyses with dashed lines at 2 S.D. Squares represent published data, with 2 S.D. error bars. Bl-T97 = Blichert-Toft et al. (1997), Now03 = Nowell et al. (2003), Weis07 = Weis et al. (2007), Choi13 = Choi et al. (2013).

B.6 Electron Microprobe Analysis

Analysis of mineral chemistry was conducted at the Open University, UK, using a Cameca SX100 electron microprobe, with five wavelength dispersive spectrometers. The configuration used is shown in table B.12. Polished slides were carbon coated to prevent charging of the sample under the electron beam. Quantitative major-element analyses were conducted under operating conditions with a beam current of 20 nA, an accelerating voltage of 20 kV and a beam size of 10 μm. T-0 intercepts were undertaken on S, Si, Cl and Na.

Before each analytical session the crystals were recalibrated (one session can be regarded as the days analyses were done, often with months between sessions). Natural standards were used for calibration (details of minerals used is stated in Table B.13) and analyses were corrected using ZAF matrix correction routine.

Natural secondary standard analyses were used to check for major-element reproducibility, which was typically less than 2% for elements with >15% in the mineral

Crystal	Elements measured		
TAP	Na Kα	Al Kα	
LTAP	Si Kα	Mg Kα	
LLIF	Fe Kα	Mn Kα	
LPET	S Kα	K Kα	Ca Kα
PET	Cl Kα	P Kα	Ti Kα

TABLE B.12: Crystal configuration used during electron microprobe analyses. All elements measured using the Kα emission . The 2d angle for TAP and LTAP was 25.745, LLIF was 4.0267 and PET and LPET was 8.75.

Element Line	Peak Time (s)	Calibration Mineral	**Element Line**	Peak Time (s)	Calibration Mineral
S Kα	25	Barite	**K Kα**	20	Feldspar
Fe Kα	15	Haematite	**Mn Kα**	20	Bustamite
Si Kα	20	Feldspar	**Mg Kα**	10	Forsterite
Cl Kα	10	Slyv	**P Kα**	30	Apatite
Ca Kα	20	Custamite	**Na Kα**	25	Jadeite
Al Kα	20	Feldspar	**Ti Kα**	15	Rutile

TABLE B.13: Time spent analysing the peak of each element, and the natural element used to calibrate each element before analytical sessions.

Appendix C

Data Tables

This appendix presents raw data collected during this project. Bulk-rock data is presented for the Lesser and Greater Caucasus, and basement samples. Then representative EMPA data is presented, separated out into minerals, for the Lesser and Greater Caucasus. Details of analytical techniques and errors can be found in Appendix B.

TABLE C.1: Bulk-rock data for Lesser Caucasus samples

	Goderzi Fm.				Lower Akhalkalaki Fm. (Stage II)										
Sample	13-091	13-092	14-023	14-025	14-054	14-027	14-028	14-034	14-044	14-039	13-076	13-086	13-089	NSPhD1	NSPhD2
Major Elements (wt%)															
SiO_2	67.2	64.7	67.0	51.5	65.3	50.4	50.4	53.3	51.1	51.2	49.2	69.3	51.9	50.1	49.9
Al_2O_3	16.7	16.2	17.0	18.6	15.7	16.2	16.0	16.7	16.4	16.4	16.8	15.6	17.0	16.4	16.5
Fe_2O_3	1.97	4.00	3.06	9.43	4.10	9.60	8.24	9.33	10.10	10.55	10.49	2.23	9.17	10.37	10.24
MgO	0.23	2.49	0.87	2.71	1.64	7.14	4.84	4.75	7.09	5.80	7.22	0.78	6.52	7.83	7.49
CaO	3.77	3.99	4.04	9.87	4.48	7.82	9.92	7.53	9.18	8.04	8.66	3.09	8.90	8.79	8.92
Na_2O	3.63	4.29	4.52	3.65	3.98	3.56	3.62	4.12	3.64	4.15	3.76	4.47	3.91	3.80	3.75
K_2O	2.92	2.26	2.23	0.42	2.72	0.86	0.95	1.43	0.85	1.11	0.74	2.53	0.99	0.82	0.79
TiO_2	0.45	0.59	0.51	1.32	0.54	1.50	1.09	1.55	1.47	1.69	1.54	0.32	1.28	1.53	1.48
MnO	0.02	0.10	0.03	0.10	0.06	0.13	0.15	0.14	0.15	0.16	0.16	0.04	0.15	0.16	0.16
P_2O_5	0.16	0.21	0.23	0.24	0.22	0.32	0.26	0.46	0.32	0.42	0.33	0.13	0.32	0.35	0.34
Total	97.07	100.38	100.40	99.40	99.34	99.74	101.32	99.61	101.07	99.70	98.95	98.51	99.98	100.15	99.49
LOI	1.01	1.49	0.92	1.55	0.58	2.14	5.80	0.21	0.77	0.13	-0.11	1.33	-0.13	-0.47	-0.03
Mg#	19.1	55.2	36.0	36.3	44.1	59.6	53.7	50.2	58.2	52.1	57.7	41.0	58.5	59.9	59.2
Minor and Trace Elements (ppm)															
Sc	3.95	14.8	5.36	31.8	9.89	22.7	25.5	19.1	31.1	21.8	23.4	3.38	-	10.4	25.2
V	42.7	159	60.0	180	82.3	178	166	185	197	177	157	22.6	145	172	169
Cr	18.0	133	12.4	180	29.6	187	189	67	194	115	191	8.20	180	237	232
Co	2.87	17.8	7.81	34.8	10.3	37.3	34.0	29.1	40.6	40.4	45.5	4.29	-	40.6	42.1
Ni	9.80	63.7	9.40	77.0	21.0	99.5	96.4	57.9	107	80.0	129	4.50	68.4	154	144
Rb	70.8	46.3	53.4	2.77	57.4	13.7	17.3	25.1	13.1	16.5	10.6	68.8	-	9.80	10.6
Sr	585	948	704	491	413	399	454	487	386	508	489	521	-	451	486
Y	7.73	18.7	6.36	28.9	13.5	26.1	23.2	27.7	29.2	28.4	28.3	5.78	-	27.2	27.9
Zr	157	193	150	123	142	146	132	194	144	192	169	95.4	-	163	156
Nb	10.1	17.8	8.11	4.78	13.3	10.2	9.55	14.4	9.28	13.5	9.64	9.16	-	9.35	9.28
Cs	2.21	0.84	0.48	0.07	1.26	0.14	0.36	0.36	0.23	0.09	0.06	2.49	-	0.10	0.06
Ba	598	633	601	146	700	224	254	378	202	344	196	548	-	204	222
La	26.0	45.3	35.0	14.0	38.6	18.0	17.2	27.6	16.9	24.3	17.8	26.5	-	18.5	18.7
Ce	45.3	83.7	63.1	29.1	62.9	36.4	33.5	52.7	34.7	48.5	37.5	45.6	-	38.5	38.6
Pr	4.83	9.18	6.42	4.05	6.85	4.62	4.12	6.36	4.48	6.15	4.89	4.76	-	4.86	4.83
Nd	16.0	32.2	20.9	16.9	22.6	18.7	16.1	24.3	18.3	24.2	19.6	15.2	-	19.3	19.1
Sm	2.80	5.44	3.35	4.22	3.98	4.35	3.75	5.26	4.44	5.53	4.61	2.44	-	4.40	4.31
Eu	0.79	1.54	0.94	1.42	1.08	1.47	1.23	1.59	1.45	1.71	1.52	0.69	-	1.50	1.48
Gd	2.02	4.39	2.26	4.61	3.15	4.50	3.81	5.10	4.86	5.38	4.69	1.69	-	4.66	4.58
Tb	0.27	0.62	0.28	0.78	0.46	0.75	0.64	0.80	0.82	0.85	0.78	0.22	-	0.76	0.75
Dy	1.35	3.38	1.25	4.76	2.46	4.34	3.79	4.69	5.00	5.00	4.58	1.06	-	4.58	4.47
Ho	0.26	0.66	0.21	1.02	0.48	0.90	0.80	0.96	1.05	1.03	0.96	0.18	-	0.96	0.93
Er	0.66	1.80	0.55	2.92	1.33	2.54	2.29	2.74	3.01	2.88	2.70	0.47	-	2.73	2.66
Yb	0.60	1.64	0.44	2.69	1.27	2.33	2.18	2.53	2.81	2.68	2.50	0.40	-	2.47	2.44
Lu	0.09	0.25	0.06	0.39	0.19	0.35	0.33	0.38	0.44	0.42	0.38	0.06	-	0.38	0.37
Hf	3.70	3.98	3.33	2.73	3.41	3.24	2.84	3.94	3.20	4.10	3.49	2.57	-	3.42	3.31
Ta	-	0.89	0.47	0.37	0.83	0.63	1.34	0.71	0.52	2.85	-	-	-	-	-
Pb	13.4	10.4	11.7	2.80	12.9	3.91	4.15	6.02	3.80	4.95	2.81	14.1	-	3.53	3.43
Th	8.61	7.36	5.82	1.58	10.5	2.43	2.70	4.05	2.05	3.36	1.75	7.09	-	1.55	1.79
U	1.86	1.66	1.34	0.14	2.12	0.50	0.73	1.09	0.56	0.90	0.38	2.21	-	0.43	0.47
Isotopic Ratios															
87Sr/86Sr	0.704295				0.704323	0.703952		0.704067		0.704176		0.704109		0.703922	0.703969
SE	0.000003				0.000004	0.000003		0.000003		0.000003		0.000003		0.000005	0.000004
143Nd/144Nd						0.512893		0.512877	0.512866	0.512864	0.512873	0.512775		0.512875	0.512870
2SE						0.000013		0.000008	0.000008	0.000008	0.000011	0.000010		0.000009	0.000009
εNd						4.98		4.65	4.45	4.40	4.58	2.68		4.63	4.52
206Pb/204Pb	18.694				18.884	18.810		18.989		18.947		18.661		18.890	
2SE	0.001				0.002	0.003		0.002		0.002		0.001		0.001	
207Pb/204Pb	15.618				15.632	15.503		15.627		15.589		15.615		15.584	
2SE	0.001				0.002	0.003		0.002		0.002		0.001		0.001	
208Pb/204Pb	38.789				38.950	38.611		38.989		38.867		38.752		38.820	
2SE	0.003				0.005	0.010		0.005		0.006		0.003		0.003	
176Hf/177Hf										0.283030					
se										0.000004					
εHf										6.01					

TABLE C.1: Bulk-rock data for Lesser Caucasus samples

	Lower Akhalkalaki Fm. (Stage II)				Upper Akhalkalaki Fm. (Stage III)					Upper Akhalkalaki Fm. (Stage IV)				
Sample	NSPhD3	NSPhD4	NSPhD5	NSPhD6	14-033	14-036	14-036a	13-083	13-084	14-029	14-030	14-045	13-080	13-081
Major Elements (wt%)														
SiO_2	50.1	49.7	51.3	50.9	59.0	52.4	51.3	61.9	62.4	59.2	59.2	55.2	62.5	58.6
Al_2O_3	16.7	16.9	16.9	16.7	16.6	16.9	17.2	16.0	16.2	16.8	16.4	16.8	15.4	16.8
Fe_2O_3	10.33	10.31	9.76	10.21	6.28	9.02	9.80	5.32	5.32	6.55	6.10	7.85	5.09	6.66
MgO	7.13	7.62	6.78	6.20	3.90	6.55	6.51	2.51	2.51	4.02	3.57	5.05	3.19	3.93
CaO	9.03	8.87	9.46	8.74	6.40	8.22	9.50	5.03	5.00	6.48	6.19	7.63	5.05	6.38
Na_2O	3.68	3.72	3.56	3.99	3.97	3.94	3.90	4.05	4.08	4.28	3.99	4.08	3.68	4.10
K_2O	0.74	0.68	1.02	1.06	1.95	1.08	0.96	2.48	2.54	2.06	2.02	1.68	2.85	2.07
TiO_2	1.47	1.44	1.34	1.44	0.89	1.39	1.41	0.76	0.76	1.02	0.84	1.10	0.66	1.04
MnO	0.16	0.16	0.16	0.16	0.10	0.15	0.16	0.09	0.09	0.11	0.10	0.13	0.09	0.12
P_2O_5	0.33	0.30	0.28	0.43	0.36	0.43	0.38	0.30	0.30	0.35	0.34	0.43	0.23	0.34
Total	99.69	99.63	100.52	99.79	100.22	100.38	100.79	98.49	100.00	100.54	99.65	100.19	98.76	100.76
LOI	0.53	-0.12	-0.21	-0.02	0.70	0.30	-0.27	0.54	0.87	-0.33	0.90	0.25	1.16	0.72
Mg#	57.8	59.4	57.9	54.6	55.1	59.0	56.8	48.3	48.3	54.9	53.7	56.0	55.4	53.9
Minor and Trace Elements (ppm)														
Sc	24.2	24.3	28.0	21.0	15.1	24.7	25.4	11.1	10.1	27.3	13.8	18.8	12.8	-
V	157	173	169	149	127	176	187	86.6	84.9	202	118	151	-	125
Cr	239	235	190	176	83.1	179	171	17.0	18.0	213	42.9	119	-	67.4
Co	41.8	43.2	37.0	34.7	21.4	37.1	37.6	15.5	15.3	43.7	20.7	30.3	17.6	-
Ni	149	152	96.0	76.5	57.2	130	88.1	24.0	21.6	123	57.6	77.2	-	55.4
Rb	9.99	7.82	19.6	14.1	37.6	13.1	12.5	51.6	54.5	10.2	41.4	23.8	58.9	-
Sr	489	445	369	499	603	518	491	457	441	527	563	585	418	-
Y	27.0	25.9	27.3	28.3	18.2	27.5	29.0	19.9	19.3	26.6	18.8	22.7	18.5	-
Zr	153	150	141	173	165	181	167	194	186	160	173	183	166	-
Nb	8.69	7.92	7.28	13.5	14.3	12.8	12.0	13.6	13.5	10.4	14.9	17.2	14.4	-
Cs	0.21	0.04	0.17	0.05	0.88	0.24	0.07	1.12	1.21	0.05	1.00	0.28	1.36	-
Ba	230	187	215	290	528	318	287	611	601	213	544	556	726	-
La	17.4	15.4	15.1	23.8	33.1	23.2	22.4	38.1	37.7	17.3	32.2	35.7	39.5	-
Ce	35.7	32.3	31.8	46.2	57.8	45.7	44.6	66.0	66.8	35.9	56.9	63.6	66.9	-
Pr	4.57	4.18	4.08	5.79	6.50	5.66	5.56	7.14	7.02	4.67	6.31	7.28	7.00	-
Nd	18.2	16.9	16.5	22.2	23.1	22.1	21.9	23.8	24.2	19.1	22.2	26.1	22.9	-
Sm	4.16	3.97	3.93	4.76	4.33	5.01	4.92	4.29	4.36	4.40	4.25	5.15	4.04	-
Eu	1.45	1.41	1.34	1.56	1.28	1.58	1.59	1.27	1.19	1.47	1.24	1.50	1.13	-
Gd	4.40	4.33	4.33	4.82	3.84	4.90	5.06	3.86	3.79	4.61	3.76	4.59	3.44	-
Tb	0.73	0.71	0.72	0.77	0.57	0.79	0.83	0.57	0.57	0.75	0.56	0.70	0.53	-
Dy	4.35	4.22	4.35	4.58	3.11	4.64	4.89	3.16	3.23	4.48	3.18	4.00	2.93	-
Ho	0.91	0.89	0.92	0.95	0.63	0.97	1.02	0.66	0.65	0.93	0.64	0.81	0.62	-
Er	2.57	2.50	2.62	2.72	1.75	2.76	2.93	1.92	1.87	2.68	1.82	2.25	1.72	-
Yb	2.34	2.28	2.45	2.52	1.61	2.55	2.67	1.74	1.78	2.46	1.69	2.09	1.66	-
Lu	0.36	0.34	0.38	0.39	0.25	0.39	0.40	0.27	0.27	0.38	0.25	0.32	0.26	-
Hf	3.19	3.14	3.10	3.53	3.60	3.72	3.56	4.04	3.91	3.25	3.72	3.94	3.65	-
Ta	-	-	-	-	0.73	0.66	0.60	0.00	0.74	0.93	0.74	1.02	0.00	-
Pb	3.54	2.96	3.34	4.39	9.33	4.95	4.82	11.0	11.2	3.40	8.95	8.55	11.9	-
Th	1.66	1.45	2.51	2.33	5.33	2.48	2.16	8.43	8.91	1.78	5.77	5.65	11.0	-
U	0.59	0.25	0.59	0.50	1.29	0.64	0.35	1.78	1.84	0.39	1.45	1.34	1.94	-
Isotopic Ratios														
87Sr/86Sr		0.703854			0.704211	0.703909		0.704607						
SE		0.000005			0.000003	0.000002		0.000003						
143Nd/144Nd					0.512806	0.512856		0.512815		0.512863				
2SE					0.000008	0.000011		0.000011		0.000009				
εNd					3.28	4.25		3.45		4.40				
206Pb/204Pb				18.901	18.817	18.870		18.915						
2SE				0.004	0.001	0.002		0.001						
207Pb/204Pb				15.558	15.620	15.622		15.626						
2SE				0.003	0.001	0.001		0.001						
208Pb/204Pb				38.718	38.876	38.891		38.948						
2SE				0.009	0.004	0.004		0.003						
176Hf/177Hf					0.283031	0.283040		0.283047						
se					0.000002	0.000002		0.000005						
εHf					6.03	6.36		6.62						

TABLE C.1: Bulk-rock data for Lesser Caucasus samples

	Scoria Cones		Abul-Samsari Fm.									Borjomi Flows		
Sample	13-099	13-101	14-031	14-032	14-035	14-037	14-038	14-049	14-040	14-041	14-042	13-095	13-097	13-098
Major Elements (wt%)														
SiO_2	58.1	57.9	56.7	50.6	69.7	70.3	64.4	64.9	60.6	62.0	65.0	61.0	62.4	62.7
Al_2O_3	16.6	16.6	16.2	16.9	15.7	15.5	16.6	16.4	16.2	16.3	16.2	16.3	16.4	16.5
Fe_2O_3	6.31	6.36	8.00	10.42	2.60	2.55	4.77	4.34	5.63	5.67	4.46	5.15	4.90	4.94
MgO	4.06	4.14	4.92	7.14	0.72	0.40	2.49	2.01	2.37	2.43	2.49	2.50	2.39	2.42
CaO	6.55	6.61	7.32	9.38	3.30	2.93	5.23	4.87	5.12	5.15	5.28	5.24	5.20	5.21
Na_2O	4.19	4.18	4.07	3.80	4.25	4.60	4.27	4.19	4.01	4.11	4.24	4.06	4.10	4.14
K_2O	1.90	1.88	1.67	0.76	2.93	2.52	2.02	2.06	2.31	2.35	1.95	2.15	2.11	2.10
TiO_2	0.88	0.89	1.12	1.50	0.40	0.37	0.71	0.59	0.85	0.85	0.59	0.77	0.70	0.71
MnO	0.10	0.10	0.13	0.16	0.04	0.05	0.08	0.07	0.09	0.09	0.07	0.08	0.08	0.08
P_2O_5	0.40	0.40	0.43	0.35	0.17	0.14	0.26	0.24	0.35	0.36	0.23	0.32	0.28	0.28
Total	99.11	99.04	100.60	100.99	100.58	100.19	100.92	99.84	97.86	99.84	100.63	97.54	98.58	99.01
LOI	-0.02	0.07	0.05	0.02	0.71	0.87	0.11	0.15	0.32	0.55	0.11	1.07	-0.05	-0.06
Mg#	56.0	56.3	54.9	57.6	35.4	23.7	50.8	47.9	45.5	45.9	52.5	49.0	49.2	49.2
Minor and Trace Elements (ppm)														
Sc	15.2	15.3	15.5	15.4	4.36	4.18	10.8	9.60	11.9	12.1	11.2	10.8	12.0	10.8
V	120	126	125	126	45.0	40.9	93.0	88.0	105	106	94.6	93.5	84.7	82.8
Cr	109	110	42.9	103	4.00	4.40	38.0	26.0	35.0	30.9	66.2	37.7	40.9	40.0
Co	21.8	22.0	28.7	23.4	5.70	5.68	14.5	11.9	15.2	15.0	13.3	14.8	15.7	14.0
Ni	62.3	65.3	57.6	84.2	7.30	5.00	26.6	18.0	19.1	19.9	28.3	20.7	18.2	21.4
Rb	37.9	38.1	31.2	49.4	84.0	61.7	43.7	46.8	40.3	41.2	40.8	42.7	50.6	45.3
Sr	686	682	544	476	503	508	519	509	509	505	496	597	629	566
Y	18.6	18.8	24.3	22.1	5.54	4.45	13.1	12.5	17.7	18.1	11.2	14.2	15.1	13.5
Zr	186	184	192	180	75.6	23.8	173	174	206	210	164	174	197	176
Nb	24.3	15.3	15.4	17.0	10.6	11.6	12.9	12.6	17.6	17.8	10.6	14.4	15.1	13.6
Cs	0.73	0.74	0.81	1.55	2.75	1.61	1.14	1.29	0.74	0.76	1.01	1.01	1.21	1.08
Ba	549	551	463	431	756	679	540	571	652	662	534	591	652	593
La	37.4	37.5	29.8	29.1	32.7	28.7	30.1	30.5	38.9	39.4	29.6	35.1	37.4	33.8
Ce	66.1	66.4	55.5	54.0	53.8	47.3	53.6	54.1	69.9	70.5	52.7	61.9	66.6	60.1
Pr	7.11	7.12	6.51	6.22	5.49	4.81	5.92	5.96	7.77	7.87	5.80	6.71	7.17	6.49
Nd	24.1	24.2	23.9	22.5	17.5	15.2	20.6	20.5	27.0	27.4	20.0	22.5	24.4	22.0
Sm	4.30	4.34	4.85	4.57	2.71	2.25	3.89	3.72	4.95	5.05	3.61	4.07	4.37	3.88
Eu	1.33	1.34	1.47	1.31	0.77	0.72	1.10	1.05	1.37	1.39	1.05	1.15	1.24	1.11
Gd	3.79	3.85	4.52	4.18	1.85	1.52	3.11	2.95	4.06	4.15	2.85	3.24	3.41	3.07
Tb	0.54	0.55	0.70	0.65	0.23	0.19	0.45	0.42	0.59	0.61	0.40	0.45	0.49	0.44
Dy	2.98	3.02	4.03	3.72	1.10	0.86	2.35	2.22	3.16	3.24	2.06	2.45	2.60	2.32
Ho	0.60	0.62	0.82	0.76	0.19	0.15	0.46	0.44	0.62	0.62	0.39	0.48	0.51	0.45
Er	1.70	1.73	2.33	2.12	0.47	0.39	1.26	1.20	1.70	1.74	1.05	1.30	1.36	1.22
Yb	1.48	1.53	2.17	1.95	0.39	0.35	1.13	1.07	1.54	1.58	0.95	1.18	1.22	1.11
Lu	0.23	0.23	0.34	0.30	0.05	0.05	0.17	0.16	0.23	0.24	0.14	0.17	0.18	0.17
Hf	4.27	3.73	3.89	3.97	2.13	0.82	3.89	3.98	4.58	4.61	3.83	3.83	4.34	3.90
Ta	0.00	-	0.83	0.92	1.11	0.79	1.30	3.71	0.94	0.98	0.84	0.00	0.00	0.00
Pb	8.92	8.97	7.51	9.81	16.2	14.3	10.6	11.4	12.3	12.3	10.8	10.7	12.4	11.0
Th	4.55	4.58	4.91	6.37	9.19	4.94	5.69	6.09	5.59	5.65	5.76	5.25	6.20	5.52
U	1.15	1.17	1.27	1.85	1.86	0.55	1.48	1.59	1.41	1.44	1.48	1.28	1.52	1.34
Isotopic Ratios														
87Sr/86Sr			0.704493	0.704200	0.704268		0.704079	0.704154	0.704282		0.704100			
SE			0.000003	0.000003	0.000003		0.000004	0.000004	0.000004		0.000004			
143Nd/144Nd	0.512772		0.512763	0.512831	0.512760		0.512813	0.512794	0.512802		0.512812			
2SE	0.000013		0.000009	0.000007	0.000009		0.000007	0.000007	0.000007		0.000007			
εNd	2.61		2.45	3.76	2.38		3.42	3.04	3.20		3.39			
206Pb/204Pb			18.644	18.829	18.679		18.702	18.704	18.790		18.693			
2SE			0.001	0.002	0.001		0.002	0.002	0.001		0.001			
207Pb/204Pb			15.624	15.620	15.617		15.613	15.613	15.622		15.615			
2SE			0.001	0.002	0.001		0.002	0.001	0.001		0.001			
208Pb/204Pb			38.734	38.871	38.775		38.778	38.784	38.859		38.775			
2SE			0.003	0.004	0.004		0.006	0.004	0.002		0.003			
176Hf/177Hf			0.282991		0.283014									
se			0.000003		0.000003									
εHf			4.62		5.44									

TABLE C.2: Bulk-rock data for Greater Caucasus samples

	Gudauri Fm.							
Sample	H1	H2	H3	H4	13-001a	13-002	13-005	13-006
Major Elements								
SiO_2	57.5	57.1	56.7	57.5	63.0	56.9	57.0	63.8
Al_2O_3	16.8	16.6	16.6	18.2	17.8	16.6	18.0	17.1
Fe_2O_3	6.59	6.59	6.98	6.80	4.44	7.07	6.75	5.02
MgO	5.80	5.88	6.37	4.60	1.94	6.45	4.52	2.33
CaO	6.39	6.32	6.73	6.66	4.51	6.65	6.52	4.04
Na_2O	3.42	3.37	3.38	3.79	4.25	3.39	3.73	4.19
K_2O	1.91	1.89	1.75	1.87	2.29	1.74	1.84	2.28
TiO_2	0.92	0.92	0.95	1.06	0.70	0.98	1.04	0.78
MnO	0.13	0.13	0.13	0.14	0.09	0.14	0.14	0.11
P_2O_5	0.28	0.27	0.26	0.27	0.30	0.26	0.27	0.24
Total	99.8	99.2	99.9	100.6	99.7	100.2	99.9	99.8
LOI	0.07	0.06	0.03	-0.26	0.40	-0.23	-0.14	0.08
Mg#	63.5	63.8	64.3	57.3	46.4	64.3	57.0	47.9
Minors and Trace Elements								
Sc	53.5	55.2	55.8	55.5	9.3	20.4	19.4	12.0
V	128	128	135	138	44.9	20.1	146	77.9
Cr	196	214	235	88.7	45.9	235	87.1	53.1
Co	28.5	27.9	30.4	20.4	10.4	32.2	19.2	-
Ni	123	111	112	33.6	28.3	126	27.2	37.9
Rb	49.1	52.1	46.4	54.0	78.5	48.8	59.3	77.1
Sr	897	947	911	726	687	922	794	437
Y	19.6	21.3	20.6	23.0	16.8	20.8	25.0	17.6
Zr	148	157	146	161	160	148	174	142
Nb	8.43	9.19	8.39	8.66	11.4	7.85	9.60	8.60
Cs	1.96	2.48	1.02	1.67	2.65	0.98	2.10	3.11
Ba	440	459	428	442	503	434	479	453
La	30.0	31.4	28.3	28.1	35.5	28.4	29.3	31.3
Ce	62.2	64.8	58.5	57.7	69.8	59.7	59.9	63.8
Pr	7.27	7.64	6.96	6.75	7.88	6.98	7.07	7.22
Nd	27.2	28.7	26.2	25.5	27.5	26.2	26.0	25.9
Sm	5.02	5.31	4.99	4.99	4.87	5.02	4.98	4.91
Eu	1.42	1.47	1.41	1.44	1.40	1.40	1.50	1.27
Gd	4.15	4.44	4.19	4.46	3.88	4.33	4.49	4.17
Tb	0.61	0.66	0.62	0.68	0.54	0.63	0.68	0.59
Dy	3.35	3.59	3.49	3.86	2.80	3.61	3.86	3.06
Ho	0.67	0.73	0.71	0.79	0.54	0.71	0.79	0.58
Er	1.87	2.05	2.00	2.20	1.54	2.03	2.30	1.55
Yb	1.73	1.90	1.82	2.06	1.31	1.86	2.01	1.27
Lu	0.26	0.28	0.28	0.31	0.20	0.28	0.31	0.19
Hf	3.63	3.73	3.47	3.83	3.80	3.55	4.01	3.44
Pb	14.6	28.1	10.4	16.7	19.1	10.4	10.2	19.7
Th	7.51	7.95	6.71	7.42	9.44	7.14	7.47	9.71
U	1.61	1.73	1.53	1.60	1.80	1.65	1.66	1.51
Isotopic Ratios								
87Sr/86Sr	0.704183	0.704196	0.704148	0.704435	0.704833	0.704169	0.704444	
SE	0.000004	0.000004	0.000003	0.000004	0.000005	0.000004	0.000003	
143Nd/144Nd	0.512737		0.512734			0.512735	0.512682	
2SE	0.000005		0.000005			0.000009	0.000010	
εNd	1.93		1.86				0.87	
206Pb/204Pb	18.590	18.595	18.627	18.598	18.608		18.591	
2SE	0.001	0.001	0.001	0.001	0.001		0.002	
207Pb/204Pb	15.614	15.617	15.619	15.616	15.620		15.615	
2SE	0.001	0.001	0.001	0.001	0.001		0.002	
208Pb/204Pb	38.653	38.667	38.711	38.660	38.683		38.652	
2SE	0.002	0.003	0.003	0.002	0.002		0.006	
176Hf/177Hf							0.282919	
2SE							0.000008	
εHf							2.09	

TABLE C.2: Bulk-rock data for Greater Caucasus samples

	Qabarjina						
Sample	H7	13-045	13-047a	13-049	13-051	13-053	13-055
Major Elements							
SiO_2	64.6	66.0	62.6	65.9	65.4	67.3	65.1
Al_2O_3	16.4	16.8	16.9	16.2	16.2	16.3	16.4
Fe_2O_3	4.20	3.64	4.47	3.81	3.71	3.00	4.01
MgO	2.55	1.48	2.39	1.87	1.80	1.00	2.18
CaO	4.07	3.37	4.27	3.51	3.53	3.23	3.90
Na_2O	4.22	4.48	4.53	4.33	4.33	4.47	4.30
K_2O	2.14	2.52	1.89	2.47	2.41	2.61	2.29
TiO_2	0.61	0.56	0.71	0.55	0.54	0.49	0.62
MnO	0.10	0.08	0.08	0.09	0.09	0.08	0.10
P_2O_5	0.18	0.22	0.24	0.18	0.18	0.15	0.21
Total	99.1	99.3	98.1	98.9	98.2	98.6	99.1
LOI	0.17	0.15	0.94	0.66	1.21	0.51	0.64
Mg#	54.6	44.6	51.4	49.3	49.0	39.7	51.8
Minors and Trace Elements							
Sc	32.3	8.52	10.7	8.33	9.03	7.10	9.42
V	72.5	43.6	83.0	55.7	58.9	26.5	62.9
Cr	85.4	40.3	43.3	46.2	44.2	11.6	52.2
Co	13.4	9.27	12.3	9.08	8.40	4.61	8.85
Ni	28.6	18.7	22.7	19.4	12.1	7.2	16.0
Rb	72.8	93.1	67.2	84.6	91.4	88.1	72.0
Sr	464	395	540	432	469	411	440
Y	15.7	15.0	16.6	15.5	16.2	15.9	15.2
Zr	164	43.4	116	112	120	195	154
Nb	8.67	9.62	25.0	8.66	9.41	8.47	7.88
Cs	5.27	4.53	4.41	6.66	7.07	6.52	5.45
Ba	401	489	592	471	484	474	422
La	28.6	32.7	34.5	30.8	32.8	32.4	29.0
Ce	56.0	65.5	67.1	59.6	63.7	62.2	56.9
Pr	6.10	7.04	7.77	6.42	6.75	6.69	6.19
Nd	21.7	25.0	27.6	21.8	23.5	22.6	21.3
Sm	4.07	4.59	5.09	3.96	4.30	4.05	3.95
Eu	1.04	1.07	1.33	1.02	1.06	1.00	1.03
Gd	3.37	3.71	3.95	3.27	3.51	3.35	3.29
Tb	0.49	0.53	0.56	0.47	0.51	0.48	0.48
Dy	2.62	2.80	2.92	2.54	2.82	2.62	2.58
Ho	0.52	0.51	0.56	0.50	0.53	0.51	0.51
Er	1.45	1.35	1.50	1.43	1.49	1.51	1.47
Yb	1.35	1.16	1.29	1.25	1.38	1.36	1.30
Lu	0.20	0.16	0.19	0.19	0.20	0.21	0.20
Hf	3.82	1.45	3.22	2.94	3.11	4.73	3.91
Pb	18.9	23.6	20.7	21.7	24.7	21.4	20.3
Th	10.0	10.2	12.9	11.9	12.9	11.7	10.6
U	2.41	1.84	2.69	2.86	3.22	2.92	2.65
Isotopic Ratios							
87Sr/86Sr	0.704869			0.704947			
SE	0.000003			0.000005			
143Nd/144Nd	0.512690			0.512659			0.512663
2SE	0.000006			0.000009			0.000009
εNd	1.02			0.41			0.48
206Pb/204Pb	18.627			18.618			18.588
2SE	0.001			0.001			0.002
207Pb/204Pb	15.619			15.618			15.600
2SE	0.001			0.001			0.002
208Pb/204Pb	38.693			38.688			38.621
2SE	0.003			0.003			0.005
176Hf/177Hf							
2SE							
εHf							

TABLE C.2: Bulk-rock data for Greater Caucasus samples

	Stage I	Stage II						
Sample	13-008	13-026	13-028	13-030	13-032	13-034	13-035	13-037
Major Elements								
SiO_2	62.8	62.2	63.4	62.0	62.2	62.3	59.5	59.2
Al_2O_3	16.3	16.0	16.4	16.0	16.5	16.5	16.6	16.6
Fe_2O_3	4.61	4.85	4.77	4.75	5.03	4.99	6.13	6.11
MgO	3.48	3.93	3.78	3.66	3.05	3.04	4.62	4.09
CaO	5.03	5.28	5.10	5.00	4.96	4.99	5.70	5.49
Na_2O	4.83	4.74	4.80	4.59	4.59	4.65	4.65	4.62
K_2O	1.62	1.68	1.88	1.90	1.93	1.92	1.83	1.84
TiO_2	0.74	0.77	0.77	0.77	0.80	0.80	1.01	1.05
MnO	0.08	0.08	0.08	0.08	0.09	0.09	0.10	0.09
P_2O_5	0.21	0.24	0.30	0.27	0.28	0.28	0.35	0.36
Total	99.6	99.7	101.2	99.0	99.5	99.5	100.5	99.5
LOI	0.07	-0.07	0.08	0.07	0.01	0.38	0.22	0.20
Mg#	59.9	61.6	61.1	60.4	54.6	54.7	59.9	57.0
Minors and Trace Elements								
Sc	11.1	12.4	11.5	11.4	13.1	12.5	13.5	12.6
V	75.0	131	103	85.2	104	85.7	100	115
Cr	103	115	111	116	66.3	75.5	158	118
Co	17.2	18.3	16.8	17.6	16.6	15.6	21.1	20.9
Ni	43.7	86.8	55.2	55.7	32.0	60.6	30.4	53.6
Rb	45.3	46.3	53.2	59.7	59.4	52.5	45.9	51.5
Sr	464	522	574	600	610	582	608	653
Y	12.4	13.0	12.3	13.5	13.5	12.6	15.1	17.1
Zr	98.0	135	125	119	155	153	166	187
Nb	6.00	6.41	7.02	8.92	10.7	7.81	9.02	11.7
Cs	1.11	1.32	3.15	2.04	2.91	3.52	2.77	3.62
Ba	412	415	491	513	459	445	506	510
La	23.5	26.2	28.9	29.9	29.1	28.4	30.6	31.8
Ce	45.6	50.0	54.6	57.1	56.4	54.1	60.2	62.7
Pr	5.12	5.66	6.07	6.47	6.23	6.06	6.92	7.36
Nd	18.2	20.0	21.2	22.8	22.4	21.3	24.8	26.6
Sm	3.48	3.67	3.84	4.18	4.18	3.92	4.66	5.23
Eu	1.07	1.13	1.17	1.17	1.18	1.16	1.38	1.41
Gd	3.03	3.16	3.14	3.29	3.44	3.25	3.92	4.14
Tb	0.43	0.45	0.43	0.46	0.48	0.44	0.54	0.59
Dy	2.36	2.32	2.22	2.37	2.48	2.32	2.79	3.05
Ho	0.46	0.45	0.43	0.45	0.47	0.44	0.53	0.57
Er	1.29	1.26	1.19	1.19	1.23	1.21	1.42	1.47
Yb	1.10	1.07	0.96	1.02	1.07	1.02	1.17	1.24
Lu	0.16	0.16	0.15	0.15	0.16	0.15	0.17	0.18
Hf	2.87	3.43	3.17	2.95	3.70	3.87	4.10	4.30
Pb	14.4	12.4	15.4	14.0	14.0	13.5	15.0	15.1
Th	8.77	9.23	9.46	10.4	8.81	8.64	9.68	10.6
U	2.24	2.30	2.52	2.62	2.27	2.29	2.32	2.44
Isotopic Ratios								
87Sr/86Sr		0.704430	0.704477				0.704561	
SE		0.000005	0.000005				0.000005	
143Nd/144Nd							0.512743	
2SE							0.000015	
εNd							2.05	
206Pb/204Pb		18.647	18.646				18.646	
2SE		0.001	0.001				0.003	
207Pb/204Pb		15.617	15.623				15.626	
2SE		0.001	0.001				0.002	
208Pb/204Pb		38.739	38.746				38.742	
2SE		0.002	0.003				0.007	
176Hf/177Hf								
2SE								
εHf								

TABLE C.2: Bulk-rock data for Greater Caucasus samples

	Stage II						Stage III	
Sample	13-038	13-040	13-043	13-059	13-062	13-067	13-025	13-056
Major Elements								
SiO_2	61.9	58.6	61.9	63.2	61.8	62.0	59.0	55.8
Al_2O_3	15.9	16.4	16.4	15.8	16.6	16.4	15.8	16.3
Fe_2O_3	4.76	5.95	5.02	4.14	4.97	5.09	6.04	7.63
MgO	3.64	4.31	3.07	2.87	3.43	3.40	4.93	5.93
CaO	4.86	5.56	4.94	4.62	4.76	4.55	5.88	6.46
Na_2O	4.66	4.46	4.57	4.72	4.27	4.36	4.51	4.54
K_2O	1.93	1.82	1.93	1.79	2.04	2.11	1.78	1.65
TiO_2	0.77	0.98	0.80	0.64	0.73	0.77	1.03	1.30
MnO	0.08	0.10	0.09	0.07	0.10	0.10	0.09	0.12
P_2O_5	0.30	0.34	0.29	0.21	0.26	0.28	0.32	0.40
Total	98.8	98.5	99.0	98.0	99.0	99.1	99.5	100.1
LOI	0.44	0.56	0.61	1.18	-0.12	-0.07	-0.08	-0.24
Mg#	60.2	58.9	54.8	57.9	57.7	56.9	61.8	60.6
Minors and Trace Elements								
Sc	11.4	13.5	12.9	10.6	13.2	12.9	16.1	15.8
V	114	109	86.3	99.5	94.8	92.4	107	138
Cr	106	163	67.0	72.2	102	107	158	188
Co	16.8	22.3	15.5	14.4	16.3	15.2	21.1	32.0
Ni	74.8	69.3	60.9	29.7	49.3	44.6	16.3	93.2
Rb	55.2	51.6	54.0	52.2	62.9	68.0	43.5	39.4
Sr	562	654	584	511	527	555	670	681
Y	12.8	16.4	12.8	11.4	15.9	16.5	12.7	18.7
Zr	120	180	158	141	130	146	92.2	197
Nb	7.47	11.2	7.96	6.04	8.56	14.8	7.92	12.7
Cs	3.59	3.12	4.39	3.37	2.37	2.61	2.42	0.95
Ba	483	506	443	386	425	449	403	546
La	29.9	32.2	28.5	23.7	30.2	32.1	26.7	29.1
Ce	57.1	63.3	54.2	45.6	60.1	63.8	51.6	58.3
Pr	6.39	7.39	6.02	5.01	6.71	7.14	5.88	6.97
Nd	22.3	26.7	21.2	17.6	23.8	25.2	20.9	25.9
Sm	4.01	5.12	3.91	3.19	4.45	4.70	3.89	5.25
Eu	1.18	1.41	1.16	1.00	1.23	1.27	1.21	1.56
Gd	3.33	4.09	3.18	2.77	3.72	3.91	3.28	4.42
Tb	0.46	0.58	0.44	0.39	0.53	0.54	0.44	0.65
Dy	2.33	2.98	2.28	2.02	2.80	2.88	2.27	3.39
Ho	0.44	0.55	0.44	0.39	0.55	0.55	0.43	0.64
Er	1.21	1.44	1.20	1.09	1.56	1.53	1.16	1.65
Yb	1.01	1.21	1.01	0.93	1.32	1.32	0.90	1.37
Lu	0.15	0.18	0.15	0.14	0.20	0.19	0.14	0.19
Hf	3.09	4.12	3.79	3.48	3.39	3.93	2.54	4.48
Pb	14.6	15.1	13.2	18.7	17.0	16.7	9.5	13.6
Th	9.39	10.0	8.38	8.11	8.88	9.42	6.09	8.92
U	2.53	2.27	2.21	2.28	2.09	2.29	1.33	2.16
Isotopic Ratios								
87Sr/86Sr	0.704475		0.704557	0.704341			0.704318	0.704214
SE	0.000004		0.000004	0.000004			0.000005	0.000003
143Nd/144Nd				0.512770				0.512801
2SE				0.000011				0.000007
εNd				2.57				
206Pb/204Pb	18.644		18.641	18.634			18.648	18.675
2SE	0.001		0.001	0.001			0.002	0.001
207Pb/204Pb	15.624		15.622	15.622			15.625	15.623
2SE	0.001		0.001	0.001			0.002	0.001
208Pb/204Pb	38.747		38.738	38.745			38.755	38.764
2SE	0.003		0.003	0.003			0.005	0.002
176Hf/177Hf				0.283002				
2SE				0.000004				
εHf				5.01				

TABLE C.2: Bulk-rock data for Greater Caucasus samples

	Stage III				Stage IV			
Sample	13-070	13-071	13-072	13-073	H5	H6	KZ1	13-012
Major Elements								
SiO_2	59.5	58.6	60.1	59.9	64.0	59.6	61.3	62.0
Al_2O_3	15.8	15.7	16.2	16.1	16.3	17.9	17.3	17.1
Fe_2O_3	6.14	6.01	5.30	5.35	4.47	5.66	5.16	5.05
MgO	5.06	4.90	4.70	4.75	3.41	2.96	2.93	2.96
CaO	5.95	5.79	5.73	5.77	4.76	5.87	5.48	5.33
Na_2O	4.53	4.40	4.48	4.53	4.47	3.83	3.97	4.03
K_2O	1.79	1.76	1.69	1.70	1.89	2.40	2.39	2.36
TiO_2	1.05	1.03	0.85	0.85	0.67	0.79	0.72	0.71
MnO	0.09	0.09	0.08	0.08	0.08	0.12	0.11	0.11
P_2O_5	0.33	0.31	0.32	0.32	0.23	0.29	0.26	0.26
Total	100.3	98.6	99.4	99.4	100.2	99.4	99.6	99.9
LOI	-0.12	-0.16	-0.07	0.11	0.05	0.11	0.00	0.13
Mg#	62.0	61.8	63.7	63.7	60.2	50.9	53.0	53.7
Minors and Trace Elements								
Sc	16.7	16.0	13.4	14.5	35.0	39.2	39.7	12.1
V	131	138	105	118.9	82.7	116	105	79.7
Cr	148	167	158	154	112	27.7	52.2	65.6
Co	23.0	23.5	21.0	21.0	16.4	13.8	13.6	12.4
Ni	84.0	86.5	93.5	96.8	61.4	8.9	13.5	37.2
Rb	42.0	46.7	48.3	45.3	56.1	75.3	76.3	70.2
Sr	665	699	646	625	529	928	809	719
Y	12.7	13.7	13.3	12.9	13.5	20.6	18.9	16.5
Zr	124	131	174	173	107	158	135	119
Nb	8.0	9.6	8.9	9.4	7.47	8.89	8.53	7.04
Cs	1.6	2.0	2.2	3.0	3.88	4.94	5.38	5.22
Ba	399	414	421	410	387	655	612	589
La	25.9	27.5	27.8	27.3	27.8	34.9	32.9	30.6
Ce	51.2	53.8	53.9	52.7	53.6	70.1	66.1	60.9
Pr	5.85	6.25	6.17	5.96	5.89	8.00	7.33	6.89
Nd	21.1	22.6	22.0	21.1	20.9	28.9	26.3	24.1
Sm	3.90	4.30	4.16	3.84	3.86	5.15	4.72	4.31
Eu	1.24	1.24	1.19	1.19	1.03	1.42	1.28	1.22
Gd	3.37	3.45	3.27	3.22	3.17	4.26	3.88	3.61
Tb	0.46	0.48	0.46	0.46	0.45	0.62	0.57	0.53
Dy	2.39	2.47	2.40	2.30	2.37	3.37	3.14	2.91
Ho	0.45	0.47	0.45	0.44	0.46	0.68	0.64	0.59
Er	1.23	1.23	1.18	1.21	1.24	1.92	1.77	1.71
Yb	0.98	1.01	1.03	1.02	1.10	1.80	1.65	1.52
Lu	0.15	0.15	0.15	0.15	0.16	0.27	0.25	0.24
Hf	3.10	3.19	4.19	4.21	2.65	3.78	3.37	3.31
Pb	8.8	10.0	14.4	11.6	15.9	18.5	19.9	20.2
Th	7.10	8.11	9.38	8.47	8.42	10.2	10.3	10.1
U	1.98	2.15	2.38	2.34	1.95	2.27	2.39	2.47
Isotopic Ratios								
87Sr/86Sr	0.704305			0.704407	0.704505	0.704360	0.704339	0.704363
SE	0.000003			0.000006	0.000004	0.000004	0.000004	0.000004
143Nd/144Nd	0.512770			0.512783		0.512738		0.512756
2SE	0.000007			0.000011		0.000004		0.000012
εNd				2.83		1.96		2.30
206Pb/204Pb	18.623			18.636	18.592	18.600	18.604	18.606
2SE	0.001			0.001	0.001	0.001	0.001	0.001
207Pb/204Pb	15.619			15.619	15.617	15.617	15.615	15.620
2SE	0.001			0.001	0.001	0.001	0.001	0.001
208Pb/204Pb	38.705			38.727	38.665	38.662	38.666	38.682
2SE	0.004			0.003	0.002	0.002	0.002	0.002
176Hf/177Hf								0.282935
2SE								0.000004
εHf								2.66

TABLE C.3: Bulk-rock data for basement samples

	Mt. Kazbek / Russian Border						Greater Caucasus Main Range Zone			
Sample	13-013	13-016	13-018	13-020	13-021	13-022	14-007	14-008	14-009	14-010
Lithology	Dyke	Bt-Gneiss	Pillow	Granite	Granite	Granite	Pale Granite	Mica Schite	Mica Schist	Dark Granite
Major Elements (wt%)										
SiO_2	49.9	66.4	47.3	66.1	65.9	-	75.8	66.6	57.9	-
Al_2O_3	15.7	15.8	16.4	15.6	15.7	-	13.2	16.1	18.2	-
Fe_2O_3	8.92	5.21	10.1	5.02	5.14	-	1.22	5.10	6.11	-
MgO	6.60	1.69	9.12	1.98	1.77	-	0.20	1.80	3.17	-
CaO	7.00	4.42	10.2	3.54	4.45	-	1.08	1.57	7.49	-
Na_2O	3.38	3.12	2.12	4.07	3.22	-	3.92	2.72	3.15	-
K_2O	1.77	2.38	1.26	1.10	2.83	-	4.09	3.35	1.17	-
TiO_2	1.85	0.62	1.43	0.61	0.61	-	0.13	0.88	1.02	-
MnO	0.18	0.08	0.17	0.07	0.10	-	0.03	0.08	0.12	-
P_2O_5	0.32	0.17	0.15	0.16	0.19	-	0.03	0.11	0.27	-
Total	95.7	100.3	98.2	98.2	101.1	-	100.1	99.8	100.9	-
LOI	3.30	0.40	1.48	1.73	1.12	-	0.42	1.52	2.31	-
Minor and Trace Elements (ppm)										
Sc	38.4	15.5	32.2	14.8	12.8	7.24	2.85	14.8	7.26	19.1
V	265		168	95.7	95.1	-	5.30			130
Cr	144	37.4	397	28.9	49.7	24.2		115	60.1	
Ni	61.3		184	7.90	7.10	-	0.72			10.5
Rb	54.4	87.9	31.1	64.1	82.2	100	147	113	62.8	56.3
Sr	200	251	252	226	200	236	74.1	166	64.2	210
Y	36.6	26.2	27.3	27.4	24.0	16.4	25.2	32.9	11.4	30.7
Zr	718	161	102	161	152	-	37.2	20.0	11.7	9.76
Nb	8.69	10.3	2.57	10.1	8.71	7.72	7.37	13.2	7.02	9.02
Cs	4.24	1.72	0.83	1.73	2.33	2.71	3.08	4.52	2.99	2.18
Ba	355	608	103	152	502	603	402	642	316	235
La	10.3	27.1	4.92	36.3	33.5	35.3	28.6	34.2	16.8	18.2
Ce	27.4	54.7	14.4	72.0	66.4	67.0	58.0	70.7	43.1	40.0
Pr	4.00	6.30	2.31	8.04	7.39	7.06	6.45	8.30	4.10	5.11
Nd	18.5	23.9	11.2	29.0	26.4	23.5	21.8	31.5	15.3	20.2
Sm	5.16	5.31	3.47	5.79	5.26	3.99	4.51	6.47	3.04	4.78
Eu	1.10	1.33	1.29	1.05	1.01	1.09	0.44	1.32	0.57	1.19
Gd	6.18	5.06	4.17	5.22	4.63	3.20	4.01	5.87	2.56	4.97
Tb	1.05	0.79	0.73	0.81	0.72	0.48	0.68	0.94	0.38	0.84
Dy	6.45	4.59	4.48	4.70	4.15	2.67	3.97	5.63	2.15	4.99
Ho	1.31	0.90	0.95	0.94	0.82	0.53	0.82	1.12	0.41	1.05
Er	3.53	2.51	2.64	2.64	2.33	1.55	2.39	3.03	1.11	3.00
Yb	2.78	2.14	2.31	2.45	2.17	1.50	2.24	2.66	1.03	2.63
Lu	0.32	0.30	0.34	0.35	0.32	0.22	0.31	0.36	0.15	0.38
Hf	2.00	0.12	1.95	0.14	0.22	0.11	1.45	0.56	0.28	0.53
Ta	-	-	-	-	-	-	-	-	-	-
Pb	1.18	11.5	7.24	12.6	16.6	21.1	28.1	10.8	5.19	12.4
Th	0.66	8.90	0.17	14.6	13.3	15.2	18.9	10.8	5.83	8.59
U	0.24	3.30	0.05	2.71	1.83	2.53	2.67	2.21	0.89	1.74
Isotopic Ratios										
87Sr/86Sr			0.703994	0.711836	0.711836	0.711836	0.720351			
2SE			0.000003	0.000006	0.000006	0.000006	0.000004			
143Nd/144Nd			0.512911		0.512186	0.512141				
2SE			0.000009		0.000012	0.000009				
εNd			5.32		-8.82					
206Pb/204Pb			18.397	20.020	19.420	18.935	18.520			
2SE			0.001	0.002	0.001	0.001	0.001			
207Pb/204Pb			15.662	15.757	16.316	15.710	15.664			
2SE			0.001	0.002	0.001	0.001	0.001			
208Pb/204Pb			38.558	41.371	41.594	39.552	38.736			
2SE			0.002	0.006	0.004	0.004	0.002			
176Hf/177Hf					0.283142					
se					0.000010					
εHf					33.76					

TABLE C.3: Bulk-rock data for basement samples

	Greater Caucasus Main Range Zone									
Sample	14-012	14-014	14-015	14-016	14-017	14-018	14-019	14-020	14-021	14-022
Lithology	Granite	Granite	Bt Schist	Diorite	Bt Sil Schist	Amphibolite	Pale Granite	Granite	Diorite	Gneiss
Major Elements (wt%)										
SiO_2	83.1	60.5	53.1	63.7	58.4	46.8	77.6	-	62.2	72.0
Al_2O_3	7.5	17.0	22.2	15.7	21.4	16.3	12.3	-	16.3	13.6
Fe_2O_3	2.80	4.94	9.19	7.88	7.35	12.7	0.80	-	5.61	3.34
MgO	1.04	3.80	3.33	2.70	2.10	4.09	0.11	-	2.67	1.06
CaO	0.60	6.24	0.78	1.20	0.67	12.1	0.52	-	5.72	2.06
Na_2O	1.40	3.16	3.77	2.71	1.45	1.92	3.68	-	3.57	3.62
K_2O	1.52	1.35	4.20	1.69	5.84	1.88	4.70	-	2.02	2.81
TiO_2	0.32	0.57	1.25	0.79	1.01	2.56	0.05	-	0.85	0.33
MnO	0.07	0.09	0.13	0.14	0.09	0.22	0.02	-	0.10	0.04
P_2O_5	0.08	0.13	0.17	0.14	0.13	0.57	0.02	-	0.17	0.12
Total	99.2	100.3	98.2	98.8	100.3	100.7	100.6	-	100.4	99.6
LOI	0.77	2.49	0.00	2.15	1.86	1.60	0.83	-	1.14	0.63
Minor and Trace Elements (ppm)										
Sc	16.5	14.6	24.9	17.3	17.5	31.5	3.91	5.54	16.1	8.66
V	124	105			112	286	0.73	21.2	97.5	50.6
Cr			118	122						
Ni	7.95	24.6			43.0	78.5	0.35	3.47	8.39	6.58
Rb	47.2	52.3	149	75.3	227	94.9	209	161	83.4	145
Sr	274	244	106	105	107	320	36.2	161	215	125
Y	20.9	17.5	28.3	20.1	23.7	61.1	42.3	17.5	32.5	26.5
Zr	119	7.04	33.6	18.9	41.2	30.9	76.0	30.9	17.2	17.7
Nb	8.25	6.43	21.3	11.3	24.2	48.3	10.2	10.9	10.2	11.7
Cs	2.49	1.68	7.47	2.43	7.37	0.38	2.16	1.73	5.42	7.48
Ba	154	158	649	406	1058	216	226	832	256	408
La	17.7	17.9	42.6	29.2	54.4	31.7	16.3	35.1	20.3	24.0
Ce	37.2	37.1	89.1	63.3	112	66.8	38.7	71.5	44.1	49.8
Pr	4.65	4.40	10.7	7.02	13.0	8.83	5.12	8.67	5.58	6.08
Nd	18.0	16.0	41.3	26.8	46.4	36.6	19.9	31.2	22.1	22.2
Sm	4.04	3.23	8.60	5.61	8.78	8.74	5.62	6.26	5.26	4.90
Eu	1.20	0.85	1.72	1.43	1.86	2.66	0.14	1.01	1.16	0.72
Gd	3.86	3.07	7.40	4.80	6.81	9.53	5.93	4.81	5.39	4.45
Tb	0.61	0.49	1.10	0.72	0.95	1.61	1.08	0.67	0.89	0.74
Dy	3.51	2.83	5.90	3.89	4.63	9.71	6.67	3.25	5.33	4.31
Ho	0.72	0.58	1.06	0.71	0.83	2.10	1.42	0.58	1.13	0.86
Er	2.04	1.68	2.48	1.83	2.18	6.13	4.05	1.47	3.17	2.46
Yb	1.76	1.53	1.66	1.53	1.90	5.55	3.41	1.12	2.83	2.27
Lu	0.25	0.22	0.22	0.23	0.27	0.80	0.47	0.15	0.40	0.32
Hf	0.54	0.39	0.82	0.32	1.21	1.34	3.27	0.95	0.85	0.62
Ta	-	-	-	-	-	-	-	-	-	-
Pb	7.20	8.97	5.58	13.2	39.7	12.7	31.6	36.4	12.3	26.9
Th	4.94	7.60	13.5	9.18	18.9	3.66	23.8	16.4	9.24	14.3
U	0.93	1.81	2.85	1.72	4.04	1.11	4.89	5.25	1.66	2.77
Isotopic Ratios										
87Sr/86Sr		0.708443			0.745821				0.708241	
2SE		0.000004			0.000011				0.000003	
143Nd/144Nd										
2SE										
εNd										
206Pb/204Pb					18.398				18.644	
2SE					0.001				0.001	
207Pb/204Pb					15.685				15.662	
2SE					0.001				0.001	
208Pb/204Pb					38.968				38.655	
2SE					0.002				0.002	
176Hf/177Hf					0.282581				0.282990	
se					0.000009				0.000004	
εHf					32.19				15.17	

TABLE C.3: Bulk-rock data for basement samples

	Dzirula Massif			Khrami Massif				Loki Massif		
Sample	14-001	14-002	14-003	14-043	14-046	14-047	14-048	14-050	14-051	14-052
Lithology	Red Granite	Dark Granite	Migmatite							
Major Elements (wt%)										
SiO_2	73.7	64.4	68.7	76.1	70.1	58.4	76.6	45.7	-	75.0
Al_2O_3	13.7	17.3	15.0	12.3	15.8	21.4	12.2	14.7	-	13.9
Fe_2O_3	0.43	4.60	3.73	1.19	2.19	7.35	1.11	10.5	-	0.34
MgO	0.11	1.90	0.84	0.12	0.32	2.10	0.43	8.51	-	0.17
CaO	0.84	2.42	2.46	0.35	1.48	0.67	0.71	12.1	-	0.27
Na_2O	2.61	2.32	3.93	4.42	3.71	1.45	3.64	2.56	-	3.64
K_2O	6.64	3.52	2.76	3.57	4.38	5.84	3.20	0.36	-	6.27
TiO_2	0.06	0.51	0.45	0.07	0.19	1.01	0.13	2.27	-	0.01
MnO	0.01	0.07	0.06	0.01	0.04	0.09	0.02	0.23	-	0.02
P_2O_5	0.06	0.14	0.12	0.02	0.12	0.13	0.07	0.57	-	0.14
Total	98.7	99.5	99.2	98.9	99.9	100.3	99.0	100.5	-	100.2
LOI	0.46	2.28	1.18	0.71	1.60	1.86	0.90	2.99	-	0.53
Minor and Trace Elements (ppm)										
Sc	0.53	13.7	13.3	2.77	6.60	7.61	3.92	27.3	8.36	1.07
V	3.20	72.2	31.1	3.18	6.53		3.38	277	82.3	1.09
Cr						54.2				
Ni	1.39	4.03	4.70	0.36	0.98		0.87	14.5	3.36	0.30
Rb	131	120	134	94.3	123	75.3	57.1	9.24	36.8	124
Sr	270	109	150	42.7	208	43.4	98.1	436	520	109
Y	4.69	23.2	29.7	33.6	32.8	18.4	12.2	25.6	12.8	8.68
Zr	12.4	54.6	122	98.2	59.7	37.6	22.6	73.7	73.0	35.6
Nb	2.09	10.9	22.1	11.5	11.2	7.42	6.68	73.2	5.77	2.07
Cs	1.53	7.00	4.27	0.28	1.30	0.93	0.45	0.38	1.24	2.48
Ba	1882	1056	483	770	1966	235	1036	230	879	430
La	5.73	30.2	43.1	20.4	53.3	40.4	23.4	42.4	22.1	2.59
Ce	5.06	60.3	87.9	44.8	107	82.2	45.4	81.6	41.8	5.27
Pr	1.29	6.78	10.5	5.81	12.7	9.54	5.22	9.89	4.90	0.63
Nd	4.81	23.7	38.0	22.1	45.7	35.6	18.1	36.8	17.7	2.4
Sm	1.02	4.75	7.91	5.70	8.86	7.20	3.66	7.06	3.24	0.71
Eu	1.29	1.15	0.91	0.47	1.55	0.93	1.21	2.19	0.99	0.43
Gd	0.88	4.35	6.82	5.56	7.19	5.76	3.03	6.15	2.54	0.83
Tb	0.14	0.69	1.04	0.94	1.06	0.79	0.45	0.89	0.37	0.18
Dy	0.78	3.96	5.44	5.63	5.72	3.89	2.31	4.70	2.04	1.25
Ho	0.16	0.81	1.05	1.19	1.12	0.66	0.42	0.91	0.42	0.27
Er	0.45	2.24	2.69	3.48	3.02	1.56	1.10	2.40	1.22	0.81
Yb	0.42	1.88	2.16	3.45	2.56	1.22	0.93	1.88	1.25	0.88
Lu	0.06	0.28	0.30	0.50	0.35	0.18	0.14	0.24	0.19	0.13
Hf	0.65	2.41	3.67	4.03	2.27	1.06	0.91	1.82	1.94	1.26
Ta	-	-	-	0.67	0.43	-	0.28	3.13	0.27	0.26
Pb	48.8	7.40	24.9	2.95	30.9	14.1	5.18	8.94	10.5	42.7
Th	1.59	12.8	21.4	19.0	16.8	14.0	7.27	5.38	7.00	1.21
U	0.92	2.49	5.31	3.10	1.75	1.86	0.85	2.17	1.71	1.22
Isotopic Ratios										
87Sr/86Sr			0.716727					0.706875		
2SE			0.000004					0.000003		
143Nd/144Nd				0.512340				0.512652		
2SE				0.000008				0.000005		
εNd				-5.82				0.26		
206Pb/204Pb			18.589					19.618		
2SE			0.001					0.001		
207Pb/204Pb			15.688					15.726		
2SE			0.001					0.001		
208Pb/204Pb			38.607					39.306		
2SE			0.004					0.003		
176Hf/177Hf										
se										
εHf										

TABLE C.4: Plagioclase compositions in the Lesser Caucasus

Formation	Goderzi Fm.										Abul-Samsari						
Formula	14-054										14-041						
SiO_2	60.67	60.03	59.05	54.58	61.70	61.62	60.00	61.71	59.47	59.50	54.54	55.54	57.64	58.63	58.42	56.03	55.01
TiO_2	0.18	0.03	0.00	0.05	0.00	0.03	0.00	0.07	0.01	0.05	0.00	0.05	0.02	0.00	0.00	0.07	0.00
Al_2O_3	24.17	24.69	25.51	28.44	23.90	24.01	25.15	23.80	25.76	25.31	28.26	27.71	26.23	25.50	25.81	27.19	28.33
Cr_2O_3	0.00	0.00	0.01	0.01	0.00	0.00	0.00	0.01	0.00	0.01	0.00	0.00	0.01	0.01	0.00	0.00	0.00
MgO	0.02	0.01	0.02	0.02	0.01	0.02	0.00	0.00	0.01	0.01	0.04	0.03	0.02	0.01	0.00	0.01	0.00
CaO	7.87	6.62	7.44	10.77	5.70	5.45	7.05	5.69	7.48	7.28	11.25	10.53	8.64	7.98	8.23	9.86	10.94
MnO	0.00	0.00	0.01	0.01	0.00	0.00	0.00	0.00	0.00	0.00	0.00	0.00	0.02	0.00	0.00	0.00	0.01
FeO	0.68	0.20	0.21	0.22	0.13	0.20	0.20	0.18	0.19	0.22	0.47	0.40	0.31	0.10	0.10	0.33	0.07
NiO	0.00	0.00	0.00	0.00	0.00	0.00	0.01	0.00	0.00	0.00							
Na_2O	5.02	7.13	6.56	5.26	7.28	7.28	6.89	7.61	6.48	6.80	5.14	5.40	6.46	7.24	6.72	5.78	5.32
K_2O	1.38	0.96	0.78	0.30	1.11	1.33	0.68	0.86	0.61	0.80	0.28	0.33	0.46	0.33	0.33	0.36	0.22
P_2O_5	0.01	0.01	0.02	0.01	0.00	0.02	0.02	0.00	0.00	0.00							
SO_3	0.01	0.00	0.01	0.00	0.00	0.00	0.00	0.00	0.00	0.02							
Total	100.00	99.69	99.62	99.67	99.82	99.96	100.01	99.92	100.01	100.00	99.97	99.97	99.81	99.82	99.62	99.64	99.90
An%	42.3	32.0	36.7	52.2	28.2	27.0	34.7	27.8	37.5	35.4	53.9	50.9	41.4	37.2	39.6	47.5	52.5
Or%	8.8	5.5	4.6	1.7	6.5	7.8	4.0	5.0	3.6	4.7	1.6	1.9	2.6	1.9	1.9	2.1	1.3

Formation	Lower Akhalkalaki Fm.									Upper Akhalkalaki Fm.					Scoria Cones		
Formula	14-034			14-028						13-083	iv				13-100	13-102	
SiO_2	53.96	55.11	54.67	53.41	53.50	53.35	53.96	53.50	54.76	56.16	54.22	55.25	52.75	55.06	56.34	56.16	44.17
TiO_2	0.06	0.07	0.04	0.05	0.03	0.04	0.13	0.06	0.09	0.07	0.02	0.03	0.06	0.00	0.13	0.13	0.01
Al_2O_3	28.13	27.18	27.77	28.78	28.63	28.39	27.90	28.26	27.45	27.45	28.16	27.97	29.49	27.95	26.73	26.24	35.67
Cr_2O_3	0.01	0.00	0.01	0.00	0.00	0.00	0.00	0.00	0.00	0.00	0.00	0.00	0.02	0.01	0.01	0.01	0.00
MgO	0.09	0.09	0.09	0.15	0.08	0.14	0.14	0.18	0.12	0.04	0.06	0.07	0.07	0.04	0.03	0.22	0.02
CaO	11.64	10.60	11.03	12.28	11.96	12.12	11.56	12.09	10.92	10.02	11.18	10.64	12.50	10.74	9.90	9.88	19.24
MnO	0.01	0.00	0.00	0.00	0.01	0.00	0.00	0.00	0.01	0.01	0.00	0.00	0.01	0.01	0.01	0.01	0.00
FeO	0.57	0.56	0.60	0.51	0.69	0.59	0.66	0.54	0.96	0.47	0.88	0.50	0.69	0.40	0.85	1.32	0.08
NiO										0.01	0.00	0.00	0.00	0.00	0.00	0.00	0.02
Na_2O	4.95	5.61	5.32	4.50	4.66	4.82	4.97	4.65	5.25	5.48	4.84	5.17	4.13	5.20	4.96	5.28	0.70
K_2O	0.25	0.31	0.27	0.22	0.24	0.24	0.28	0.24	0.32	0.33	0.38	0.31	0.27	0.28	0.76	0.54	0.00
P_2O_5										0.04	0.01	0.03	0.02	0.03	0.05	0.09	0.00
SO_3										0.01	0.02	0.03	0.01	0.01	0.02	0.03	0.02
Total	99.66	99.52	99.79	99.90	99.79	99.68	99.59	99.51	99.87	100.09	99.77	100.00	100.02	99.73	99.78	99.92	99.93
An%	55.7	50.2	52.6	59.3	57.9	53.9	55.3	58.1	52.5	49.3	54.8	52.2	61.6	52.4	50.0	49.2	93.8
Or%	1.4	1.7	1.5	1.3	1.4	1.7	1.6	1.4	1.8	1.9	2.2	1.8	1.6	1.6	4.6	3.2	0.0

TABLE C.5: Olivine compositions in the Lesser Caucasus

Formation	**Lower Akhalkalaki Fm.**													
Formula	NS-PhD-1					14-034								
SiO_2	39.38	36.76	37.19	38.58	37.36	37.97	38.01	38.52	38.33	38.55	38.64	37.78	38.41	38.01
TiO_2	0.00	0.00	0.01	0.03	0.04	0.01	0.02	0.00	0.02	0.00	0.00	0.02	0.03	0.05
Al_2O_3	0.00	0.00	0.01	0.01	0.02	0.54	2.15	0.00	0.02	0.00	0.00	0.00	0.01	0.01
Cr_2O_3	0.02	0.00	0.02	0.03	0.01	0.03	0.02	0.01	0.01	0.01	0.03	0.00	0.04	0.00
MgO	43.56	31.82	34.27	40.49	35.85	35.79	38.49	39.41	39.12	39.18	39.38	39.03	39.24	38.43
CaO	0.21	0.32	0.32	0.22	0.29	0.35	0.19	0.18	0.18	0.19	0.18	0.17	0.18	0.17
MnO	0.25	0.52	0.41	0.31	0.39	0.37	0.29	0.32	0.33	0.31	0.31	0.33	0.33	0.33
FeO	16.42	30.44	27.66	20.45	25.50	24.92	20.87	21.86	21.76	21.94	21.44	21.76	21.79	22.89
NiO														
Na_2O	0.00	0.00	0.00	0.00	0.01	0.00	0.06	0.03	0.00	0.01	0.02	0.02	0.00	0.01
K_2O	0.00	0.00	0.00	0.00	0.00	0.00	0.00	0.00	0.00	0.00	0.00	0.00	0.00	0.00
P_2O_5														
SO_3														
Total	99.83	99.87	99.90	100.12	99.46	99.98	100.08	100.34	99.77	100.19	100.00	99.11	100.05	99.89
Mg#	82.5	65.1	68.8	77.9	71.5	71.9	76.7	76.3	76.2	76.1	76.6	76.2	76.2	75.0

Formation	**Upper Akhalkalaki Fm.**										**Scoria Cones**			
Formula	14-036a										13-100		13-102	
SiO_2	39.62	39.05	38.92	38.25	38.16	39.19	37.80	37.66	38.97	39.27	38.40	39.18	38.59	38.98
TiO_2	0.00	0.00	0.00	0.00	0.04	0.03	0.03	0.03	0.02	0.00	0.04	0.00	0.02	0.03
Al_2O_3	0.03	0.03	0.02	0.00	0.03	0.01	0.00	0.02	0.02	0.04	0.00	0.07	0.00	0.00
Cr_2O_3	0.02	0.03	0.03	0.01	0.02	0.01	0.00	0.02	0.02	0.03	0.02	0.00	0.00	0.00
MgO	44.53	43.63	41.94	39.90	38.79	43.12	35.74	38.42	42.43	43.84	39.73	41.61	39.75	42.42
CaO	0.20	0.21	0.21	0.27	0.26	0.21	0.35	0.29	0.21	0.21	0.27	0.20	0.11	0.20
MnO	0.22	0.25	0.28	0.34	0.36	0.27	0.41	0.35	0.26	0.23	0.35	0.34	0.35	0.29
FeO	14.92	16.43	18.34	20.92	22.05	16.66	25.08	22.41	17.75	15.94	20.95	18.60	21.25	18.71
NiO	0.31	0.25	0.20	0.13	0.13	0.23	0.10	0.11	0.20	0.23	0.16	0.11	0.09	0.09
Na_2O	0.02	0.00	0.02	0.02	0.01	0.02	0.01	0.02	0.01	0.00	0.00	0.00	0.02	0.00
K_2O	0.00	0.00	0.00	0.00	0.00	0.00	0.00	0.00	0.00	0.00	0.00	0.00	0.00	0.00
P_2O_5	0.01	0.02	0.02	0.05	0.03	0.03	0.02	0.04	0.00	0.03	0.03	0.04	0.02	0.04
SO_3	0.01	0.00	0.00	0.00	0.00	0.00	0.00	0.00	0.02	0.00	0.01	0.05	0.03	0.01
Total	99.89	99.91	99.98	99.88	99.86	99.79	99.54	99.35	99.89	99.83	99.94	100.20	100.23	100.77
Mg#	84.2	82.6	80.3	77.3	75.8	82.2	71.8	75.3	81.0	83.1	77.2	80.0	76.9	80.2

TABLE C.6: Pyroxene compositions in the Lesser Caucasus

Foramtion	**Goderzi Fm.**		**Lower Akhalkalaki Fm.**						**Upper Akhalkalaki Fm.**						**Scoria Cones**				
Formula	14-054		14-034			NS-PhD1	14-028		13-083						13-100				
	cpx	cpx	opx	opx	cpx	cpx	cpx	cpx	opx	opx	opx	opx	cpx	cpx	opx	opx	opx	cpx	cpx
SiO_2	52.57	52.60	54.54	53.53	51.59	50.74	51.30	52.92	53.15	52.78	53.39	53.29	53.70	48.98	54.31	54.14	53.56	52.00	53.74
TiO_2	0.30	0.30	0.22	0.39	0.56	1.33	0.98	0.63	0.30	0.35	0.29	0.24	0.23	1.02	0.06	0.25	0.18	0.23	0.08
Al_2O_3	2.92	2.93	1.07	1.79	2.13	3.18	2.38	1.29	2.97	2.55	2.35	1.58	0.75	6.01	2.03	2.52	2.08	2.78	1.12
Cr_2O_3	0.64	0.52	0.00	0.04	0.07	0.14	0.03	0.07	0.05	0.02	0.03	0.02	0.00	0.03	0.06	0.20	0.13	0.11	0.00
MgO	16.11	15.88	27.44	26.13	14.37	14.77	15.36	17.07	26.89	25.41	26.37	24.36	16.38	16.05	28.48	28.72	26.66	15.78	17.02
CaO	20.01	20.35	1.75	1.69	18.80	21.20	18.60	17.58	1.52	1.73	1.73	1.16	20.17	16.00	1.05	1.63	1.22	21.54	23.70
MnO	0.14	0.16	0.33	0.35	0.33	0.20	0.29	0.30	0.31	0.37	0.35	0.63	0.20	0.26	0.35	0.24	0.37	0.16	0.20
FeO	6.20	6.26	14.39	15.66	11.53	8.03	10.58	9.77	14.43	17.02	15.59	18.36	8.18	10.82	13.39	11.85	15.50	7.03	4.26
NiO	0.03	0.05							0.06	0.01	0.03	0.03	0.05	0.03	0.01	0.09	0.04	0.00	0.02
Na_2O	0.45	0.49	0.03	0.04	0.51	0.39	0.30	0.22	0.02	0.03	0.06	0.01	0.35	0.36	0.03	0.04	0.04	0.36	0.08
K_2O	0.00	0.00	0.00	0.00	0.00	0.00	0.00	0.00	0.00	0.00	0.00	0.00	0.01	0.00	0.00	0.00	0.00	0.00	0.00
P_2O_5	0.02	0.01							0.00	0.01	0.00	0.00	0.02	0.10	0.00	0.03	0.00	0.00	0.00
SO_3	0.01	0.01							0.01	0.00	0.01	0.02	0.00	0.00	0.04	0.01	0.02	0.04	0.01
Total	99.42	99.54	99.76	99.61	99.88	99.97	99.81	99.84	99.71	100.28	100.19	99.69	100.03	99.66	99.82	99.72	99.78	100.01	100.24
En%	47.4	46.7	74.6	72.3	41.8	42.8	44.3	48.5	74.5	70.2	72.5	68.6	46.2	47.7	77.5	78.6	73.6	44.8	46.7
Fs%	10.2	10.3	22.0	24.3	18.8	13.0	17.1	15.6	22.4	26.4	24.1	29.0	12.9	18.1	20.4	18.2	24.0	11.2	6.6
Wo%	42.3	43.0	3.4	3.4	39.3	44.1	38.6	35.9	3.0	3.4	3.4	2.4	40.9	34.2	2.1	3.2	2.4	44.0	46.7

Foramtion	**Abul-Samsari**																			
Formula	14-042												14-038	14-042						
	opx	opx	opx	opx	opx	opx	opx	opx	opx	opx	cpx	cpx	cpx	cpx	cpx	cpx	cpx	cpx	cpx	cpx
SiO_2	53.69	50.52	51.44	50.46	51.16	51.93	54.31	54.46	53.48	53.51	52.33	50.87	53.03	51.99	52.54	52.16	51.21	52.56	52.47
TiO_2	0.16	0.16	0.12	0.14	0.06	0.16	0.11	0.14	0.23	0.16	0.27	0.25	0.35	0.43	0.31	0.42	0.53	0.31	0.42
Al_2O_3	2.71	5.37	3.83	4.28	3.67	4.24	2.40	2.24	3.63	2.84	2.48	3.15	1.87	4.07	3.30	2.74	5.58	3.86	4.02
Cr_2O_3	0.22	0.03	0.02	0.15	0.01	0.17	0.33	0.28	0.04	0.15	0.16	0.01	0.11	0.36	0.57	0.12	0.16	0.11	0.13
MgO	27.46	23.27	22.64	23.84	22.42	24.81	27.48	27.74	26.81	26.07	17.18	12.32	16.02	15.03	15.69	15.40	14.06	15.33	15.22
CaO	1.12	1.12	1.06	1.14	1.01	1.21	1.16	1.15	1.15	1.45	15.61	20.80	19.93	19.78	20.10	20.52	19.18	19.56	19.50
MnO	0.26	0.41	0.61	0.34	0.62	0.37	0.24	0.25	0.27	0.32	0.27	0.45	0.20	0.17	0.14	0.17	0.17	0.15	0.15
FeO	13.97	18.86	20.36	16.57	21.01	17.03	13.89	13.98	14.46	15.63	10.74	11.26	7.88	7.32	6.63	7.66	8.10	7.25	7.07
NiO	0.09	0.03	0.00	0.02	0.00	0.06	0.09	0.11	0.06			0.03	0.03	0.04	0.06	0.03	0.05	0.02	0.03
Na_2O	0.05	0.09	0.05	0.07	0.04	0.04	0.07	0.01	0.03	0.06	0.40	0.81	0.27	0.62	0.58	0.40	0.69	0.69	0.75
K_2O	0.00	0.00	0.00	0.00	0.00	0.00	0.00	0.00	0.00	0.00	0.00	0.00	0.00	0.00	0.00	0.00	0.00	0.00	0.00
P_2O_5	0.02	0.03	0.00	0.02	0.01	0.00	0.00	0.01	0.00			0.00	0.04	0.01	0.03	0.03	0.03	0.01	0.03
SO_3	0.00	0.00	0.00	0.00	0.00	0.01	0.00	0.00	0.00			0.05	0.00	0.01	0.00	0.00	0.03	0.00	0.00
Total	99.73	99.90	100.11	97.01	100.01	100.04	100.06	100.36	100.15	100.17	99.43	100.00	99.72	99.82	99.93	99.65	99.76	99.85	99.79
En%	76.1	67.1	65.0	70.2	64.2	70.4	76.1	76.2	75.0	72.7	49.9	36.7	46.1	45.1	46.3	44.7	43.4	45.8	45.8
Fs%	21.7	30.5	32.8	27.4	33.7	27.1	21.6	21.5	22.7	24.4	17.5	18.8	12.7	12.3	11.0	12.5	14.0	12.2	11.9
Wo%	2.2	2.3	2.2	2.4	2.1	2.5	2.3	2.3	2.3	2.9	32.6	44.5	41.2	42.6	42.7	42.8	42.6	42.0	42.2

TABLE C.7: Plagioclase compositions in the Gretaer Caucasus

Formation	Qabarjina. Fm.					Mt. Kazbek: Stage I					Mt. Kazbek: Stage II				
Sample	13-049_5	13-049_7	13-049_10	13-049_1a	13-049_1b	13-008_1	13-008_11	13-008_21	13-008_25	13-008_29	13-059_12	13-059_30	13-059_36	13-026_1	13-026_8
SiO_2	61.65	61.81	56.66	57.14	61.94	58.16	53.83	61.37	57.80	59.72	56.87	62.18	59.49	64.09	57.52
TiO_2	0.02	0.04	0.02	0.00	0.02	0.00	0.04	0.00	0.00	0.00	0.03	0.03	0.01	0.00	0.03
Al_2O_3	24.25	24.28	27.58	27.64	24.52	25.89	28.75	23.60	26.14	25.01	26.67	23.21	25.11	21.27	26.09
Cr_2O_3	0.00	0.00	0.00	0.00	0.00	0.01	0.00	0.03	0.00	0.00	0.00	0.00	0.01	0.00	0.00
MgO	0.01	0.02	0.01	0.00	0.00	0.02	0.03	0.01	0.02	0.01	0.01	0.01	0.00	0.02	0.01
CaO	5.92	6.13	10.15	9.57	5.62	7.70	11.30	5.90	8.07	6.87	8.98	5.13	7.25	3.53	8.51
MnO	0.00	0.01	0.00	0.01	0.00	0.00	0.01	0.00	0.00	0.00	0.00	0.00	0.01	0.00	0.00
FeO	0.03	0.22	0.15	0.07	0.06	0.24	0.56	0.23	0.21	0.26	0.20	0.22	0.18	0.30	0.26
NiO	0.00	0.00	0.01	0.00	0.00	0.01	0.00	0.02	0.00	0.01	0.00	0.00	0.01	0.00	0.01
Na_2O	7.94	7.37	5.36	6.28	8.21	6.61	4.81	8.08	6.63	7.10	6.05	7.96	7.10	7.95	6.68
K_2O	0.42	0.87	0.53	0.21	0.46	0.40	0.32	0.49	0.42	0.53	0.28	0.52	0.35	2.12	0.38
P_2O_5	0.00	0.02	0.03	0.01	0.03	0.02	0.00	0.00	0.01	0.01	0.00	0.00	0.01	0.00	0.02
SO_3	0.00	0.00	0.00	0.00	0.01	0.01	0.01	0.00	0.01	0.00	0.00	0.00	0.01	0.00	0.00
Cl	0.00	0.00	0.00	0.00	0.00	0.00	0.00	0.00	0.00	0.00	0.01	0.00	0.01	0.02	0.00
Total	100.23	100.78	100.50	100.92	100.88	99.07	99.66	99.73	99.32	99.53	99.10	99.27	99.56	99.30	99.52
An%	28.5	29.9	49.6	45.2	26.7	38.2	55.5	28.0	39.3	33.8	44.3	25.4	35.3	17.3	40.4

Formation	Mt. Kazbek: Stage III					Mt. Kazbek: Stage IV					Gudauri Fm.				
Sample	13-073_09	13-073_26e	13-073_26g	13-025_1b	13-025_9	H5_23a	KZ1_12	13-012_4a	13-012_4b	H6_8b	H1_23a	H3_17d	H4_8a	H4_18f	H4_3a
SiO_2	70.82	61.30	59.77	53.74	59.67	63.89	56.75	53.85	60.84	56.77	49.89	57.44	50.34	55.79	51.27
TiO_2	1.40	0.00	0.01	0.04	0.00	0.28	0.01	0.02	0.00	0.00	0.10	0.02	0.04	0.23	0.71
Al_2O_3	14.23	24.82	25.73	29.21	25.19	21.37	26.88	29.29	24.80	27.21	30.64	26.38	31.10	26.85	27.36
Cr_2O_3	0.00	0.00	0.00	0.00	0.00	0.00	0.02	0.00	0.00	0.00	0.01	0.00	0.01	0.00	0.01
MgO	0.35	0.00	0.02	0.02	0.01	0.06	0.01	0.02	0.01	0.01	0.12	0.02	0.10	0.04	0.42
CaO	1.11	6.11	7.48	11.48	7.12	7.21	9.41	11.37	6.35	9.56	15.35	8.76	14.39	10.20	12.24
MnO	0.04	0.01	0.00	0.01	0.00	0.02	0.00	0.00	0.00	0.01	0.01	0.00	0.01	0.00	0.05
FeO	3.39	0.17	0.27	0.14	0.19	0.91	0.04	0.08	0.06	0.03	0.88	0.17	0.44	0.78	2.49
NiO	0.01	0.00	0.02	0.00	0.00	0.00	0.01	0.00	0.00	0.00	0.00	0.01	0.00	0.01	0.00
Na_2O	5.37	8.04	7.06	4.71	7.11	4.50	5.79	5.15	7.56	5.97	2.23	5.81	3.07	4.53	3.30
K_2O	3.47	0.49	0.57	0.30	0.37	2.02	0.20	0.14	0.42	0.20	0.75	0.85	0.15	0.67	1.16
P_2O_5	0.23	0.00	0.03	0.02	0.01	0.06	0.02	0.00	0.00	0.02	0.10	0.06	0.04	0.05	0.27
SO_3	0.00	0.00	0.00	0.02	0.03	0.04	0.00	0.02	0.00	0.02	0.01	0.01	0.01	0.00	0.01
Cl	0.20	0.00	0.00	0.00	0.00	0.03	0.00	0.00	0.00	0.00	0.03	0.00	0.00	0.04	0.02
Total	100.61	100.94	100.95	99.71	99.70	100.37	99.13	99.94	100.05	99.79	100.12	99.54	99.69	99.18	99.29
An%	7.4	28.8	35.7	56.4	34.9	40.6	46.8	54.5	30.9	46.4	75.7	43.2	71.5	53.1	62.5

Table C.8: Pyroxene compositions in the Greater Caucasus

Formation	Gudauri Fm.										Mt. Kazbek: Stage I				Mt. Kazbek: Stage II		
Sample	H1_3a	H1_5a	H2_1d	H3_4line	H3_5b	H3_7a	H2_5c	H3_1c	H3_4a	H3_6c	13-008_4	13-008_9	13-008_14	13-008_16	13-059_3	13-059_8	13-059_31
Mineral	opx	opx	opx	opx	opx	opx	cpx	cpx	cpx	cpx	opx	opx	opx	opx	opx	opx	cpx
SiO_2	54.18	54.14	55.13	53.41	53.64	52.70	53.19	51.62	46.12	51.29	52.98	53.97	54.06	52.91	53.90	53.23	51.81
TiO_2	0.19	0.22	0.18	0.22	0.19	0.45	0.29	0.97	1.06	0.62	0.06	0.34	0.23	0.20	0.11	0.19	0.52
Al_2O_3	3.81	2.74	1.46	2.86	2.48	1.07	2.26	3.53	2.09	3.99	0.67	1.50	2.10	2.09	0.35	0.67	2.99
Cr_2O_3	0.30	0.20	0.10	0.15	0.05	0.36	0.13	0.28	0.18	0.31	0.03	0.02	0.08	0.10	0.00	0.02	0.02
MgO	30.58	28.45	28.84	27.30	26.92	23.55	15.30	14.71	21.98	16.43	22.79	26.29	29.08	23.43	25.13	23.93	15.95
CaO	1.74	1.13	1.42	1.22	1.10	1.82	21.60	18.45	12.75	20.35	0.69	1.44	1.29	3.12	0.73	0.59	20.68
MnO	0.17	0.30	0.31	0.40	0.39	0.49	0.19	0.28	0.29	0.19	0.67	0.36	0.24	0.44	0.56	0.65	0.16
FeO	9.10	12.74	12.78	13.91	14.82	19.18	6.64	9.20	14.91	5.95	21.77	16.17	12.65	17.42	18.69	20.30	7.01
NiO	0.03	0.02	0.00	0.03	0.01	0.06	0.00	0.03	0.04	0.01	0.02	0.03	0.03	0.01	0.03	0.02	0.03
Na_2O	0.04	0.05	0.05	0.01	0.02	0.01	0.39	0.52	0.24	0.34	0.05	0.02	0.04	0.14	0.02	0.01	0.47
K_2O	0.00	0.00	0.00	0.00	0.00	0.00	0.00	0.00	0.00	0.00	0.00	0.00	0.00	0.00	0.00	0.00	0.00
P_2O_5	0.00	0.04	0.00	0.00	0.02	0.00	0.03	0.01	0.04	0.03	0.00	0.00	0.00	0.00	0.00	0.03	0.02
SO_3	0.00	0.00	0.00	0.03	0.02	0.01	0.01	0.00	0.03	0.00	0.00	0.03	0.00	0.00	0.00	0.02	0.01
Cl	0.00	0.00	0.00	0.00	0.00	0.00	0.00	0.01	0.00	0.00	0.00	0.00	0.00	0.00	0.00	0.01	0.00
Total	100.12	100.02	100.27	99.53	99.64	99.71	100.03	99.59	99.73	99.52	99.73	100.18	99.80	99.88	99.52	99.66	99.68
En%	82.79	78.13	77.89	75.88	74.72	66.12	44.28	44.39	55.63	47.77	64.20	72.23	78.38	66.10	69.53	66.95	45.89
Fs%	13.82	19.63	19.35	21.69	23.07	30.20	10.78	15.58	21.18	9.71	34.41	24.93	19.13	27.57	29.02	31.86	11.32
Wo%	3.38	2.24	2.76	2.43	2.20	3.68	44.94	40.03	23.19	42.52	1.39	2.84	2.49	6.33	1.45	1.19	42.78

Formation	Mt. Kazbek: Stage III										Mt. Kazbek: Stage IV				Qabarjina Fm.			
Sample	13-025_14	13-025_20	13-073_09	13-073_16j	13-073_27h	13-025_23	13-073_02h	13-073_02k	13-073_02o	13-073_22a	H5_1a	H5_4d	13-012_3	13-012_18	H7_12b	H7_12d	H7_15a	H7_5c
Mineral	opx	opx	opx	opx	opx	cpx	cpx	cpx	cpx	cpx	opx	opx	opx	opx	opx	opx	opx	opx
SiO_2	53.50	55.36	55.02	54.73	54.90	51.83	50.68	52.58	52.17	54.39	58.36	52.95	51.19	52.44	52.11	54.36	53.24	53.45
TiO_2	0.39	0.25	0.18	0.31	0.23	0.82	0.81	0.54	0.62	0.32	0.33	0.14	0.17	0.12	0.16	0.12	0.16	0.22
Al_2O_3	1.43	2.39	1.57	2.36	2.25	3.19	3.79	2.43	2.69	3.65	3.68	1.47	2.00	0.61	1.42	1.57	2.01	1.61
Cr_2O_3	0.03	0.56	0.16	0.04	0.08	0.52	0.24	0.14	0.58	0.18	0.04	0.02	0.03	0.03	0.04	0.35	0.20	0.15
MgO	24.86	30.84	28.20	28.99	29.14	16.17	15.29	16.09	17.01	16.73	18.15	16.72	20.02	20.29	22.34	29.47	26.98	26.59
CaO	2.62	1.78	1.21	1.57	1.35	20.73	20.47	21.74	21.09	16.76	1.85	1.51	0.60	0.61	0.88	1.06	1.16	1.15
MnO	0.50	0.18	0.31	0.23	0.23	0.14	0.19	0.15	0.16	0.16	0.46	0.97	0.85	0.87	0.68	0.30	0.38	0.46
FeO	17.10	9.09	13.95	12.61	12.35	6.26	7.70	6.37	5.57	5.99	14.89	25.09	25.03	25.26	21.78	12.02	15.29	16.20
NiO	0.03	0.09	0.04	0.07	0.13	0.05	0.07	0.07	0.04	0.07	0.02	0.03	0.02	0.01	0.01	0.03	0.03	0.00
Na_2O	0.06	0.04	0.02	0.02	0.04	0.43	0.47	0.31	0.44	1.00	0.82	0.50	0.04	0.00	0.01	0.02	0.04	0.00
K_2O	0.00	0.00	0.00	0.00	0.00	0.00	0.00	0.00	0.00	0.27	1.12	0.33	0.00	0.00	0.00	0.00	0.00	0.00
P_2O_5	0.00	0.02	0.00	0.00	0.00	0.04	0.04	0.01	0.01	0.08	0.04	0.00	0.00	0.00	0.01	0.00	0.01	0.00
SO_3	0.01	0.03	0.03	0.00	0.00	0.04	0.00	0.00	0.00	0.03	0.00	0.00	0.00	0.03	0.00	0.00	0.00	0.02
Cl	0.00	0.01	0.00	0.00	0.00	0.00	0.00	0.00	0.01	0.02	0.02	0.01	0.00	0.00	0.01	0.00	0.00	0.00
Total	100.54	100.63	100.69	100.93	100.70	100.22	99.75	100.42	100.38	99.64	99.79	99.74	99.94	100.28	99.43	99.29	99.51	99.85
En%	68.41	82.86	76.44	77.95	78.68	46.76	44.55	45.60	48.19	52.06	65.19	52.45	58.04	58.13	63.49	79.71	74.13	72.84
Fs%	26.40	13.71	21.21	19.02	18.71	10.16	12.59	10.12	8.86	10.45	30.02	44.15	40.71	40.61	34.72	18.24	23.58	24.90
Wo%	5.19	3.44	2.35	3.03	2.61	43.09	42.87	44.28	42.95	37.49	4.79	3.41	1.24	1.26	1.80	2.06	2.30	2.26

TABLE C.9: Amphibole compositions in the Greater Caucasus

Formation	Mt. Kazbek: Stage I		Mt. Kazbek: Stage II		Qabarjina Fm.										
Formula	13-008_12	13-008_1	13-059_15	13-059_26	H7_11a	H7_3a	H7_3b	H7_3c	H7_3d	H7_1a	H7_1b	H7_2a	H7_2b	H7_2c	H7_10
SiO_2	49.66	40.70	47.39	45.45	44.39	42.88	43.42	42.63	42.40	43.29	43.26	41.16	46.67	49.11	54.52
TiO_2	1.23	3.94	1.45	2.46	2.45	3.16	3.17	3.17	3.36	3.19	2.98	2.91	2.13	1.97	0.35
Al_2O_3	5.80	12.89	6.54	8.43	11.05	11.20	10.67	11.03	10.98	11.46	11.20	11.16	11.12	9.65	5.68
Cr_2O_3	0.05	0.04	0.05	0.03	0.12	0.07	0.11	0.22	0.07	0.17	0.33	0.03	0.07	0.10	0.01
MgO	17.95	13.48	15.41	14.93	15.81	14.47	14.53	14.63	14.31	14.39	14.47	12.52	12.13	12.30	17.26
CaO	10.63	11.46	10.80	11.32	11.07	11.08	11.07	11.14	11.04	11.33	11.21	10.20	5.73	4.44	1.67
MnO	0.13	0.13	0.29	0.16	0.16	0.21	0.21	0.19	0.18	0.19	0.18	0.25	0.35	0.47	0.43
FeO	8.10	10.71	12.44	11.96	9.46	10.69	10.02	9.91	10.34	9.51	9.74	15.80	14.34	16.94	15.21
NiO	0.01	0.02	0.03	0.02	0.04	0.01	0.03	0.00	0.01	0.03	0.00	0.02	0.03	0.02	0.01
Na_2O	2.08	3.26	1.52	2.09	2.16	2.24	2.07	2.26	2.11	2.15	2.12	1.75	1.48	1.69	1.25
K_2O	0.73	0.48	0.32	0.39	0.38	0.46	0.45	0.47	0.44	0.45	0.44	0.49	0.15	0.17	0.76
P_2O_5	0.04	0.02	0.05	0.05	0.02	0.01	0.04	0.01	0.04	0.04	0.06	0.07	0.06	0.09	0.05
SO_3	0.03	0.02	0.02	0.01	0.00	0.00	0.00	0.00	0.04	0.00	0.00	0.00	0.04	0.00	0.00
Cl	0.11	0.02	0.09	0.06	0.01	0.02	0.03	0.03	0.02	0.02	0.02	0.04	0.06	0.08	0.01
Total	96.56	97.17	96.40	97.35	97.12	96.50	95.81	95.68	95.34	96.22	96.00	96.39	94.35	97.02	97.20

Formation	Mt. Kazbek: Stage III					Mt. Kazbek: Stage IV									
Formula	13-073_04	13-073_08	13-070_3	13-070_4	13-070_8	13-012_2a	13-012_2b	13-012_11	H6_2a	H6_4a	H6_7b	KZ1_1a	KZ1_2a	KZ1_3a	KZ1_4c
SiO_2	43.35	42.88	59.10	46.14	44.41	40.57	43.20	42.51	41.95	42.92	41.97	42.12	40.99	42.19	40.67
TiO_2	3.13	3.19	0.05	1.56	2.36	2.31	2.29	2.38	2.52	2.45	2.42	2.30	2.40	1.96	1.73
Al_2O_3	11.71	12.00	24.20	11.91	12.75	14.20	12.37	13.07	12.72	12.13	12.79	12.65	13.38	11.87	13.64
Cr_2O_3	0.05	0.05	0.00	0.02	0.05	0.02	0.02	0.03	0.09	0.03	0.03	0.03	0.00	0.03	0.01
MgO	15.59	15.44	0.01	14.83	7.98	13.47	15.81	15.16	15.80	15.79	15.55	15.50	14.16	10.32	12.63
CaO	11.62	11.56	6.34	11.72	10.17	11.05	11.32	11.16	11.63	11.24	11.58	11.54	11.84	11.49	11.15
MnO	0.10	0.10	0.00	0.12	0.15	0.17	0.13	0.14	0.15	0.16	0.12	0.14	0.14	0.34	0.33
FeO	9.53	9.81	0.18	6.31	15.42	11.85	9.14	10.24	8.81	9.60	8.70	9.49	10.33	14.98	13.19
NiO	0.10	0.11	0.00	0.01	0.02	0.00	0.00	0.01	0.00	0.00	0.00	0.01	0.00	0.01	0.03
Na_2O	2.43	2.58	7.26	3.08	2.88	2.28	2.25	2.26	2.07	2.12	2.18	2.12	1.90	1.71	1.98
K_2O	0.46	0.46	0.61	0.71	1.30	0.85	0.74	0.77	0.87	0.76	0.88	0.86	0.79	0.21	0.79
P_2O_5	0.06	0.03	0.00	0.03	0.00	0.05	0.06	0.02	0.05	0.02	0.02	0.00	0.04	0.05	0.05
SO_3	0.02	0.01	0.00	0.00	0.00	0.04	0.02	0.03	0.00	0.00	0.00	0.01	0.02	0.02	0.02
Cl	0.02	0.02	0.02	0.13	0.02	0.04	0.03	0.03	0.02	0.03	0.05	0.03	0.05	0.04	0.07
Total	98.15	98.23	97.77	96.58	97.52	96.91	97.38	97.80	96.68	97.24	96.30	96.78	96.04	95.23	96.29

References

Adamia, S., Alania, V., Chabukiani, A., Chichua, G., Enukidze, O., and Sadradze, N. (2010). Evolution of the Late Cenozoic basins of Georgia (SW Caucasus): a review. *Geological Society, London, Special Publications*, 340(1):239–259.

Adamia, S., Mumladze, T., Sadradze, N., Tsereteli, E., Tsereteli, N., and Varazanashvili, O. (2008). Late Cenozoic tectonics and geodynamics of Georgia (SW Caucasus). *Georgian International Journal of Science and Technology*, 1(1):77–107.

Adamia, S., Zakariadze, G., and Chkhotua, T. (2011). Geology of the Caucasus : A Review. *Turkish Journal of Earth Science*, 20:1–57.

Aigner-Torres, M., Blundy, J., Ulmer, P., and Pettke, T. (2007). Laser ablation icpms study of trace element partitioning between plagioclase and basaltic melts: an experimental approach. *Contributions to Mineralogy and Petrology*, 153(6):647–667.

Albarede, F. and Beard, B. (2004). Analytical Methods for Non-Traditional Isotopes. *Reviews in Mineralogy and Geochemistry*, 55(1):113–152.

Allen, M., Jackson, J., and Walker, R. (2004). Late Cenozoic reorganization of the Arabia-Eurasia collision and the comparison of short-term and long-term deformation rates. *Tectonics*, 23(2):TC2008, doi:10.1029/2003TC001530.

Allen, M. B. and Armstrong, H. A. (2008). Arabia-Eurasia collision and the forcing of mid-Cenozoic global cooling. *Palaeogeography, Palaeoclimatology, Palaeoecology*, 265(1-2):52–58.

Allen, M. B., Jones, S., Ismail-Zadeh, A., Simmons, M., and Anderson, L. (2002). Onset of subduction as the cause of rapid Pliocene-Quaternary subsidence in the South Caspian basin. *Geology*, 30(9):775–778.

Allen, M. B., Kheirkhah, M., Emami, M. H., and Jones, S. J. (2011). Right-lateral shear across Iran and kinematic change in the Arabia-Eurasia collision zone. *Geophysical Journal International*, 184(2):555–574.

Allen, M. B., Kheirkhah, M., Neill, I., Emami, M. H., and Mcleod, C. L. (2013). Generation of Arc and Within-plate Chemical Signatures in Collision Zone Magmatism: Quaternary Lavas from Kurdistan Province, Iran. *Journal of Petrology*, 54(5):887–911.

Allen, M. B., Vincent, S. J., Alsop, G. I., Ismail-zadeh, A., and Flecker, R. (2003). Late Cenozoic deformation in the South Caspian region: Effects of a rigid basement block within a collision zone. *Tectonophysics*, 366:223–239.

Austermann, J. and Iaffaldano, G. (2013). The role of the Zagros orogeny in slowing down Arabia-Eurasia convergence since ∼5 Ma. *Tectonics*, 32:351–363.

Avagyan, A., Sosson, M., Philip, H., Karakhanian, A., Rolland, Y., Melkonyan, R., Rebaï, S., and Davtyan, V. (2005). Neogene to Quaternary stress field evolution in Lesser Caucasus and adjacent regions using fault kinematics analysis and volcanic cluster data. *Geodinamica Acta*, 18(6):401–416.

Avdeev, B. and Niemi, N. A. (2011). Rapid Pliocene exhumation of the central Greater Caucasus constrained by low-temperature thermochronometry. *Tectonics*, 30(2):TC2009, doi:10.1029/2010TC002808.

Bachmann, O. and Dungan, M. A. (2002). Temperature-induced Al-zoning in hornblendes of the Fish Canyon magma, Colorado. *American Mineralogist*, 87:1062–1076.

Baker, J., Peate, D., Waight, T., and Meyzen, C. (2004). Pb isotopic analysis of standards and samples using a 207Pb-204Pb double spike and thallium to correct for mass bias with a double-focusing MC-ICP-MS. *Chemical Geology*, 211(3-4):275–303.

Ballato, P., Uba, C. E., Landgraf, A., Strecker, M. R., Sudo, M., Stockli, D. F., Friedrich, A., and Tabatabaei, S. H. (2011). Arabia-Eurasia continental collision: Insights from late Tertiary foreland basin evolution in the Alborz Mountains, morthern Iran. *Geological Society of America Bulletin*, 123:106–131.

Bebout, G. E., Bebout, A. E., and Graham, C. M. (2007). Cycling of B, Li, and LILE (K, Cs, Rb, Ba, Sr) into subduction zones: SIMS evidence from micas in high-P/T metasedimentary rocks. *Chemical Geology*, 239(3–4):284–304.

Best, M. G. (1970). Kaersutite-Peridotite Inclusions and Kindred Megacrysts in Basanitic Lavas , Grand Canyon , Arizona. *Contributions to Mineralogy and Petrology*, 27:25–44.

Bianchini, G., Beccaluva, L., and Siena, F. (2008). Post-collisional and intraplate cenozoic volcanism in the rifted apennines/adriatic domain. *Lithos*, 101(12):125–140.

Bindeman, I. N., Davis, A. M., and Drake, M. J. (1998). Ion microprobe study of plagioclase-basalt partition experiments at natural concentration levels of trace elements. *Geochimica et Cosmochimica Acta*, 62:1175–1193.

Blichert-Toft, J., Chauvel, C., and Albare, F. (1997). Separation of Hf and Lu for high-precision isotope analysis of rock samples by magnetic sector-multiple collector ICP-MS. *Contributions to Mineralogy and Petrology*, 127:248–260.

Blundy, J., Cashman, K., and Humphreys, M. (2006). Magma heating by decompression-driven crystallization beneath andesite volcanoes. *Nature*, 443(7107):76–80.

Blundy, J. D. and Holland, T. J. B. (1990). Calcic amphibole equilibria and a new amphibole-plagioclase geothermometer. *Contributions to Mineralogy and Petrology*, 104(2):208–224.

Borghini, G., Rampone, E., Zanetti, A., Class, C., Cipriani, A., Hofmann, A. W., and Goldstein, S. L. (2016). Pyroxenite Layers in the Northern Apennines Upper Mantle (Italy)Generation by Pyroxenite Melting and Melt Infiltration. *Journal of Petrology*, 57(4):625653.

Brunet, F. F., Korotaev, M. V., Ershov, A. V., and Nikishin, A. M. (2003). The South Caspian Basin: A review of its evolution from subsidence modelling. *Sedimentary Geology*, 156:119–148.

Buckley, V. J. E., Sparks, R. S. J., and Wood, B. J. (2006). Hornblende dehydration reactions during magma ascent at Soufriére Hills Volcano, Montserrat. *Contributions to Mineralogy and Petrology*, 69(4):319–327.

Bybee, G., Ashwal, L., Shirey, S., Horan, M., Mock, T., and Andersen, T. (2014). Pyroxene megacrysts in proterozoic anorthosites: Implications for tectonic setting, magma source and magmatic processes at the moho. *Earth and Planetary Science Letters*, 389:74 – 85.

Cashman, K. and Blundy, J. (2013). Petrological cannibalism: the chemical and textural consequences of incremental magma body growth. *Contributions to Mineralogy and Petrology*, 166(3):703–729.

Cawood, P. a., Hawkesworth, C. J., and Dhuime, B. (2012). The continental record and the generation of continental crust. *Geological Society of America Bulletin*, 125(1-2):14–32.

Cawthorn, R. G. and Collerson, K. D. (1974). The Recalculation of Pyroxene Parameters and the Estimation of Ferrous and Ferric lron Content from Electron Microprobe Analyses. *American Mineralogist*, 59:1203–1208.

Chapman, N. (1975). An Experimental Study of Spinel Clinopyroxenite Xenoliths from the Duncansby Ness Vent , Caithness , Scotland. *Contributions to Mineralogy and Petrology*, 230:223–230.

Charlier, B., Duchesne, J.-C., Vander Auwera, J., Storme, J.-Y., Maquil, R., and Longhi, J. (2010). Polybaric fractional crystallization of high-alumina basalt parental magmas in the EgersundOgna massif-type anorthosite (Rogaland, SW Norway) constrained by plagioclase and high-alumina orthopyroxene megacrysts. *Journal of Petrology*, 51(12):2515–2546.

Chernyshev, I., Lebedev, V., Bubnov, S., Arakelyants, M., and Goltsman, Y. (2002). Isotopic geochronology of Quaternary volcanic eruptions in the Greater Caucasus. *Geochemistry International*, 40:848–852.

Chernyshev, I. V., Bubnov, S. N., Lebedev, V. A., Goltsman, Y. V., Bairova, E. D., and Yakushev, A. I. (2014). Two Stages of Explosive Volcanism of the Elbrus Area: Geochronology, Petrochemical and Isotopic - Geochemical Characteristics of Volcanic Rocks, and Their Role in the Neogene-Quaternary Evolution of the Greater Caucasus. *Stratigraphy and Geological Correlation*, 22(1):96–121.

Chernyshev, I. V., Lebedev, V. A., and Arakelyants, M. M. (2006). K-Ar dating of quaternary volcanics: Methodology and interpretation of results. *Petrology*, 14(1):62–80.

Choi, M. S., Cheong, C.-S., Kim, J., and Shin, H. S. (2013). Hafnium isotope analysis of mixed standard solutions by multi-collector inductively coupled plasma mass spectrometry: an evaluation of isobaric interference corrections. *Journal of Analytical Science and Technology*, 4:1.

Chugaev, A. V., Chernyshev, I. V., Lebedev, V. A., and Eremina, A. V. (2013). Lead Isotope composition and origin of the quaternary lavas of Elbrus Volcano, the Greater Caucasus: High-precision MC-ICP-MS data. *Petrology*, 21(1):16–27.

Clift, P. D., Vannucchi, P., and Morgan, J. P. (2009). Crustal redistribution, crustmantle recycling and Phanerozoic evolution of the continental crust. *Earth-Science Reviews*, 97(14):80–104.

Colgan, J. P., Dumitru, T. A., McWilliams, M., and Miller, E. L. (2006). Timing of Cenozoic volcanism and Basin and Range extension in northwestern Nevada: New constraints from the northern Pine Forest Range. *GSA Bulletin*, 118:126–139.

Condie, K. C. (2014). Growth of continental crust: a balance between preservation and recycling. *Mineralogical Magazine*, 78(3):623–637.

Copley, A. and Jackson, J. (2006). Active tectonics of the Turkish-Iranian Plateau. *Tectonics*, 25:1–19.

Şengör, A. M. C. (2003). East Anatolian high plateau as a mantle-supported, north-south shortened domal structure. *Geophysical Research Letters*, 30(24):2–5.

Davidson, J., Turner, S., Handley, H., Macpherson, C., and Dosseto, A. (2007). Amphibole "sponge" in arc crust? *Geology*, 35(9):787–790.

Davidson, J., Turner, S., and Plank, T. (2013). Dy/Dy*: Variations arising from mantle sources and petrogenetic processes. *Journal of Petrology*, 54(3):525–537.

Davidson, P. M. (1994). Ternary iron, magnesium, calcium carbonates: A thermodynamic model for dolomite as an ordered derivative of calcite-structure solutions. *American Mineralogist*, 79:332–339.

Davies, J. H. and von Blanckenburg, F. (1995). Slab breakoff: A model of lithosphere detachment and its test in the magmatism and deformation of collisional orogens. *Earth and Planetary Science Letters*, 129:85–102.

de Laeter, J. R., Bohlke, J. K., de Bievre, P., Hidaka, H., Peiser, H. S., Rosman, K. J. R., and Taylor, P. D. P. (2003). Atomic weights of the elements. Review 2000 (IUPAC Technical Report). *Pure and Applied Chemistry*, 75(6):683–800.

de Lumley, M.-A., Bardintzeff, J.-M., Bienvenu, P., Bilcot, J.-B., Flamenbaum, G., Guy, C., Jullien, M., de Lumley, H., Nabot, J.-P., Perrenoud, C., Provitina, O., and Tourasse, M. (2008). Probable volcanic impact on the death of the Dmanisi Hominids. *Comptes Rendus Palevol*, 7(1):61–79.

de Sant Ana Barros, M. A., Júnior, F. C., Nardi, L. V. S., and Lima, E. F. (2009). Paleoproterozoic bimodal post-collisional magmatism in the southwestern Amazonian Craton, Mato Grosso, Brazil: Geochemistry and isotopic evidence. *Journal of South American Earth Sciences*, 27(1):11–23.

Deniel, C. and Pin, C. (2001). Single-stage method for the simultaneous isolation of lead and strontium from silicate samples for isotopic measurements. *Analytica Chimica Acta*, 426:95–103.

Dewey, J. F., Hempton, M. R., Kidd, W. S. F., and Sengor, A. M. C. (1986). Shortening of continental lithosphere: the neotectonics of eastern anatolia, a young collision zone. *Geological Society Special Publication*, 19:3–36.

Dilek, Y. and Altunkaynak, S. (2007). Cenozoic crustal evolution and mantle dynamics of post-collisional magmatism in western anatolia. *International Geology Review*, 49(5):431–453.

Dilek, Y., Imamverdiyev, N., and Altunkaynak, S. (2010). Geochemistry and tectonics of Cenozoic volcanism in the Lesser Caucasus (Azerbaijan) and the peri-Arabian region: collision-induced mantle dynamics and its magmatic fingerprint. *International Geology Review*, 52(4-6):536–578.

Dilek, Y. and Moores, E. M. (1999). A tibetan model for the early tertiary western united states. *Journal of the Geological Society*, 156(5):929–941.

Droop, G. T. R. (1987). A general equation for estimating Fe3+ concentrations in ferromagnesian silicates and oxides from microprobe analyses, using stoichiometric criteria. *Mineralogical Magazine*, 51:431–435.

Elkins-Tanton, L. T. (2005). Continental magmatism caused by lithospheric delamination. *Geological Society of America Special Papers*, 388:449–461.

Elliott, T., Plank, T., Zindler, A., White, W., and Bourdon, B. (1997). Element transport from slab to volcanic front at the mariana arc. *Journal of Geophysical Research: Solid Earth*, 102(B7):14991–15019.

England, P. C. and Houseman, G. A. (1988). The mechanics of the Tibetan Plateau. *Philosophical Transactions of the Royal Society of London. Series A, Mathematical and Physical Sciences*, 326:301–320.

Erdmann, S., Martel, C., Pichavant, M., and Kushnir, A. (2014). Amphibole as an archivist of magmatic crystallization conditions: problems, potential, and implications for inferring magma storage prior to the paroxysmal 2010 eruption of Mount Merapi, Indonesia. *Contributions to Mineralogy and Petrology*, 167(6):1–23.

Ershov, A. V., Brunet, M. F., Korotaev, M. V., Nikishin, A. M., and N. Bolotov, S. (1999). Late Cenozoic burial history and dynamics of the Northern Caucasus molasse basin: Implications for foreland basin modelling. *Tectonophysics*, 313:219–241.

Ershov, A. V., Brunet, M.-F., Nikishin, A. M., Bolotov, S. N., Nazarevich, B. P., and Korotaev, M. V. (2003). Northern Caucasus basin: thermal history and synthesis of subsidence models. *Sedimentary Geology*, 156(1-4):95–118.

Ershov, A. V. and Nikishin, A. M. (2004). Recent geodynamics of the caucasus-arabia-east africa region. *Geotectonics*, 38(2):123–136.

Ewart, A. (1982). The mineralogy and petrology of tertiary-recent orogenic volcanic rocks: with special reference to the andesitic-basaltic compositional range. In Thorp, R. S., editor, *Andesites: Orogenic Andesites and Related Rocks*, pages 25–95. John Wiley and Sons.

Ewart, A. and Griffin, W. (1994). Application of proton-microprobe data to trace-element partitioning in volcanic rocks. *Chemical Geology*, 117(1-4):251–284.

Faure, G. and Mensing, T. M. (2005). *Isotopes: Principles and Applications*. Wiley.

Fitton, J. G., James, D., and Leeman, W. P. (1991). Basic magmatism associated with late cenozoic extension in the western united states: Compositional variations in space and time. *Journal of Geophysical Research: Solid Earth*, 96(B8):13693–13711.

Forte, A., Cowgill, E., Bernardin, T., Kreylos, O., and Hamann, B. (2009). Late Cenozoic deformation of the Kura fold-thrust belt, southern Greater Caucasus. *Geological Society of America Bulletin*, 122(3-4):465–486.

Forte, A. M., Cowgill, E., Murtuzayev, I., Kangarli, T., and Stoica, M. (2013). Structural geometries and magnitude of shortening in the eastern Kura fold-thrust belt, Azerbaijan: Implications for the development of the Greater Caucasus Mountains. *Tectonics*, 32(3):688–717.

Forte, A. M., Cowgill, E., and Whipple, K. X. (2014). Transition from a singly vergent to doubly vergent wedge in a young orogen: The Greater Caucasus. *Tectonics*, 33:2077–2101.

Fuhrman, M. L. and Lindsley, D. H. (1988). Ternary-feldspar modeling and thermometry. *American Mineralogy*, 73:201–215.

Gabunia, L., Vekua, A., Lordkipanidze, D., Swisher, C. C., Ferring, R., Justus, A., Nioradze, M., Tvalchrelidze, M., Anton, S. C., Bosinski, G., Joris, O., de Lumley, M. A., Majsuradze, G., and Mouskhelishvili, A. (2000). Earliest Pleistocene hominid cranial remains from Dmanisi, Republic of Georgia: Taxonomy, geological setting, and age. *Science*, 288(5468):1019–1025.

Galer, S. J. G. (1999). Optimal double and triple spiking for high precision lead isotopic measurement. *Chemical Geology*, 157(3-4):255–274.

Garcia, M. O. and Jacobson, S. S. (1979). Crystal clots, amphibole fractionation and the evolution of calc-alkaline magmas. *Contributions to Mineralogy and Petrology*, 69(4):319–327.

Garcia, T., Feraud, G., Falgueres, C., de Lumley, H., Perrenoud, C., and Lordkipanidze, D. (2010). Earliest human remains in Eurasia: New Ar-40/Ar-39 dating of the Dmanisi hominid-bearing levels, Georgia. *Quaternary Geochronology*, 5(4):443–451.

Gazis, C. A., Lanphere, M., Taylor, H. P., and Gurbanov, A. (1995). $^{40}Ar/^{39}Ar$ and $^{18}O/^{16}O$ studies of the Chegem ash-flow caldera and the Eldjurta Granite : Cooling of two late Pliocene igneous bodies in the Greater Caucasus Mountains , Russia. *Earth and Planetary Science Letters*, 134:377–391.

Gerke, T. L., Kilinc, A. I., and Sack, R. O. (2005). Ti-content of high-Ca pyroxenes as a petrogenetic indicator: an experimental study of Mafic Alkaline Rocks from the Mt. Erebus volcanic region, Antarctica. *Contributions to Mineralogy and Petrology*, 148:735745.

Ginibre, C., Wörmer, G., and Kronz, A. (2002). Minor- and trace-element zoning in plagioclase: implications for magma chamber processes at Parinacota Volcano, northern Chile. *Contributions to Mineralogy and Petrology*, 143:300–315.

Golonka, J. (2004). Plate tectonic evolution of the southern margin of Eurasia in the Mesozoic and Cenozoic. *Tectonophysics*, 381:235–273.

Govinaraju, K., Potts, P. J., Webb, P. C., and Watson, J. S. (1994). 1994 Report on Whin Sill dolerite WS-E from England and Pitscurrie microgabbro PM-S from Scotland - Assessment by 104 international laboratories. *Geostandards Newsletter*, 18(2):211–300.

Green, D. H. and Falloon, T. J. (2005). Primary magmas at mid-ocean ridges, "hotspots," and other intraplate settings: Constraints on mantle potential temperature. *Geological Society of America Special Papers*, 388:217–247.

Green, T. and Watson, E. (1982). Crystallization of apatite in natural magmas under high pressure, hydrous conditions, with particular reference to orogenic rock series. *Contributions to Mineralogy and Petrology*, 79(1):96–105.

Gudjanidze, G. E. (2003). *Geological Map of Georgia [map]. Scale 1:500000.* Georgian State Department of Geology and National Oil Company "Saqnavtobi".

Guo, Z., Wilson, M., Liu, J., and Mao, Q. (2006). Post-collisional, Potassic and Ultrapotassic Magmatism of the Northern Tibetan Plateau: Constraints on Characteristics of the Mantle Source, Geodynamic Setting and Uplift Mechanisms. *Journal of Petrology*, 47(6):1177–1220.

Guo, Z., Wilson, M., Zhang, L., Zhang, M., Cheng, Z., and Liu, J. (2014). The role of subduction channel mélanges and convergent subduction systems in the petrogenesis of post-collisional K-rich mafic magmatism in NW Tibet. *Lithos*, 198-199:184–201.

Hammarstrom, J. M. and Zen, E.-a. (1986). Aluminum in hornblende; an empirical igneous geobarometer. *American Mineralogist*, 71(11-12):1297–1313.

Hart, S. R. (1984). A large-scale isotope anomaly in the Southern Hemisphere mantle. *Nature*, 309(28):753–757.

Hartley, M. and Thordarson, T. (2009). Melt segregations in a Columbia River Basalt lava flow: A possible mechanism for the formation of highly evolved mafic magmas. *Lithos*, 112:434–446.

Hawkesworth, C. J., Dhuime, B., Pietranik, a. B., Cawood, P. a., Kemp, a. I. S., and Storey, C. D. (2010). The generation and evolution of the continental crust. *Journal of the Geological Society*, 167(2):229–248.

Hawkesworth, C. J. and Kemp, A. I. S. (2006). The differentiation and rates of generation of the continental crust. *Chemical Geology*, 226:134–143.

Helz, R. T. and Thornber, C. R. (1987). Geothermometry of Kilauea Iki lava lake, Hawaii. *Bulletin of Volcanology*, 49(5):651–668.

Hermann, J. and Rubatto, D. (2009). Accessory phase control on the trace element signature of sediment melts in subduction zones. *Chemical Geology*, 265(34):512 – 526.

Hermann, J., Spandler, C., Hack, A., and Korsakov, A. V. (2006). Aqueous fluids and hydrous melts in high-pressure and ultra-high pressure rocks: Implications for element transfer in subduction zones. *Lithos*, 92(34):399–417.

Hernando, I. R., Petrinovic, I. A., Llambias, E. J., D'Elia, L., Gonzalez, P. D., and Aragon, E. (2016). The role of magma mixing and mafic recharge in the evolution of a back-arc quaternary caldera: The case of payn matr, western argentina. *Journal of Volcanology and Geothermal Research*, 311:150–169.

Holt, P. J., Allen, M. B., van Hunen, J., and Bjørnseth, H. M. (2010). Lithospheric cooling and thickening as a basin forming mechanism. *Tectonophysics*, 495(3-4):184–194.

Humphreys, M. C. S., Blundy, J. D., and Sparks, R. S. J. (2006). Magma evolution and open-system processes at Shiveluch volcano: Insights from phenocryst zoning. *Journal of Petrology*, 47(12):2303–2334.

Hunt, A. (2011). *Deciphering the sources of Cenozoic intra-plate volcanism in central Mongolia : A geochemical study*. PhD thesis, The Open University.

Ionov, D. A., Dupuy, C., O'Reilly, S. Y., Kopylova, M. G., and Genshaft, Y. S. (1993). Carbonated peridotite xenoliths from spitsbergen: implications for trace element signature of mantle carbonate metasomatism. *Earth and Planetary Science Letters*, 119(3):283 – 297.

Irvine, T. N. and Barragar, W. R. A. (1971). A guide to the chemical classification of the common volcanic rocks. *Canadian Journal of Earth Science*, 8:523–548.

Jagoutz, O. and Behn, M. D. (2013). Foundering of lower island-arc crust as an explanation for the origin of the continental moho. *Nature*, 504(7478):131–134.

Johnson, M. C. and Rutherford, M. J. (1989). Experimental calibration of the aluminum-in-hornblende geobarometer with application to long valley caldera (california) volcanic rocks. *Geology*, 17(9):837–841.

Jweda, J. (2014). *Geochemistry of the Tatara-San Pedro continental arc volcanic complex and implications for magmatism in the Chilean Southern Volcanic Zone*. PhD thesis, Columbia University.

Kaislaniemi, L., van Hunen, J., Allen, M. B., and Neill, I. (2014). Sublithospheric small-scale convection–A mechanism for collision zone magmatism. *Geology*, 42(4):291–294.

Karakhanian, A., Djrbashian, R., Trifonov, V., Philip, H., and Arakelian, S. (2002). Holocene-historical volcanism and active faults as natural risk factors for Armenia and adjacent countries. *Journal of Volcanology and Geothermal Research*, 113:319–344.

Karakhanian, A., Jrbashyan, R., Trifonov, V., Philip, H., Arakelian, S., Avagyan, A., Baghdasaryan, H., Davtian, V., and Ghouskassyan, Y. (2003). Volcanic hazards in the region of the Armenian Nuclear Power Plant. *Journal of Volcanology and Geothermal Research*, 126(1-2):31–62.

Kelemen, P. B., Hanghø j, K., and Greene, A. R. (2007). 3.18 - One View of the Geochemistry of Subduction-Related Magmatic Arcs, with an Emphasis on Primitive Andesite and Lower Crust. In Holland, H. D. and Turekian, K. K., editors, *Treatise on Geochemistry*, pages 1–70. Pergamon, Oxford.

Keskin, M. (2003). Magma generation by slab steepening and breakoff beneath a subduction-accretion complex: An alternative model for collision-related volcanism in Eastern Anatolia, Turkey. *Geophysical Research Letters*, 30(24):8046.

Keskin, M., Pearce, J. A., and Mitchell, J. G. (1998). Volcano-stratigraphy and geochemistry of collision-related volcanism on the Erzurum-Kars Plateau , northeastern Turkey. *Journal of Volcanology and Geothermal Research*, 85:355–404.

Kessel, R., Schmidt, M. W., Ulmer, P., and T., P. (2005). Trace element signature of subduction-zone fluids, melts and supercritical liquids at 120–180 km depth. *Nature*, 437:724 – 727.

Khalaf, E. E. D. A. H. (2012). Origin and evolution of post-collisional volcanism: an example from Neoproterozoic Dokhan volcanics at Gabal Nugara area, Northeastern Desert, Egypt. *Arabian Journal of Geosciences*, 5:663–695.

Kheirkhah, M., Allen, M., and Emami, M. (2009). Quaternary syn-collision magmatism from the Iran/Turkey borderlands. *Journal of Volcanology and Geothermal Research*, 182(1-2):1–12.

Kincaid, C. and Silver, P. (1996). The role of viscous dissipation in the orogenic process. *Earth and Planetary Science Letters*, 142:271–288.

King, S. D. and Anderson, D. L. (1998). Edge-driven convection. *Earth and Planetary Science Letters*, 160:289–296.

Klaver, M., Smeets, R. J., Koornneef, J. M., Davies, G. R., and Vroon, P. Z. (2015). Pb isotope analysis of ng size samples by TIMS equipped with a 10^{13} Ω resistor using a ^{207}Pb-^{204}Pb double spike. *Journal of Analytical and Atomic Spectrometry*.

Klimm, K., Blundy, J. D., and Green, T. H. (2008). Trace element partitioning and accessory phase saturation during H2O-saturated melting of basalt with implications for subduction zone chemical fluxes. *Journal of Petrology*, 49(3):523–553.

Knesel, K. M., Souza, Z. S., Vasconcelos, P. M., Cohen, B. E., and Silveira, F. V. (2011). Young volcanism in the Borborema Province, NE Brazil, shows no evidence for a trace of the Fernando de Noronha plume on the continent. *Earth and Planetary Science Letters*, 302(1-2):38–50.

Koronovskii, N. V. (2016). Stages of recent volcanism and problems of their correlation with landscape formation in the central caucasus. *Geotectonics*, 50(5):491–508.

Koronovsky, N. and Demina, L. (1996). Collisional volcanism pattern of the caucasian segment of the alpine belt. *Doklady of Academy of Sciences*, 350:510–522.

Koulakov, I., Zabelina, I., Amanatashvili, I., and Meskhia, V. (2012). Nature of orogenesis and volcanism in the Caucasus region based on results of regional tomography. *Solid Earth*, 3(2):327–337.

Kyle, P. R., Moore, J. A., and Thirlwall, M. F. (1992). Petrologic evolution of anorthoclase phonolite lavas at mount erebus, ross island, antarctica. *Journal of Petrology*, 33(4):849–875.

Lambart, S., Laporte, D., and Schiano, P. (2009). An experimental study of pyroxenite partial melts at 1 and 1.5 GPa: Implications for the major-element composition of Mid-Ocean Ridge Basalts. *Earth and Planetary Science Letters*, 288(12):335 – 347.

Le Bas, M. J., Maitre, R. W. L. E., and Streckeisen, A. (1986). A Chemical Classification of Volcanic Rocks Based on the Total Alkali-Silica Diagram. *Journal of Petrology*, 27(1984):745–750.

Le Fèvre, B. and Pin, C. (2001). An extraction chromatography method for Hf separation prior to isotopic analysis using multiple collection ICP-mass spectrometry. *Analytical chemistry*, 73(11):2453–2460.

Leake, B. E., Woolley, A. R., Arps, C. E. S., Birch, W. D., Gilbert, M. C., Grice, J. D., Hawthorne, F. C., Kato, A., Kisch, H. J., Krivovichev, V. G., Linthout, K., Laird, J., Mandarino, J., Maresch, W. V., Nickel, E. H., Rock, N. M. S., Schumacher, J. C., Smith, D. C., Stephenson, N. C. N., Ungaretti, L., Whittaker, E. J. W., and Youzhi, G. (1997). Nomenclature of amphiboles; report of the subcommittee on amphiboles of the international mineralogical association commission on new minerals and mineral names. *Mineralogical Magazine*, 61(2):295–321.

Lebedev, V., Chernyshev, I., Dudauri, O. Z., Arakelyants, M., Bairova, E. D., Goltsman, Y., Chugaev, A. V., and Vashakidze, G. (2003). The Samsari Volcanic Centre as an Example of Recent Volcanism in the Lesser Caucasus: K-Ar Geochronological and Sr-Nd isotopic Data. *Doklady Earth Sciences*, 393A:1323–1328.

Lebedev, V., Chernyshev, I., and Sharkov, E. (2011a). Geochronological Scale and Evolution of Late Cenozoic Magmatism with the Caucasian Segment of the Alpine Belt. *Doklady Earth Science*, 441:521–526.

Lebedev, V., Chernyshev, I., Vashakidze, G., Gudina, M., and Yakushev, A. (2012). Geochronology pf Miocene Volcanism in the Northern part of the Lesser Caucasus (Erusheti Highland, Georgia). *Doklady Earth Sciences*, 44:585–590.

Lebedev, V., Vashakidze, G., Arutyunyan, E., and Yakushev, A. (2011b). Geochronology and Evolutuion of Quaternary Volcanism at the Keli Highlands, Greater Caucasus. *Geochemistry International*, 49:1120–1144.

Lebedev, V. A. and Bubnov, S. N. (2006). Basic magmatism in the geological history of the Elbrus Neovolcanic area, greater Caucasus: Evidence from K-Ar and Sr-Nd isotope data. *Doklady Earth Sciences*, 406(1):37–40.

Lebedev, V. A., Bubnov, S. N., Chernyshev, I. V., Chugaev, A. V., Dudauri, O. Z., and Vashakidze, G. T. (2007a). Geochronology and genesis of subalkaline basaltic lava rivers at the Dzhavakheti highland, Lesser Caucasus: K-Ar and Sr-Nd isotopic data. *Geochemistry International*, 45(3):211–225.

Lebedev, V. A., Bubnov, S. N., Dudauri, O. Z., and Vashakidze, G. T. (2008a). Geochronology of Pliocene volcanism in the Dzhavakheti Highland (the Lesser Caucasus). Part 1: Western part of the Dzhavakheti Highland. *Stratigraphy and Geological Correlation*, 16(2):204–224.

Lebedev, V. A., Bubnov, S. N., Dudauri, O. Z., and Vashakidze, G. T. (2008b). Geochronology of Pliocene volcanism in the Dzhavakheti Highland (the Lesser Caucasus). Part 2: Eastern part of the Dzhavakheti Highland. Regional geological correlation. *Stratigraphy and Geological Correlation*, 16(5):553–574.

Lebedev, V. A., Bubnov, S. N., Dudauri, O. Z., and Vashakidze, G. T. (2011c). Geological (volcanological) map of Javakheti volcanic area (Lesser Caucasus), 1:200000, ed.2011-1. *Moscow*.

Lebedev, V. A., Chernyshev, I. V., and Arakelyants, M. M. (2004). Geochronology of the NeogeneQuaternary Dacitic Volcanism in the Northwestern Lesser Caucasus (Georgia). *Stratigraphy and Geological Correlation*, 12(1):85–101.

Lebedev, V. A., Chernyshev, I. V., Chugaev, A. V., Dudauri, O. Z., and Vashakidze, G. T. (2006). K-Ar age and Sr-Nd characteristics of subalkali basalts in the Central Georgian Neovolcanic region (Greater Caucasus). *Doklady Earth Sciences*, 408(1):657–661.

Lebedev, V. A., Chernyshev, I. V., Chugaev, A. V., Goltsman, Y. V., and Bairova, E. D. (2010a). Geochronology of eruptions and parental magma sources of Elbrus volcano, the Greater Caucasus: K-Ar and Sr-Nd-Pb isotope data. *Geochemistry International*, 48(1):41–67.

Lebedev, V. A., Chernyshev, I. V., Chugaev, A. V., and Vashakidze, G. T. (2007b). Geochronology of Quaternary volcanism of the Krestovyi Pass Region, Kazbek Neovolcanic Area, Greater Caucasus. *Doklady Earth Sciences*, 413(1):272–276.

Lebedev, V. A., Parfenov, A. V., Vashakidze, G. T., Chernyshev, I. V., and Gabarashvili, Q. A. (2014). Major Events in Evolution of the Kazbek Neovolcanic Center, Greater Caucasus: Isotope-Geochronological Data. *Doklady Earth Science*, 458(1):1092–1098.

Lebedev, V. A., Sakhno, V. G., and Yakushev, A. I. (2009). Long-lived center of youngest volcanism in the Borzhomi region of Georgia: Isotopic-geochronological evidence. *Doklady Earth Sciences*, 427(2):1020–1024.

Lebedev, V. A., Sakhno, V. G., and Yakushev, A. I. (2010b). Total duration and spatial migration of Quaternary volcanism in the Elbrus region, Greater Caucasus. *Doklady Earth Sciences*, 430(1):80–85.

Lebedev, V. A., Sharkov, E. V., Keskin, M., and Oyan, V. (2010c). Geochronology of Late Cenozoic volcanism in the area of Van Lake, Turkey: An example of development dynamics for magmatic processes. *Doklady Earth Sciences*, 433(2):1031–1037.

Lebedev, V. A. and Vashakidze, G. T. (2014). The catalogue of Quaternary volcanoes of the Greater Caucasus based on geochronological, volcanological and isotope-geochemical data. *Journal of Volcanology and Seismology*, 8(2):93–107.

Lebedev, V. A., Vashakidze, G. T., Arutyunyan, E. V., and Yakushev, A. I. (2011d). Geochronology and Evolution of Quaternary Volcanism at the Keli Highland, Greater Caucasus. *Geochemistry International*, 49(11):1120–1144.

Lebedev, V. A., Vashakidze, G. T., and Sakhno, V. G. (2008c). Potential volcanic danger in the Keli highland (Greater Caucasus): Evidence from isotopic-geochronological study of the youngest lavas. *Doklady Earth Sciences*, 418(1):169–173.

Li, B., Bagas, L., Gallardo, L. A., Said, N., Diwu, C., and McCuaig, T. C. (2013). Back-arc and post-collisional volcanism in the Palaeoproterozoic Granites-Tanami Orogen, Australia. *Precambrian Research*, 224:570–587.

Lofgren, G. E., Huss, G. R., and Wasserburg, G. (2006). An experimental study of trace-element partitioning between Ti-Al-clinopyroxene and melt: Equilibrium and kinetic effects including sector zoning. *American Mineralogist*, 91(10):1596–1606.

Maggi, A. and Priestley, K. (2005). Surface waveform tomography of the Turkish-Iranian plateau. *Geophysical Journal International*, 160:1068–1080.

Martin, R. J., O'Connor, T., Adamia, S., Szymanski, E., and Krasovec, M. (2012). Borjomi-kazbegi fault: Does it exist? *AGU Fall Meeting Abstracts*.

Mayringer, F., Treloar, P. J., Gerdes, a., Finger, F., and Shengelia, D. (2011). New age data from the Dzirula massif, Georgia: Implications for the evolution of the Caucasian Variscides. *American Journal of Science*, 311(5):404–441.

Mazhari, S. A., Bea, F., Amini, S., Ghalamghash, J., Molina, J. F., Montero, P., Scarrow, J. H., and Williams, I. S. (2009). The Eocene bimodal Piranshahr massif of the Sanandaj Sirjan Zone , NW Iran : a marker of the end of the collision in the Zagros orogen. *Journal of the Geological Society*, 166:53–69.

McKenzie, D. and O'Nions, R. (1991). Partial Melt Distributions from Inversion of Rare Earth Element Concentrations. *Journal of Petrology*, 32:1021–1091.

McQuarrie, N. and van Hinsbergen, D. J. J. (2013). Retrodeforming the arabia-eurasia collision zone: Age of collision versus magnitude of continental subduction. *Geology*, 41(3):315–318.

Mellors, R. J., Jackson, J., Myers, S., Gok, R., Priestley, K., Yetirmishli, G., Turkelli, N., and Godoladze, T. (2012). Deep earthquakes beneath the northern Caucasus: Evidence of active or recent subduction in Western Asia. *Bulletin of the Seismological Society of America*, 102(2):862–866.

Mibe, K., Kawamoto, T., Matsukage, K. N., Fei, Y., and Ono, S. (2011). Slab melting versus slab dehydration in subduction-zone magmatism. *Proceedings of the National Academy of Sciences*, 108(20):8177–8182.

Missenard, Y. and Cadoux, A. (2012). Can Moroccan Atlas lithospheric thinning and volcanism be induced by Edge-Driven Convection? *Terra Nova*, 24:27–33.

Morimoto, N., Fabries, J., Ferguson, A. K., Ginzburg, I. V., Ross, M., Seifert, F. A., Zussman, J., Aoki, K., and Gottardi, G. (1988). Nomenclature of pyroxenes. *American Mineralogist*, 73(9-10):1123–1133.

Mosar, J. O. N., Kangarli, T., Bochud, M., Glasmacher, U. A., Rast, A., Brunet, M.-F., Sosson, M., Institut, U. M. R., Terre, D., Case, P., Azur, C., Albert, R., and Sophia, E. (2010). Cenozoic Recent tectonics and uplift in the Greater Caucasus : a perspective from Azerbaijan. *Geological Society, London, Special Publications*, 340:261–280.

Muir, I. D. and Mattey, D. A. (1982). Pyroxene fractionation in ferrobasalts from galapagos spreading centre. *Mineralogical magazine*, 45:193–200.

Mumladze, T., Forte, A. M., Cowgill, E. S., Trexler, C. C., Niemi, N. A., Yilmaz, M. B., and Kellogg, L. H. (2015). Subducted, detached, and torn slabs beneath the Greater Caucasus. *GeoResJ*, 5:36–46.

Münker, C., Weyer, S., Scherer, E., and Mezger, K. (2001). Separation of high field strength elements (Nb, Ta, Zr, Hf) and Lu from rock samples for MC-ICPMS measurements. *Geochemistry, Geophysics, Geosystems*, 2.

Murphey, M. D., Sparks, R. S. J., Barclay, J., Carroll, M. R., and Brewer, T. S. (2000). Remobilization of andesite magma by intrusion of mafic magma at Souftiere Hills Volcano, Montserrat, West Indies. *Journal of Petrology*, 41(1):21–42.

Neill, I., Meliksetian, K., Allen, M. B., Navarsardyan, G., and Karapetyan, S. (2013). Pliocene-Quaternary volcanic rocks of NW Armenia: Magmatism and lithospheric dynamics within an active orogenic plateau. *Lithos*, 180-181:200–215.

Neill, I., Meliksetian, K., Allen, M. B., Navasardyan, G., and Kuiper, K. (2015). Petrogenesis of mafic collision zone magmatism: The armenian sector of the turkish-iranian plateau. *Chemical Geology*, 403:24–41.

Nimis, P. (1995). A clinopyroxene geobarometer for basaltic systems based on crystal-structure modeling. *Contributions to Mineralogy and Petrology*, 121(2):115–125.

Niu, Y. and O'Hara, M. J. (2009). {MORB} mantle hosts the missing Eu (Sr, Nb, Ta and Ti) in the continental crust: New perspectives on crustal growth, crustmantle differentiation and chemical structure of oceanic upper mantle. *Lithos*, 112(12):1–17.

Niu, Y., Zhoa, Z., Zhu, D., and Mo, X. (2013). Continental collision zones are primary sites for net continental crust growth - a testable hypothesis. *Earth-Science Reviews*, 127:96 – 110.

Nomade, S., Scao, V., Guillou, H., Messager, E., Mgeladze, A., Voinchet, P., Renne, P. R., Courtin-Nomade, A., Bardintzeff, J. M., Ferring, R., and Lordkipanidze, D. (2016). New 40Ar/39Ar, unspiked K/Ar and geochemical constraints on the Pleistocene magmatism of the Samtskhe-Javakheti highlands (Republic of Georgia). *Quaternary International*, 395:45–59.

Nowell, G. M., Pearson, D. G., Ottley, C. J., Schwieters, J., and Dowall, D. (2003). Long-term performance characteristics of a plasma ionisation multi-collector mass spectrometer (PIMMS): The Thermofinnigan neptune. In Holland, G. and Tanner, S. D., editors, *Plasma Source Mass Spectrometry: Applications and Emerging Technologies*, pages 307–320. The Royal Society of Chemistry.

O'Connor, T., Szymanski, E., Krasovec, M., and Adamia, S. (2006). Rethinking the tectonic model of the caucasus: an investigation of the southern section of the proposed brojomi-kazbegi fault. *Geophys Res Abs*, page p. 09746.

Okay, A. I., Zattin, M., and Cavazza, W. (2010). Apatite fission-track data for the Miocene Arabia-Eurasia collision. *Geology*, 38(1):35–38.

Orejana, D., Villaseca, C., and Paterson, B. a. (2006). Geochemistry of pyroxenitic and hornblenditic xenoliths in alkaline lamprophyres from the Spanish Central System. *Lithos*, 86(1-2):167–196.

Özdemir, Y. and Güleç, N. (2014). Geological and geochemical evolution of the quaternary süphan stratovolcano, eastern anatolia, turkey: Evidence for the lithosphereasthenosphere interaction in post-collisional volcanism. *Journal of Petrology*, 55(1):37–62.

Palme, H. and O'Neill, H. (2014). 3.1 - cosmochemical estimates of mantle composition. In Holland, H. D. and Turekian, K. K., editors, *Treatise on Geochemistry (Second Edition)*, pages 1 – 39. Elsevier, Oxford, second edition edition.

Patchett, P. J. and Tatsumoto, M. (1980). A routine high-precision method for Lu-Hf isotope geochemistry and chronology. *Contributions to Mineralogy and Petrology*, 75(3):263–267.

Pearce, J. A., Bender, J., Delong, S. E., Kidd, W. S. F., Low, P. J., Guner, Y., Saroglu, F., Yilmaz, Y., Moorbath, S., and Mitchell, J. (1990). Genesis of collision volcanism in Eastern Anatolia, Turkey. *Journal of Volcanology and Geothermal Research*, 44(1-2):189–229.

Pertermann, M. and Hirschmann, M. M. (2002). Trace-element partitioning between vacancy-rich eclogitic clinopyroxene and silicate melt. *American Mineralogist*, 87:1365–1376.

Pertermann, M. and Hirschmann, M. M. (2003). Partial melting experiments on a MORB-like pyroxenite between 2 and 3 GPa: Constraints on the presence of pyroxenite in basalt source regions from solidus location and melting rate. *Journal of Geophysical Research*, 108(B2):2125, doi:10.1029/2000JB000118.

Pfänder, J. A., Münker, C., Stracke, A., and Mezger, K. (2007). Nb/Ta and Zr/Hf in ocean island basalts Implications for crustmantle differentiation and the fate of Niobium. *Earth and Planetary Science Letters*, 254(12):158 – 172.

Philip, H., Cisternas, A., Gvishiani, A., and Gorshkuv, A. (1989). The Caucasus : an actual example of the initial stages of continental collision. *Tectonophysics*, 161:1–21.

Plank, T. (2005). Constraints from thorium/lanthanum on sediment recycling at subduction zones and the evolution of the continents. *Journal of Petrology*, 46(5):921–944.

Plank, T. and Langmuir, C. H. (1998). The chemical composition of subducting sediment and its consequences for the crust and mantle. *Chemical Geology*, 145(3-4):325–394.

Platt, J. P. and England, P. C. (1994). Convective removal of lithosphere beeath mountain belts: Thermal and mechanical consequences. *American Journal of Science*, 293:307–336.

Plechov, P. Y., Shcherbakov, V. D., and Dirksen, O. V. (2008). Opacitization conditions of hornblende in Bezymyannyi Volcano andesites (March 30, 1956 eruption. *Petrology*, 16(1):19–35.

Poli, S. and Schmidt, M. W. (2002). Petrology of subducted slabs. *Annual Review of Earth and Planetary Sciences*, 30(1):207–235.

Potts, P. J., Tindle, A. G., and Webb, P. (1992). *Geochemical reference material compositions: rocks, minerals, sediments, soils, carbonates, refractories & ores used in research & industry*. Taylor & Francis.

Prelević, D., Foley, S. F., Romer, R., and Conticelli, S. (2008). Mediterranean tertiary lamproites derived from multiple source components in postcollisional geodynamics. *Geochimica et Cosmochimica Acta*, 72:2125–2156.

Putirka, K. (2016). Amphibole thermometers and barometers for igneous systems and some implications for eruption mechanisms of felsic magmas at arc volcanoes. *American Mineralogist*, 101:841–858.

Putirka, K. D. (2008). Thermometers and barometers for volcanic systems. *Reviews in Mineralogy and Geochemistry*, 69(1):61–120.

Raczek, I., Jochum, K. P., and Hofmann, A. W. (2003). Neodymium and strontium isotope data for USGS reference materials BCR-1, BCR-2, BHVO-1, BHVO-2, AGV-1, AGV-2, GSP-1, GSP-2 and eight MPI-DING reference glasses. *Geostandards Newsletter*, 27(2):173 – 179.

Ramsey, M. H., Potts, P. J., Webb, P. C., Watkins, P., Watson, J. S., and Coles, B. J. (1995). An objective assessment of analytical method precision: comparison of ICP-AES and XRF for the analysis of silicate rocks. *Chemical Geology*, 124(1-2):1–19.

Rapp, R. P. and Watson, E. B. (1995). Dehydration melting of metabasalts at 8–32 kbar: Implications for continental growth and crust-mantle recycling. *Journal of Petrology*, 36:891–931.

Rebaï, S., Philip, H., Dorbath, L., Borissoft, B., Haessler, H., and Cisternas, A. (1993). Active Tectonics in the Lesser Caucasus: Coexistence of compressive and extensional structures. *Tectonics*, 12(5):1089–1114.

Reilinger, R., McClusky, S., Vernant, P., Lawrence, S., Ergintav, S., Cakmak, R., Ozener, H., Kadirov, F., Guliev, I., Stepanyan, R., Nadariya, M., Hahubia, G., Mahmoud, S., Sakr, K., ArRajehi, A., Paradissis, D., Al-Aydrus, a., Prilepin, M., Guseva, T., Evren, E., Dmitrotsa, A., Filikov, S. V., Gomez, F., Al-Ghazzi, R., and Karam, G. (2006). GPS constraints on continental deformation in the Africa-Arabia-Eurasia continental collision zone and implications for the dynamics of plate interactions. *Journal of Geophysical Research: Solid Earth*, 111:1–26.

Rhodes, J., Dungan, M., Blanchard, D., and Long, P. (1979). Magma mixing at mid-ocean ridges: Evidence from basalts drilled near 22 n on the mid-atlantic ridge. *Tectonophysics*, 55:35–61.

Ridolfi, F. and Renzulli, A. (2012). Calcic amphiboles in calc-alkaline and alkaline magmas: thermobarometric and chemometric empirical equations valid up to 1130 C and 2.2 GPa. *Contributions to Mineralogy and Petrology*, 163:877–895.

Ridolfi, F., Renzulli, A., and Puerini, M. (2010). Stability and chemical equilibrium of amphibole in calc-alkaline magmas: an overview, new thermobarometric formulations and application to subduction-related volcanoes. *Contributions to Mineralogy and Petrology*, 160:45–66.

Robertson, A. H. F. (2000). Mesozoic-tertiary tectonic-sedimentary evolution of a south tethyan oceanic basin and its margins in southern turkey. *Geological Society, London, Special Publications*, 173(1):97–138.

Roeder, P. and Emslie, R. (1970). Olivine-liquid equilibrium. *Contributions to Mineralogy and Petrology*, 29(4):275–289.

Rolland, Y., Perincek, D., Kaymakci, N., Sosson, M., Barrier, E., and Avagyan, A. (2012). Evidence for ∼80-75Ma subduction jump during Anatolide-Tauride-Armenian block accretion and ∼48Ma Arabia-Eurasia collision in Lesser Caucasus-East Anatolia. *Journal of Geodynamics*, 56-57:76–85.

Rudnick, R. and Gao, S. (2003). 3.01 - composition of the continental crust. In Holland, H. D. and Turekian, K. K., editors, *Treatise on Geochemistry*, pages 1 – 64. Pergamon, Oxford.

Ruprecht, P. and Wörner, G. (2007). Variable regimes in magma systems documented in plagioclase zoning patterns: El Misti stratovolcano and Andahua monogenetic cones. *Journal of Volcanology and Geothermal Research*, 165(34):142 – 162.

Rutherford, M. J. and Hill, P. M. (1993). Magma ascent rates from amphibole breakdown: An experimental study applied to the 1980–1986 mount st. helens eruptions. *Journal of Geophysical Research*, 98(B11):19667–19685.

Saintot, A., Brunet, M. F., Yakovlev, F., Sebrier, M., Stephenson, R., Ershov, A., Chalot-Prat, F., and McCann, T. (2006). The Mesozoic-Cenozoic tectonic evolution of the Greater Caucasus. In Gee, D. G. and Stephenson, R. A., editors, *Geological Society London Memoirs*, volume 32, pages 277–289. Geological Society, London.

Samaniego, P., Martin, H., Monzier, M., Robin, C., Fornari, M., Eissen, J.-P., and Cotten, J. (2005). Temporal evolution of magmatism in the northern volcanic zone of the Andes: The geology and petrology of Cayambe Volcanic Complex (Ecuador). *Journal of Petrology*, 46(11):2225–2252.

Sarker, G. and Abers, G. A. (1999). Lithospheric temperature estimates from seismic attenuation across range fronts in southern and central Eurasia. *Geology*, 27:427–430.

Schmidt, M. W. (1992). Amphibole composition in tonalite as a function of pressure: an experimental calibration of the al-in-hornblende barometer. *Contributions to Mineralogy and Petrology*, 110(2):304–310.

Scholl, D. W. and von Huene, R. (2007). Crustal recycling at modern subduction zones applied to the pastissues of growth and preservation of continental basement crust, mantle geochemistry, and supercontinent reconstruction. *Geological Society of America Memoirs*, 200:9–32.

Seghedi, I., Maenco, L., Downes, H., Mason, P. R. D., Szakács, A., and Pécskay, Z. (2011). Tectonic significance of changes in post-subduction Pliocene-Quaternary magmatism in the south east part of the Carpathian-Pannonian Region. *Tectonophysics*, 502:146–157.

Sharkov, E., Lebedev, V., Chugaev, A., Zabarinskaya, L., Rodnikov, A., Sergeeva, N., and Safonova, I. (2014). The Caucasian-Arabian segment of the Alpine-Himalayan collisional belt: Geology, volcanism and neotectonics. *Geoscience Frontiers*, 5:1–11.

Shaw, D. M. (1970). Trace element fractionation during anatexis. *Geochimica et Cosmochimica Acta*, 34(2):237 – 243.

Shcherbakov, V. D., Plechov, P. Y., Izbekov, P. E., and Shipman, J. S. (2011). Plagioclase zoning as an indicator of magma processes at Bezymianny Volcano, Kamchatka. *Contributions to Mineralogy and Petrology*, 162(1):83–99.

Sisson, T. and Bacon, C. (1999). Gas-driven filter pressing in magmas. *Geology*, 27(7):613–616.

Skobeltsyn, G., Mellors, R. J., Gök, R., Turkelli, N., Yetirmishli, G., and Sandvol, E. (2014). Upper mantle S wave velocity structure of the East Anatolian-Caucasus region. *Tectonics*, 33:207–221.

Skora, S. and Blundy, J. (2010). High-pressure hydrous phase relations of radiolarian clay and implications for the involvement of subducted sediment in arc magmatism. *Journal of Petrology*, 51(11):2211–2243.

Smith, I. E. and Milsom, J. S. (1984). Late cenozoic volcanism and extension in eastern papua. *Geological Society, London, Special Publications*, 16(1):163–171.

Somin, M. L. (2011). Pre-jurassic basement of the greater caucasus : Brief overview. *Turkish Journal of Earth Sciences*, 20:545–610.

Song, S., Niu, Y., Su, L., Zhang, C., and Zhang, L. (2014). Continental orogenesis from ocean subduction, continent collision/subduction, to orogen collapse, and orogen recycling: The example of the North Qaidam UHPM belt, NW China. *Earth-Science Reviews*, 129:59–84.

Sosson, M., Rolland, Y., Mller, C., Danelian, T., Melkonyan, R., Kekelia, S., Adamia, S., Babazadeh, V., Kangarli, T., Avagyan, A., Galoyan, G., and Mosar, J. (2010). Subductions, obduction and collision in the Lesser Caucasus (Armenia, Azerbaijan, Georgia), new insights. *Geological Society, London, Special Publications*, 340(1):329–352.

Stampfli, G. M. and Borel, G. D. (2002). A plate tectonic model for the Paleozoic and Mesozoic constrained by dynamic plate boundaries and restored synthetic oceanic isochrons. *Earth and Planetary Science Letters*, 196(1-2):17–33.

Stern, R. J. and Scholl, D. W. (2010). Yin and yang of continental crust creation and destruction by plate tectonic processes. *International Geology Review*, 52(1):1–31.

Thirlwall, M. F. (1991). Long-term reproducibility of multicollector Sr and Nd isotope ratio analysis. *Chemical Geology: Isotope Geoscience section*, 94(2):85–104.

Thirlwall, M. F. (2000). Inter-laboratory and other errors in Pb isotope analyses investigated using a 207Pb-204Pb double spike. *Chemical Geology*, 163(14):299–322.

Thirlwall, M. F. (2002). Multicollector ICP-MS analysis of Pb isotopes using a 207Pb-204Pb double spike demonstrates up to 400 ppm/amu systematic errors in Tl-normalization. *Chemical Geology*, 184(34):255–279.

Thompson, M., Potts, P. J., Kane, J. S., Webb, P. C., and Watson, J. S. (2000). GeoPT4. An International Proficiency Test for Analytical Geochemistry Laboratories - Report on Round 4 (March 1999). *Geostandards Newsletter*, 24(1):E1–E37.

Thompson, R. N. (1974). Some high-pressure pyroxenes. *Mineralogical Magazine*, 2(September):768–787.

Thompson, R. N., Gibson, S. A., Dickin, A. P., and Smith, P. M. (2001). Early cretaceous basalt and picrite dykes of the southern etendeka region, nw namibia: Windows into the role of the tristan mantle plume in paranetendeka magmatism. *Journal of Petrology*, 42(11):2049–2081.

Turner, S., Arnaud, N., Liu, J., Rogers, N., Hawkesworth, C., Harris, N., Kelley, S., van Calsteren, P., and Deng, W. (1996). Post-collision, shoshonitic volcanism on the tibetan plateau: Implications for convective thinning of the lithosphere and the source of ocean island basalts. *Journal of Petrology*, 37(1):45–71.

Tutberidze, B. (2012). Cenozoic Volcanism of the Caucasian Mobile Belt in Georgia , its Geological-Petrological Peculiarities and. *Turkish Journal of Earth Science*, 21:799–815.

Ulfbeck, D., Baker, J., Waight, T., and Krogstad, E. (2003). Rapid sample digestion by fusion and chemical separation of Hf for isotopic analysis by MC-ICPMS. *Talanta*, 59(2):365–373.

Upton, B., Aspen, P., and Hinton, R. (2001). Pyroxenite and granulite xenoliths from beneath the Scottish Northern Highlands Terrane: evidence for lower-crust/upper-mantle relationships. *Contributions to Mineralogy and Petrology*, 142(2):178–197.

van Hunen, J. and Allen, M. B. (2011). Continental collision and slab break-off: A comparison of 3-D numerical models with observations. *Earth and Planetary Science Letters*, 302(1-2):27–37.

Vincent, S. J., Morton, A. C., Carter, A., Gibbs, S., and Barabadze, T. G. (2007). Oligocene uplift of the Western Greater Caucasus: an effect of initial Arabia-Eurasia collision. *Terra Nova*, 19(2):160–166.

Watson, E. B. (1980). Apatite and phosphorus in mantle source regions: An experimental study of apatite/melt equilibria at pressures to 25 kbar. *Earth and Planetary Science Letters*, 51(2):322–335.

Watson, J. S. (1996). Fast , Simple Method of Powder Pellet Preparation for X-Ray Fluorescence Analysis. *X-Ray Spectrometry*, 25(February):173–174.

Weis, D., Kieffer, B., Hanano, D., Nobre Silva, I., Barling, J., Pretorius, W., Maerschalk, C., and Mattielli, N. (2007). Hf isotope compositions of U.S. Geological Survey reference materials. *Geochemistry, Geophysics, Geosystems*, 8(6).

Weis, D., Kieffer, B., Maerschalk, C., Barling, J., De Jong, J., Williams, G. a., Hanano, D., Pretorius, W., Mattielli, N., Scoates, J. S., Goolaerts, a., Friedman, R. M., and Mahoney, J. B. (2006). High-precision isotopic characterization of USGS reference materials by TIMS and MC-ICP-MS. *Geochemistry Geophysics Geosystems*, 7(8).

Wenk, H. R. and Weiss, L. E. (1982). Al-rich calcic pyroxene in pseudotachylite: An indicator of high pressure and high temperature? *Tectonophysics*, 84(I 982):329–341.

Westaway, R. (1994). Present-day kinematics of the Middle East and eastern Mediterranean. *Journal of Geophysical Research*, 99:12071–12090.

Wilkinson, J. F. G. (1976). Contributions to Mineralogy and Some Subcalcic Clinopyroxenites from Salt Lake Crater , Oahu , and Their Petrogenetic Significance. *Contributions to Mineralogy and Petrology*, 201:181–201.

Williams, H. M., Turner, S. P., Pearce, J. A., Kelley, S. P., and Harris, N. B. W. (2004). Nature of the Source Regions for Post-collisional, Potassic Magmatism in Southern and Northern Tibet from Geochemical Variations and Inverse Trace Element Modelling. *Journal of Petrology*, 45(3):555–607.

Wilson, M. (1989). *Igneous Petrogenesis: A global tectonic approach*. Springer, Netherlands.

Woodhead, J. D. and Hergt, J. M. (2000). Pb-Isotope Analyses of USGS Reference Materials. *Geostandards Newsletter*, 24(1):33–38.

Workman, R. K. and Hart, S. R. (2005). Major and trace element composition of the depleted MORB mantle (DMM). *Earth and Planetary Science Letters*, 231(1-2):53–72.

Yaxley, G. M., Crawford, A. J., and Green, D. H. (1991). Evidence for carbonatite metasomatism in spinel peridotite xenoliths from western victoria, australia. *Earth and Planetary Science Letters*, 107(2):305 – 317.

Zabelina, I., Koulakov, I., Amanatashvili, I., Khrepy, S. E., and Al-Arifi, N. (2016). Seismic structure of the crust and uppermost mantle beneath caucasus based on regional earthquake tomography. *Journal of Asian Earth Sciences*, 119:87–99.

Zakariadze, G. S., Dilek, Y., Adamia, S., Oberhänsli, R., Karpenko, S., Bazylev, B., and Solov'eva, N. (2007). Geochemistry and geochronology of the Neoproterozoic Pan-African Transcaucasian Massif (Republic of Georgia) and implications for island arc evolution of the late Precambrian Arabian–Nubian Shield. *Gondwana Research*, 11(1-2):92–108.

Zeck, H. P., Kristensen, a. B., and Williams, I. S. (1998). Post-collisional volcanism in a sinking slab setting-crustal anatectic origin of pyroxene-andesite magma, Caldear Volcanic Group, Neogene Alboran volcanic province, southeastern Spain. *Lithos*, 45:499–522.

Zhang, J., Davidson, J. P., Humphreys, M. C. S., Macpherson, C. G., and Neill, I. (2015). Magmatic enclaves and andesitic lavas from mt. lamington, papua new guinea: Implications for recycling of earlier-fractionated minerals through magma recharge. *Journal of Petrology*, 56(11):2223–2256.

Zor, E. (2008). Tomographic evidence of slab detachment beneath eastern Turkey and the Caucasus. *Geophysical Journal International*, 175:1273–1282.